Processing considerations of silk fibroin for nanomedicine and eco-sensing applications

Saphia Matthew

Strathclyde Institute of Pharmacy and Biomedical Sciences

University of Strathclyde

Glasgow, UK

A thesis presented in fulfilment of the requirements for the degree of Doctor of Philosophy.

Feb 2023

Declaration

This thesis is the result of the author's original research. It has been composed by the author and has not been previously submitted for examination which has led to the award of a degree.

Signed:

Date: 04/02/2024

Acknowledgements

I would like to gratefully acknowledge the support, guidance and, encouragement from my first supervisor, Professor Philipp Seib, throughout my PhD. My sincerest gratitude to my second supervisor Professor Yvonne Perrie for supporting me with nanoparticle manufacture methods. I would also like to thank Dr Deborah Bowering, Dr Thomas McGlone, Dr Alice Turner and, Dr Christoph Busche for training in FTIR, thermal analysis, scanning electron microscopy and, contact angle goniometry.

I would like to thank the financial support from Medical Research Scotland and for funding my PhD. I would like to gratefully acknowledge the EPSRC Future CMAC Research Hub and SIPBS for facilitating equipment and support throughout my research.

I would like to thank the members of the Seib lab. Particularly to Dr John Totten, Dr Suttinee Phuagkhaopong, Dr Gemma Egan, Dr Jirada Kaewchuchuen and, Dr Kimia Witte for welcoming, training and, supporting me when starting out the PhD. Thanks to KJ, Lana and, Erum for allowing me to share my experience and providing me with different ideas.

Finally, thank you to my family and friends for their love and sharing their time with me throughout the PhD.

Abstract

Silk has demonstrated utility across a range of biomedical applications as it can be processed into several different material formats, such as films and nanoparticles. The translation of silk nanoparticle production to industrial scales can be aided through insight into the property drifts incited by nanoprecipitation scale-up and the identification of critical process parameters to maintain throughout scaling. Therefore, the principle hypothesis of this thesis is that silk processing methods can have improved scalability, specifically the manufacture of silk nanoparticles which are suitable for anticancer nanomedicine applications.

To validate this hypothesis, nanoprecipitation conditions for the manufacture of native silk nanoparticles are established using a simple semi-batch method at the lab scale that reduced special-cause variation and improved mixing efficiency (Matthew, S. A. L. *et al*., *ACS Biomater. Sci. Eng*. **2020**, *6*, 6748−6759) (**Chapter 2**). The stirring rate was an important parameter affecting nanoparticle size and yield, while the initial dropping height directly affected nanoparticle yield. Varying the nanoparticle standing time in the mother liquor between 0 and 24 h did not significantly affect nanoparticle physicochemical properties.

Next, the impact of key process and formulation parameters on the flow and mixing properties of native silk nanoprecipitation, as well as the resulting nanoparticle performance characteristics, are assessed in semi-batch and microfluidic format (Matthew, S. A. L. *et al*., *RSC Adv.* **2022**, *12*, 7357−7373) (**Chapter 3**). At flow rates where the shear rate was below the critical shear rate for silk, increasing the concentration of silk in both bulk and micro-mixing processes resulted in particle populations of increased sphericity, lower size, and lower polydispersity index. At high flow rates, where the critical shear rate was exceeded, the increased supersaturation with increasing concentration was counteracted by increased rates of shear-induced assembly.

Then, the reproducibility of silk nanoprecipitation on volumetric scale-up in low-shear, semi-batch systems is reported and the reproducibility of chip parallelization for volumetric scale-up in a high shear, staggered herringbone micromixer is estimated (Matthew, S. A. L. *et al*., *Molecules* **2022**, *27*, 2368) (**Chapter 4**). Silk precursor feeds processed in an unstirred semi-batch system displayed significant changes in the nanoparticle physicochemical and crystalline properties following a 12-fold increase in volumetric scale between 1.8 and 21.9 mL. Conversely, microfluidic manufacture showed high between-batch repeatability and between-chip reproducibility across four participants and microfluidic chips.

Silk nanoparticle properties can be improved by heterogenous chemical modification of the surface. Silk nanomedicines can then be achieved using surface adsorption to load the preformed nanoparticles with antioxidants. Due to the impact of COVID-19 (SARS-CoV-2) our working practices were impacted, and a new project was devised. Semi-crystalline silk eco-sensors were designed using scalable origami folding of silk films and manufacture optimized by investigating process parameters, including diazonium coupling chemistry and natural dye adsorption (Matthew, S. A. L. *et al*. *ACS Appl*. *Bio Materials* **2022**, *5*, 3658–3666) (**Chapter 5**). Iron oxide spiking resulted in semi-autonomous movement in the presence of a magnetic field and azo-modification increased the film electromagnetic field strength. The optimized native and azo-silk, iron oxide spiked films could be loaded with natural dyes which indicated pH by eye and digital image colorimetry. A practical application was demonstrated—a battery-free origami silk boat—as a colorimetric sensor for waterborne pollutants which was reusable at least five times.

Overall, this thesis established key process and formulation parameters of silk nanoprecipitation in semi-batch and microfluidic formats and introduces silk eco-sensors by merging heterogeneous chemical modification, surface adsorption of natural dyes, responsive actuation, and origami techniques (**Chapter 6**).

Research Outputs

Publications

i. **Matthew**, **S. A. L.**; Seib, F. P. Silk Bioconjugates: From Chemistry and Concept to Application, *ACS Biomater. Sci. Eng.* **2024**, *10*, 12–28. DOI: 10.1021/acsbiomaterials.2c01116. (Journal IF: 5.8; Citations: 6)

ii. **Matthew***, **S. A. L.**; Egan*, G.; Witte, K.; Kaewchuchuen, J.; Phuagkhaopong, S.; Totten, J. D.; Seib, F. P. Smart Silk Origami as Eco-Sensors for Environmental Pollution, *ACS Appl. Bio Materials* **2022**, *5*, 3658–3666. DOI: 10.1021/acsabm.2c00023. (Journal IF: 4.7; Citations: 2)

iii. **Matthew**, **S. A. L.**; Rezwan, R.; Perrie, Y.; Seib, F. P. Volumetric scalability of microfluidic and semi-batch silk nanoprecipitation methods, *Molecules* **2022**, *27*, 2368. DOI: 10.3390/molecules27072368. (Journal IF: 4.6; Citations: 6)

iv. **Matthew**, **S. A. L.**; Rezwan, R.; Kaewchuchuen, J.; Perrie, Y.; Seib, F. P. Mixing and flow-induced nanoprecipitation for morphology control of silk fibroin self-assembly, *RSC Adv.* **2022**, *12*, 7357−7373. DOI: 10.1039/D1RA07764C. (Journal IF: 3.9; Citations: 5)

v. **Matthew**, **S. A. L.**; Totten, J. D.; Phuagkhaopong, S.; Egan, G.; Witte, K.; Perrie, Y.; Seib, F. P. Silk nanoparticle manufacture in semi-batch format, *ACS Biomater. Sci. Eng*. **2020**, *6*, 6748−6759. DOI: 10.1021/acsbiomaterials.0c01028. (Journal IF: 5.8; Citations: 14)

vi. Kaewchuchuen, J.; **Matthew**, **S. A. L.**; Phuagkhaopong, S.; Bimbo, L. M.; Seib, F. P. Functionalising silk hydrogels with hetero- and homotypic nanoparticles, *RSC Adv.* **2024**, *14*, 3525-3535. DOI: 10.1039/D3RA07634B. (Journal IF: 3.9)

vii. Egan, G.; Phuagkhaopong, S.; **Matthew**, **S. A. L.**; Connolly, P.; Seib, F. P. Impact of silk hydrogel secondary structure on hydrogel formation, silk leaching and *in vitro*

response, *Sci. Rep*. **2022**, *12*, 3729. DOI: 10.1038/s41598-022-07437-4. (Journal IF: 4.6; Citations: 10)

Conference contributions

Abstracts for conference contributions are listed in Appendices A – C.

A. **Matthew, S. A. L.**; Phuagkhaopong, S.; Perrie; Y.; Seib, F. P. (2022) 'Silk fibroin-anthracycline nano-sized delivery systems for breast cancer treatment'. Poster presentation at **3rd International Workshop on Insect Bio-inspired Technologies** 17 November 2022 09:00 – 18 November 2022 12:30, Edinburgh, United Kingdom.
B. **Matthew, S. A. L.**; Rezwan, R.; Perrie, Y.; Seib, F. P. (2022) 'Morphology control of silk fibroin nanoprecipitation under bulk and microfluidic mixing regimes'. Poster presentation at **RSC Chemical Nanoscience and Nanotechnology Network Annual Symposium** 17 January 2022 12:00 – 18 January 2022 14:00, London, United Kingdom.
C. **Matthew, S. A. L.**; Rezwan, R.; Kaewchuchuen, J.; Perrie, Y.; Seib, F. P. (2022) 'Flow control of silk fibroin nanoparticle morphology in microfluidic and semi-batch mixing regimes'. Oral Presentation at the **RSC Particle Characterization Interest Group The FORGE: Hybrid Conference on Particle Characterization** 23 March 2022 09:00 – 24 March 2022 13:00, Belfast, United Kingdom.

Grants Awarded

i. Mac Robertson Travel Grant 2022, University of Glasgow and the University of Strathclyde.

Table of Contents

List of Figures

List of Tables

List of Abbreviations

Abbreviation	Explanation
°C	Degrees Celsius
× g	G-force
Aq.	Aqueous
ANOVA	Analysis of variance
DLS	Dynamic light scattering
DSC	Dynamic scanning calorimetry
EPR	Enhanced permeation and retention effect
FDA	Food and Drug Administration
FSD	Fourier self-deconvolution
FTIR	Fourier transform infrared spectroscopy
FWHM	Full width at half-maximum
h	Hours
Lab	The CIELAB color space; Lightness-a axis-b axis
LiBr	Lithium bromide
log D	Distribution coefficient
log P	Partition coefficient
min	Minute
mV	Millivolt
MW	Molecular weight
Na_2CO_3	Sodium carbonate
PDB	Protein Data Bank
PDI	Polydispersity index
PEG	Polyethylene glycol
pKa	Apparent acid dissociation constant
PI	95% prediction interval
r	95% repeatability limit
R	95% reproducibility limit
RGB	The RGB color space
SD	Standard deviation
SEM	Scanning electron microscope
SD	Standard deviation
s_L	Between-participant standard deviation

s_r	Repeatability standard deviation
s_R	Reproducibility standard deviation
$s_{\bar{x}}$	Standard deviation of participant averages
TGA	Thermogravimetric analysis
TST-activated mPEG	Methoxypolyethylene glycol activated with cyanuric chloride
$\bar{x}$	Average of participant averages

Chapter 1: Introduction

This chapter introduces the topics of nanomedicine and silk processing by reviewing seminal and recent research within these fields. Firstly, the current successes and limitations of nanomedicine are explored. Second, the processes of, and barriers to, systemic delivery of nanomedicines to the tumor and endocytosis by cancer cells are described. Then, the optimization of nanomedicine properties to overcome these barriers and improve tumor targeting is examined. Silk fibroin structure and properties are then described and the advantages of using silk fibroin for biomedical and nanomedicine applications are highlighted. The processing methods of silk fibroin into nanoparticles are then evaluated and the bottlenecks of the engineering methods listed. Further processing of silk fibroin by chemical modification using homogeneous and heterogenous chemistries are described and compared within a biomedical context. Finally, the hypothesis, aims and, objectives of the thesis are defined.

1.1 Nanomedicine

Nanotechnology encompasses the analysis or manipulation of matter at the nanoscale (1-1000 nm) and can result in the production of nanomaterials with at least one nanoscale dimension.[1] At this scale, the nanostructure size and shape influences the material's physicochemical properties, widening the scope of new material functionality. The application of nanotechnology to medicine has produced the interdisciplinary field of nanomedicine, with the overall goal of improving patient quality of life.[2-5] When administered to a stratified patient population, nanomedicines can: improve toxicological profiles; control and aid visualization of biodistribution; and, increase therapeutic efficacy of lipophilic, immunogenic or unstable agents.[6, 7] Due to their unique properties, nanomedicines can stabilize and deliver a range of small molecules, proteins, nucleic acids and imaging agents to their target organ, tissue, cell or subcellular compartment. Nanomedicines designed for intracellular activation must be taken up and trafficked through sub-cellular compartments to the desired organelle (detailed below).

The creation of nanoparticle tools has already aided medical diagnostics, *via* nanoimaging agents, and medical treatment, *via* nanomedicines.[2-5, 8] To date, there are around 90 clinically approved nanomedicines and nanoimaging agents.[9] Over 60% of the commercially available products are accounted for by lipid-based and nanocrystal formulations,[9] which achieve greater drug-loading capacities compared to polymeric, protein-based, inorganic and composite nanocarriers.[6, 7, 9, 10] Drug delivery remains the major application of clinical nanomedicine, providing treatment options for diseases ranging from cancer (e.g., liposomal doxorubicin Doxil®, liposomal cytarabine plus daunorubicin in a synergistic 5:1 molar ratio Vyxeos® and, recombinant fusion protein Denileukin diftitox Ontak®) to anemia (e.g., polymer-protein conjugate Mircera®).[11-14] Inorganic metallic and metal oxide nanoparticles are being explored as both nanoimaging and therapeutic platforms, although the Food and Drug Administration (FDA) approval has so far been limited to iron and superparamagnetic iron oxide nanoparticles, (e.g., Feraheme®, NanoTherm™).[6, 9] However,

the early research and development pipeline for inorganic nanoparticles remains active, for example: silica quantum dots and gold nanoparticles for imaging have reached clinical trials (phase I/II) to validate safety and efficacy before commercialisation.[6, 9, 15, 16]

Further advancement of nanomedicine coalesces *in situ* diagnosis and treatment *via* nanotheranostics. This concept requires multi-functional therapeutic nanocarriers which can accumulate in the organ of interest and exhibit responsiveness to the disease-state: emitting a monitorable signal alongside payload release.[2-5, 8, 17-19] In cancer therapy, this offers a method for patient stratification as tumor uptake of the nanocarrier can be screened: ensuring each patient receives an appropriate treatment plan. [2-5, 8, 13, 17-19] Yet, with no clinical approvals to date, nanotheranostic agents remain in their infancy, with 17 products currently in various stages of clinical trials listed in the World Health Organization's International Clinical Trials Registry Platform (ICTRP).[2, 17, 18]

For both diagnosis and treatment, clinical nanomedicine has provided advantages over traditional small-molecule therapies and conventional diagnostic modalities. The pharmacokinetic and pharmacodynamic properties of the nanomedicine are dictated by the carrier when the drug is bound to, or encapsulated by, the carrier. The physicochemical, geometrical and, mechanical properties of the carrier can then be tuned to reduce adverse systemic effects of small-molecule therapies and increase sensitivity of diagnostic modalities.[15-17, 20, 21] Further improvements, particularly within the realms of multi-functionality and large-scale GMP manufacture, highlight the promise this field harbors. Regardless, there are still multiple hurdles to overcome, including: multi-drug cancer resistance; targeted delivery; quality control of lab-scale nanomedicine production; and, reproducible scale-up to GMP manufacture.[13, 16, 20, 22] Consequently, this chapter will summarize the rationale for, and advantages of, therapeutic silk nanomedicines, specifically in the treatment of cancer.

1.1.1 Therapeutic delivery to tumor environments

The original promise of cancer nanomedicines was to provide a 'magic bullet' following systemic administration to target tumors passively through the circulatory system while

reducing off-target side effects from classic chemotherapy.[23] This idea now utilizes the paradigm of the enhanced permeability and retention (EPR) effect discovered in 1986.[24] The EPR effect proposed that nanoparticles extravasate through large inter-endothelial gaps into solid tumors and are retained there due to poor lymphatic drainage.[25, 26] Some success has been achieved in cancer nanomedicine using passive targeting,[11, 12, 27] with fourteen systemically administered nanomedicine anticancer agents approved for clinical use. The majority are liposomal nanoformulations of off-patent, small-molecule cytotoxic agents which display improved pharmacokinetics and reduced toxicity compared to the free form drugs.[13, 26, 28] For example, patients treated with PEGylated liposomal doxorubicin (Doxil®) exhibit less cardiotoxicity, less hair loss, a five-fold greater tumor exposure half-life and, a three orders of magnitude prolonged clearance compared to patients treated with free doxorubicin.[28, 29] The improved tolerance to liposomal doxorubicin and longer drug dosing that can be achieved compared to free doxorubicin also make Doxil® suitable for incorporation into combination therapy regimens.[28] However, the clinical efficacy of many cancer nanomedicines and survival rates compared to the free form drugs have not lived up to initial expectations.[26] The poor improvement to efficacy is in part due to the reformulation of clinically approved cytotoxic agents, which means the mechanism of action and vulnerability to drug resistance remains the same as the free drugs already on the market.[29] Another barrier to improved efficacy is provided by the EPR effect having been scarcely observed in human patients, with active endothelial transcytosis being observed to play a more major role in nanoparticle extravasation in human tumours.[26]

The capacity of passively targeted nanomedicines for accumulation in human tumors is still unclear.[14] For example, Wilhelm *et al.* reported in 2016 that only around 0.7% of the injected doses of various nanomedicines accumulates in the tumor following systemic administration.[30-32] However, this result conflicts with the outcome of a 2001 clinical trial in which ≥ 0.7% of the injected dose of radiolabeled liposomes accumulated in the solid tumor for 83% of patients.[14, 33] Indeed, Lammers *et al.* argue that the proportion of the injected dose

which accumulates in the tumor as opposed to off-target sites has a larger influence on the benefit to patients, whereby normalizing the tumor accumulated dose by unit weight of tissue would provide a more useful measure of tumor accumulation.[28] Lammers also reasons that the absolute number of nanoparticles administered influences the tumor delivery and treatment efficacy based on *in vivo* results reported by Ouyang and colleagues.[34, 35] The authors demonstrated a threshold dose of 10^{12} nanoparticles per injection per mouse to overwhelm the uptake rate of phagocytic Kupffer cells in the liver, which results in lower hepatic clearance rates, longer circulation times and greater tumor accumulation.[34, 35] Applying an extrapolated dosing threshold of 1.5×10^{15} nanoparticles per injection per human patient is supported by the success of nanomedicines administered above this threshold compared to those administered at lower doses.[35]

Other hurdles for nanoparticle tumor accumulation and penetration result from the physiological features of the tumor microenvironment, including low interstitial pH and hypoxia,[36, 37] dense interstitial matrix, higher interstitial fluid pressure and irregular tumor vascularization due to cancer cell hyperplasia.[38] The leaky tumor blood vessels may cause reduced opportunities for nanomedicines to enter the tumor, whereas the higher interstitial fluid pressure lowers diffusion between the interstitium and intravascular space by lowering the fluid pressure gradient.[30] In addition, the concentration of tumor associated macrophages can be highest near the tumor blood vessel, as reported by Wilhelm *et al.* for SKOV-3 xenograft mouse models bearing solid tumours.[32] The authors demonstrated that 70.4% of tumor blood vessels were associated with perivascular tumor associated macrophages using 2-dimensional immunofluorescent histopathology analysis.[32] The localization of tumor associated macrophages near the tumor vasculature can result in a high likelihood of premature nanoparticle phagocytosis upon extravasation.[32] For example, using intravital imaging, flow cytometry and histology studies in a HT-1080 xenograft mouse model 24 h after intravenous administration of a 100 nm poly(lactic-co-glycolic acid)-polyethylene glycol-BODIPY™ carrier encapsulating a platinum(IV)-BODIPY™ payload, Miller *et al.* reported that

even though tumor associated macrophages only comprised roughly 4% of the tumor cell population, they internalized more than 30% of the systemically administered nanoparticle dose.[39] Relative to tumor cells, this equated to tumor associated macrophages internalizing 40% of the total nanoparticle dose.[39] The authors also reported that, per cell of the bulk tumor, tumor associated macrophages took up the greatest number of nanoparticles and accumulated the most payload.[39] Increased uptake into leukocytes near the tumor vasculature was corroborated by imaging uptake of the carrier in tumor-bearing fractalkine Cx3cr1GFP/ þ reporter mice.[39]

Nanoparticle uptake by tumor associated macrophages may also play a role in tumor shrinkage, due to their role in significantly increasing nanoparticle delivery to the tumor, releasing payload to neighboring cancer cells[39] and, migrating to metastatic tumor sites.[40] Using intravital imaging and flow cytometry, Miller *et al*. reported that following administration to the HT-1080 xenograft mouse model, the platinum(IV)-BODIPY™ payload was shown by to have better distribution throughout the tumor tissue compared to the 100 nm poly(lactic-co-glycolic acid)-polyethylene glycol-BODIPY™ carrier.[39] Flow cytometry also indicated that the payload transferred from tumor associated macrophages to tumor cells, as more than double the amount of payload compared to the carrier accumulated in the tumor cells.[39] Histology and intravital imaging also indicated that payload concentrations were higher by over threefold within roughly one cell-length of tumor associated macrophages while the vehicle concentration was not elevated.[39] As a consequence, DNA damage of tumor cells was greatest within the phagocyte-neighboring region.[39] Another study in an orthotopic murine glioma model studying the delivery efficiency of cyclodextrin-based nanoparticles using fluorescent microscopy and flow cytometry showed that macrophages took up roughly 60-80% of the total nanoparticle cell uptake using intracranial and intravenous administration. [40] Strikingly, the macrophages that took up nanoparticles migrated into circulation and settled in metastatic tumours.[40]

Consequently, the physiological features of the tumor microenvironment, in tandem with cellular features like plasma membrane pumps, can cause multidrug resistance, by causing the nanomedicine to accumulate at the periphery of the tumor and being unable to penetrate deeper.[30] The physiological barriers to payload delivery to the tumor cells are further exacerbated by the chemical features of the tumor microenvironment, including faulty apoptotic mechanisms and the over-expression of efflux transporters, which lower the drug efficacy following delivery to the target cells.[30, 38, 41, 42] Hence, understanding the endocytosis pathways by which nanomedicines are trafficked in both the cancer and healthy cells is a precondition to improving the nanomedicine uptake by cancer cells and the delivery of the payload to the target intracellular organelle or receptor.

1.1.2 Endocytosis: gateway of a nanomedicine

Endocytosis classifies the cellular pathways used for the uptake of extracellular material and the maintenance of cell homeostasis, namely macropinocytosis, phagocytosis, and receptor-mediated endocytosis.[3, 7, 43, 44] This is accomplished through internalization of the cellular membrane and incorporated components, such as surface signaling receptors and bound ligands which are internalized during receptor-mediated endocytosis.[45, 46] The process begins with absorption of matter bound to the plasma membrane in endocytic vesicles, formed by the 'pinching off' of membrane invaginations (Figure 1.1).[7] Cargo is then trafficked to the early endosome, which acts as the cell 'sorting station'. From here, intracellular transport is dependent on the endosome cargo, with recycling routes available *via* exosome biogenesis.[7] From the late endosome, escape routes are accessible through retrieval of cargo to the cytoplasm.[7] Transport to the lysosomes can offer a further breakdown route through lysosomal enzyme degradation,[47] as these membrane-bound organelles have an acidic pH environment and contain degradative hydrolase enzymes.[45, 47-50] In polarized cells, cargo transport across the poles can also occur in a process termed 'transcytosis'.[7]

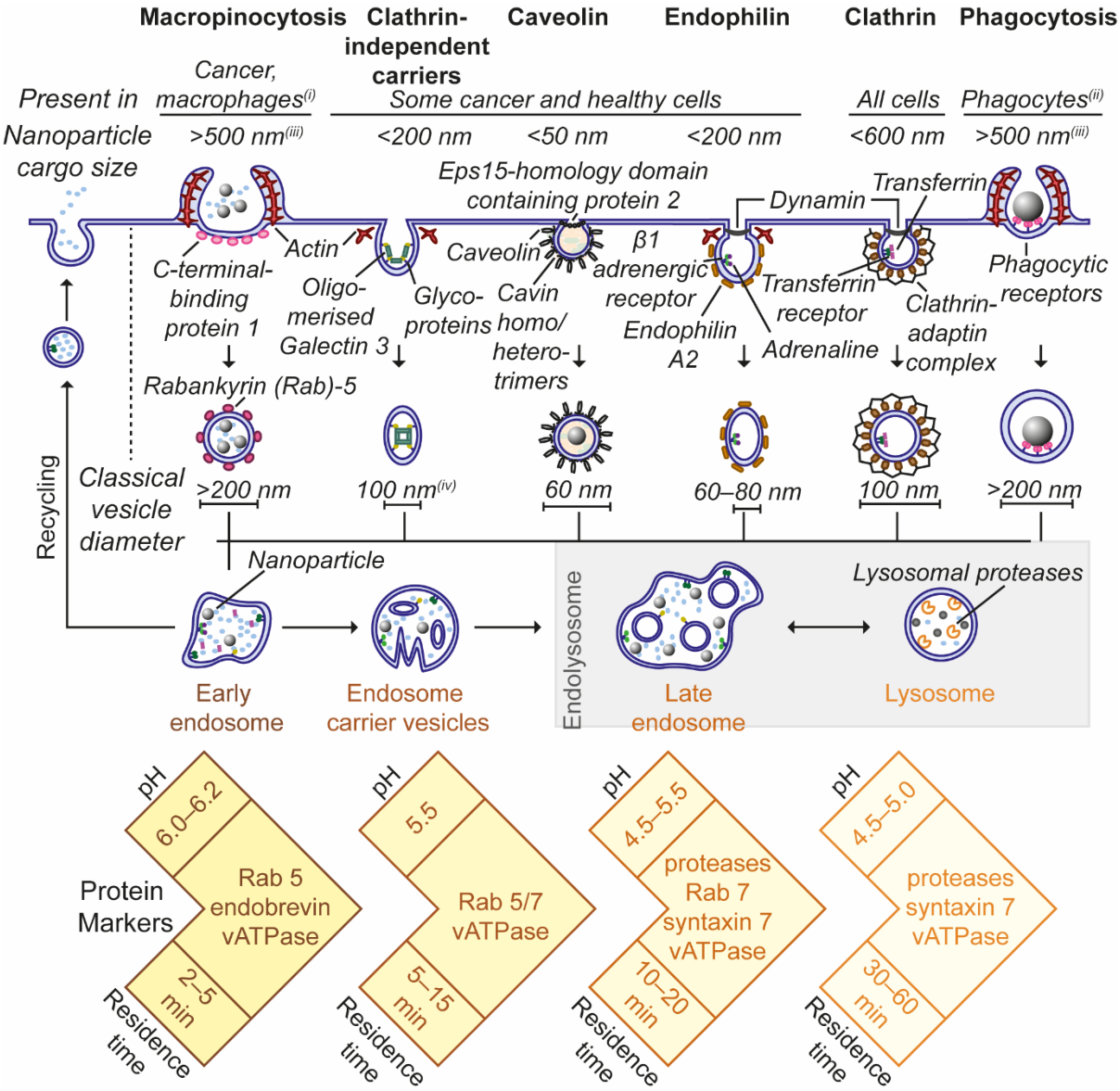

Figure 1.1. Endocytic and membrane recycling pathways in mammalian cells from *in vitro* studies. The typical organelle pH,[44, 47, 50, 51] main organelle marker proteins,[44, 51] and residence times[44] of nanoparticles within each organelle are shown on the bottom of the diagram. (i) Macropinocytosis has been demonstrated to be upregulated in cancer cell lines expressing oncogenic Ras[51, 52]; macrophages, endothelial cells, and epithelial cells in the presence of growth factors; epithelial cells in the presence of pathogens; and, has been implicated in neuronal axon growth and the immune protection mechanisms of microglia. (ii) Non-professional phagocytic cells may not be able to utilize their phagocytic machinery as they do not express the phagocytic receptors required to bind extracellular cargo.[51] Phagocytic receptor gene knock-in human epithelial cells were capable of phagocytosis, as confirmed *in vitro* by cytometry and confocal microscopy.[53] (iii) Some studies have shown these pathways can be utilized for particles as small as 50 nm in diameter.[44, 51] (iv) The vesicle diameters formed by the clathrin-independent/dynamin-independent pathway utilizing clathrin-independent carriers, glycosylphosphatidylinositol-anchored proteins-enriched early endosomal compartments are generally reported to be similar to vesicle diameters of the clathrin-mediated and fast endophilin-mediated endocytosis pathways.[44, 52, 54]

Nanoparticle internalization may occur *via* membrane fusion with fusogenic carriers or through multiple trafficking pathways, notably: macropinocytic; clathrin-independent/dynamin-independent-mediated; caveolin-mediated; fast endophilin-mediated; clathrin-mediated; and, phagocytic endocytosis.[44, 51] Macropinocytosis involves the endocytosis of fluids and particles up to roughly 1 μm in diameter in the bulk phase by actin polymerization, which mediates membrane ruffling macropinosome fission.[44, 51] Due to the similarity of macropinocytosis to phagocytosis[44] and clathrin-independent/dynamin-independent-mediated endocytosis,[51] it is unclear if nanoparticles can be internalized by macropinocytosis *in vivo*.[51] The process is constitutively present in macrophages and dendritic cells to readily identify pathogens,[54] and is upregulated in some cancer cell lines[51, 52] to facilitate the transport of nutrients, growth factors, and inorganic salts required for cell metabolism.[55, 56] This pathway provides a drug delivery target for cells expressing oncogenic Ras in which it is upregulated compared to their healthy counterparts.[52] Clathrin-independent/dynamin-independent-mediated endocytosis is constitutive in mammalian cultured cells and is associated with nanoparticles less than 200 nm in diameter due to the small tubule opening.[44, 51] The mechanism begins with adsorption of extracellular Galectin 3 to membrane glycoproteins and glycolipids, polymerization of Galectin 3 and, finally, actin and other proteins control tubule fission.[51] Caveolin-mediated endocytosis has been proposed for fatty acid transport in adipocytes, endothelial cells, muscle cells, and some cancer cells which bear the required cytosolic caveolin, extracellular cavin proteins and, Eps15-homology domain containing protein 2 to form the flask-like caveolae.[7, 44, 49, 51, 57, 58] Due to the small 50 nm opening of the caveolae, and poor specificity of inhibitors for this pathway it is unclear if nanoparticles can be internalized by caveolae.[7, 44, 51, 59-63] Fast endophilin-mediated endocytosis has been proposed for cargo below 200 nm in diameter in some healthy and cancer cells.[51, 52] The dynamin-dependent process driven by a number of ligand-receptor interactions, such as endophilin A2 with membrane receptors.[51] Actin polymerization enables the formation of tubules several hundred nanometers long and membrane scission is dependent on dynamin.[51] Clathrin-mediated endocytosis is also a dynamin and adrenaline-dependent process that contributes to fluid phase endocytosis for all

cells,[46, 51, 55, 57, 64-66] and has been implicated in multiparticle endocytosis of nanoparticles ranging in size from 30–550 nm.[44] The clathrin-coated pits can stretch to diameters of roughly 600 nm around particle aggregates and are formed by binding of cytosolic adaptins, cytosolic clathrin, and extracellular transferrin to transferrin membrane receptors.[44, 51] Phagocytosis is similarly a receptor-driven process, but is limited to specialized phagocytes that express the phagocytic membrane receptors to tightly bind opsonized, extracellular substances and is not typical to cancer cells.[44, 51, 52] As for micropinocytosis, actin polymerization and membrane ruffling then mediates phagosome fission.[44, 51] A range of nanoparticle sizes, from roughly 3 μm to 50 nm in diameter, have been argued to be internalized through phagocytosis.[44, 51, 52] Ultimately, hybrid pathways may also be present which operate by using parts of the classical pathways and the endocytic pathway observed for one cell type *in vitro* may differ from *in vivo* analysis.[51]

The selective trafficking of nanocarriers and their low molecular weight, weakly basic payloads to the lysosome was first discovered in 1972 by Trouet *et al*. for a DNA-daunorubicin complex.[67, 68] Trafficking to the lysosome was subsequently coined as 'lysosomotropic delivery' by De Duve *et al.* and is characteristic of successful drug delivery systems as this route evades drug efflux.[45, 49, 69, 70] The discovery led to De Duve proposing piggyback endocytosis in 1974 as a rationale for targeting specific intracellular trafficking pathways, using the property of a specific nanomedicine rather than the payload (Figure 1.2).[49, 69, 71] Piggyback endocytosis has remained a focus of drug delivery, and has resulted in clinically-approved lysosomotropic anticancer nanomedicines, such as Doxil®[11, 72] and Abraxane®[12, 72] which are used as second-line therapies for chemotherapy resistant breast tumours.[46, 49, 69, 73]

An understanding of the relationship between each nanomedicine and the endocytic route observed in the relevant cell models *in vitro* and *in vivo* is vital to increase clinical applicability.[46] For instance, the success of lysosome-targeted delivery hinges on many nanomedicine physicochemical and biological properties, including carrier biocompatibility, preferential internalization by the target cells, stability of the payload to acidic pH and

lysosomal enzyme action and, pH-responsive release of the payload from the carrier.[69] Poor nanomedicine properties can limit efficacy and increase systemic toxicity due to biological effects such as low cytoplasmic release of the cargo from the endosome, and cargo efflux to the extracellular medium by membrane-bound pumps respectively.[69, 74] For example, live cell microscopy studies conducted using murine B16BL6 melanoma cells and human BLM melanoma cells demonstrated uptake and lysosomal sequestration of Doxil®, which was linked with lower *in vitro* cytotoxicity and intracellular bioavailability compared to free doxorubicin.[75] Lysosomotropic delivery of Doxil® was also observed *in vivo* using high resolution intravital imaging of mice bearing a B16BL6 or BLM dorsal skinfold chamber tumours.[75] In the absence of the liposomal carrier, doxorubicin diffused rapidly through the cytoplasm to the nucleus while entrapment within the stable liposomal carrier prevented extracellular doxorubicin release and predominantly resulted in trafficking to the lysosomes.[75] The authors hypothesized that the membrane permeability of doxorubicin is reduced by protonation within the lysosomes. The consequent slow intracellular release into the cytoplasm contributes to the lower therapeutic potency of Doxil® compared to free doxorubicin.[75] As nanomedicines hold a therapeutic advantage over the free drug when efficacy is increased at the maximal tolerated dose without increased off-target toxicity, the primary argument in support of an enhanced therapeutic index of doxorubicin when encapsulated as Doxil® arises from reduced cardiotoxicity.[76, 77]

By careful molecular design of nanomedicines, cargo half-life and cytosol accumulation can be increased by the incorporation of endosomal escape units which weaken the endosomal membrane: facilitating payload escape from degradation by hydrolytic enzymes or acidic pH and allowing the payload to travel through the cytoplasm to the target cell compartment.[69, 78-80] There are multiple endosomal escape mechanisms, namely: the proton sponge effect whereby the carrier molecules become protonated in the endosome, causing an influx of chloride ions, osmotic swelling and membrane rupture; membrane fusion of liposomal carriers with the endosome, mediated by ion pairing between cationic carrier lipids

with anionic endosomal lipids; pore formation in the endosomal membrane by self-assembling peptides; and, membrane disruption by polymers or peptides which interact with the endosomal membrane.[79] Lipid nanoparticle endosomal escape units for liposomal and lipid carriers have included lipid dioleoylphosphatidylethanolamine for membrane fusion-based escape and pH-responsive or cationic lipids for proton sponge-based escape.[80] Polymer and peptide nanoparticle endosomal escape units have also incorporated pH-responsiveness and multiple cationic charged sequences such as poly-histidine peptides.[78, 80]

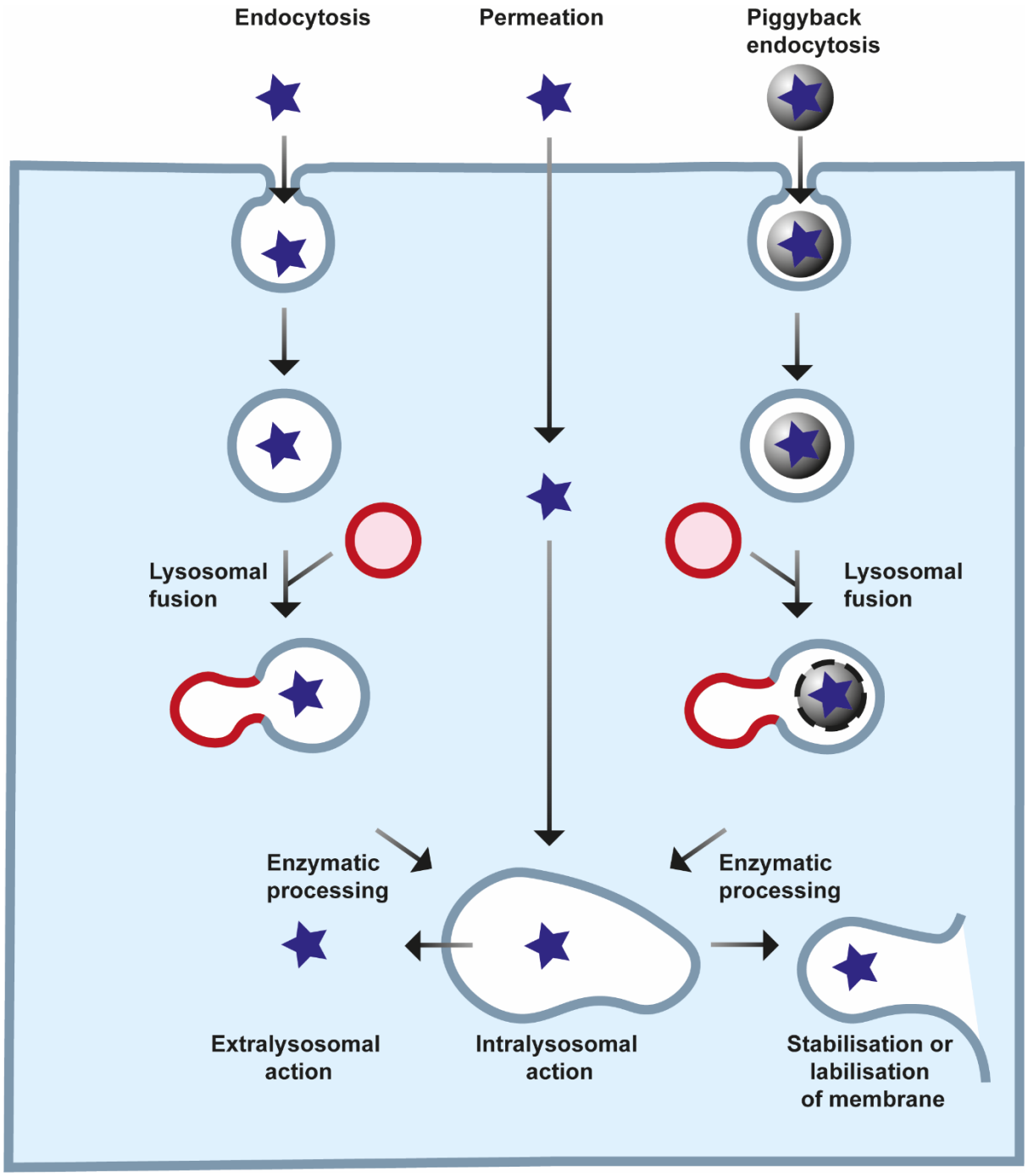

Figure 1.2. Lysosomotropic delivery *via* endocytosis, piggyback endocytosis and permeation cell entry routes, adapted from De Duve *et al.*.[69]

Although targeting receptor-mediated endocytosis can result in enhanced uptake, the protein corona and nanoparticle physicochemical properties can interfere with ligand-receptor binding. For example, due to the size-limit of 50-60 nm for caveolae-based vesicles, this route is inherently favored by smaller nanoparticles, as reported by Cheng *et al*. for the uptake of

gold nanoparticles in HepG2 cells and by Ho *et al*. for polystyrene nanoparticle uptake in HUVEC cells.[57] In addition, understanding of the endocytic uptake for both native and therapeutically-loaded nanoparticles is crucial to ensure payload delivery to the desired organelle, as transport mechanisms and rates can differ upon therapeutic loading. This was exemplified by variants of recombinant, spider silk nanoparticles, including polyanionic eADF4(C16).[62] Following loading of polycationic species by electrostatic adsorption, cellular uptake increased almost two-fold compared to the native nanoparticles, due to changes in physicochemical properties such as surface charge and hydrophilicity.[62]

1.2 Cancer-targeted nanomedicine

Two of the primary obstacles to the clinical translation of current cancer nanomedicines arise from the heterogeneous biology of tumors between patients and the complexity of the physiological response to nanomedicines.[20] Consequently, patient stratification has been proposed as a method to match nanoformulations with tumor heterogeneity.[20, 26, 73] For example, as the EPR effect and tumor microenvironment vary significantly between patients and tumor types. Therefore, several preliminary clinical studies proposed stratifying the subpopulations of cancer patients for which nanoparticle accumulation *via* the EPR effect is likely using non-invasive imaging.[81-83] This type of work would provide predictive markers for patients who would benefit from passively targeted nanoparticles and expedite targeted treatment to the patients who require it.[20, 82]

Further objectives include the identification of mechanisms by which tumor size can be reduced, so that cellular or acellular targets can be identified and targeted.[32] Pertinent examples include tumor associated macrophage depletion and extra-cellular matrix degradation as co-injection or sequential injection schemes to increase nanoparticle targeting to cancer cells.[32] The chemoattraction of macrophages and other immune cells to tumor sites is useful for targeted delivery of nanoparticles, especially to hypoxic regions distant from blood vessels, which does not rely on passive accumulation. This has been used in numerous

studies, for example using macrophages loaded with gold nanoshells to infiltrate tumor spheroids *in vitro*[84] and murine metastatic breast cancer *in vivo*.[85] Alternative pre-treatment strategies to increase nanoparticle delivery efficiency to cancer cells by using external stimuli include hyperthermia and radiation, vascular normalization, extra-cellular matrix modification, photodynamic therapy, and chemotherapy priming.[81]

Overchuk and Zheng suggest that nanoparticle delivery and intra-tumoral behaviour should also be thoroughly investigated in the pre-clinical stages.[81] Quantifying targeting efficiency and correlating it with therapeutic efficacy would enable a standardization between modalities for comparison.[32] Currently, most preclinical studies analyze the gross accumulation and sub-tumoral localization of the active pharmaceutical ingredient using analytical techniques like mass spectrometry, high-performance liquid chromatography, gamma counting and, fluorescent microscopy with histology.[81] Intracellular uptake analysis with optical tissue clearing techniques is beneficial over flow cytometry for parsing nanoparticle spatial distribution with respect to cancer cells and vascular structures at single-cell resolution.[81] Intravital microscopy can also enable *in situ* evaluation of tumor microenvironmental changes with time in the same animal.[81]

1.2.1 Physicochemical properties of nanoparticles

The size and surface charge of nanomedicines can manipulate their stealth properties in the circulatory system and alter their cellular interactions at the tumor site.[30] For example, cationic nanomedicines with zeta potentials above +10 mV are cytotoxic, induce hemolysis, interact with serum constituents, undergo rapid clearance by the mononuclear phagocytic system in the bloodstream and, undergo rapid hepatic clearance, resulting in systemic cytotoxicity and a short circulation half-life.[30, 86] Anionic nanomedicines with zeta potentials below –10 mV have lower cellular uptake than cationic nanomedicines but also cause rapid mononuclear phagocytic system clearance, while rapid hepatic clearance occurs at zeta potentials below -40 mV.[30, 86] As a result, neutral nanomedicines with zeta potentials around ±10 mV have the longest circulation but have lower colloidal stability without the adsorption of an electrostatic

or steric stabiliser.[30, 86] Within the tumor, nanomedicines with low zeta potential magnitude can diffuse through the interstitial fluid more easily than those with high charges as they avoid being trapped by the electrostatic band pass formed by the extracellular matrix.[30] Although cationic nanomedicines exhibit non-specific cytotoxicity in the systemic circulation, within the tumor they prove advantageous as they can act as an adjuvant, trigger adsorption-mediated endocytosis and, lysosomal escape at the target cell.[30, 78-80, 86]

The nanomedicine size has been shown to significantly impact biodistribution, tumor accumulation and circulation time.[30, 87] For example, an increase in nanoparticle diameter, especially above 100 nm, has generally been associated with increased clearance by Kupffer cells in the liver, reduced hepatobiliary clearance and, insignificant renal clearance.[30, 87] Additionally, as the EPR effect is size-dependent, nanomedicines with diameters around 100 nm have been observed to accumulate in solid tumors, although smaller nanoparticles can have enhanced tumor penetration.[30, 87]

Increased tumor penetration can be achieved by tuning the nanomedicine physicochemical properties to overcome the barriers to diffusion in the interstitial matrix.[30] For example, smaller nanoparticles more readily diffuse through the tumor tissue, although nanoparticles with diameters less than 20 nm can be more quickly cleared by renal excretion.[30] Smaller nanoparticles have reduced drug carrying capacity both by entrapment and surface adsorption.[20] Additionally, the surface area of nanoparticles increases as the diameter decreases, lowering the controlled-release capacity.[20, 88-92] Further optimization of nanoparticle properties for tumor penetration may be accelerated by visualization of the nano-bio interactions occurring in the tumor microenvironment through real-time intravital microscopy and 3D *in vitro* tumor models.[20]

For example, Wilhelm *et al.* used *in vitro* co-cultures of SKOV-3 cancer cells and Raw264.7 murine macrophages in a 3D Matrigel-microchannel system to mimic the intra-tumoral microenvironment.[32] After a 24 h incubation, the cell interaction with 15, 55 and 100 nm trastuzumab-coated gold nanoparticles was measured with fluorescence microscopy.[32]

Less than 14 per 1 million of 55 nm Trastuzumab-coated nanoparticles were estimated to have reached the cancer cells due to intratumoral cellular (tumor associated macrophages) and acellular (extra-cellular matrix) barriers.[32] This meant that the nanoparticles interacted with 2 out of 100 cancer cells while the remainder were trapped in the extracellular matrix or phagocytosed by the perivascular tumor associated macrophages.[32] The smaller nanoparticle size of 15 nm was able to penetrate these model tumors deeper but these particles may need to be present in a high enough concentration to aggregate before uptake can occur.[32] The authors suggested that the 100 nm particles were too large to diffuse through the extra-cellular matrix.[32] For all nanoparticle sizes, the extra-cellular matrix and tumor associated macrophages sequestered more than 88% of extravasated nanoparticles.[32] The impact of the extracellular matrix on the diffusion characteristics of nanoparticles with different mechanical properties was assessed using 100 nm nanoparticles composed from different carrier materials (e.g., gold, silver, liposome and, poly(lactic-co-glycolic acid)).[32] Additionally, 55 nm gold nanoparticles were incubated with mouse serum to investigate the impact of the matrix on the diffusion of nanoparticles with and without a protein corona.[32] Importantly, across the range of nanoparticles with different mechanical properties and protein coronas, the matrix reduced the diffusion rate of all nanoparticles and resulted in <8% of the cancer cells being accessed: reinforcing extra-cellular matrix degradation as a treatment strategy.[32]

1.2.2 Hierarchical structure of nanoparticles

The impact of hierarchical structure and morphology are poorly understood as the effects have been observed to be highly dependent on the tumor model and cell line.[20] Morphology can affect nanomedicine circulation time due to altered immune responses, endothelial cell adherence and flow behavior. [93] The morphology dictates the curvature of the particles and whether phagocytosis will occur, or cells will spread on the particle surface. Illustrating this concept, the circulation time of polymeric worm-like nanoparticles with aspect ratios greater than 20 were observed to be longer than for spherical polymeric nanoparticles due to their decreased internalization by macrophages.[93] Further, cylindrical polymer micelles of lengths

between 2 to 8 μm and diameters between 22 to 60 nm have been shown in rodent models to have longer circulation times than spherical stealth polymersomes roughly 100 nm in diameter.[94] Cell adherence of non-spherical nanoparticles is greater due to their higher specific surface area, while non-spherical nanoparticles also have complicated flow patterns in blood vessels compared to the sequestered flow of spherical particles between red blood cells and vessel walls.[93] The increased opportunity for cell adherence combined with their greater surface area result in non-spherical nanomedicines having a greater affinity for endothelial cells than spherical nanomedicines. Consequently, non-spherical nanoparticles have a greater capacity for targeted delivery to endothelial cells[20] and a higher capacity for margination to the target tumour.[93] For example, polyethylene glycol coated inorganic nanorods (15 × 54 nm) were shown to have a higher rate of tumor penetration than their nanosphere counterparts (35 nm), although both had similar hydrodynamic diameters between 30 to 40 nm and similar aqueous diffusion rates.[20] Finally, the internal crystal structure impacts the flexibility of the nanomedicine, which has been implicated in the particle stability,[95] payload release rate,[95] formation of the protein corona,[57, 96, 97] clearance by the immune system[93, 98] and uptake by the target cell.[93, 98]

1.2.3 Surface functionalisation

Some improvements to cancer nanomedicines can be provided by surface functionalization of nanomedicines to engineer ligands for active targeting to tumor-expressed receptors and stimulus-responsive stealth coatings which prevent undesired biological responses in circulation.[26] Over recent decades, several nanoimaging agents and nanomedicines engineered with active targeting or stimulus-responsiveness have been clinically approved or entered clinical trials, resulting in improved tumor accumulation and reduced side effects.[99-101] Examples of actively targeted nanomedicines which have received clinical approval are antibody-drug conjugates, which consist of a monoclonal antibody designed to target a specific receptor overexpressed on the cancer cell surface and an antineoplastic agent conjugated through a non-cleavable (e.g., Trastuzumab emtansine Kadcyla®) or a stimulus-responsive

linker (e.g., Sacituzumab govitecan Trodelvy®, Trastuzumab deruxtecan Enhertu®).[99] In addition, actively targeted nanoimaging agents which incorporate mannose to target the CD-206 receptor on the surface of macrophages have progressed to the clinic for sentinel lymph node identification (e.g., ^{99m}Technetium-labelled, mannose-dextran conjugate Lymphoseek™).[101-104] However, simple liposomal and micellar nanoformulations predominate over actively targeted or stimulus-responsive nanoformulations in the group of >50 anticancer nanomedicines in clinical trials currently.[26, 99, 105] The high failure rate associated with the translation of surface functionalized nanomedicines from preclinical research to clinical approval is due to many unsolved biological and technological issues, particularly the considerable work required to understand the nano-bio interactions which interfere with nanomedicine stability and biodistribution.[99]

1.2.3.1 Active targeting

Tumor cell uptake can also be improved by active targeting, whereby nanomedicine surfaces are decorated with targeting ligands that bind specific, endocytosis-prone receptors which are overexpressed on the surface of tumor cells. Active targeting is important for tissue accumulation in patients and tumors in which the EPR effect is not the predominant mechanism of tumor accumulation. Improved drug delivery and efficacy compared to passively targeted controls has been achieved by targeting cell membrane receptors including the epidermal growth factor receptor (e.g., in mice bearing murine mammary carcinoma, mice bearing human cervical cancer and human colorectal cancer xenografts),[106-108] the transferrin receptor (e.g., in mice bearing human prostate cancer and human colon adenocarcinoma xenografts),[109, 110] integrins (e.g., in human glioblastoma and human mesenchymal stem cell lines),[20, 60, 62] the folate receptor (e.g., in human breast adenocarcinoma cell lines)[111, 112] and, the asialoglycoprotein receptor (e.g., in human hepatoma patients).[113]

Dai *et al.* have suggested that the reduction in tumor size and increased survival rate of actively targeted cancer nanomedicines in mouse models may be due to indiscriminate macrophage cytotoxicity and cell death.[32] Using pre-clinical *in vivo* and *in vitro* mouse tumor

models, the authors quantified the targeting efficiency of passively targeted trastuzumab-coated and actively targeted folic acid-Trastuzumab coated gold nanoparticles.[32] The actively and passively targeted 55 nm Trastuzumab-coated gold nanoparticles were administered intravenously to preclinical human ovarian SKOV-3 xenograft mouse models with solid tumours.[32] Using flow cytometry with inductively coupled plasma-mass spectrometry, the average nanoparticle-to-tumor delivery efficiency for actively targeted particles after 24 h was 0.59% of the injected nanoparticle dose and 0.25% for the passively targeted particles.[32] However, flow cytometry indicated that 0.0015 and 0.003% of the injected dose of active and passively targeted nanoparticles, respectively, interacted with SKOV-3 cells and that there was no significant delivery efficiency between actively and passively targeted nanoparticles.[32] Conversely, the tumor associated macrophages had accumulated 0.038% of the injected dose of active and 0.02% of passive targeting nanoparticles, which is about 7-38 times the delivery efficiency to cancer cells.[32] The remainder of extravasated particles were in acellular regions.[32] Nevertheless, active targeting was beneficial in reducing nanoparticle accumulation in the reticuloendothelial system organs.[32]

The most common surface functionalization method involves targeting the tumor vasculature using the arginylglycylaspartic acid peptide which can bind to αvβ3 integrin receptors which are selectively overexpressed on the surface of tumor endothelial cells.[20] Targeting the tumor vasculature can enable delivery of therapeutics that inhibit angiogenesis, which reduces tumor growth, causes regression and suppresses metastasis in mice *in vivo*.[20] Additionally, surface modification with cyclic arginylglycylaspartic acid peptide has been shown to significantly increase the tumor parenchyma-penetrating depth.[20] However, although the idea of active targeting was conceived over 30 years ago, only a few examples have reached clinical trial, such as HER2 targeted liposome (MM302)154), a targeted polymeric nanoparticle (BIND014), and targeted siRNA nanoparticle (CALAA-01).[20]

The majority of understanding from nanomedicine cell interactions has been based on *in vitro* studies, which may not be an accurate model for heterogeneous tumors *in vivo*.

Additionally, the relationship between uptake mechanism and intracellular trafficking is not linear, with many biochemical checkpoints determining the final nanoparticle destination.[57] Poor understanding of uptake and trafficking mechanisms *in vivo*, alongside patient-to-patient receptor expression heterogeneity, has contributed to the poorer clinical performance of active *versus* passive anti-cancer nanomedicines.[114] High resolution *in vivo* imaging may increase understanding of the interactions occurring within the heterogeneous tumor microenvironment.[20]

1.2.3.2 Stealth coatings

Surface functionalization can also be used to engineer stealth nanoparticles by coating nanomedicines in hydrophilic, anti-fouling polymers like polyethylene glycol and protein polymers like XTEN™ and proline/alanine-rich sequences, which have the added benefit of greater biodegradability.[106, 115-126] These stealth coatings limit immune clearance by reducing opsonization, although the coating also can lower cellular uptake by, and endosomal escape in, the target cells compared to native nanomedicines, notably those with positive charge.[26] Research has been accomplished to tether cleavable linkers to the surface which theoretically ensure the stealth coating remains during systemic circulation but is selectively removed in the tumour microenvironment due to the presence of low pH or enzyme activity.[26] However, no self-adaptive nanomedicines have reached clinical trials to date.[26] Hence, current progress in anticancer silk nanomedicine methodology will be next discussed, including rational silk nanomedicine design to account for physiological features of the tumour environment.

1.3 Silk structure

Numerous insect species and Arachnida produce silk proteins which have species-dependent amino acid primary sequence.[127] All silk fibroins and spidroins are characterized by the presence of a block copolymer-like heavy chain[128] which dictates many of the protein's properties (e.g., β-sheet crystallinity, high tensile strength, amphiphilicity, thermal stability).[129] Silk fibroin isolated from *Bombyx mori* (*B. mori*) cocoons is particularly beneficial for

nanomedicine applications as the species is well-characterized and is the only clinically approved silk.[130, 131]

Mulberry silk from *B. mori* consists of a heavy (≈391 kDa) and a light (≈26 kDa) chain, linked by one disulfide bond at the heavy chain C-terminus (Figure 1.3).[132] For *B. mori* silk, the heavy chain has a block co-polymer repeating amino acid sequence of 11 short hydrophilic regions and 12 hydrophobic blocks with nonrepetitive C- and N-termini while the light chain has a nonrepeating amino acid sequence.[130] The hydrophobic blocks make up 94% of the heavy chain, and contain mostly glycine-X repeats, where X is alanine (A) (65%), serine (S) (23%), or tyrosine (Y) (9%).[130, 132-134] The repetitive blocks can fold into anti-parallel β-sheet crystallites by forming hydrogen bonds, Van der Waals bonds and hydrophobic interactions. The strength of the intermolecular bonds, the high density and degree of order within the β-sheet crystallites impart high mechanical strength.[129]

In the natural world, as it leaves the spinneret of the silkworm, the hydrophobic silk fibroin thread is coated with sericin, which acts as a binding agent during cocoon spinning. [129, 135] However, as the silk fibroin and sericin mixture has been observed to induce an inflammatory response in humans,[136] the sericin must be removed by “degumming” the silk cocoons.[134, 137] Indeed, isolation of the protein from the spun cocoon has become the standard technique due to the greater ease of extraction compared to silk gland dissection. Degumming methods include chemical, enzymatic, and physical processes to break down the sericin protein and break the intermolecular bonds holding the fibroin and sericin together. The most well-used method involves boiling chopped silk cocoon pieces in an aqueous alkaline solution.[138] These processes invariably cause chain scission to the fibroin peptide backbone, resulting in a polydisperse mixture of silk fibroin polypetides.[139, 140]

The silk fibroin extracted from degumming has a hydrophobic structure enriched with β-sheets, termed Silk II.[129] The β-sheet crystallites and hierarchical structure of the silk fibers result in insolubility in water and most organic solvents,[129, 130] which makes the silk obtained from degumming difficult to process into formats other than silk fabrics.[129, 136] To dissolve the

β-sheet crystals, hexafluoroisopropanol[141] or saturated solutions of aqueous chaotropic agents (e.g., lithium bromide) at 60°C are typically used in a process called regeneration.[142] The input of chemical and thermal energy acts to break hydrogen and Van der Waals bonds in the Silk II secondary structure to a metastable, water soluble Silk I partially ordered structure which has a higher percentage of α-helix and random coils, although the average molecular weight can also be reduced.[129, 140, 143] The aqueous liquid silk is typically dialyzed against water to remove chaotropic salts before further processing.

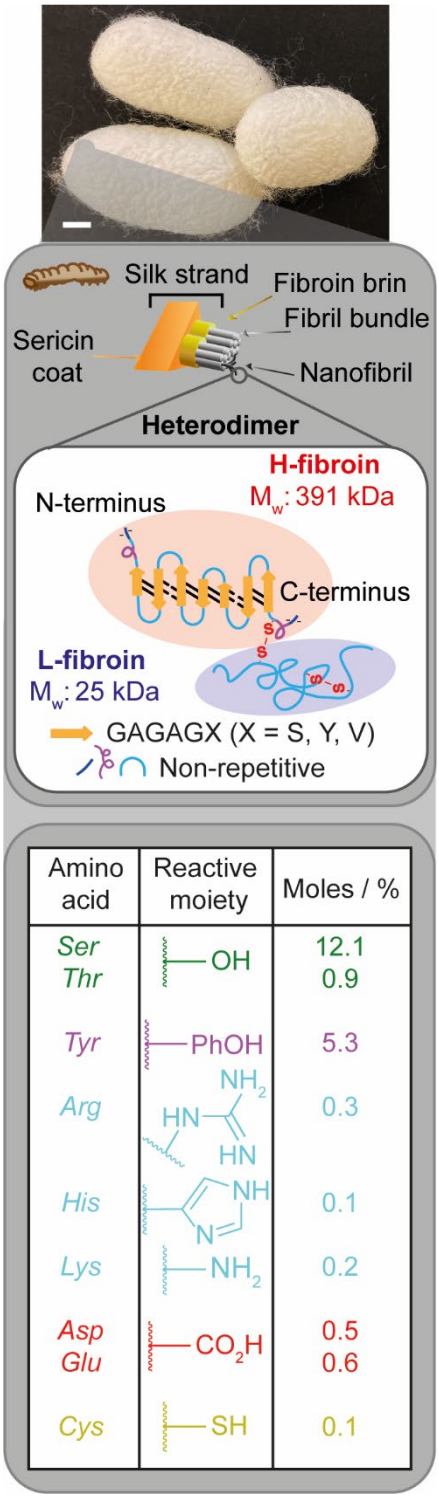

Figure 1.3. Schematic representations and the reactive amino acid composition of *Bombyx mori* silk fibroin. The scale bar is 0.5 cm in length. The structural composition and reactive amino acid content of silk fibroin have been assembled from references.[132, 144] Image adapted from[145].

1.3.1 Silk as a biomedical material

For thousands of years, we have processed silk fibers into textiles and clothing. The silk spun by *B. mori* silkworms during their fifth instar is the market leader for silk goods due to its good mechanical properties and the ease with which silkworm breeding and silk cocoon collection can be scaled-up and industrialized.[136]

B. mori silk has been used clinically for several millennia in traditional healthcare.[136] Since the discovery of aseptic technique in the 1860s, sterile silk products have been used as a suture material,[146-149] wound dressings[150] and, reconstructive surgery support structures,[151] due to favorable biological properties, including biocompatibility, biodegradability and, handling.[136, 146-148] The complete removal of sericin from the silk fiber is important for non-immunogenicity of silk biomaterials, as residual sericin contamination has been reported to be a potential cause of immune rejection responses.[136] Nevertheless, degummed *B. mori* silk has been approved as a biomaterial by the US Food and Drug Administration since 1993.[136] In 2019, the first regenerated silk product, Silk Voice®, a composite hyaluronic acid-silk nanoparticle hydrogel was clinically approved as a support structure to expedite vocal cord repair.[131, 136]

There are many favorable clinical properties of degummed and regenerated silk,[135] namely the capacity to be processed into a variety of multi-scale, hierarchical structures including films, scaffolds, hydrogels, microparticles and nanoparticles.[137] A variety of silk biomaterials have shown comparable *in vitro* cytocompatibility and *in vivo* biocompatibility with other biopolymers like collagen and polylactic acid.[136] In addition, silk biomaterials have shown biodegradability,[152] pH[153] and temperature[154] responsiveness, and stabilization of therapeutic payloads.[155, 156] Due to the presence of reactive amino acids like tyrosine and serine,[132, 157] silk surfaces can also be decorated to improve the physiological response. For example, silk films coupled to acidic aniline derivatives[132, 158] showed greater cell attachment of human mesenchymal stem cells compared to native silk films *in vitro*. Conversely, evasion of the mononuclear phagocyte system can be achieved through bioconjugation of silk nanoparticles

to stealth polymers like polyethylene glycol.[159, 160] For example, Totten *et al.* demonstrated that TNF-α production by murine macrophages *in vitro* was significantly lower after incubation with polyethylene glycol-bound silk nanoparticles as opposed to native silk nanoparticles.[159]

The limitations of silk biomaterials arise due to the heterogeneity of silk molecular structure within and between degummed and regenerated silk batches. The molecular structure heterogeneity occurs due to the genetic heterogeneity between native silkworms[161, 162] and a polydisperse mixture of silk molecules occurs due to the kinetically controlled amide backbone scission during processing.[139, 156, 162-165] With respect to the greenness of silk processing, silk sericulture and cocoon acquisition act as a carbon sink,[166] although standardization and scale-up of newer regeneration processes are still required to reduce the use of energy, water and toxic chemicals.[138, 167] For example, a recent improvement to reduce the volume of water required for regeneration in the absence of additional pH sensitive compounds has been to remove the dialysis step of the chaotropic salt-liquid silk mixture before processing the liquid silk into silk nanoparticles.[168]

1.3.2 Silk as a nanomedicine

Silk fibroin has generated considerable research interest as a carrier material for nanomedicines due to the controllable physicochemical properties of the resultant silk nanoparticles.[169] For example, silk nanomedicines can be optimized for different modes of administration (e.g., intravitreal,[170] intravenous,[171] topical,[172] inhalation[173]) by changing the silk nanoparticle manufacturing process to tune the nanoparticle size, which can vary between 40 nm to microns in diameter for spherical carriers.[153, 172, 174] To illustrate, using *in vivo* tumor models, silk nanoparticles between 100 nm and 200 nm were distributed to the tumor sites *via* intravenous administration.[171, 175] Conversely, low polydispersity silk nanoparticles with an average size of 42 nm in diameter were capable of *in vivo* transdermal delivery in rabbits by paracellular uptake through the stratum corneum to the dermis, a route which was not available to larger particles which sequester in the stratum corneum.[172] Furthermore, the morphology of silk nanomaterials can be controlled by varying the manufacturing process, with

examples ranging from spherical nanoparticles to rod shaped microparticles,[155, 176] and nano- and microfibres.[177, 178] Hence, adsorption to silk fibroin nanoparticle carriers with optimized critical quality attributes can improve the pharmacokinetic and pharmacodynamic properties of the payload.

Surface potential is another key physicochemical property of silk nanoparticle carriers which dictates the surface adsorption capability towards acids and bases. Silk fibroin nanoparticles have a net negative surface charge at physiological pH,[152, 160, 174, 179] due to the silk pI of 4 to 5.[180] Molecular modelling experiments indicated that the negative charge of silk fibroin at physiological pH is caused by the presence of ionizable groups, such as glutamic and aspartic acids,[181] which also makes the silk nanoparticles pH-responsive. The surface electronegativity at physiological pH has been implicated in the lysosomatropic drug delivery[182] of silk nanoparticles verified by live cell confocal microscopy of MCF-7 cells[183] and monocytes.[184] Upon trafficking to the acidic lysosomes (roughly pH 4.5), and to a lesser extent in the acidic tumor microenvironment (pH 6.5 to 6.9), the pH-responsiveness of the ionizable groups can trigger the release of surface adsorbed drugs, an observation corroborated by *in vitro* drug release experiments with the weakly basic drug doxorubicin.[160, 185] Doxorubicin release was further increased during carrier degradation, with significantly increased release of doxorubicin in the presence of papain at pH 4.5, which served as a model for lysosomal enzymes.[152] However, the surface electronegativity limits the loading of negatively charged small molecules and biologics (i.e., nucleic acids) and can cause repulsion between the silk nanoparticle and the target cell membrane.[186, 187]

To improve uptake by the target tissue, silk nanoparticles can be functionalized by targeting and stealth ligands. The conjugation of biologically active ligands improves silk nanomedicine efficacy by enabling receptor-mediated endocytosis and reducing reticuloendothelial system clearance.[129] Due to the presence of chemically reactive amino acid groups within the silk fibroin peptide sequence, active targeting and stealth coating can be achieved by chemical modification of the silk amino acid side chains (Table 1.1).[129] For

example, bioconjugation of the arginylglycylaspartic acid sequence, folate and H2.1 Her2-binding peptide (Table 1.1) to silk fibroin particles improves their adhesive properties to cancer cells that overexpress integrins, folate receptors and Her2 receptors, respectively.[129] The conjugation of folate has also been shown to aid the cellular uptake by folate responsive cancer cells.[129,185] Alternatively, stealth coating nanoparticles by post-synthetic conjugation of polyethylene glycol has been shown to stabilize colloidal silk drug carriers in physiological model solutions,[160] improve the *in vitro* drug release of doxorubicin at pH 4.5,[160] reduce *in vitro* coagulation and platelet activation in human whole blood,[184] and alter the macrophage response.[159] Consequently, it is clear that the progress of silk nanomedicines to the clinic requires leverage of conjugation techniques.

Table 1.1. Post-synthetic chemical modification of silk fibroin nanoparticles for active targeting.

Nanoparticle carrier material	Chemical modification	Therapeutic payload	Cancer cell line	Reference
Gold	Silk fibroin nanoparticles	Doxorubicin	Hela	[188]
Silk	SP5-52 peptide	Gemcitabine	LL-2	[189]
	Technetium-99 and tween 80	Doxorubicin	C-6, LN-229	[190]
	Cellulose acetate	Au-Ag	MCF-7	[191]
	Lyp-1	Quercetin	4 T1	[192]
	Chondroitin sulfate	Curcumin	264.7 macrophages	[193]
	Calcium chloride	Doxorubicin	4 T1	[194]
	Cylic-arginylglycylaspartic acid	Curcumin	CACO-2, HeLa	[195]
	Molecularly imprinted polymer	-	LDH, NIH 3T3	[196]
	Folic acid	Doxorubicin	HeLa	[197]
	Her2 peptide	Doxorubicin	D2F2E2/LUC	[198]
	Genipin	Cisplatin	A549	[199]

1.4 Silk nanoparticle manufacture

Processing liquid silk feeds for clinical development requires development of manufacturing methodologies that are scalable, safe, lower cost, sustainable and reproducible between batches.[130] In conjunction, the chemistry, manufacturing and controls and good manufacturing practice requirements for nanomedicines increase in complexity as the technology moves from preclinical development to clinical development and then to commercialization so as to ensure a standardized quality.[20] The manufacture of simple nanoparticle systems, such as liposomes and polymeric nanoparticles, have been successfully scaled-up using batch and continuous manufacturing unit operations which are readily available or custom designed in the pharmaceutical industry.[20] However, complex nanoparticle systems that have biological targeting ligands, biological components, carry a combination of therapeutics, use layer-by-layer assembly, or are composite materials, can pose challenges to reproducible scale-up as they require multiple steps or sensitive components, and can require the modification of

existing technology and the development of novel manufacturing processes.[20] This is pertinent to silk fibroin, which possesses the limitations of being highly sensitive to processing conditions during degumming, dissolution, formulation, and purification, such as pH, temperature, and chemical impurities.[200]

Moving from lab-scale to clinical scale typically requires screening formulation factors or methods to ensure reproducible results. Consequently, designing nanoparticle manufacture methods at the lab-scale that are amenable to scale-up is important. Although many lab-scale studies use bulk phase synthesis in semi-batch or batch format, examples of methods that are amenable for scale-up to clinical development include non-wetting template technology,[201] coaxial turbulent jet mixer technology,[202] photolithography,[203] and microfluidic[204] technologies which have the advantages of homogeneity, reproducibility, tunability and, high throughput (multiple kg day^{-1} can be produced). Optimizing formulation conditions at lab-scale and conducting early scale-up studies using these technologies can accelerate clinical translation.[20]

The progression of some nanomedicines to the clinic have been complicated by a lack of standardized physicochemical and biological characterization, unreproducible formulation methods, insufficient characterization techniques and, insufficient comparisons between nanoparticle systems.[20] In order to increase the reproducibility of nanoformulation manufacture details and characterization methodology, the Minimum Information Reporting in Bio-Nano Experimental Literature guidelines were proposed.[205] Arguments against these one-size-fits-all rules is that they make characterization pipelines especially difficult for poorly funded research fields, early-stage researchers and complex nanoparticle systems, so they have not been universally accepted in the academic scientific literature.[20, 206, 207] Nevertheless, it is clear that better standardization and clearer reporting of methods at the lab-scale would be of long-term benefit to improve consistency across studies.[20]

1.4.1 Silk nanoparticle formation in batch format

There has been considerable research interest in using silk nanoparticles as carriers of DNA and small molecule drugs such as doxorubicin which can be loaded during or after formulation (Table 1.1). For larger particles (0.2–10 μm), top-down methods such as jet milling,[208] bead milling,[209, 210] and ball milling[211] provide simple approaches which are easy to scale and do not require toxic organic solvents.[212] However, the large sizes and wide polydispersity index of particle batches produced, combined with the reduction in silk II content during grinding means these particles are more likely to be cytotoxic with short circulation times.[212] Consequently different bottom-up methods have been used to make silk nanoparticles in the bulk phase, namely, instrumental-induced and chemical-induced methods.

Instrumental-induced silk nanoparticle formation involves exposing silk solution to physical forces like heat changes, pressure changes, electric fields, ultraviolet light, and shearing (Table 1.2).[200] Solution-enhanced dispersion by supercritical fluids processing exposes a silk and supercritical CO_2 solution is exposed to high pressure and temperature which atomizes the solution into small droplets with enhanced mixing to form nanoparticles after the CO_2 evaporates.[213-215] Silk particles may also be prepared by utilizing electric fields to ionize an aqueous silk solution, whereby the physicochemical properties of the resulting nanoparticles can be tuned by silk feed concentration and electric field voltage.[216, 217] Electric fields formed by immersing conductive electrodes into a silk solution for a few minutes result in silk electric-gel formation at the positive electrode due to the local reduction in pH, which yields the constituent nanoparticles after freeze-drying.[218, 219] Another method to fabricate nanoparticles uses shearing forces, whereby silk is forced through specially designed nozzles to tune particle properties with flow rate.[216, 217] For example, electrospraying also uses high voltage electric fields across a capillary nozzle to force the silk solution out as droplets and the evaporation of water causes nanoprecipitation.[217] Spray-freeze-drying involves spraying silk solution through an ultrasonic nozzle into liquid nitrogen and the nanoparticles are recovered by freeze-drying.[220] Laminar jet break-up involves breaking up the sprayed silk

solution with a laminar jet and forming the silk II structure with methanol or water vapour.[220] The capillary-microdot method uses a microcapillary to distribute silk solution on glass slides and the nanoparticles are formed by freeze-drying.[221] Finally, photolithography uses UV-induced protein crosslinking through a photomask of a specific pattern to obtain microparticles which are recovered by washing with water.[203]

Chemical-induced silk nanoparticle formation requires the addition of other chemicals to a silk solution to induce covalent chemical or intermolecular bonding to expedite the silk I to silk II secondary structure transition which occurs during nanoparticle formation (Table 1.2).[200] Cross-linking reactions introduce strong covalent bonds to initiate silk II formation by mixing silk with chemical crosslinkers like 1-ethyl-3-(3-dimethylaminopropyl)carbodiimide.[222] Self-assembly methods initiate protein-protein interactions by complex layer-by-layer silk deposition steps in the presence or absence of a particle template.[223-225] Polymer blending comprises four steps: air-drying of composite polymer-silk films or hydrogels for controlled silk self-assembly; dissolution of silk in water; sonication; and, centrifugation to clean and concentrate the suspension. [176, 197, 226, 227] The polymer blending technique has been used to optimize silk nanoparticle properties by using silk-poly vinyl alcohol blends to make air-dried films and altering processing parameters such as initial silk feed concentration, weight ratio of silk and polyvinyl alcohol, and sonication.[176, 228] However, this method results in nanoparticles which are toxic and are predicted to possess an undesirable circulation time in clinical applications due to the high polydispersity index (0.40–0.68) and large nanoparticle size (ranging from 0.3–20 μm) measured by dynamic light scattering (DLS).[176, 228] Other fabrication methods proceed *via* a water-in-oil emulsion intermediate. For example, the reverse microemulsion technique involves mixing a silk solution into a surfactant-organic solvent mixture such as Triton-X 100 and cyclohexane, which is then broken using an alcohol antisolvent like ethanol and methanol to recover the nanoparticles.[229] Alternatively, emulsion solvent evaporation uses paraffin to generate a water-in-oil emulsion, which is then evaporated off by heating leaving the aqueous nanoparticle suspension.[230] Finally,

emulsification diffusion homogenizes the silk solution with a water-immiscible organic solvent to form a water-in-oil emulsion and the nanoparticles purified using centrifugation.[231, 232]

Simple coacervation is one of the most reported bulk phase methods in the literature and can be conducted by salting out or by desolvation with organic anti-solvents. Salting out involves increasing the ionic strength of an aqueous silk solution with a strong ionic solution like potassium phosphate to pull out water from the silk hydration shell and facilitate protein-protein interactions.[197, 233] Additionally, as the silk I to silk II transition occurs at around pH 5, acidic conditions result in silk II crystalline nanoparticles, whereas basic conditions result in silk I rich nanoparticles.[169, 233] The ability to tune secondary structure by varying pH, ionic strength and silk feed concentration is useful for loading weakly basic drugs.[169, 233] However, the nanoparticle sizes of 0.5–2.0 μm from salting out, the <10% drug loading saturation and, the large batch-to-batch variability are not advantageous for anti-cancer applications.[169]

Table 1.2. Bottom-up production methods to fabricate silk nanoparticles. Adapted from references[212, 233].

	Method	Advantages	Disadvantages	Sizes/Payloads (Refs)
Chemical	**Salting Out**	Tunable physicochemical properties Tunable secondary structure Simple process No organic solvent Simple scale-up Mild conditions	Challenging to load hydrophobic and pH-sensitive payloads High polydispersity index Complex purification from salt-out agents	0.486–2.0 μm Alcian blue Rhodamine B Crystal Violet Doxorubicin ([233, 169, 234])
	Desolvation	Tunable physicochemical properties Simple process Simple scale-up Mild conditions	Difficult to produce nanoparticles >200 nm Complex purification from organic solvents Challenging to load hydrophobic payloads Low drug loading capacity	35–300 nm Alpha mangostin Doxorubicin ([185, 222, 235-237])
	Polymer blending	Tunable physicochemical properties Tunable secondary structure Simple process Simple scale-up Mild conditions No organic solvent	Challenging to load hydrophobic payloads Complex purification from polymer residues Silk I secondary structure mainly produced	0.3–100 μm Bovine serum albumin Dextran Rhodamine B ([176, 226])
	Self-assembly	Tunable physicochemical properties Tunable morphology Tunable secondary structure Mild conditions	Complex process Low throughput	0.02–6 μm Linalyl acetate Plasmid DNA ([223-225])
	Reverse microemulsion	Simple process Tunable physicochemical properties	Complex purification from organic solvents and surfactants	167–169 nm Rhodamine B ([229])

	Emulsion solvent evaporation	Simple process Mild conditions	Microparticles produced Complex purification from organic solvents	80–150 μm Bovine serum albumin ([238])
	Emulsification diffusion	Simple scale-up Simple process Mild conditions	Microparticles produced Complex purification from organic solvents Silk I secondary structure mainly produced	60–150 μm Metformin ([231, 232])
	Cross-linking reaction	Simple process Tunable physicochemical properties	Complex purification from crosslinker reagents	0.3–1 μm Alpha mangostin ([222])
Instrumental	**Supercritical Fluid Solution**	No organic solvent Simple scale-up High drug loading capacity	Expensive Complex process Silk I secondary structure mainly produced	28–194 nm Curcumin Indocyanine green ([215, 239])
	Electrospraying	No organic solvent Tunable physicochemical properties High drug loading capacity	Expensive Silk I secondary structure mainly produced	59–75 nm Cisplatin ([217])
	Electric field	No organic solvent Tunable physicochemical properties	Silk I secondary structure mainly produced	0.2–3.0 μm Bovine serum albumin ([218, 219])
	Spray-freeze-drying	No organic solvent Tunable physicochemical properties High drug loading capacity Cost effective	Microparticles produced Complex process Silk I secondary structure mainly produced Challenging to load hydrophobic and pH-sensitive payloads	3–20 μm Cisplatin ([199])
	Laminar jet break-up	No organic solvent Mild conditions High drug loading capacity	Silk I secondary structure mainly produced Microparticles produced	100–440 μm Salicylic acid Propranolol Insulin-like growth factor ([220])

	Capillary-microdot printing	Tunable physicochemical properties	Complex purification from organic solvent Complex scale-up Low yield Silk I secondary structure mainly produced	20–140 nm Curcumin ([221])
	Photolithography	No organic solvent Monodisperse size and morphology High throughput	Microparticles produced Not applicable for payloads sensitive to UV exposure	5–100 μm ([203])

Organic anti-solvent desolvation is a popular formulation method as it comprises a simple one-step addition of aqueous liquid silk feed to a water-miscible, organic anti-solvent, followed by purification of the silk nanoparticles from the cytotoxic anti-solvent. [185, 235-237] The method utilizes the Marangoni effect[240] to govern the silk I to silk II transition and nanoparticle formation. Silk desolvation was first reported by Zhang *et al.* in 2007, whereby using at least 70% (*v/v*) of acetone resulted in low polydispersity index nanoparticles with sizes ranging between 35–125 nm as measured by transmission electron microscopy with a β-sheet crystalline silk II secondary structure measured by X-ray diffraction, Fourier transform infrared spectroscopy (FTIR) and differential scanning calorimetry (DSC).[236] Zhang *et al*. reported that out of polar protic solvents including the first three monohydric alcohols and polar aprotic solvents including tetrahydrofuran and acetonitrile, acetone gave the most favourable particle properties. This may be due to its intermediate polarity and shape[236] which enable rapid transition of the α-helix to β-sheet secondary structure transition; reducing the polarity of monohydric alcohols has been found to increase the transition when added to silk films.[241] Additionally, the type of silk used during desolvation governs the resulting particle properties due to the different molecular structures. To illustrate, desolvation of silk extracted from *Antherea mylitta* (*A. mylitta*) cocoons with dimethyl sulfoxide resulted in nanoparticles roughly 160 nm in size compared to nanoparticle sizes of roughly 180 nm for silk extracted from *B. mori* cocoons.[242]

Recently, particles were generated in acetone by varying silk feed concentration between 5–10% *w/v* and varying silk molecular weight.[243] The silk molecular weight was varied by performing the degumming procedure for 1 h, 0.5 h, and 0.17 h to generate molecular weights of < 171 kDa, 31−268 kDa and 171−460 kDa.[243] The authors found that although the PDI did not vary significantly, ranging between roughly 0.20–0.32, increasing the silk feed molecular weight and silk feed concentration increased the nanoparticle size from 58 nm to 254 nm as measured by DLS.[243] Reducing the temperature to -20 °C generally resulted in smaller nanoparticles being formed.[243] Principal component analysis revealed that the silk

feed concentration had a greater influence on the particle diameter than the molecular weight of the silk feed.[243] Drawbacks to the desolvation method include the difficulty in tuning nanoparticle size above 200 nm without knock-on increases to the PDI and the need to purify the nanoparticle product from toxic antisolvents.[243]

The variety of bulk methods investigated is partly a consequence of the challenges that the silk feed polydispersity and self-assembly properties pose to reproducible manufacture. The inherent difficulty in achieving reproducible manufacture is exacerbated in batch format due to its time-dependent nature. This can lead to product property deviation throughout formulation and long cleaning cycles to remove silk biofouling which lowers throughput. Consequently, optimizing silk formulation using continuous methodology has been proposed as a solution to increase reproducibility and sustainability of silk nanoparticle manufacture.

1.4.2 Silk nanoparticle formation in continuous format

There remains a need to develop and optimize nano-formulation technology with increased scalability, reproducibility, and throughput to reduce production costs, safety concerns, and negative environmental impact. Continuous production provides advantages over batch formats in safety, cost, and environmental impact as the production line is a one-step process that does not need to be interrupted by long emptying and cleaning cycles. Additionally, the reproducibility of product properties can be ensured as in-line monitoring systems can be designed to ensure the critical quality attributes of the products in the output stream are within the designated safe ranges, and production stopped should deviation occur. Chemical-induced silk nanoparticle formulation methods that can be translated into continuous format include desolvation,[174, 179, 228] emulsification[155, 244] and, polymer blending.[245]

Microfluidic mixing is a pertinent production technology to continuous silk nanoparticle formulation as precise manipulation of process factors including total flow rate and flow rate ratios enables the control of particle properties.[246-248] Early microfluidic channel designs were made from polydimethylsiloxane using soft lithographic techniques. However,

polydimethylsiloxane is incompatible with organic solvents, acids and bases[249, 250] which can result in channel deformation and swelling during formulation and cleaning steps. Alternative materials including glass, stainless steel and, polypropylene improve the range of solvent compatibility but can be more expensive and difficult to produce.[249, 250] Indeed, silk microfluidic devices have also been utilized for bio-microelectrical mechanical system and chemical analysis applications and can be fabricated by micromoulding on polydimethylsiloxane reverse moulds[251] and by lithium bromide etching.[252] To address the challenge of biofouling and channel failure during formulation, channel surfaces can be treated with proteins and polymers to reduce surface adsorption.[253]

Microfluidic devices may increase the rate of translation from bench to clinic as the laminar flow fluid dynamics in the specialized mixing chambers can induce high mixing rates and the high total flow rates that can be achieved can lead to commercially-relevant throughput.[254] The mixing chamber design should take into consideration the formation mechanism to ensure fluid dynamics and mixing times produce a narrow distribution of nanoparticle properties without aggregation.[254] The control over silk nanoparticle formation has been improved by commonly used microfluidic designs including staggered herringbone,[174, 179] swirl,[255] hydrodynamic flow-focusing,[245, 256] double-junction[257] and, T-mixers.[155] For example, the microfluidic T-mixer proved advantageous over batch emulsification to improve control over nano-microparticle size (51–2500 nm)[244] and microparticle morphology (6–80 μm spheres to 5–35 μm × 4.5–65 μm rods).[155] The co-focusing mixer when used for polymer blending silk and polyvinyl alcohol (2.8–6.8 μm) resulted in monodisperse microparticle size distribution (6.6 μm, PDI 0.13) compared to batch format (5.8 μm, PDI 0.65).[245] However, the double-junction, flow-focusing and T-mixer require a low flow rate (μL/h) which make them unsuitable for high throughput (kg day^{-1}) commercial production.

The commercially-relevant NanoAssemblr™ system uses a staggered herringbone mixer to provide advantages over batch format including low millisecond mixing times, high

total flow rates of 12 mL min^{-1} and, full scalability to commercial formulation systems operating under current good manufacturing practice conditions.[258, 259] Silk desolvation performed by Wongpinyochit *et al*.[174] in the NanoAssemblr™ using *B. mori* silk degummed using the sodium carbonate method for 1 h with isopropanol and acetone antisolvents achieved physiologically-relevant nanoparticles (110 nm to 310 nm) with low polydispersity (0.1 to 0.25), negative surface potential (-20 to -30 mV) and a silk II structure (48–51% β-sheet content). The authors found that increasing the antisolvent:silk flow rate ratio from 1:1 to 5:1 increased the magnitude of the negative surface charge, decreased the size, decreased the size distribution, increased the colloidal stability over 42 days at 4 °C and, increased the yield. Scanning electron microscopy showed that increasing the total flow rate from 1 to 12 mL min^{-1} generally increased the presence of aggregates. The nanoparticles were not cytotoxic to a murine macrophage RAW 264.7 cell line with an IC_{50} above 100 mg mL^{-1} and were trafficked to the lysosomes after 3 h.[174]

Solomun *et al*. expanded upon this work by comparing the desolvation of sodium carbonate degummed *B. mori* silk with isopropanol in manual semi-batch format with the microfluidic NanoAssemblr™ system.[179] The optimal microfluidic process factors of a 5:1 flow rate ratio and a 1 mL min^{-1} flow rate were set to optimize the silk degumming time.[179] As for previous work,[174] the nanoparticles showed good biocompatibility in RAW 264.7 cells with an IC_{50} over 250 μg mL^{-1}.[179] The authors found that 1 and 1.5 h degummed silk in microfluidic and semi-batch formats resulted in similar nanoparticle sizes (101−114 nm) and size distributions (0.088–0.107).[179] The surface potential was significantly reduced in microfluidic manufacture (−28 to−29 mV) compared to semi-batch format (−39 to−43 mV).[179] In both manual and microfluidic format, increasing degumming time from 10 minutes to 1 and 1.5 h decreased the nanoparticle size and size distribution while the yield increased from 8% to roughly 20%.[179] Although the low volumetric throughput of optimal formulation (1 mL min^{-1}) and low yields[174, 179] are key disadvantages of desolvation using the staggered herringbone

mixer, operating microfluidic channels in parallel provides a solution to increase throughput for larger scale production.

To address low volumetric throughput, microfluidic swirl mixers have recently (2022) been used to manufacture silk nanoparticles by desolvation with ethanol at high flow rates (10–50 mL min^{-1}) with good reproducibility and low distribution of nanoparticle size.[228] Nanoparticle purification was achieved with tangential flow filtration,[228] which provides a scalable technique to remove organic solvent and unbound payloads.[255] The nanoparticle properties were varied with total flow rate, silk feed concentration and the number of mixing elements.[228] The authors used nanoparticle tracking analysis to measure the average nanoparticle size. The nanoparticle tracking results are similar to measurements by DLS but the single particle analysis gives a greater accuracy size distribution, as small nanoparticles in a polydisperse samples are not underestimated.[260] The authors used *B. mori* silk degummed using the sodium carbonate method for 30 minutes and found that the nanoparticle size and size distribution decreased with total flow rate increasing from 10 to 50 mL min^{-1}, with spherical morphologies for nanoparticles of sizes below 200 nm produced at 20 mL min^{-1} observed by transmission electron microscopy. Increasing the number of mixing elements from one to four resulted in larger nanoparticles at each flow rate. Increasing the silk feed concentration from 0.5 to 3% *w/v* increased the nanoparticle size across all flow rates and from roughly 100 to 300 nm at 10 mL min^{-1}. The maximum negative surface potential of the nanoparticles was -28 mV and the negative surface potential increased in magnitude with mixing elements. The negative surface charge in conjunction with all nanoparticles bearing a silk II structure by FTIR analysis resulted in colloidal stability when stored in water at 4 °C for 30 days. Although the authors did not report the nanoparticle yield, the swirl mixer proved advantageous over the standard T-mixer as smaller nanoparticles with narrower size distribution were produced when compared to using the same processing parameters.[228]

1.5 Synthetic modification of silk nanomedicines and silk films

Silk fibroin has several chemically reactive amino acid groups which can be leveraged for homogeneous or heterogeneous bioconjugation (Figure 1.3). Functionalized silk nanoparticles for improved drug delivery by active targeting are listed in Table 1.1.[129, 261] Chemical modification can be performed using the reactivity of natural amino acids in the silk protein chain although these routes are typically associated with low chemoselectivity, multiple reaction steps and, low yields due to complicated purification. Carbodiimide, NHS-ester and diazonium coupling have been popular methods to functionalize silk fibroin through silk primary amines or carboxylic acid side chains (Figure 1.4).

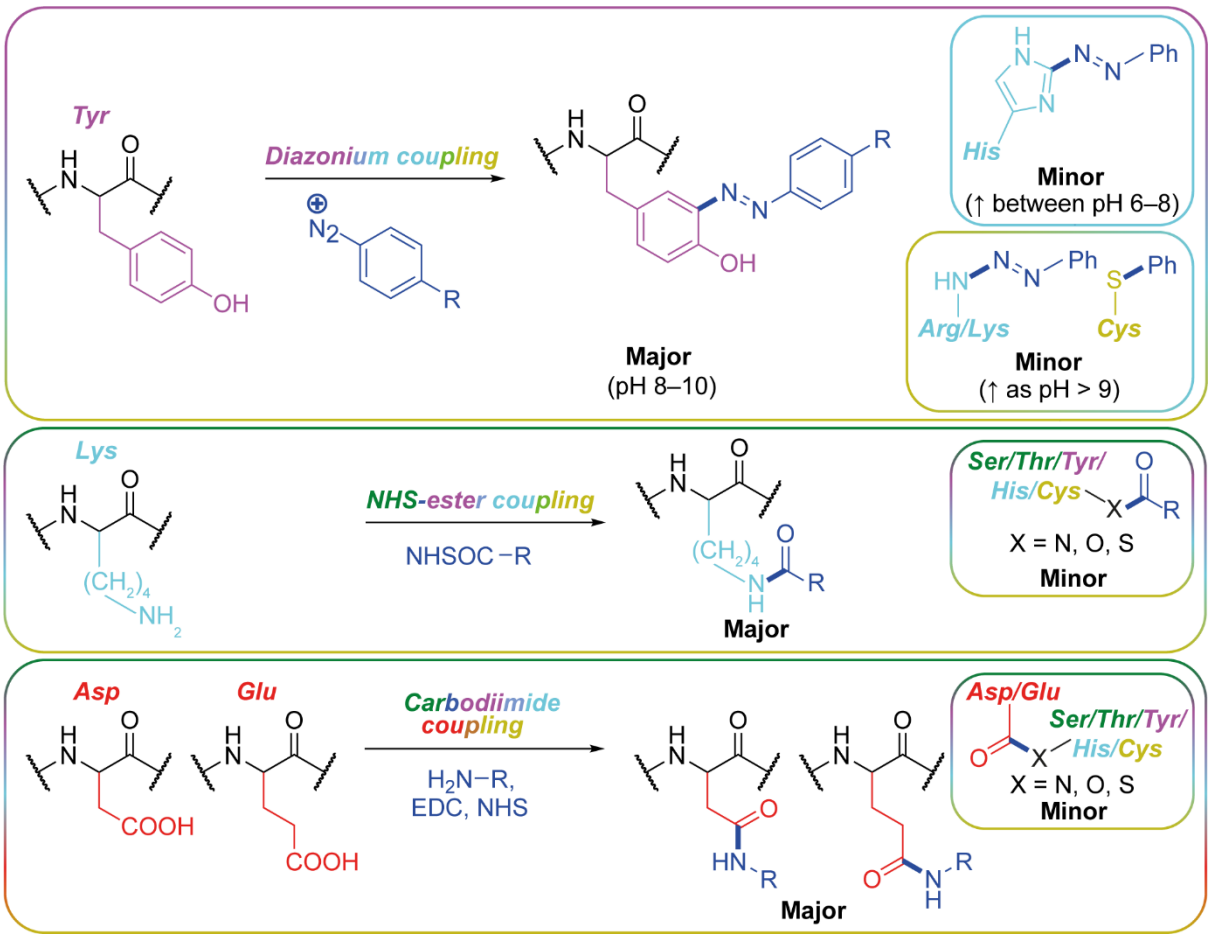

Figure 1.4. Popular bioconjugation techniques which display a range of chemoselectivities and utilize the reactive silk fibroin natural amino acid chemistry. The reaction schemes have been adapted from references.[132, 157, 262, 263]

Homogeneous reactions, which are conducted in the solution-phase, are advantageous for functionalization of silk substrates as they enable downstream processing of liquid silk into different material formats and morphologies. For example, to improve anticancer efficacy by folate-mediated targeting, Horo *et al.* functionalized silk using homogeneous carbodiimide coupling to first increase amine content with ethylenediamine before performing coupling reactions with NHS ester-activated folate. The functionalized silk was purified from small molecule side products and unreacted reagents by dialysis and then processed using layer-by-layer deposition to form a coating for chitosan-gold microparticles.[188] The functionalized silk was analyzed by FTIR to determine a 14% conjugation efficiency of ethylenediamine and by UV-visible spectroscopy to determine a 18.3% conjugation efficiency of folate.[188] Compared to the uncoated particles, the silk-folate coating resulted in decreased burst drug release as it served as a diffusion barrier to encapsulated doxorubicin and increased the *in vitro* cytotoxicity in HeLa cell lines.[188] However, homogeneous reactions can suffer limitations due to the amphipathic nature of silk fibroin. For example, due to the low solubility of silk fibroin in organic solvents, many reactions are conducted in aqueous media. Consequently, the non-polar regions of the silk molecule form non-covalent interactions and undergo folding which can protect reactive amino acids from incoming reactants, resulting in low reaction yields and complicated purifications to separate the product from unreacted substrates.

Heterogeneous chemical modification can involve functionalization of silk fibroin nanoparticles, fibers or films with stealth ligands such as polyethylene glycol[159, 160] or biologically active molecules like RGD,[114, 195] folate[112, 197] and, targeting peptides[189] for active targeting. Late-stage heterogeneous functionalization of these silk formats can simplify purification, ensure modification of the reactive groups present at the material surface, improve performance and, open up new applications.[132, 157] Indeed, Subia *et al.* reported the first chemically functionalized silk nanoparticles for active targeting using heterogeneous synthesis with acetone desolvated *A. mylitta* silk nanoparticles (roughly 200 nm). The authors used

carbodiimide coupling chemistry to produce *A. mylitta* silk-folate nanoparticles. Carbodiimide coupling can result in a low extent of modification due to the low carboxylic acid and primary amine content of silk in conjunction with the heterogeneous distribution of these residues along the protein sequence. Notably, the authors did not quantify the conjugation efficiency, although the functionalized nanoparticles were stable, spherical and, had significantly greater endocytosis by human MDA-MB-231 triple-negative breast cancer cells compared to native silk nanoparticles. Folic acid competition studies indicated that the nanoparticles were recognized by the folate receptor, as endocytosis was blocked in the presence of excess folic acid.[112] The authors loaded the folate-silk nanoparticles post-synthetically with doxorubicin,[112] but drug loading could also be conducted *in situ*.[107] For example, *in situ* paclitaxel loading during ethanol desolvation of 0.5% *w/v* silk fibroin was reported to give 10% *w/w* drug loading.[107] The resulting silk-paclitaxel nanoparticles could undergo heterogeneous carbodiimide coupling with an anti-EGFR-iRGD dual-functional peptide and exceeded 75% conjugation efficiency, measured using fluorescence spectroscopy. The peptide association with epidermal growth factor receptors and αvβ3/αvβ5 integrins increased the *in vitro* and *in vivo* anticancer efficacy compared to native silk controls. Additionally, the *in vivo* tumor targeting was greater compared to the silk controls, as determined by near infrared fluorescence imaging at 12 to 72 h after injection into HeLa-bearing mice. However, receptor engagement *in vivo* was not proven with soluble paclitaxel negative controls or soluble targeting residue competition studies.[107] Important limitations to heterogeneous synthesis post-drug loading include the heightened complexity of purification, the possibility of side-reactivity with the payload, and reduction to drug loads during purification.

Diazonium coupling chemistry with silk fibroin produces an azobenzene derivative through an electrophilic aromatic substitution between a diazonium salt with silk tyrosine side chains (Figure 1.4).[158] Diazonium coupling reactions have been used to alter the polarity of the silk molecule by functionalization with a range of moieties such as sulfonic acids, carboxylic acids, ketones and, alkanes.[158] The reaction is advantageous over other tyrosine

functionalization methods for numerous reasons, namely: it is conducted in mild, basic borate buffer (pH 9.0) in which silk fibroin is stable; readily available aniline derivatives can be used; electron-withdrawing and electron-donating anilines are tolerated; the reaction proceeds rapidly and can be quenched in 5–30 minutes;[158] homogeneous and heterogeneous functionalization are possible; the installation of the azobenzene group can be monitored by ^{1}H-NMR or UV-visible spectroscopy at 325 nm; and, the functionalized silk can be recovered by size exclusion chromatography or centrifugation.[158] The reaction has tunable levels of modification by changing the ratio of diazonium salt to tyrosine or by changing the silk concentration.[158] For example, the conversion efficiency can be maximized to roughly 70% tyrosine conversion with dilute silk solutions and 0.9 equivalents of aniline derivatives containing electron withdrawing substituents.[158] However, the reaction conjugation efficiency can be impeded to roughly 20% by using aniline derivatives with electron donating substituents or by low aqueous solubility of the diazonium salts.[158] The drawbacks of the reaction include side reactions with histidine residues and silk gelation when conducted at high silk concentrations or when using an aniline derivative with hydrophobic substituents.[158]

One method to increase conjugation efficiency is to use reactions with low chemoselectivity like glutaraldehyde cross-linking (Figure 1.5). Silk nanoparticles (40–120 nm) assembled using acetone desolvation were used as a carrier for long-acting insulin formulations by surface functionalization with insulin. Silk-insulin crosslinks were established using 0.7% glutaraldehyde for 8 h, the particles purified using repeated centrifugation and, ELISA used to demonstrate 90 to 115% recovery of insulin.[264] Conjugation of insulin to the silk nanoparticles resulted in greater stability of insulin in human serum and trypsin solution *in vitro*.[264] The disadvantages of glutaraldehyde cross-linking include the denaturant properties of glutaraldehyde on proteins,[264] the low chemoselectivity resulting in undesired properties of the conjugate, and the high energy required to break strong covalent bonds for payload release.

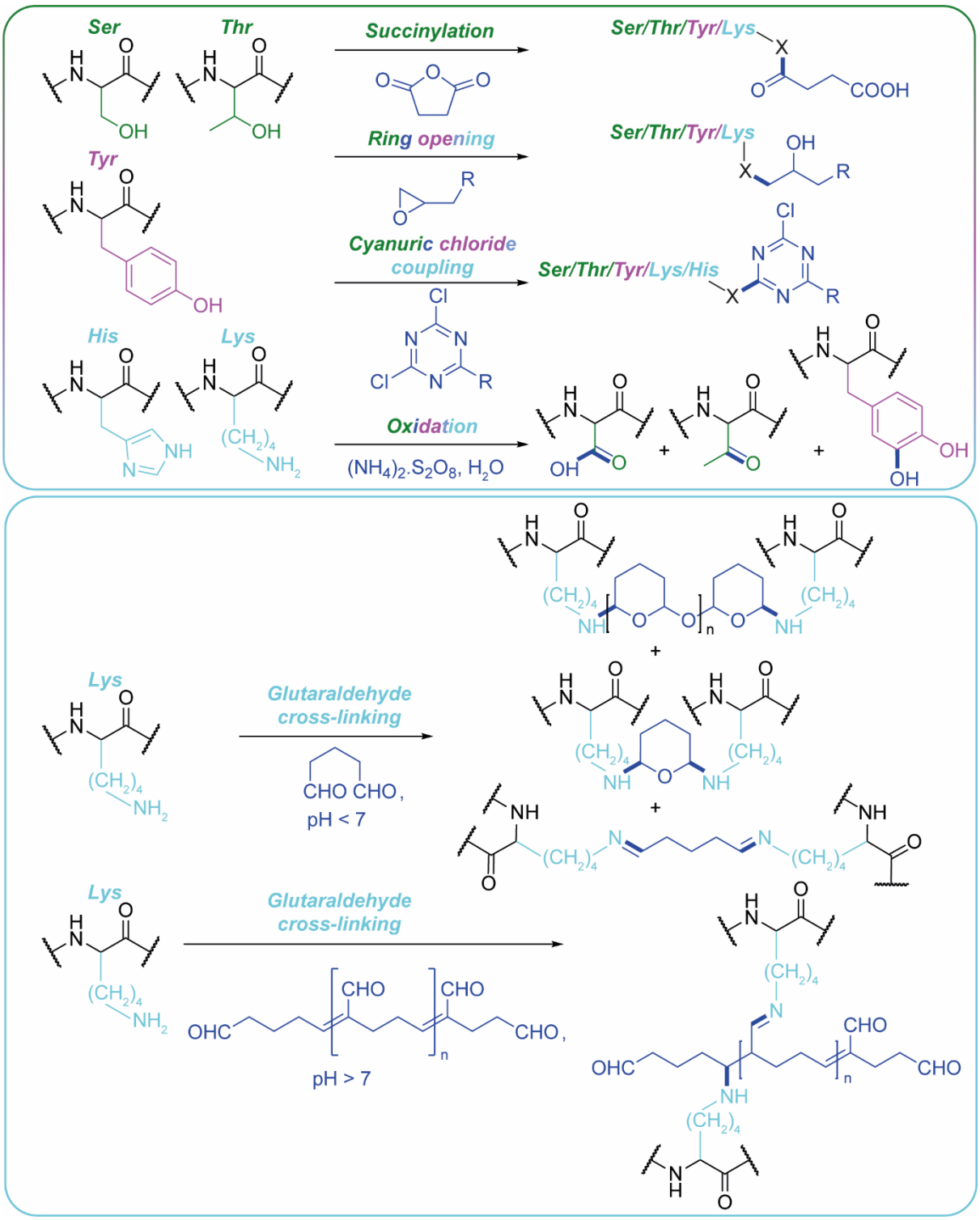

Figure 1.5. Bioconjugation techniques which display low chemoselectivity and utilize the reactive silk fibroin natural amino acid chemistry. The reaction schemes have been adapted from references.[132, 157, 262, 265-268]

Chemoselective silk bioconjugation can be achieved using enzymatic catalysts like horse-radish peroxidase[269] and N-acetylgalactosamine transferase[270] which act on natural amino acids. Enzymatic catalysis presents a biorthogonal synthesis route as the reactions are performed under physiological conditions, are highly site-selective and, can increase reaction yields while avoiding the need for co-factors or toxic metal catalysts. However, purification from residual enzymes can provide a challenge, especially during reactions which induce gelation as the enzymes can become incorporated into the hydrogel network.[269]

Alternatively, chemically modifying naturally reactive amino acids after protein expression to introduce click handles opens up multi-step synthetic routes, due to the highly specific and efficient nature of biorthogonal click chemistry (Figure 1.6).[271, 272] For example, Scheibel and colleagues manufactured first-generation spider silk-inspired proteins using carbodiimide coupling of cast films with azidopropylamine. The installation of the azido moiety was monitored by FTIR and used as a handle for copper-catalyzed azide-alkyne cycloaddition to functionalize the film surfaces with alkyne-terminated, hydrophobic glycopolymers with molecular weights ranging from 10 to 30 kg mol^{-1}. Cycloaddition was confirmed using FTIR and fluorescence spectroscopy although the conjugation efficiency was not determined. Functionalized films had a reduction in water contact angles, improved cell adhesion of mouse embryo fibroblasts and increased extracellular matrix adsorption from solution compared to native films.[273] However, a limitation of the azide-alkyne cycloaddition for biomedical applications is the requirement for a toxic copper catalyst.[273]

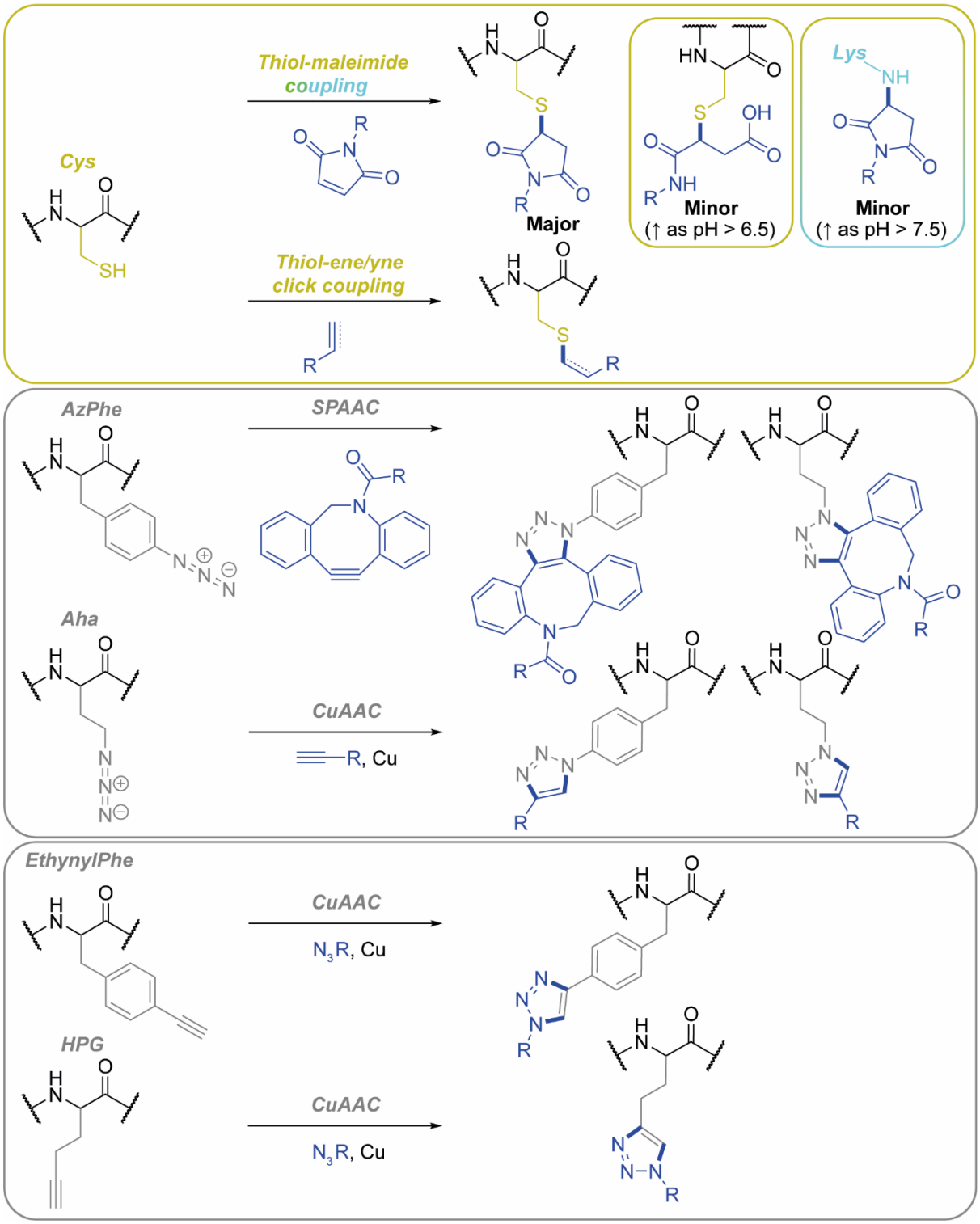

Figure 1.6. Bioconjugation of recombinant silk fibroin using bioorthogonal thiol-maleimide, thiol-ene, and azide-alkyne click chemistry. Reaction schemes have been adapted from references.[274-278]

Hence, second-generation silks were developed by Scheibel and colleagues for thiol-ene click chemistry. The N-terminal end of a spider silk-inspired protein was genetically modified by the insertion of a short amino acid tag containing one cysteine (GCGGSGGGGSGGGG) and *Escherichia coli* used for heterologous production of the recombinant protein.[279] The coupling efficiency of the recombinant protein with fluorescein-maleimide was assessed as 70–90%[279] and the silk could be processed into patterned films by wet-casting[280] and Janus fibers by electrospinning.[281] The exposed cysteines on the films and Janus fibers could undergo thiol-maleimide Michael addition with maleimide-functionalized gold nanoparticles for applications ranging from biomedical sensors and thermal therapies to water splitting.[280, 281] Limitations of second-generation silks include the low degree of functionalization arising from the installation of one reactive cysteine per molecule and the lability of cysteine-maleimide conjugates to exchange reactions, which raises concerns towards conjugate stability *in vivo*.

Third-generation silks contain a biorthogonal non-canonical amino acid tag which provide an advantage over native silks by enabling site-specific chemical modification in one step and without the addition of enzymatic catalysts (Figure 1.7). Importantly, the simplified synthetic routes imparted by using third-generation silk compared to natural silk substrates can potentially reduce the cost of purification and increase product yields. For example, Teramoto and colleagues genetically engineered *B. mori* larvae to install a mutant, broad substrate recognition, phenylalanyl-tRNA synthetase.[282] Feeding transgenic silkworms with *p*-chloro-, *p*-bromo-, and *p*-azido-substituted analogues of L-phenylalanine *in vivo* resulted in their incorporation into spun silk fibers.[276] Incorporation of non-canonical amino acids was optimized using *p*-azido-phenylalanine which enabled the scaled-up production of azido-functionalized silk.[283, 284] The azido-silk could be degummed using 30 minute sodium carbonate or urea degumming methods and processed into fibers, films and porous sponges.[284, 285] Heterogeneous strain promoted azide-alkyne cycloaddition, a copper-free click reaction, was conducted with fluorescent tracers,[286] polymers,[285] or biotin ligands.[284] To

simplify silk processing, a photostable *p*-ethynylphenylalanine-modified silk was synthesized using the phenylalanyl-tRNA synthetase transgenic silkworms. However, terminal alkyne incorporation is not applicable for biomedical materials as this click handle requires copper catalysis to undergo cycloaddition.[277] General limitations of these third-generation silks include the instability of the azide group in light, the requirement for extracting silk directly from the silkworm gland or from the fiber using only mild degumming conditions to prevent decomposition of the reactive azido group and, low azido and alkyne contents (roughly 0.6%).[287]

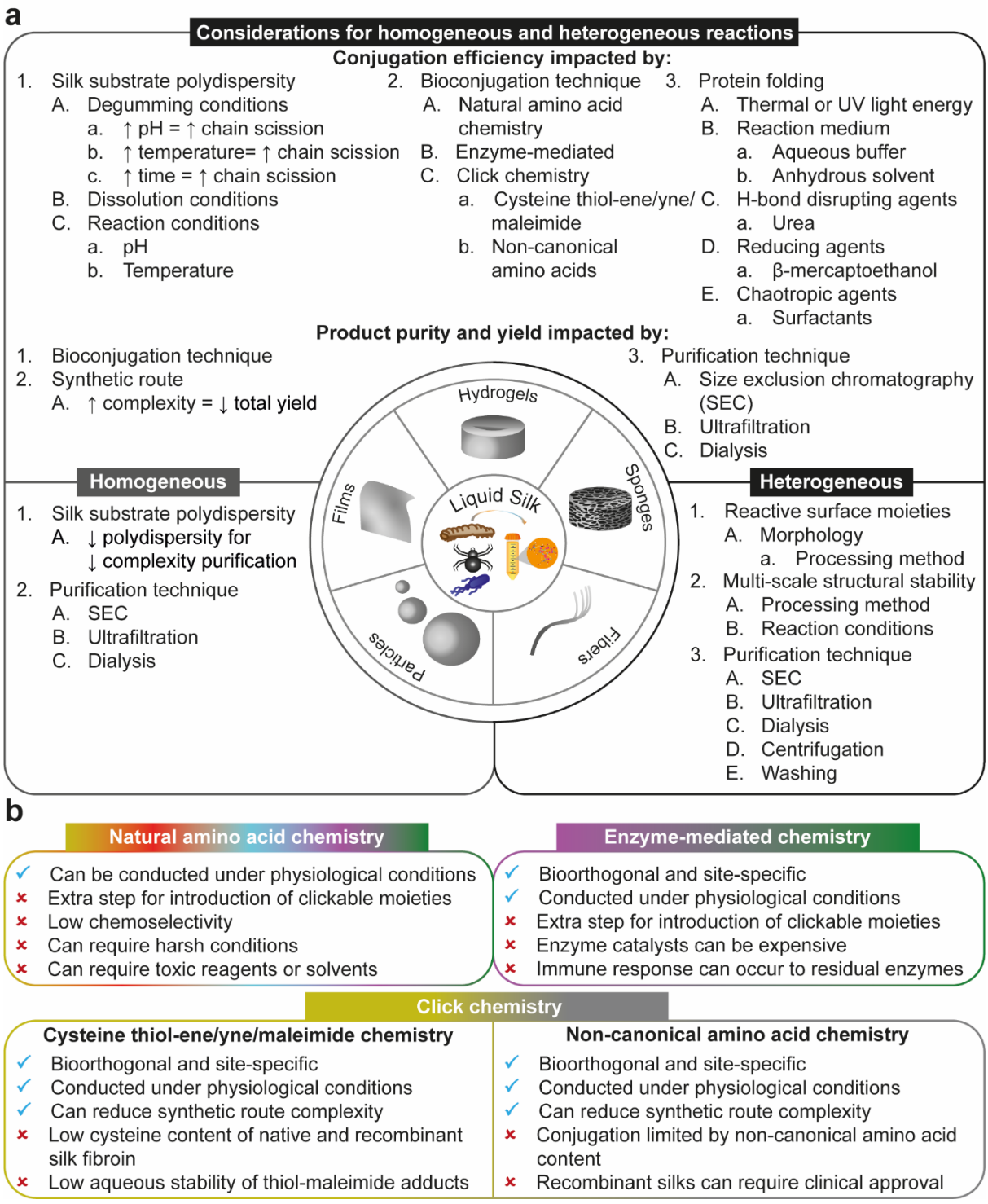

Figure 1.7. Selected considerations for the bioconjugation of silk fibroin using (a) homogeneous and heterogeneous reactions, and (b) selected advantages and disadvantages of the bioconjugation techniques discussed herein. Image adapted from[145].

Further developments have focused on increasing click handle contents by partial replacement of tyrosine residues, which are more prevalent than phenylalanine and are distributed homogeneously throughout the repetitive and non-repetitive sequences of the fibroin heavy chain.[132, 144] For example, Teramoto and colleagues developed and expressed a mutant *B. mori* tyrosyl-tRNA synthetase in transgenic *B. mori* larvae to incorporate orally administrated 3-azidotyrosine. However, low replacement ratios prevented quantification of incorporation by MALDI-TOF-MS, although click chemistry with fluorescent tracers qualitatively demonstrated incorporation of 3-azidotyrosine.[287] Overall, using click-capable, recombinant silks as a substrate shortens synthetic routes and can simplify the purification of novel silk-based materials with improved properties.

1.6 Hypothesis, Aims and Objectives

The hypothesis of this thesis is that the scalability of silk processing can be improved, specifically, silk nanoparticle manufacture for drug delivery applications using microfluidic-assisted and semi-batch nanoprecipitation in low molecular-weight alcohols. Desirable nanoparticle properties for drug delivery include narrow size distributions between 100-200 nm, targeting capability, long shelf lives, high drug loading capacity (> 10%) and responsive drug release in the target tissue. The overall aim of this thesis is to characterize the processing parameters which control the outcomes of silk nanoparticle manufacture for drug delivery and of 3D silk film fabrication for eco-sensing by exploiting nanoprecipitation and origami folding, respectively (Figure 1.8). The main aim can be divided into four experimental chapters which are laid out as follows:

i. Chapter 1 provides a broad introduction to the properties of silk fibroin and applications in drug delivery.
ii. Chapter 2 describes the design and assessment of the semi-batch manufacturing method for reproducible production of silk nanoparticles. The impact of varying the stirring rate and standing time on nanoparticle critical quality attributes, such as the particle size, surface

charge, morphology, secondary structure, and yield were analyzed. This chapter was published in ACS Biomaterials Science and Engineering, 2020, 6, 6748–6759 (DOI: 10.1021/acsbiomaterials.0c01028).

iii. Chapter 3 details the assessment of semi-batch and microfluidic manufacture for the control of silk nanoparticle morphology. The flow and mixing properties of the semi-batch and microfluidic systems were characterized. The impact of varying key formulation and process factors on the nanoparticles' critical quality attributes were analyzed. This chapter was published in RSC Advances, 2022, 12, 7357– 7373 (DOI: 10.1039/d1ra07764c).

iv. Chapter 4 details the assessment of semi-batch and microfluidic manufacture for scalable production of silk nanoparticles. The impact of varying the volumetric scale of manufacture was assessed in semi-batch format while a round robin study consisting of four participants was utilized to estimate the volumetric scalability of microfluidic manufacture. This chapter was published in Molecules, 2022, 27, 2368 (DOI: 10.3390/molecules27072368).

v. Chapter 5 describes the assessment of processing methods on the properties of 3D magnetic, native and azo-silk films loaded with anthocyanin and curcumin for eco-sensing. The film thickness, iron oxide content, and silk fiber content were optimized for hydrophobicity, locomotion, shape preservation, ease of origami folding and color analysis. The pH-sensitivity, storage stability and, semi-autonomy of the optimized silk eco-sensors were then determined. This chapter was published in ACS Applied Bio Materials 2022, 5, 3658–3666. (DOI: 10.1021/acsabm.2c00023).

vi. Chapter 6 provides the outcomes for this thesis and future work directions.

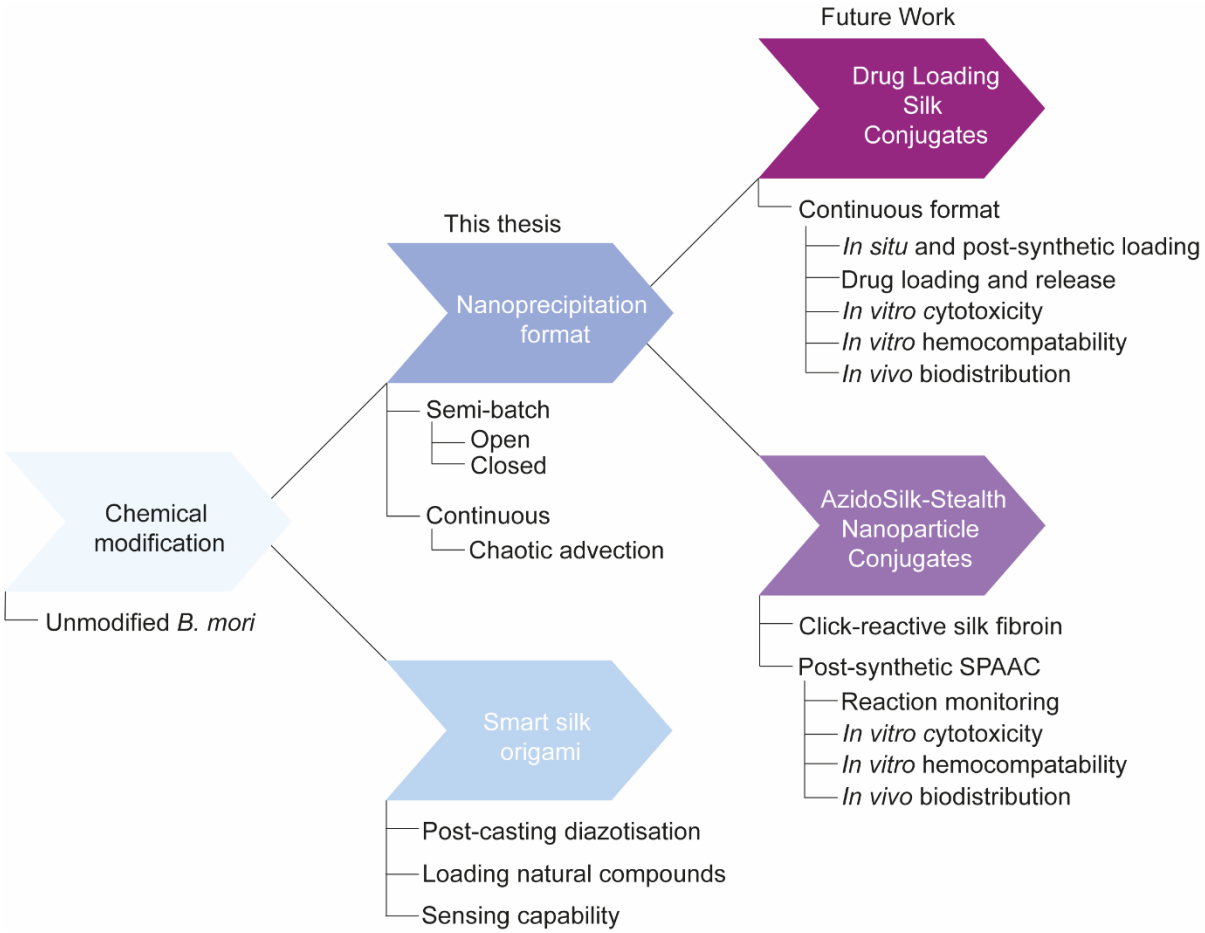

Figure 1.8. Hypothesis, aims and, future work of this thesis.

Chapter 2: Silk Nanoparticle Manufacture in Semi-Batch Format

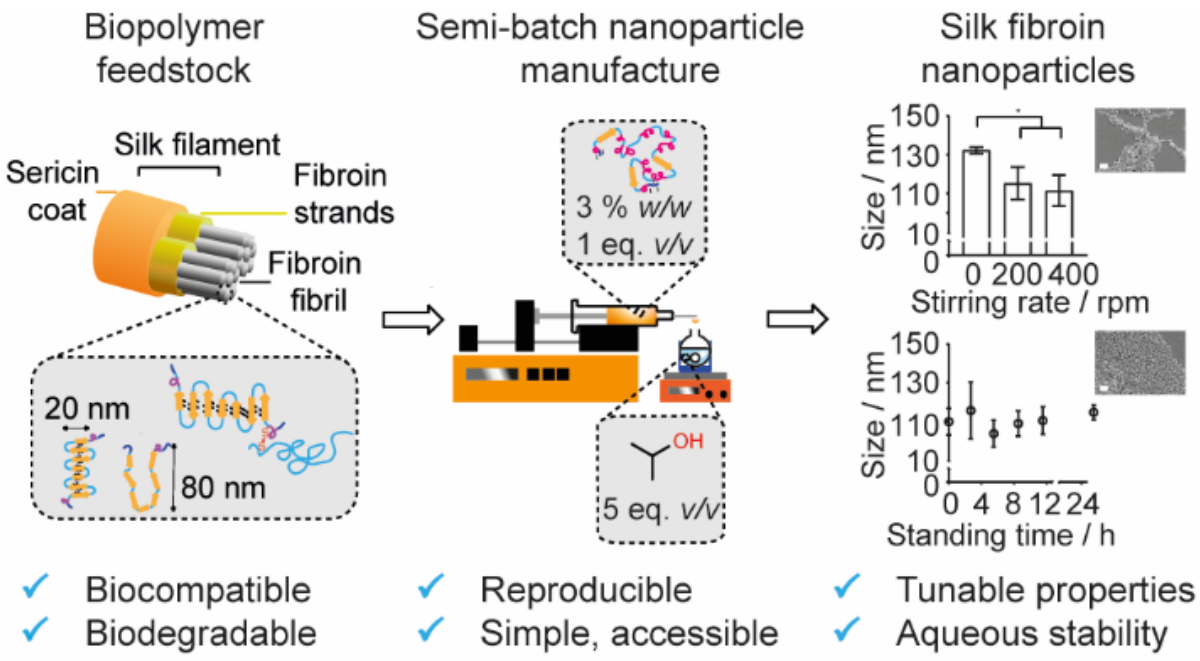

This chapter contains the results from the published article in ACS Biomaterials Science and Engineering (Matthew, S. A. L.; Totten, J. D.; Phuagkhaopong, S.; Egan, G.; Witte, K.; Perrie, Y.; Seib, F. P. Silk nanoparticle manufacture in semi-batch format, *ACS Biomater. Sci. Eng*. **2020**, *6*, 6748−6759. DOI: 10.1021/acsbiomaterials.0c01028). For this work, I designed, analyzed, and carried out all experiments and prepared the manuscript draft.

2.1 Introduction

The mulberry silk produced by the *Bombyx mori* (*B. mori*) silkworm is one of the most extensively studied silks, with ancient and far-reaching applications ranging from domestic to medical textiles.[130, 288] The ability to regenerate silk fibroin protein from the silk cocoon has realized an advent of new material formats with adjustable physical properties; most notable among these formats are porous scaffolds,[289] hydrogels,[290] films[291] and particles.[135] Silk fibroin offers several exploitable characteristics, including broad biocompatibility and biodegradability,[184, 291] low immunogenicity[291] and the presence of reactive amino acids amenable to chemical modification.[160] This amenability makes reverse-engineered silk a promising precursor for clinical applications,[130, 290] as evidenced by the granting in 2019 of the first FDA approval for a regenerated silk hydrogel for human vocal fold reinforcement (Silk Voice®, Sofregen Medical Inc., Medford, MA, USA).[131]

B. mori silk fibroin is a structural protein composed of a light (≈ 26 kDa)[130] and a heavy chain (≈ 391 kDa),[130] which are linked by a disulphide bond.[130] The heavy chain has a block copolymer sequence of short hydrophilic amorphous regions interspersed with long hydrophobic $(GAGAGX)_n$ and $(GAGAGY)_n$ residues.[130] These hydrophobic motifs, which are capable of β-sheet self-assembly and constitute over 50% of the primary structure, impart high mechanical strength to the fibre.[291] Silk is a natural biopolymer with metastable tertiary structures; therefore, the structure of silk-based materials can be tuned to their desired function by modifying their crystallinity[130, 289, 290, 292] and hierarchical composition.[293]

This structural versatility, coupled with the amphiphilic nature of silk, also permits silk to undergo a variety of favorable intermolecular interactions with lipophilic and hydrophilic therapeutic payloads[289, 294] by in situ[294] or post-synthetic loading.[153, 185, 294] These interactions can also stabilize synthetic drugs[289, 294] and biological molecules[289, 294] by surface adsorption or encapsulation, thereby sterically shielding a drug cargo from biological clearance. The drug release behavior can be designed according to a tissue-specific stimulus, to improve efficacy and reduce off-target effects whilst preserving drug structure and activity.[170, 289, 294] Silk

nanoparticles are especially suited for drug targeting of solid tumors as these nanoparticles exhibit increased drug release at low pH,[135, 160] which is a signature of tumor environments. In addition, silk nanoparticles have shown desirable critical quality attributes, including *in vitro* endocytosis-mediated uptake,[185] lysosomotropic drug release[183] and proteolysis,[152, 183] which indicate their value as anticancer nanomedicines.

Preparation of silk particles of sub-micron size (25–180 nm) can be achieved by six major bottom-up methods (reviewed previously[295]): capillary microdot printing,[221] desolvation,[153, 160, 179, 185] supercritical CO_2[296] and electrospraying,[216] emulsification[244] and ionic liquid dissolution.[237] Among these methods, desolvation provides one of the most accessible and least energy intensive lab-scale methods and is commonly used for the manufacture of protein nanoparticles.[297] Desolvation of silk is a nanoprecipitation process whereby an aqueous silk solution is mixed with a water-miscible organic solvent in which the heavy-chain hydrophilic blocks have low solubility (e.g., isopropanol and acetone). This process has no requirement for method-specific, expensive apparatus[295] and produces silk nanoparticles with cores enriched in β-sheet structures without the need for further chemical cross-linking steps.

Currently, optimized lab-scale desolvation methodology uses a semi-batch format consisting of a manual drop-by-drop addition of 3–5% *w/v* silk into at least a 200% *v/v* excess of the organic antisolvent.[153, 160, 185] In comparison to batch processes, where an empty reactor is charged with all species simultaneously, semi-batch desolvation is defined by the feed of the solute into a vessel pre-charged with antisolvent, or vice versa.[298] Semi-batch nanoprecipitation can be scaled-up from the bench,[298] with the process further aided by computational simulations.[299, 300] However, when compared to pilot-scale operations, the manual method suffers from special-cause variations in flow rate, droplet size and dropping height. Additionally, although particle size and polydispersity are controlled by rapid mixing,[298, 299] which is facilitated by agitation,[298, 300] stirring is not a common practice in manual silk desolvation procedures.

Designing procedures which reduce processing times and batch-to-batch variability will aid the progress of pharmaceutical products from the bench to the market.[290, 294] The aim of this Chapter was to establish a simple, semi-automated and higher throughput drop-by-drop technique for semi-batch silk nanoprecipitation. I investigated the impact of several process parameters, including stirring rate and standing time, on the physicochemical properties (e.g., particle size, polydispersity, zeta potential, stability, secondary structure, morphology and yield) of the resulting silk nanoparticles.

2.2 Materials and Methods

Unless otherwise stated, studies were conducted at 18–22 °C. All reagents and solvents were acquired from Acros Organics™ or Sigma Aldrich at > 98% purity, unless otherwise stated, and utilized without additional purification.

2.2.1 Regeneration of *B. mori* silk

Silk fibroin was extracted from *B. mori* cocoons by alkaline degumming. Briefly, *B. mori* cocoons were cut into approximately 5 × 5 mm sections and boiled, with manual stirring, in 0.02 M aqueous Na_2CO_3 (2 L) at 98–105 °C for 1 h. Degummed silk fibers were rinsed in ultrapure H_2O (1 L) three times for 0.33 h each. The silk was then dried for at least 24 h at room temperature.

Dry silk fibers were dissolved in 9.3 M aqueous LiBr solution at 60 °C for 4 h to give a 25% *w/v* silk solution. The silk solution was dialyzed (molecular weight cut off 3500 g mol^{-1}, Slide-A-Lyzer®, Thermo Scientific, Rockford, IL, USA) against ultrapure H_2O (1 L) for 48 h, and then purified by centrifugation over four cycles, each for 0.33 h at 3000 × *g* and 5 °C (Jouan BR4i centrifuge equipped with S40 swing rotor). Silk concentrations were determined gravimetrically over 24 h at 60 °C and then adjusted to 3% *w/v* with ultrapure H_2O.

2.2.2 General drop-by-drop manufacture of silk nanoparticles in semi-batch format

Silk nanoparticles were manufactured at room temperature using a syringe pump (Harvard Apparatus 22, Holliston, MA, USA) equipped with a BD PLASTIPACK™ syringe and blunt needle (23G × 0.25") (Figure 2.1). Inclination of the syringe-pump was 0–0.1°. The isopropanol antisolvent was added to a short-neck round-bottom flask (to give a final 5:1 *v/v* ratio of isopropanol:silk). A 3% *w/v* silk solution was then added drop-by-drop at a rate of 1 mL min^{-1} (≈ 27 drops min^{-1} and 37 µL min^{-1}). The resulting suspensions were incubated at room temperature for the designated time, and then transferred to polypropylene ultracentrifugation tubes, made up to 43 mL with ultrapure H_2O and centrifuged at 48,400 × *g* for 2 h at 4 °C (Beckmann Coulter Avanti® J-E equipped with JA-20 rotor). The supernatant was aspirated, and the pellet was resuspended in ultrapure H_2O (20 mL) and sonicated twice for 30 seconds at 30% amplitude with a Sonoplus HD 2070 sonicator (ultrasonic homogenizer, Bandelin, Berlin, Germany). An additional volume of ultrapure H_2O (23 mL) was added and the centrifugation, washing and resuspension steps were repeated twice more. The final pellet was collected and resuspended in 2–3 mL water. This final silk nanoparticle suspension was stored at 4 °C until use. Unless stated otherwise, each experiment was repeated in triplicate using three different aqueous silk precursor stock solutions.

Calculations for needle residence time and shear rate are based on the literature dynamic viscosity (27 mPas) of regenerated 3% aqueous silk[301] and density (1.02 g mL^{-1}) calculated herein for the 3% *w/v* aqueous silk solution, and assumed Newtonian flow.[301] The Reynold's number was estimated as 2 using the internal diameter of the needle[302] (0.33 mm) and indicated laminar flow. An upper limit of the residence time was estimated using the linear velocity (1.94 mm s^{-1}) and the needle length.[303] The maximum shear rate was taken as the wall shear rate and for simplicity, the shear rate calculations used the geometry of a straight cylinder. Calculations for the 3 and 10 mL syringes used in the study were undertaken similarly using the internal diameters as stated by the manufacturer.

2.2.3 Reproducibility of semi-automated silk nanoparticle manufacture

Silk nanoparticles were manufactured in a 10 mL flask at a 6 mL total volume (Figure 2.1). Silk was added from a height of 5.5 cm from the bottom of the isopropanol meniscus. The mother liquor suspension was then incubated for 2 h before purification. This procedure was repeated a further fifteen times using five silk precursor solutions.

2.2.4 The effect of stirring rate on manufacture and silk nanoparticle properties

Silk nanoparticles were manufactured in a 10 mL flask at a 6 mL total volume (Figure 2.1). Silk was added from a height of 7.5 cm from the bottom of the isopropanol meniscus and stirring was accomplished with an egg-shaped stir bar (15 × 6 mm) at 200 and 400 rpm. The mother liquor suspension was then incubated for 2 h before purification. This procedure was repeated in triplicate using three silk precursor solutions.

2.2.5 The effect of standing time on manufacture and silk nanoparticle properties

Silk nanoparticles were manufactured in a 50 mL flask at a 36 mL total volume. Silk was added from a height of 7.5 cm from the bottom of the isopropanol meniscus with stirring at 400 rpm with an egg-shaped stir bar (15 × 6 mm). An aliquot (6 mL) was taken immediately following complete addition of the silk precursor and stirring was stopped. Further aliquots (6 mL) were taken at 2.7, 5.5, 8.5, 11.5 and 24 h following stirring for 0.02 h at 400 rpm to ensure suspension homogeneity. This procedure was repeated in triplicate using three silk precursor solutions.

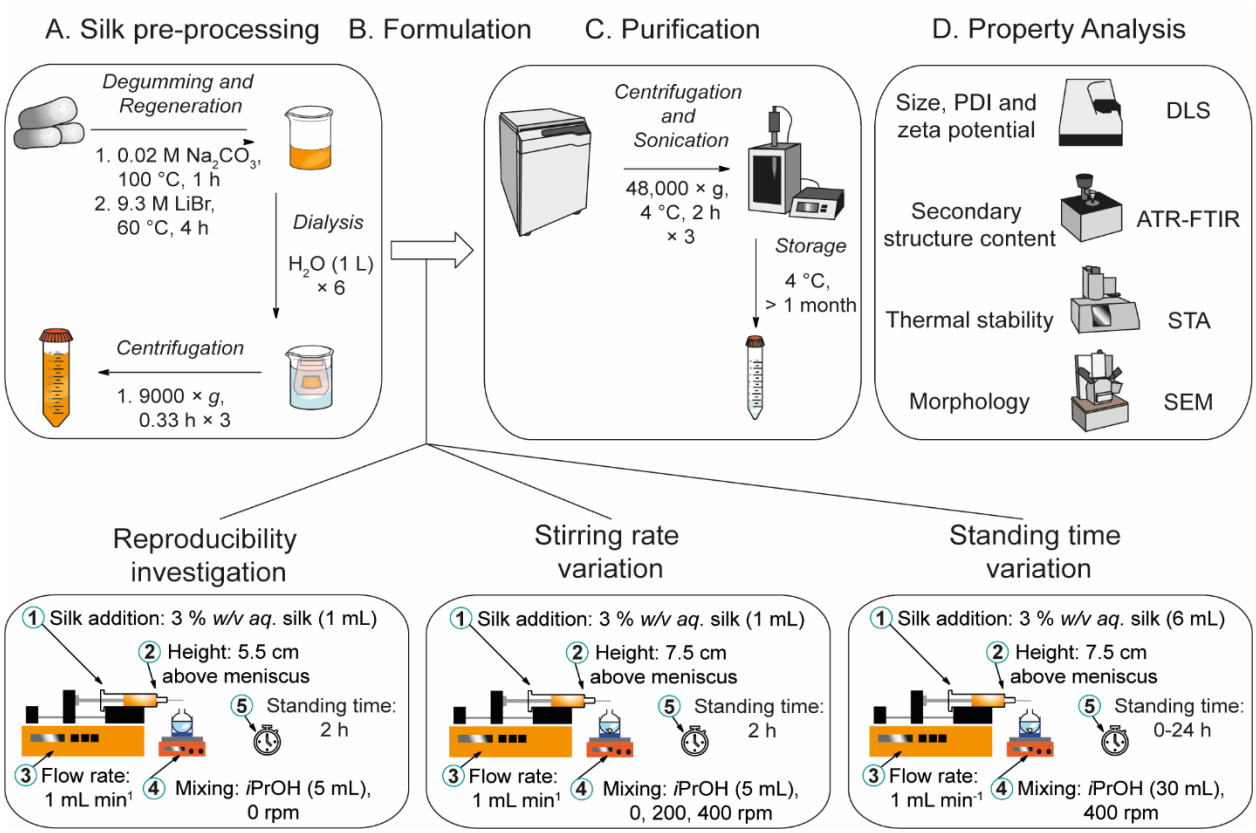

Figure 2.1. The nanoprecipitation workflow in a drop-by-drop open system for the preparation of silk nanoparticles. The five processing steps are: 1) Loading of a bubble-free 3% *w/v* aqueous silk solution into a syringe equipped with blunt needle. 2) The relative positions of the needle and round-bottom flask. 3) The flow rate control of silk solution at 1 mL min^{-1}. 4) The stirring rate during addition. 5) The nanoparticle standing time in the mother liquor following completion of silk addition.

2.2.6 Yield of silk nanoparticles

The nanoparticle concentrations were determined by recording the total mass of the suspension in a pre-weighed centrifuge tube. A known mass of each suspension was then frozen at -80 °C for 5 h in pre-weighed microcentrifuge tubes, followed by freeze-drying (Christ Epsilon 1-4, Martin Christ Gefriertrocknungsanlagen GmbH, Osterode, Germany) for 24 h at -10 °C and 0.14 mbar. The dry mass was recorded and the yield calculated using equation 2.1.

$$\text{Yield}/\% = \frac{\text{particle concentration } \left(\%\frac{w}{w}\right) \times \text{mass (mg)}}{\text{silk concentration } \left(\%\frac{w}{v}\right) \times \text{volume (mL)}} \times 100 \quad (\mathbf{2.1})$$

This process was repeated in duplicate and the average yield reported, and freeze-dried samples were stored in a vacuum desiccator until use.

2.2.7 Silk nanoparticle physicochemical characterization and stability in water

The size (Z-average of the hydrodynamic diameter), polydispersity and zeta potential of silk nanoparticles were determined as described elsewhere.[174] Briefly, silk nanoparticles were analyzed in ultrapure H_2O at 25 °C by dynamic light scattering (DLS) (Zetasizer Nano-ZS Malvern Instrument, Worcestershire, UK). Unless otherwise stated, samples were vortexed for 20 seconds and sonicated twice at 30% amplitude for 30 seconds prior to measurement. Refractive indices of 1.33 and 1.60 for H_2O and protein, respectively, were used for particle size measurement. All analyses were conducted in triplicate.

The particle size and zeta potential of silk nanoparticles generated in the stirring studies were determined on days 0, 10, 18, 24, 28, 35 and 42 by DLS. The particle size and zeta potential of silk nanoparticles generated in standing time studies were determined at days 0, 42 and 63 by DLS. The silk nanoparticles from all studies were stored at 4 ˚C. At $t > 0$ days, the silk nanoparticles were vortexed for 20 seconds before size and zeta potential analysis.

2.2.8 Secondary structure measurements of silk nanoparticles

Air-dried silk films and freeze-dried silk were used as silk I structure references, while autoclaved silk films and silk films treated with 70% *v/v* ethanol/ultrapure H_2O were used as positive controls for silk II structure. Silk films, powders and nanoparticles were analyzed by Fourier transform infrared spectroscopy (FTIR) on an ATR-equipped TENSOR II FTIR spectrometer (Bruker Optik GmbH, Ettlingen, Germany). Each nanoparticle and freeze-dried silk sample was flash frozen at -80 °C for at least 5 h, then lyophilized for 24 h. Each FTIR measurement was run for 128 scans at 4 cm^{-1} resolution in absorption mode over the wavenumber range of 400 to 4000 cm^{-1} and corrected for atmospheric absorption using Opus

(Bruker Optik GmbH, Ettlingen, Germany). The amide I regions of the FTIR spectra were analyzed in OriginLab 19b® (Northampton, Massachusetts, USA), as described elsewhere.[304] The second derivative of the background-corrected absorption spectrum was obtained and smoothed twice using a seven-point Savitzky-Golay function with a polynomial order of 2. A non-zero linear baseline was interpolated between 2–3 of the highest points between 1600 and 1710 cm^{-1}. Peak positions in the amide I region were then identified using the second derivative and peaks fitted using non-linear least squares with a series of Gaussian curves (Figure 2.2). Band positions, widths and heights were allowed to vary and peak area was allowed to take any value below or equal to 0. The deconvoluted spectra were area-normalized and the secondary structure content was calculated with reference to literature band assignments[155, 305] using the relative areas of each band.

The correlation coefficient I was calculated according to previous analyses.[306] The air-dried silk film of an aqueous silk precursor batch was used as the reference for all silk films, freeze-dried silk and nanoparticle silk samples. The second derivative curves of the absorption spectra were smoothed twice with a five-point Savitzky-Golay function and a polynomial order of 2 and then compared over the spectral range 1600–1700 cm^{-1} using equation 2.2.

$$R = \frac{\sum x_i y_i}{\sqrt{\sum x_i^2 \sum y_i^2}} \qquad (\mathbf{2.2})$$

where x_i and y_i are the derivative values of the air-dried silk film and sample of interest at the frequency i.

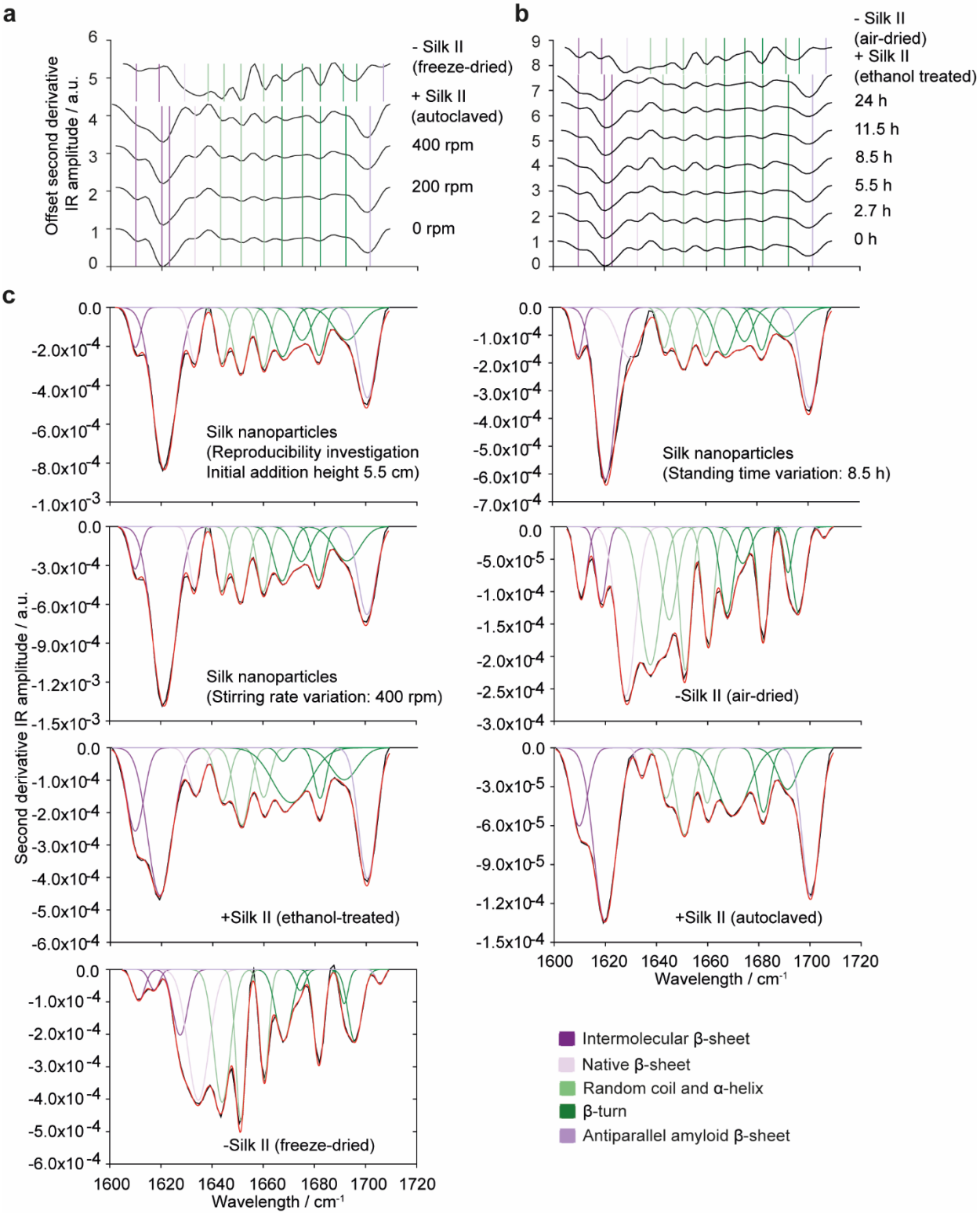

Figure 2.2. Exemplary smoothed second derivative FTIR spectra and peak assignment of silk nanoparticles manufactured by varying (a) stirring rate and (b) standing time and (c) exemplary peak fitting of the amide I region for nanoparticles formulated using the designated parameters and silk II controls.

2.2.9 Thermal analysis of silk nanoparticles

A known volume and mass of each silk sample and freeze-dried silk control was frozen at -80 °C for 5 h, followed by freeze-drying for 24 h at -10 °C and 0.14 mbar. First cycle differential scanning calorimetry and thermogravimetric analysis were carried out on the dried samples (1.95–4.89 mg) in aluminum pans from 20–350 °C at a scanning rate of 10 °C min^{-1} and under a nitrogen flow of 50 mL min^{-1} (STA Jupiter 449, Netzsch, Gerätebau GmbH, Germany). Thermograms were analyzed using OriginLab 19b® (Northampton, Massachusetts, USA). The desorption enthalpy was normalized to a corrected mass during volatilization as described previously.[307]

2.2.10 Scanning electron microscopy (SEM) of silk nanoparticles

Aqueous silk nanoparticle suspensions were adjusted to a concentration of 1 mg mL^{-1}. An aliquot (20 µL) of each sample was then pipetted onto a silicon wafer and lyophilized for 24 h at -10 °C and 0.14 mbar. The specimens were sputter-coated with gold using a low vacuum sputter coater (Agar Scientific Ltd, Essex, UK) and analyzed with the secondary electron detector of an FE-SEM SU6600 instrument (Hitachi High Technologies, Krefeld, Germany) at 5 kV and 40 k magnification. The images were processed using ImageJ v1.52n (National Institutes of Health, Bethesda, MD, U.S.A) and Abode Illustrator (Adobe, San Jose, CA, USA).

2.2.11 Statistical analyses

Data were analyzed using Microsoft® Excel® 2019 (Microsoft Office 365 ProPlus Software, Redmond, WA, U.S.A), Minitab® (Minitab® Statistical Software, State College, PA, USA) and GraphPad Prism 8.2.1 (GraphPad Software, La Jolla, CA, U.S.A.). The test for equal variance was undertaken on multiple groups using Bartlett's method. Sample pairs were analyzed using Welch's independent *t*-test. Multiple groups were evaluated by one-way analysis of variance (ANOVA), followed by Tukey's multiple comparison post-hoc test, or by the Brown-Forsythe and Welch ANOVA tests, followed by the Dunnett T3 multiple comparison post-hoc test. Silk nanoparticle stability was evaluated by ANOVA followed by Dunnett's post hoc test to compare between t = 0 day control and t > 0 day samples. All data were assumed to have normal

distributions. Asterisks denote statistical significance determined using post-hoc tests as follows: *p < 0.05, **p < 0.01, ***p < 0.001, ****p < 0.0001. Unless otherwise specified, all data are presented as mean values ± (SD) and the number of experimental repeats (*n*) is noted in each figure legend.

2.3 Results

2.3.1 Silk nanoparticle characterization

The DLS and mass measurement values indicated an influence of the stirring rate on the physicochemical properties and yield of silk nanoparticles (Figure 2.1 and Figure 2.3). When the silk solution was added from a height of 7.5 cm, an increase in the stirring rate from 0 to 400 rpm significantly decreased the silk nanoparticle size (ANOVA, $p < 0.05$) from 134 nm to 114 nm (Figure 2.3c). Varying the stirring rate between 0 and 400 rpm had no significant impact on the polydispersity or negative surface charge, which ranged from 0.12 to 0.14 and -30 to -33 mV, respectively (Figure 2.3d and Figure 2.3e). However, increasing the stirring rate significantly decreased the yield from 23 to 9% (ANOVA, $p < 0.01$) (Figure 2.3f).

The effect of droplet velocity on nanoparticle formation in the absence of stirring was determined by varying the height from which the silk solution was dropped (henceforth, initial addition height). A decrease in the initial addition height from 7.5 cm ($v_{droplet} \approx 1.21$ ms^{-1}) to 5.5 cm ($v_{droplet} \approx 1.03$ ms^{-1}) significantly decreased the yield of nanoparticles (*t*-test, $p < 0.01$) from 23 to 18%. By contrast, the physicochemical properties were not affected by decreasing the initial addition height to 5.5 cm, as the nanoparticles had an average size, polydispersity and zeta potential of 131 nm, 0.11 and -30 mV, respectively.

The growth of nanoparticles in the mother liquor was also investigated by varying the nanoparticle standing time before purification (Figure 2.1). Over a 24 h interval, the standing time had no significant effect on nanoparticle physicochemical properties or yield. Overall, the silk nanoparticle size ranged from 104–116 nm, with a polydispersity ranging from 0.11–0.14.

The negative surface charge ranged from -30 to -35 mV and the yield varied between 9 and 15% *w/w* of silk (Figure 2.3).

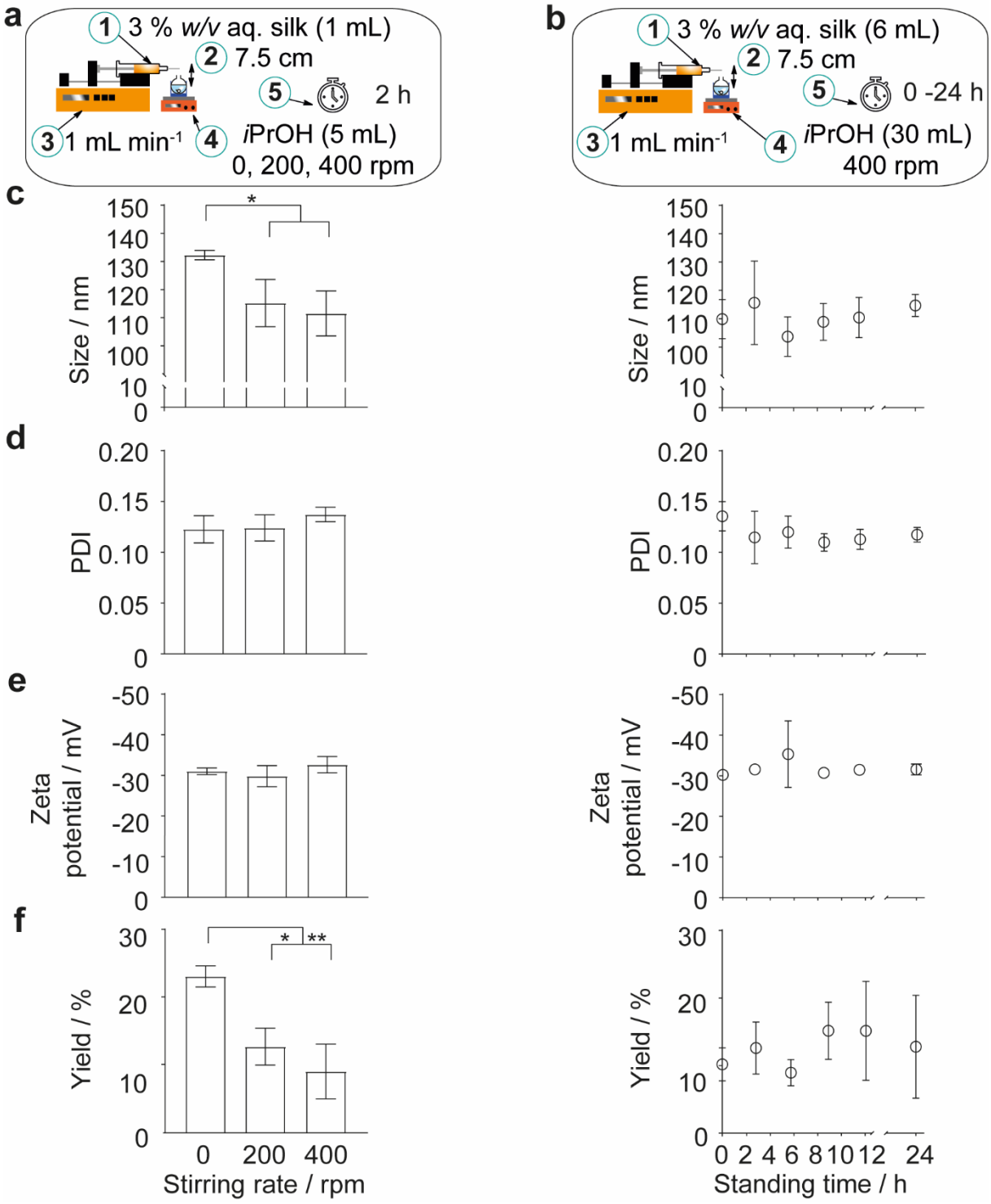

Figure 2.3. Impact of stirring rate and standing time on the physicochemical properties and yield of nanoparticles produced by drop-by-drop desolvation. (a) Schematic of the five processing parameters used to investigate the stirring rate and **(b)** the standing time for silk nanoparticle manufacture. **(c)** Hydrodynamic diameter, **(d)** polydispersity index (PDI), **l** zeta potential and **(f)** yield of silk nanoparticles. Error bars are hidden in the bars and plot symbols when not visible, ± SD, *n* = 3. Multiple groups were evaluated by one-way analysis of variance (ANOVA), followed by Tukey's multiple comparison post-hoc test. Asterisks denote statistical significance determined using post-hoc tests as follows: *p < 0.05, **p < 0.01.

2.3.2 Secondary structure measurement

The impact of the process conditions on silk nanoparticle secondary structure was determined by attenuated total reflectance-FTIR (ATR-FTIR) analysis and deconvolution of the characteristic protein amide I band (1600-1710 cm^{-1}) (Figure 2.2). Silk nanoparticle secondary structure did not vary significantly with changes in the initial addition height, stirring rate or formulation standing time. For stirring and standing time studies, the high nanoparticle β-sheet content (54–57%) correlated with the 55% β-sheet composition measured for autoclaved and ethanol-treated silk films, which served as positive controls for silk II structure (Figure 2.4). Additionally, the α-helix and random coil content (18–21%) of silk nanoparticles was comparable to autoclaved (20%) and ethanol-treated films (19%). Autoclaving provides thermal energy to break labile bonds in the silk film, with uptake of water acting to plasticize the material. This directly contrasts with nanoprecipitation, where water is removed from the silk hydration shell. The silk nanoparticle structure from both studies showed a significantly higher percentage of β-sheets (ANOVA, $p < 0.0001$) and less α-helix and random coil content (ANOVA, $p < 0.0001$) compared to the negative silk II structure controls (air-dried silk film and freeze-dried silk powder with 17–25% β-sheet and 47–56% α-helix and random coil content) (Figure 2.4c).

The spectral correlation coefficient method of comparing second derivative ATR-FTIR spectra in the amide I region (1600–1700 cm^{-1}) was also used to measure formulation-induced structural changes in silk nanoparticles *versus* those in an air-dried silk film. Silk nanoparticle correlation coefficients ranged from 0.27–0.31 and showed no significant variation with initial addition height, stirring rate or formulation standing time (Figure 2.4c). The stirring and standing time studies revealed discrepancy between the correlation coefficients of silk nanoparticles and those of the autoclaved films (0.10) (ANOVA, $p < 0.0001$) and the ethanol-treated silk films (0.18) (ANOVA, $p < 0.05$). This disagreement with the band deconvolution findings could reflect offsets in the second derivative baselines. Regardless, the

nanoprecipitation-associated β-sheet enrichment, identified by band deconvolution, was supported by the significantly lower nanoparticle correlation coefficients compared to the negative silk II controls of air-dried (0.95) and freeze-dried (0.92) silk (ANOVA, $p < 0.0001$).

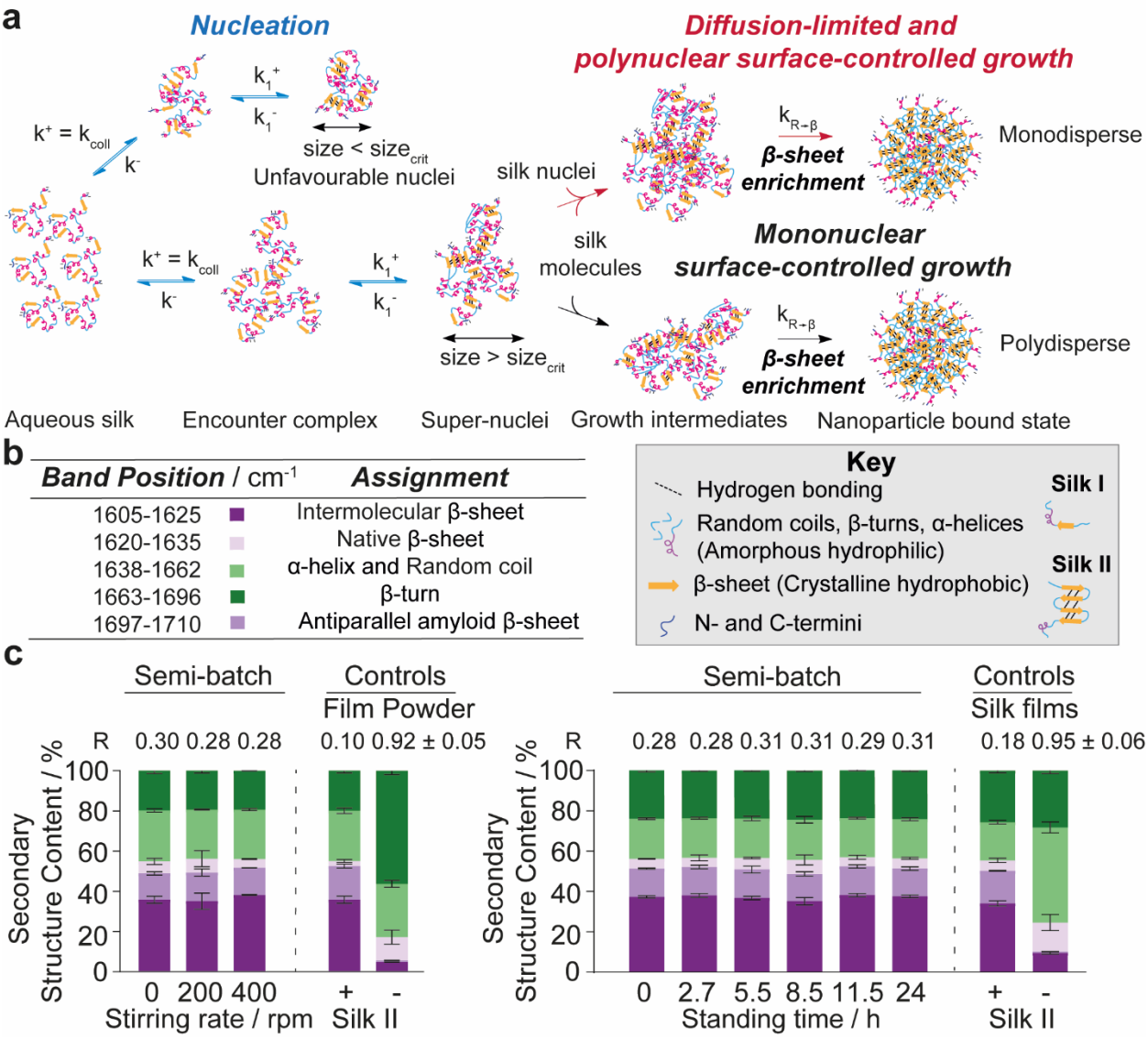

Figure 2.4. Changes in stirring rate or standing time results in silk nanoparticles with comparable secondary structure. (a) Schematic of protein-protein association and β-sheet assembly of silk fibroin during nanoprecipitation *via* desolvation. Silk molecules, nanoparticles and stoichiometry of association are not drawn to scale. **(b)** FTIR band assignments and schematic key. Secondary structure content of silk nanoparticles manufactured using different **(c)** stirring rates and **(d)** standing times. Silk films treated with 70% ethanol and autoclaving to obtain high β-sheet content were used as positive controls for silk II structure, with an untreated silk film and freeze-dried silk powder serving as negative controls. The correlation coefficients I of silk nanoparticle, film and powder second-derivative amide I spectra were calculated using the silk II negative control film as reference, n = 3, ± SD. The correlation coefficients, total β-sheet and α-helix and random coil contents were evaluated by one-way analysis of variance (ANOVA), followed by Tukey's multiple comparison post-hoc test. The intermolecular β-sheet, native β-sheet, β-turn and anti-parallel amyloid β-sheet contents were evaluated using the Brown-Forsythe and Welch ANOVA tests, followed by the Dunnett T3 multiple comparison post-hoc test.

2.3.3 Thermal analysis

The simultaneous thermal analysis first cycle results of silk nanoparticles manufactured at stirring rates between 0–400 rpm and silk II negative controls are shown in Figure 2.5 and Table 2.1. Thermogravimetric analysis (TGA) was used to confirm differences in water content and thermal stabilities of silk nanoparticles caused by formulation (Figure 2.5). Thermograms of all silk nanoparticles and controls showed three regions with two weight loss steps: the loss of adsorbed and strongly bound water between 20-140 °C followed by silk decomposition above 170 °C. The increase in mass at low temperatures in TGA measurements was due to buoyancy effects resulting from variations in air density with heating.[308] No significant differences in water content were observed with increased stirring rate, with nanoparticles containing 12–14% *w/w* water across all formulations. Nanoparticles displayed a significantly delayed (ANOVA, $p < 0.05$) onset decomposition temperature ranging between 273.2–277.3 °C compared to the freeze-dried powder, negative silk II control (261.4 °C). This higher stability to thermal degradation suggests that nanoparticle structure is composed of a higher crystalline fraction compared to amorphous, freeze-dried silk. Nevertheless, there was no significant difference between the decomposition temperatures of silk nanoparticles manufactured at different stirring rates, ranging between 298.5–304.0 °C.

Differential scanning calorimetry (DSC) measurements confirmed that the formulation stirring rate did not affect the primary or secondary structure of silk nanoparticles (Figure 2.5). The desorption enthalpy ranged between -207.8 and -282.7 J g^{-1} and the temperature of desorption ranged from 36.1 to 43.6 °C, with no significant variation observed with stirring rate. The water desorption–associated and final glass transitions at 59.3 and 201.5 °C, respectively, were not identifiable for all nanoparticle samples. The glass transition at 201.5 °C was also shifted to a higher temperature and was less steep when compared to the silk I structure (184.5 °C). This indicates that the molecular mobility of silk molecules was reduced upon their incorporation into the nanoparticle structure. The crystallization exotherm (random coil to β-sheet transition), present for the negative controls at 241.0 °C, was absent from the

nanoparticle curves. No significant difference was noted between the decomposition temperatures (ranging between 282.9 and 289.5 °C) of silk nanoparticles manufactured at different stirring rates.

Table 2.1. First cycle simultaneous thermal analysis data of silk nanoparticles manufactured at different stirring rates.

	Thermal Property	Stirring rate / *rpm*			-Silk II
		0	**200**	**400**	**Freeze-dried silk**
DSC	**T_g / °C**	59.3 ± 0.01	59.4[a]	59.3[a]	47.7 ± 0.5
	T_d (DSC) / °C	39.1 ± 5.3	36.1 ± 0.3	43.6 ± 13.9	60.7 ± 8.8
	ΔH_d / $J\ g^{-1}$	-207.8 ± 98.0	-266.4 ± 14.3	-239.4 ± 18.8	-276.9 ± 4.21
	T_g' / °C	-	196.9[a]	206.0[a]	184.5 ± 0.7
	T_o (crystallization) / °C	-	-	-	225.6 ± 11.1
	T_c / °C	-	-	-	241.0 ± 0.8
	ΔH_c / $J\ g^{-1}$	-	-	-	9.9 ± 2.3
	T_o / °C	274.0 ± 0.3	266.6 ± 7.3	268.9 ± 9.0	-
	T_{dec} / °C	289.5 ± 0.5	282.9 ± 6.1	284.2 ± 7.7	274.9 ± 0.7[b]
TGA	**Water content / % (w/w)**	13.0 ± 1.7	13.7 ± 2.1	12.6 ± 2.0	5.8 ± 0.8
	T_o / °C	277.3 ± 0.2	273.2 ± 2.9	274.3 ± 3.8	198.5 ± 2.2
	T_o' / °C	-	-	-	261.4 ± 2.0
	T_{dec} / °C	299.6 ± 6.6	298.5 ± 9.0	304.0 ± 4.6	222.3 ± 13.3
	T_{dec}' / °C	-	-	-	275.0 ± 2.7

a. $n = 1$
b. An altered decomposition profile was noted for one control sample.

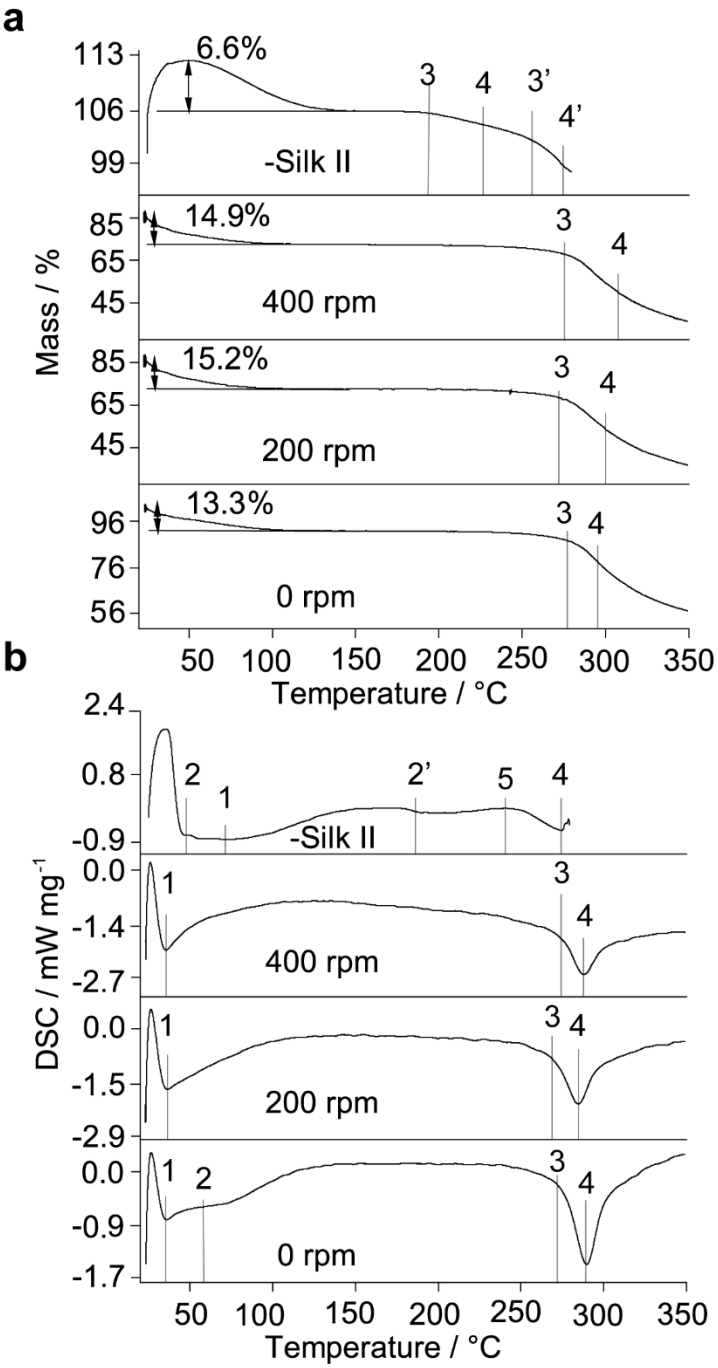

c

Notation	Thermal event
1	T_d
2	T_g
3	T_o
4	T_{dec}
5	T_c

Figure 2.5. Representative first cycle raw (a) thermogravimetric analysis (TGA) thermograms and (b) differential scanning calorimetry (DSC) of silk nanoparticles manufactured at different stirring rates. (c) Thermal event assignment key. Water content (%, *w/w*), dehydration temperature (T_d), glass transition temperatures (T_g), extrapolated onset temperature of crystallization and decomposition (T_o), crystallization temperature (T_c) and decomposition temperatures (T_{dec}) are reported.

2.3.4 Silk nanoparticle aqueous stability

The particle size, polydispersity and zeta potential stability of nanoparticles manufactured with stirring rates between 0 and 400 rpm were determined for up to 42 days. Nanoparticles manufactured across all stirring rates showed size stability and constant polydispersity in water for up to 42 days (Figure 2.6). By contrast, the zeta potential of nanoparticles manufactured without stirring varied significantly across 42 days. The particle size, polydispersity and zeta potential stability of nanoparticles manufactured with standing times between 0 and 24 h were also determined for up to 63 days. All formulations showed size and polydispersity stability in water for up to 63 days (Figure 2.6). The negative surface charges of silk nanoparticles after 0, 2.7 and 11.5 h standing times significantly decreased at 42 days at 4 °C and then increased.

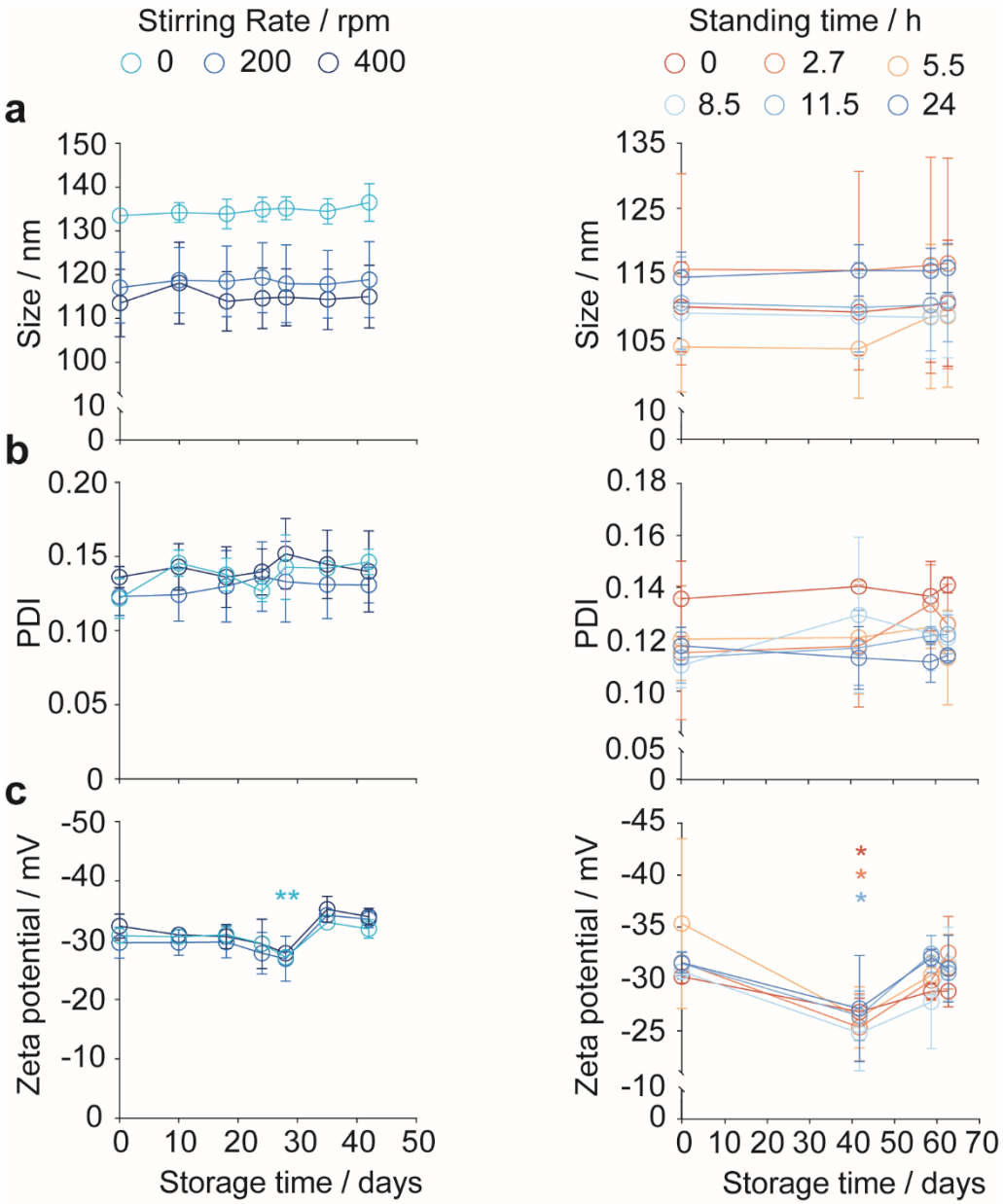

Figure 2.6. Stability of silk nanoparticles manufactured in semi-batch format by varying the stirring rates and standing times. (a) Hydrodynamic diameter, **(b)** polydispersity index (PDI), **(c)** zeta potential of silk nanoparticles stored in water at 4 °C. Diluted nanoparticle suspensions were vortex mixed prior to DLS analysis, ±SD, *n* = 3. Unless otherwise stated, silk nanoparticle stability was evaluated by ANOVA followed by Dunnett's post hoc test to compare between *t* = 0 day control and *t* > 0 day samples. The PDI stability of nanoparticles manufactured with 0 h standing times was evaluated using the Brown-Forsythe and Welch ANOVA followed by Dunnett's T3 post hoc test. Asterisks denote statistical significance for each formulation between t = 0 and t > 0 days, determined using post-hoc tests as follows: *p < 0.05, **p < 0.01.

2.3.5 Scanning electron microscopy of silk nanoparticles

Silk nanoparticle morphology was analyzed qualitatively by SEM (Figure 2.7). Silk nanoparticles manufactured with stirring rates of 200 and 400 rpm at 6 mL scale had spherical shapes and narrow size distributions at day 24. Nanoparticles manufactured with standing times of 0 and 24 h at the 36 mL scale showed generally spherical morphologies and uniform size distribution when imaged at day 55. Overall, nanoparticles showed a coarse surface topography.

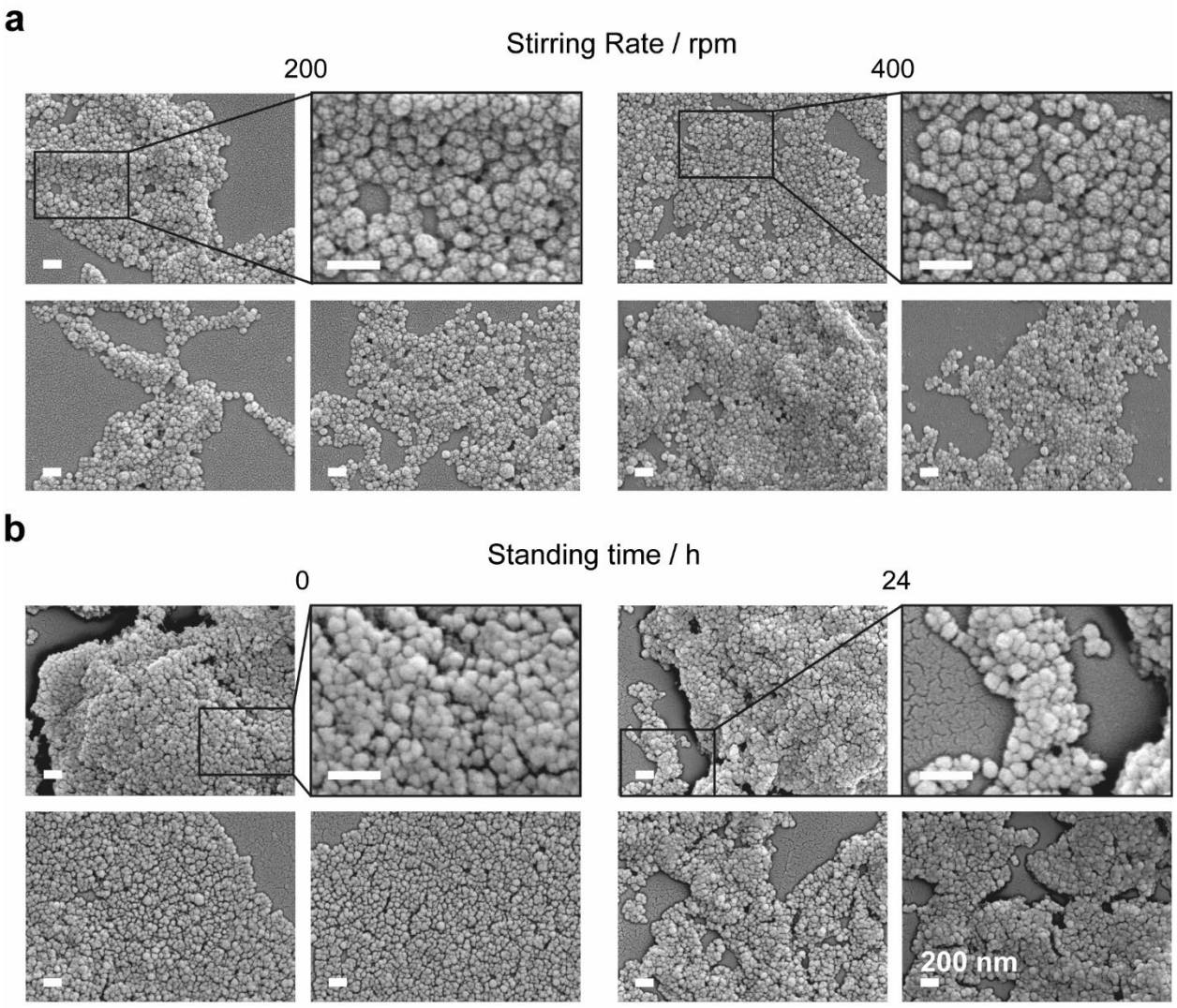

Figure 2.7. Scanning electron microscopy images of silk nanoparticles manufactured using (a) stirring rates of 200 and 400 rpm and (b) standing times of 0 and 24 h. Nanoparticles manufactured at stirring rates of 200 and 400 rpm were imaged at day 24, *n* = 1. Nanoparticles manufactured using standing times of 0 and 24 h were imaged at day 55, *n* = 1. Scale bars = 200 nm.

2.4 Discussion

Silk particles have attracted increased attention for drug delivery applications because their manufacture can be tailored for a desired size (from nano- to microscale), crystallinity and surface chemistry.[135, 295, 309] The nanoparticles produced by desolvation are well suited to anticancer applications due to their sub-micron size,[160, 174, 179, 183, 185] which would allow

extravasation through leaky tumor vasculature,[22] followed by endocytosis and lysosomal trafficking in malignant cells.[183] However, nanoparticle manufacture and drug loading has not always translated from small-scale, bench procedures to those following current Good Manufacturing Practices (i.e., 21 Code of Federal Regulations Part 210–212) in the manufacturing sector.[310, 311] This has prompted the implementation of continuous techniques,[174, 179, 244] which can offer greater ease of scale-up.[310] One powerful approach includes microfluidic-assisted nanoprecipitation, which uses laminar flow focusing to achieve micromixing conditions and solvent shifting by diffusion.[174, 179, 310] Production can be scaled up by microfluidic-chip parallelization or increasing channel diameters, although working at large total volumes can cause problems due to low production rates and the limitations of scaling imposed by complex mixer designs. Consequently, improving the reproducibility of lab-scale methodology for semi-batch manufacture of silk nanoparticles is still an area of much interest.

Understanding the parameters that impact silk nanoprecipitation will aid in the optimization of silk nanoparticle physicochemical properties for *in vivo* performance as nanomedicines. The consequences of varying silk stock reverse-engineering processes[179] and antisolvent species[174, 290] and their relative ratios, on the outcome of nanoprecipitation in semi-batch[312] and continuous format[174] are already reported. For example, 1 h degumming times for silk cocoons resulted in greater molecular weight polydispersity of silk stocks and in favorable nanoparticle size, polydispersity and zeta potential when compared to shorter degumming times.[179] Several research groups have also investigated the effect of the antisolvent species used for nanoprecipitation on the resulting nanoparticle properties,[174, 236] as the antisolvent molecular and macroscopic properties contribute to the mixing conditions. Increasing the volume ratio of the antisolvent to silk solution imposes high supersaturation conditions in both semi-batch[236, 312] and microfluidic formats,[174] resulting in faster nucleation and smaller nanoparticle sizes. Hence, in the current study, the optimized formulation variables[153, 174, 179] for preparing silk nanoparticles were used to investigate several little-

understood preparation parameters, namely initial addition height, nanoparticle stirring rate and standing time.

A semi-automated drop-by-drop procedure for silk desolvation in semi-batch format was designed to replace the manual addition of silk to organic antisolvent using a syringe or pipette. It is probable that homogeneous silk nucleation occurred by antisolvent-induced desolvation (Figure 2.4a). I do not consider seeded crystallization as the 3% *w/v* silk concentration used lay below the ≈10% *w/w* critical micelle concentration[301] of regenerated silk fibroin. Additionally, the silk addition rate of 1 mL min^{-1} ensured laminar flow in the syringes and needle. The maximum wall shear rates in the syringes were estimated between 55 and 261 ms^{-1} while the wall shear rate in the needle was estimated as 4724 s^{-1}. Combined with the low residence time of 33 ms, these shear rates would not be expected to provide sufficient work (≈ 10^5 Pa)[313] for shear-induced nucleation of the silk molecules.

Silk nanoparticles were reproducibly and reliably manufactured at a 6 mL scale when key processing parameters were set at levels for optimal nanoparticle properties, as determined in previous work.[153, 174, 179] As unreliable nanoparticle manufacture has been implemented in the reduced efficacy of the generic Doxil® formulation, LipoDox®,[310, 314] one might speculate that increasing the reproducibility of silk nanoparticle manufacture will ultimately lead to better *in vitro* and *in vivo* therapeutic profiling. For example, across sixteen repeats using three aqueous silk batches over three days, silk nanoparticles produced at a 5.5 cm initial addition height and without stirring had an average size of 131 ± 7 nm and low polydispersity of 0.11 ± 0.02. The polydispersity was similar to previously reported values obtained using the same silk concentration and silk-to-antisolvent volumetric ratio in manual and microfluidic-assisted methodology.[153, 160, 174, 179] Although the nanoparticle sizes were larger than the literature values (≈ 100–115 nm),[153, 160, 174, 179] they lay within the optimal size range (100 to 200 nm) for drug delivery vehicles.[315] The nanoparticles were obtained in an average yield of 18 ± 3%, comparing favorably with previous reports in manual and microfluidic formats.[153, 174] The zeta potential of -30 ± 2 mV was higher than previously reported values

obtained with manual silk addition.[160, 179] This phenomenon was also observed for microfluidic-assisted manufacture[174, 179] and probably reflects different silk molecule packing arrangements resulting from varying fluid dynamics due to the different flask geometries between the studies.

Silk nanoparticles were highly crystalline, featuring a high β-sheet content of 56 ± 1% and spectral correlation coefficient of 0.27 ± 0.03 over the amide I region, in agreement with previous studies.[174, 179] Increasing the initial addition height to 7.5 cm resulted in higher droplet impact velocity and kinetic energy, thereby causing larger disturbances in the antisolvent and facilitating mass transfer and solvent shifting. Surprisingly, this change did not significantly affect nanoparticle physicochemical properties, although it resulted in significantly increased yield.

The inverse relationship between nanoparticle size and formulation stirring rate has been observed for globular protein nanoparticles[316] and polymer emulsions.[317] As a nanoprecipitation process, aqueous silk desolvation is fundamentally a diffusion-limited solvent shift of water molecules from the silk hydration shell and their replacement with isopropanol molecules. Therefore, mixing efficiency is an important factor that dictates nanoprecipitation outcomes, and magnetic stirring increases the control of macro- to micromixing rates.[300] In lab-scale semi-batch manufacture, the silk nanoparticle size and yield showed inverse dependence on the stirring rate, through 0 to 400 rpm (Figure 2.3). While stirring has been used for desolvation of regenerated silk obtained from *Antheraea mylitta*,[242] I believe this is the first report highlighting the importance of stirring rate in a semi-batch system on the outcome of silk fibroin desolvation. When manufactured at 400 rpm stirring rate and 6 mL scale, the nanoparticle size compared well with literature values for manual semi-batch manufacture, which is typically conducted between 40–50 mL scale without stirring.[160, 179] It is likely that reducing the mixing time by active stirring will result in increased reproducibility of nanoparticle physicochemical properties during scale-up, although experimental proof is needed.

Silk nanoprecipitation occurs during mixing with an antisolvent in which the solubility of at least one type of hydrophilic block is low, and this results in particle nucleation upon supersaturation (i.e., when the silk concentration exceeds the equilibrium solubility).[297, 318] Nucleation follows a minimum Gibbs free energy self-assembly process *via* protein–protein association until a critical nucleus size is reached.[318] This is then followed by particle growth and protein conformational changes for induced fit (Figure 2.4a).[318] For most cases, the general mechanism of protein–protein association is defined by at least three steps.[318] The initial steps are diffusion-limited and occur following complete solvent-antisolvent mixing. First, a random collision of proteins produces a non-specific encounter complex, which minimizes repulsive long-range electrostatics.[318] This short-lived complex can then go on to form nuclei with favorable intermolecular interactions, although no change in secondary structure occurs. This process is enthalpy-driven: the establishment of new short-range attractive forces between silk molecules offsets the entropic loss upon incorporation into the nuclei.

The consequent reduction in protein concentration reduces the rate of further nucleation and, for nuclei exceeding the critical size, leads to growth by thermodynamically controlled stepwise or aggregative mechanisms.[299, 319] The final step involves a structural change between the favorable growth intermediates and the nanoparticle bound state to maximize attractive intra- and intermolecular interactions. In the case of silk fibroin, this involves conversion of random coil and α-helix content to β-sheet structure.[130, 174] Across all semi-batch formulations, as in previous microfluidic-assisted work,[174, 179] the mixing efficiency correlated with nanoparticle size, while the secondary structure content and thermal stability of silk nanoparticles remained consistent. Hence, nanoprecipitation can be assumed to occur *via* diffusion-controlled association in the regime where $k_{R\rightarrow\beta+} >> k_1^-$ (Figure 2.4a),[318] so β-sheet formation occurs at a faster rate than silk molecule diffusion. Applying this assumption to silk fibroin desolvation, the high turbulence created by increasing the stirring rate would increase the meso- and micromixing rates, thereby reducing the total mixing time.[299, 320] Consequently, nucleation rates will increase, causing a fast reduction in supersaturation and arresting further

nucleation, thereby resulting in a growth phase with greater homogeneity. The reduction in local silk concentration with lower mixing times also disfavors surface-controlled growth processes of nuclei and lowers the chance of successful diffusion-limited collisions of silk molecules with nuclei[321] prior to structural rearrangement.

Alternatively, as stirring rate and mixing efficiency increases, solvent shifting from hydrated silk pockets was likely improved prior to β-sheet enrichment. This would result in tighter packing of the internal nanoparticle architecture. However, variation in the stirring rate caused no significant difference in water content or desorption enthalpy by simultaneous thermal analysis. Furthermore, as water absorption occurs predominantly in the amorphous regions,[322] variations in secondary structure would be expected. Nevertheless, β-sheet crystalline content did not vary significantly between nanoparticle formulations, as measured by amide I band deconvolution.[174, 304, 306] The elevated decomposition temperatures, absence of crystallization exotherms and shallower glass transition profiles of nanoparticles compared to freeze-dried silk (Figure 2.5) reinforced the high nanoparticle crystallinity determined by FTIR.[305, 323] Simultaneous thermal analysis also showed no significant differences between the thermal stabilities of nanoparticles manufactured with different stirring rates. Macromolecule thermal stability is dependent on molecular weight and length,[323] so this finding indicated that silk molecules incorporated into nanoparticles from all formulations were of a similar weight and length distribution, again reinforcing previous work.[179]

I speculate that the reduction in nanoparticle yield with stirring is due to several factors, including silk film formation on flask walls and insufficient *g*-force for the sedimentation of smaller nanoparticles during centrifugation. Stirring at 400 rpm resulted in the poorest reproducibility of size and yield, which may indicate that hydrodynamic confounders caused by slight differences in feed point position were introduced between experiments. Surprisingly, no significant differences were observed for polydispersity with stirring: suggesting that, in the static system, size distribution was controlled by diffusion-limited or polynuclear surface-controlled growth.[321] The moderate polydispersity of all formulations arose, in part, due to the

time dependence of antisolvent composition, the local regions of high supersaturation at the droplet-antisolvent interface and the non-uniform nucleation inherent in the semi-batch process. Although particle size was affected, the zeta potential remained at a constant level as stirring rate was varied, suggesting that packing geometries were affected by active stirring although secondary structure content remained consistent.

Particle growth is a thermodynamically driven process and primarily occurs *via* three diffusion-limited mechanisms: stepwise growth[319] proceeding through molecular adsorption until the equilibrium silk saturation concentration is reached; Ostwald ripening,[324] whereby the dissolution of small particles results in growth of larger particles; and aggregation proceeding according to Smoluchowski kinetics.[299] The rate of silk nanoparticle growth was also investigated over 24 h by varying the standing time in the mother liquor before purification. No significant differences in nanoparticle physicochemical properties, yield (Figure 2.3) or secondary structure content (Figure 2.4c) were observed for standing times between 0 and 24 h.

The isoelectric point of crystalline silk fibroin lies between pH 4 and pH 5.[325] Therefore, silk nanoparticles and silk molecules in the mother liquor have a net negative surface charge. This results in repulsive long-range electrostatic interactions between nanoparticles, providing a high-energy barrier for aggregation and agglomeration and conferring colloidal stability. These repulsive interactions exist between nanoparticles, precursor silk molecules and newly-formed silk nuclei. Hence, once silk nanoparticles reach a key size, they no longer act as templates for stepwise growth, as the repulsive energy barrier and entropic loss is no longer offset by the establishment of favorable short-range bonds and reduction in surface energy. The conversion of amorphous content to β-sheet structure upon nanoprecipitation can also be considered irreversible at room temperature, in the absence of chaotropic agents.[179] The tightly-bound crystalline architecture, poor solubility of the silk hydrophilic blocks in the mother liquor and the low polydispersity of nanoparticle size consequently result in unfavorable nanoparticle growth *via* Ostwald ripening. This means that screening of operating conditions

for nanoparticle manufacture at room temperature can be conducted with maximum time efficiency, increasing throughput.

For example, at 6 mL scale and 0 h standing time, the nanoparticle production rate was estimated as 0.41 g/h using semi-automated silk dispensing and 0.12 g/h using manual silk addition, assuming 23% nanoparticle yields.[179] The former value assumed the use of one syringe pump equipped with two syringes, while both processes require an operator intensive set-up time of one minute. Based on this, the time taken to prepare nanoparticle batches for conducting a clinically relevant *in vivo* study with five rats was calculated. Assuming a nanoparticle blood concentration[184] of 250 μg mL^{-1} and a rat blood volume of 25.6 mL, 6.4 mg of silk nanoparticles would be required per rat. The time taken to obtain the total required mass of 32 mg is 0.08 h and 0.26 h using the semi-automated and manual set-ups, respectively. However, the total production rate is lowered by the 6 h purification process, assuming the use of one eight-place centrifuge. Nevertheless, the total production rate can be increased by syringe-pump platform and centrifuge parallelization.

The characterization of the effect of ageing on nanoparticle physicochemical properties is important for maximizing shelf life and preventing undesired complications. For this reason, I also examined the long-term stability of silk nanoparticles from all formulations in aqueous conditions for over 1 month at 4 °C to assess storage capabilities (Figure 2.6). Similar to previous studies,[153, 174, 179] the zeta potential of nanoparticles from all formulations on the day of manufacture was lower than -25 mV, indicating sufficient electrostatic repulsion between particles for moderate aqueous stability. Indeed, silk nanoparticles manufactured across all stirring rates and standing times showed size stability over the entire study period. Some fluctuations in polydispersity and zeta potential occurred for nanoparticles produced from some formulations and, while these changes were significant, they did not follow a trend indicative of time-dependent flocculation, coagulation or dissolution.[174] This observation was reinforced by morphological assessments conducted over the time course by SEM, which showed spherical granules without apparent agglomeration or adhesion (Figure 2.7). The

sizes of the freeze-dried particles imaged by SEM were relatively small compared to the Z-average size measured using DLS, probably due to the removal of the solvation sphere and bound water during freeze-drying.[242]

2.5 Conclusions

The use of a semi-automated liquid dispensing setup provided consistent, standardized, and higher throughput manufacture of silk nanoparticles *via* drop-by-drop desolvation in a semi-batch format. Operational parameters investigated for their effect on nanoparticle formation indicated that decreasing the initial addition height from 7.5 to 5.5 cm reduced the nanoparticle yield. The stirring rate was also a key process parameter that affected silk nanoparticle size, yield and experiment reproducibility, as stirring at 400 rpm provided the smallest nanoparticle size and the lowest yield of silk nanoparticles. Nanoparticles from all formulations displayed spherical morphologies and showed stability of size and polydispersity for over 1 month when stored as aqueous suspensions at 4 °C. The standing time of silk nanoparticles in the mother liquor was also not a key process parameter, and time-efficient manufacture can be achieved at room temperature.

Chapter 3: Mixing and flow-induced nanoprecipitation for morphology control of silk fibroin self-assembly

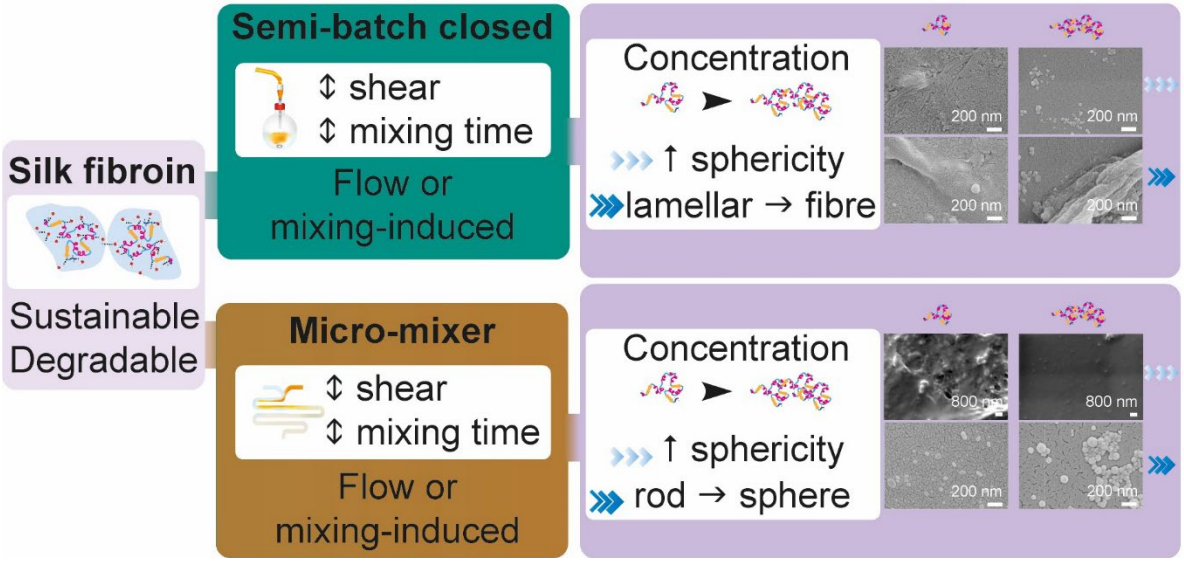

This chapter contains the results from the published article in RSC Advances (Matthew, S. A. L.; Rezwan, R.; Kaewchuchuen, J.; Perrie, Y.; Seib, F. P. Mixing and flow-induced nanoprecipitation for morphology control of silk fibroin self-assembly, *RSC Adv.* **2022**, *12*, 7357−7373. DOI: 10.1039/D1RA07764C). For this work, I designed, analyzed, and carried out all theoretical and semi-batch experimental work in conjunction with theoretical and experimental microfluidic work with the NanoAssemblr™. I prepared the manuscript draft. Refaya Rezwan carried out experimental work assessing the effect of silk concentration in the NanoAssemblr™ at the flow rate of 1 mL min^{-1} and nanoparticle stability using manufacture in the NanoAssemblr™.

3.1 Introduction

The control of silk fibroin multiscale structure under shear flow is important to the function of this biopolymer in the natural world and can be exploited in organic solvent-induced nanoprecipitation processes. Silk fibroin produced by the *Bombyx mori* silkworm is increasingly proposed for a range of drug delivery applications,[294] as this biopolymer exhibits several favorable characteristics, including biocompatibility and biodegradability,[184, 237, 291] and a number of products have been translated to the clinic.[130] A variety of material types[130] and crystallinities[130, 289, 290, 292] can also be accessed from the reverse-engineered silk solution, as the block copolymer primary structure can exist in a range of polymorphic states, notably silk I–II.[326] The silk I polymorph has a high composition of β-turns, helices and random coils which bestow aqueous solubility. This metastable solution is found in the silkworm gland or is obtained by regeneration of the degummed silkworm cocoon.[327]

The rate of structural conversion of aqueous silk I to the more thermodynamically stable and solid silk II structure can be increased by displacement of the protein hydration layer with a water-miscible organic solvent[153, 174, 179] and the application of physical shear forces under flow.[327] The intermolecular hydrogen-bonding ability of silk molecules under shear flow enables the spinning of liquid silk dope at ambient conditions and remarkably little work input.[313] Similarly, this fundamental property determines the outcome of high shear fluid processing of the regenerated aqueous solutions into structures such as nanoparticles.

The physicochemical properties of nanoparticle drug delivery systems dictate the *in vivo* performance following parenteral administration, including immunogenicity, volume of distribution, controlled drug release and intracellular trafficking.[315] Nanoparticles smaller than 100 nm in size can be filtered from systemic circulation by the hepatic endothelial fenestration, thereby lowering plasma half-life by accumulation in the liver.[315] Conversely, the plasma half-life of nanoparticles above 200 nm in size can be reduced due to opsonization and clearance by the mononuclear reticuloendothelial system.[315] Therefore, nanoparticles of sizes between 100 and 200 nm with a low polydispersity index have shown the greatest clinical success as

drug delivery systems.[315] The nanoparticle morphology can also impart specific delivery and rheological properties[328, 329] and a change from spherical to cylindrical carriers has been shown to improve circulation *in vivo*.[330]

Silk particles of sub-micron size (25–200 nm) are suitable for drug delivery and can be manufactured by eight major methods (reviewed previously[295]): capillary microdot printing,[221] desolvation,[153, 160, 179, 185] supercritical CO_2,[296] electrospraying,[216] emulsification,[244] ionic liquid dissolution,[237] milling[208] and electrogelation.[219] Of these methods, desolvation is an accessible, low-energy–expenditure nanoprecipitation process which has been used to tune the key quality attributes of protein[174, 179, 297] and polymeric[331] nanoparticles. The one-step fabrication technique involves solvent shifting of aqueous, molecularly dissolved silk using at least a 200% *v/v* excess of a water-miscible organic solvent[153, 160, 185] in which at least one of the blocks has a low solubility, resulting in supersaturation and spontaneous precipitation.[299, 331]

Silk nanoformulations have many advantages, but further progress is needed for the manufacture of non-spherical particles by nanoprecipitation and for a better understanding of the silk self-assembly mechanism in semi-batch and continuous formats. Nanoprecipitation occurs due to the interdiffusion of the antisolvent and water molecules; therefore, it is highly dependent on the mixing conditions, as well as on the composition of the aqueous, solute and antisolvent components used in the mixture.[299, 331] This raises concerns regarding the commonly accepted lab-scale process of manual drop-by-drop silk feeding to an organic antisolvent in semi-batch format (e.g.,[153, 312]), as this method results in a time-dependent change in the mixture composition. For this reason, in the last decade, microfluidics has emerged as an alternative to dropwise fabrication, as it can provide a continuous route that subjects all solute molecules to the same conditions, thereby allowing increased control over the mixture composition. Microfluidics have been used most extensively for silk water-in-oil emulsions, with narrow polydispersity particles with rod and spherical morphologies achieved by flow-focusing droplet microfluidics (145–200 μm).[155, 256] However, the micro-size of the emulsions obtained using microchannels[155, 256, 257] limits the application of the resulting

particles. The low flow rates required for the generation of nano-sized emulsions (51–1500 nm)[244] can also limit the throughput speed of production on scale-up.

One solution has been the use of the staggered herringbone micromixer, which can provide high-throughput microfluidic-assisted manufacture of nanoparticles (110-310 nm) using silk nanoprecipitation in acetone and isopropanol antisolvents[174]. High mixing efficiency occurs in the microchannel as the fluid interface is stretched and folded by asymmetric bas-relief herringbone structures that cause chaotic advection by creating continually switching transverse vortices.[258] The staggered herringbone micromixer therefore decreases the mixing time compared to laminar flow regimes and semi-batch macromixing.[258] Use of this micromixer has demonstrated a dependence of the physicochemical properties of the nanoparticles on the solvent properties, the total flow rate and the flow rate ratio of the aqueous and organic phases.[174]

An optimal nanoparticle batch, with a size of 110 nm, a polydispersity of 0.14, a zeta potential of -29.8 mV, a spherical morphology and aqueous stability, has been obtained in a staggered herringbone micromixer using a flow ratio of 5:1 isopropanol to silk and a total flow rate of 1 mL min^{-1}.[174] These conditions were used in further work to analyze the impact of the precursor molecular weight on nanoparticle properties by varying the sericin degumming time of silk cocoons.[179] In both manual semi-batch and continuous formats, increasing the degumming time resulted in a greater molecular weight polydispersity of the silk stocks and reduced the nanoparticle size, polydispersity and zeta potential.[179] By comparison, semi-batch production resulted in a significant decrease in surface charge,[179] indicating that changes in the mixing time and the supersaturation between the two formats impacted the process of silk–silk association. However, spherical particle morphologies were consistently obtained for regenerated silk stocks.

The aim of the present Chapter was to control the morphology and multiscale structure of silk self-assembly by varying the shear processing and supersaturation conditions under bulk and microfluidic mixing regimes. The effects of mixing on self-assembly were assessed

across a range of silk precursor concentrations and shear rates using semi-batch mixing conditions of low and high mixing times as examples of bulk mixing processes for comparison with the staggered herringbone micromixer. This comparative work illustrates that control of silk nanoprecipitation across multiple length scales can be achieved under conditions of high shear and fast mixing and provides a platform for tuning high-shear, semi-batch processes.

3.2 Experimental

3.2.1 Materials

All studies were carried out at 18–22 °C, unless otherwise stated. Reagents and solvents were acquired from Acros Organics™ or Sigma Aldrich at > 98% purity and used without additional purification. Runs for nanoparticle production in continuous format were defined as complete nanoparticle collection using one silk precursor solution (1 mL). Nanoparticle batches were obtained in continuous format and in semi-batch format using 0.5% *w/v* aqueous silk by mixing the product suspensions from three runs that used the same silk precursor solution prior to ultracentrifugation. Each independent experiment was repeated in triplicate using three different silk precursor stock solutions.

3.2.2 Regeneration of *B. mori* silk

Silk fibroin from *B. mori* cocoons was regenerated using the 1 h sodium carbonate and 4 h lithium bromide method as detailed in Chapter 2. First, *B. mori* cocoons were chopped into roughly 5 × 5 mm sections and boiled in 0.02 M aqueous Na_2CO_3 (2 L) at 98–105 °C for 1 h with manual agitation. The degummed fibers were washed in ultrapure H_2O (1 L) three times for 0.33 h each and the silk dried for at least 24 h at room temperature.

A 25% *w/v* silk solution was achieved by dissolving the dry silk fibers in 9.3 M aqueous LiBr solution at 60 °C for 4 h. The silk solution was purified by dialysis (molecular weight cut off 3500 g mol^{-1}, Slide-A-Lyzer®, Thermo Scientific, Rockford, IL, USA) against ultrapure H_2O (1 L) for 48 h, and centrifuged over four cycles, each for 0.33 h at 3000 × *g* and 5 °C (Jouan

BR4i centrifuge equipped with S40 swing rotor). The silk concentration was measured by gravimetry over 24 h at 60 °C and adjusted to the desired concentration by the addition of ultrapure H_2O.

3.2.3 General drop-by-drop manufacture of silk nanoparticles in semi-batch format

Silk nanoparticles were manufactured by the addition of a 3% *w/v* silk solution (1 mL) to isopropanol (5 mL) in a short-neck round-bottom flask. The silk feed was supplied at room temperature using a syringe pump (Harvard Apparatus 22, Holliston, MA, USA) held at an inclination of 0–0.1° and equipped with a BD PLASTIPACK™ syringe, polyethylene Luer lock fluid line (2.54 x 305 mm) and blunt needle (Figure 3.1). The flask was stoppered, and the mother liquor was incubated at room temperature for no longer than 0.5 h before dilution with ultrapure H_2O in a polypropylene ultracentrifugation tube and centrifugation at 48,400 × g for 2 h at 4 °C (Beckmann Coulter Avanti® J-E equipped with JA-20 rotor). The supernatant was removed, the pellet was resuspended in ultrapure H_2O (20 mL) and the suspension was sonicated twice for 30 seconds at 30% amplitude with a Sonoplus HD 2070 sonicator (ultrasonic homogenizer, Bandelin, Berlin, Germany). Ultrapure H_2O (23 mL) was added to the suspension, and the centrifugation, washing and resuspension steps were repeated for a total of three times. The final pellet was suspended in ultrapure H_2O (2–3 mL) and stored at 4 °C until use. Each experiment was repeated in triplicate using three different silk precursor stocks.

Calculations for needle residence time and shear rate were based on the literature value for dynamic viscosity (27 mPas) of regenerated 3% aqueous silk[301] and the calculated density (1.02 g mL^{-1}) for the 3% *w/v* aqueous silk solution, with an assumed Newtonian flow (Table 3.1).[301] The Reynolds number was estimated based on the internal diameter of the needle.[302] An upper limit of the residence time was estimated using the linear velocity and the needle length.[303] The maximum shear rate was taken as the wall shear rate and, for simplicity, the shear rate calculations used the geometry of a straight cylinder. Calculations for the 3, 10 and 50 mL syringes used in the study were performed similarly, using the internal diameters stated by the manufacturer (Table 3.2).

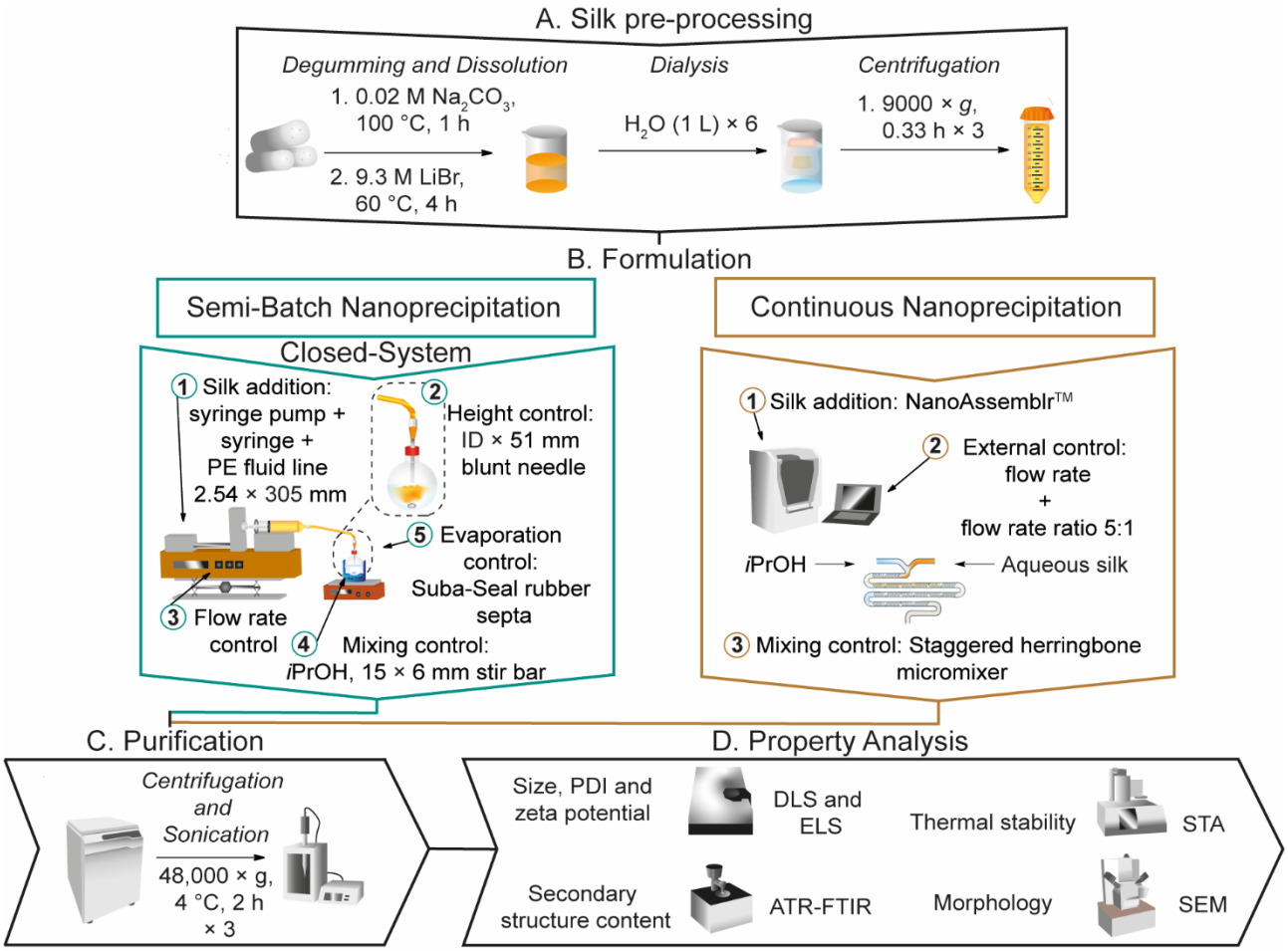

Figure 3.1. The nanoprecipitation workflow for the preparation and purification of silk nanoparticles *via* desolvation in isopropanol. In semi-batch format, the four formulation processing steps are: 1) Loading of a bubble-free aqueous silk solution into a syringe equipped with blunt needle. 2) The silk feed position. 3) The flow rate control of silk solution. 4) Control of mixing time *via* the stirring rate during addition. In continuous format, the three formulation processing steps are: 1) Loading of bubble-free aqueous silk and isopropanol into syringes and the NanoAssemblr™ microfluidic chip. 2) The flow rate control of silk solution and the flow rate ratio control of isopropanol: silk. 3) Control of mixing time *via* the micromixer chip design.

Table 3.1. The estimated flow characteristics of the needles used in the semi-batch system and the micro-mixer indicated that increasing the flow rate of silk in the feed needle in semi-batch format and of the aqueous silk-isopropanol mixture in the microchannel increased the wall shear rate.[a]

Semi-batch format					Micro-mixer		
Needle internal diameter / *mm*	**Flow rate / *mL min^{-1}***	**Residence time / *ms***	**Maximum shear rate / *s^{-1}***	**R_e**	**Flow rate / *mL min^{-1}***	**Maximum shear rate / *s^{-1}***	**R_e**
0.33	0.017	15,335	80	0.04	0.001	80.1	0.04
	1.000	261	4,724	2.5			
	3.510	74	16,581	8.5	0.059	4,727	2.4
	7.000	37	33,068	17			
	8.485	31	40,083	21			
	16.96	15	80,119	41	0.50	40,073	20
0.41	3.510	115	8,646	6.9			
0.6	3.510	246	2,759	4.7			
0.84	3.510	481	1,005	3.4	1.00	80,114	40
1.19	3.510	966	354	2.4			
1.60	3.510	1,746	145	1.8			

a. The average wall shear rate under laminar and Newtonian flow is reported. The micromixer geometry was simplified to a rectangular channel by ignoring the groove depth. Residence times in the fluid line and needles were estimated using the linear velocity while the volumetric flow rate was used for the micromixer.

Table 3.2. Estimated flow characteristics of the 3 mL syringes used in the closed semi-batch system at a silk volume of 1 mL indicated that shear-induced nucleation did not occur.

Flow rate / *mL min^{-1}*	Residence time / *s*	Critical work / *10^{-3} Pa*	Maximum shear rate / *s^{-1}*	Volumetric flow rate / *10^{-10} m^3 s*	Average velocity / *10^{-5} m s^{-1}*	Cross-sectional area / *10^{-5} m^2*	R_e
0.017	3529	1.88	0.00444	2.83	0.481	5.89	0.00157
1.000	18	33.2	0.261	167	28.3		0.093
3.510	17	389	0.917	585	99.3		0.325
7.000	9	775	1.83	1167	198		0.648
8.485	7.07	1.09	0.0757	1414	25.3	56.0	0.255
16.96	3.54	2.19	0.151	2827	50.5		0.509

3.2.4 The effects of flow rate and initial addition height in closed, semi-batch format

Silk nanoparticles were manufactured in 10 mL round-bottom flasks using a blunt needle (0.33 x 51 mm). At room temperature, a 3% *w/v* silk solution was added to isopropanol at flow rates of 0.017, 1.000, 3.510 or 7.000 mL min^{-1}, while varying the initial addition height at 0.7, 2.1 or 3.5 cm from the isopropanol surface. The Reynolds numbers at 0.017, 1.000, 3.510 and 7.000 mL min^{-1} (calculated as 5.4×10^{-3}, 0.32, 1.1 and 2.2 for the fluid line, and as 0.04, 2.5, 8.5 and 17 for the needle) indicated laminar flow (Table 3.1,Table 3.3).

Table 3.3. Estimated flow characteristics of the fluid line used in the closed semi-batch system indicated that shear-induced nucleation did not occur.

Flow rate / *mL min^{-1}*	Residence time / *ms*	Critical work / *10^3 Pa*	Maximum shear rate / *s^{-1}*	Volumetric flow rate / *10^{-10} m^3 s*	Average velocity / *10^{-5} m s^{-1}*	Cross-sectional area / *10^{-6} m^2*	R_e
0.017	5451	0.0046	0.18	2.83	5.59	5.07	0.0054
1.000	93	0.27	10	167	329		0.316
3.510	26	0.94	36	585	1155		1.108
7.000	13	1.90	73	1167	2302		2.209
8.485	11	2.3	88	1414	2791		2.678
16.96	5	4.6	176	2827	5578		5.353

3.2.5 The effect of needle diameter in the closed, semi-batch format

The 3% *w/v* silk solution was added at a rate of 3.510 mL min^{-1} to isopropanol from an initial addition height of 3.5 cm from the isopropanol surface. The needle diameter was varied between 0.33, 0.41, 0.60, 0.84, 1.19 and 1.60 mm. The Reynolds numbers for the needle diameters of 0.41, 0.60, 0.84, 1.19 and 1.60 mm were calculated as 6.9, 4.7, 3.4, 2.4 and 1.8, respectively (Table 3.1).

3.2.6 The effect of stirring rate and feed addition height in the closed, semi-batch format

Silk nanoparticles were manufactured using a blunt needle (0.33 × 51 mm). The silk solution flow rate was 1.000 mL min^{-1}, the initial addition height was 0.0, 1.75 or 3.5 cm from the isopropanol surface, and the stirring rate, provided by an egg-shaped stir bar (15 × 6 mm), was 0, 200, 400 or 800 rpm. The Reynolds number of the stirred vessel, estimated using a cylindrical geometry as ≈ 1300, 2500 and 5030 at stirring rates of 200, 400 and 800 rpm, respectively (Table 3.4), indicated turbulent flow within the vessel at 400 and 800 rpm.

Table 3.4. Estimated flow characteristics of the reactors used in the closed semi-batch system.

Stirring rate / *rpm*	Frequency / *rps*	Length / *m*	Diameter / *m*	Viscosity / *kg ms*$^{-1}$	Density / *kg m*$^{-3}$	R_e
200	21	0.015	0.0060	0.0032	837	1257
400	42					2514
800	84					5029

3.2.7 The effect of flow rate and concentration in the closed, semi-batch format

Silk nanoparticles were manufactured using a blunt needle (0.33 × 51 mm). Silk solution was added to isopropanol at rates of 0.017, 1.000, 8.485 or 16.96 mL min^{-1} from an addition height of 1.75 cm and the stirring rate was varied from 0 to 400 rpm using the egg-shaped stir bar. The silk concentration was 0.5, 2 or 3% *w/v*. The Reynolds numbers at 8.485 and 16.96 mL min^{-1} (calculated as 2.7 and 5.4 for the fluid line and 21 and 41 for the needle) indicated laminar flow (Table 3.1).

3.2.8 Dual indicator system for mixing time in the semi-batch format

The rotational speed investigated at the 5 mL scale ranged from 200–800 rpm in increments of 200 rpm, and the initial addition height was 0, 1.75 or 3.5 cm. The round bottom flask was submerged in water in a clear acrylic box (10.3 × 10.3 × 5 cm) to reduce surface reflections. An LED panel (RALENO, Seattle, WA, USA) was fixed at the back of the stirring plate to provide constant illumination at 5600K colour temperature and at 100% brightness.

The dual indicator system for mixing time described by Melton *et al*.[332] and Weheliye *et al*.[333, 334] was used, with some adaptations. Stock solutions of thymol blue (0.095 mg mL^{-1}) and methyl red (0.135 mg mL^{-1}) were prepared in ethanol. The working solution was prepared by mixing and diluting the stock solutions to give 4.3 mg mL^{-1} thymol blue and methyl red in 70% *v/v* ethanol. To each 5 mL aliquot of the working solution, 0.5 M HCl was added at 0.5 mL L^{-1}, and the system was equilibrated for at least 10 revolutions. An equivalent amount of

NaOH (10.5 µL of 0.15 M NaOH) was then added to the mixture using a 20 µL Eppendorf pipette (attached to a clamp stand for control of the feed location and height). The mixing process was captured on an iPhone SE (Apple, Cupertino, CA, USA) reverse camera at a capture speed and resolution of 240 fps and 1080 p using FiLMiC Pro (FiLMiC Inc., Seattle, WA, USA). Each condition was repeated at least four times.

Images were extracted at 240 fps using FFmpeg.[335] The images were processed using custom MATLAB (Mathworks, Natick, USA) scripts to apply rectangular masks of 18,000 pixels and to calculate the standard deviation of the normalized green channel intensity, as described by Rodriguez *et al*.[336] The standard deviation of the fully mixed condition was calculated as the average of the final ten images, and the mixing time ($t_{95\%}$) was estimated as the time required to reach 95% of the standard deviation at the fully mixed condition (Table 3.5).

Table 3.5. The estimated mixing characteristics of the semi-batch reactor and the micromixer indicated that increasing the feed height and stirring rate in semi-batch format decreased the bulk mixing time and increasing the flow rate in microfluidic format reduced the mixing time.

Semi-batch reactor			Micro-mixer		
Feed height / *cm*	**Stirring rate/ *rpm***	**Mixing time/ *s***	**Flow rate / mL min^{-1}**	**Residence time / *ms***	**Mixing time / *ms***
0	200	16 ± 5.1	0.001	120,000	14,500
	400	15.7 ± 3.7			
	800	5.3 ± 1.1	0.059	2,034	306
1.75	200	28.0 ± 3.7			
	400	8.4 ± 3.0	0.50	240	40
	800	2.0 ± 1.0			
3.50	200	16.9 ± 3.5	1.00	120	21
	400	3.3 ± 3.0			
	800	0.7 ± 0.1			

3.2.9 Semi-batch droplet analysis

3.2.9.1 Volume and time of flight

The semi-batch system was used to determine the average volume of a droplet at flow rates of 0.017, 1.000, 3.510, 7.000, 8.485 and 16.96 mL min^{-1}. During the time taken to extrude a total volume of 1 mL, the number of droplets was captured on an iPhone SE (Apple, Cupertino, CA, USA) reverse camera at a capture speed of 30 fps at 0.017 mL min^{-1} and 240 fps for flow rates greater than 0.017 mL min^{-1}. The resolution was kept constant at 1080 p using FiLMiC Pro (FiLMiC Inc., Seattle, WA, USA). The experiments were repeated in triplicate.

3.2.9.2 Fluid velocity, droplet diameter and diffusion scales

The closed semi-batch system was used to determine the flow rate within droplets extruded at flow rates of 0.017, 1.000, 3.510, 7.000, 8.485, and 16.96 mL min^{-1} at relevant heights between 0 and 3.5 cm (Figure 3.2a). At least three droplets of 3% *w/v* silk solution with 0.3% *w/w* iron(III) oxide (synthetic spherical particle with 99.995% < 325 mesh (~45 μm) size, > 96.8% purity, 4.6 g cm^{-3} solid density and 0.8 – 1.2 g cm^{-3} bulk density from Inoxia Ltd, Sweden) were imaged on an iPhone SE (Apple, Cupertino, CA, USA) reverse camera equipped with 15× macro lens (Shenzhen Apexel Technology Co., Guangdong, Shenzhen, China) at a focal length of 1.5 cm. The resolution was kept constant at 1080 p using FiLMiC Pro (FiLMiC Inc., Seattle, WA, USA) and images were extracted at 240 fps using Ffmpeg.[335] The images were processed using custom MATLAB (Mathworks, Natick, USA) scripts to perform greyscale conversion, contrast-limited adaptive histogram equalization and binary image conversion based on luminance. The particle velocities were measured by manual tracking using ImageJ v1.52n (National Institutes of Health, Bethesda, MD, U.S.A). An LED panel (RALENO, Seattle, WA, USA) was fixed behind the droplets to provide constant illumination at 5600K color temperature and at 80% brightness. The droplet diameters of at least three droplets were imaged on a Photron FASTCAM SA 1.1 Model 675K M1 (Photron, San Diego, CA, US) at 3× magnification and measured using Photron FASTCAM Viewer

(Photron, San Diego, CA, US). The diffusion length and time scales were calculated assuming Fickian diffusion and a silk diffusion coefficient of 2.45×10^5 cm^2 s^{-1} (Table 3.6).[337]

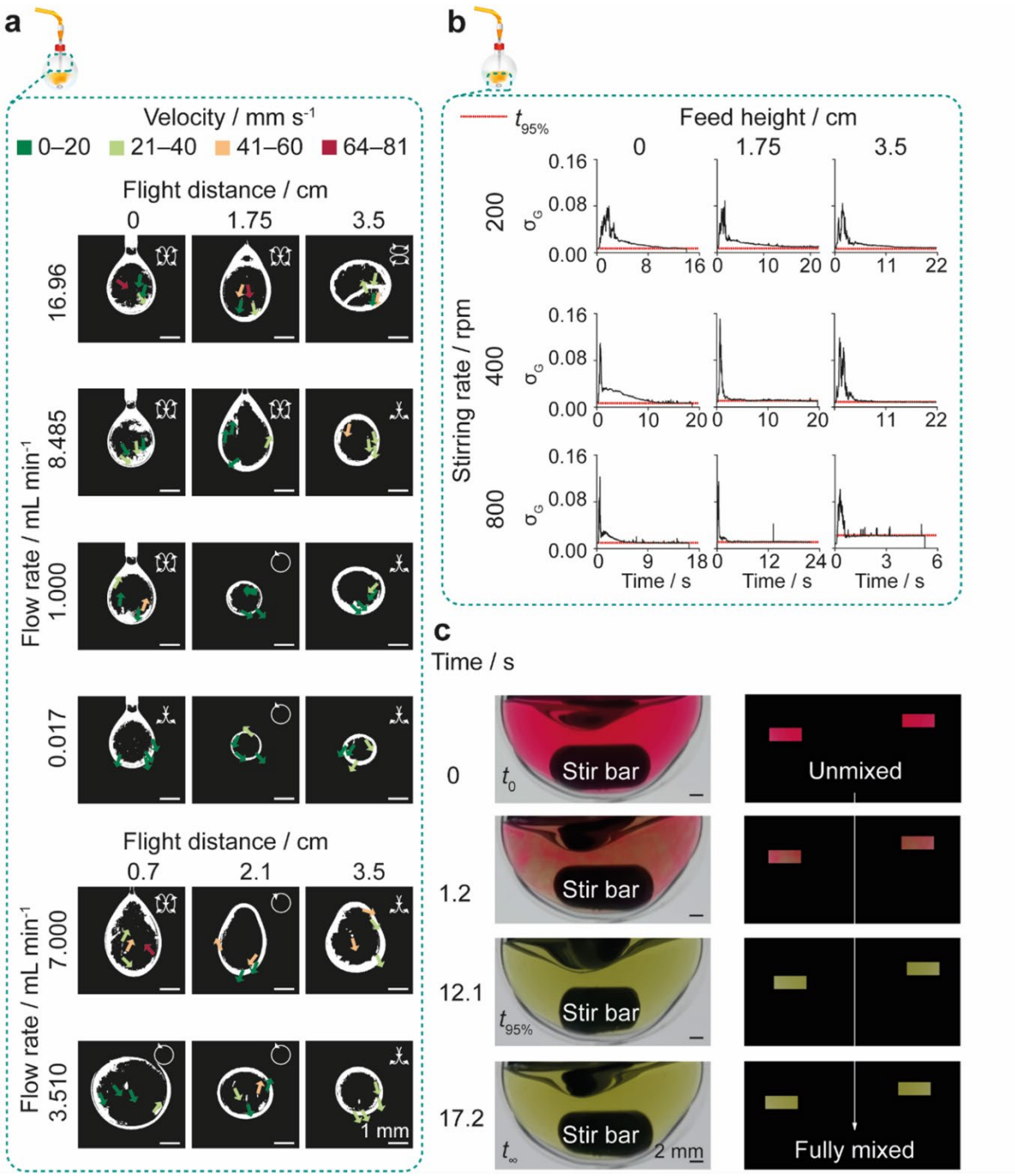

Figure 3.2. Exemplary characterization of flow and mixing properties in the closed semi-batch system. Circulatory flow in silk droplets produced at all flow rates and feed heights was observed using silk doped with iron oxide nanoparticles. The mixing time in the reactor decreased as stirring rate and feed height increased and was measured using the color change of a methyl red and thymol blue mixture from acidic pH (red) to neutral pH (yellow). **(a)** Processed binary images of the circulatory flow field of droplets extruded from the closed semi-batch system. Insets show the two-dimensional direction of flow. **(b)** The variation of standard deviation of the normalized green channel (σ_G) across scale in the open semi-batch system and across feed height and stirring rate in the closed semi-batch system. **(c)** The raw images and processed masks showing the color evolution within the flask at the optimal stirring rate of 400 rpm and feed height of 1.75 cm.

Table 3.6. Droplet characteristics impacting flow and mixing-induced silk self-assembly indicated that circulatory flow occurred across all factor combinations, resulting in convection dominating over diffusion. ± SD, *n* = *3.*

Height / *cm*	Flow rate / *mL min^{-1}*	Number of drops / *mL^{-1}*	Droplet volume / *µL*	Droplet diameter / *mm*	Diffusion length scale[a] / *µm*	Diffusion time scale[a] / *s*	Time of flight / *s*	Droplet velocity / *m s^{-1}*	Fluid velocity / *mm s^{-1}*
0	0.017	NA		0.33	NA	7.42	NA	0.020 ± 0.007	8 ± 5
	1.000							0.028 ± 0.010	16 ± 12
	8.485							0.066 ± 0.072	38 ± 27
	16.96							0.056 ± 0.022	36 ± 23
0.7	3.510	28 ± 2	36.3 ± 3.2	2.73 ± 0.16	18.9 ± 4.1	508 ± 59.2	0.025 ±	0.335 ± 0.007	26 ± 19
	7.000	3 ± 1	305.6 ± 48.1	2.76 ± 0.17	14.2 ± 1.2	521 ± 63.9	0.014 ±	0.203 ± 0.016	35 ± 16
1.75	0.017	126 ± 2	7.9 ± 0.1	2.43 ± 0.04	31.3 ± 0.0	404 ± 13.1	0.067 ± 0	0.373 ± 0.062	12 ± 6
	1.000	33 ± 4	31.0 ± 4.1	2.59 ± 0.12	27.8 ± 0.6	457 ± 41.2	0.053 ±	0.344 ± 0.130	13 ± 12
	8.485	98 ± 17	10.5 ± 2.0	3.96 ± 0.63	24.8 ± 4.9	1090 ± 354	0.047 ±	0.392 ± 0.032	29 ± 13
	16.96	92 ± 55	15.1 ± 11.2	3.38 ± 0.97	25.8 ± 3.2	833 ± 446	0.046 ±	0.240 ± 0.146	33 ± 19
2.1	3.510	28 ± 2	36.3 ± 3.2	3.44 ± 0.15	27.4 ± 1.3	809 ± 69.9	0.051 ±	0.490 ± 0.005	29 ± 17
	7.000	148 ± 20	6.8 ± 0.9	2.51 ± 0.78	26.3 ± 1.8	464 ± 271	0.053 ±	0.425 ± 0.006	28 ± 13
3.5	0.017	126 ± 2	7.9 ± 0.1	2.24 ± 0.05	40.3 ± 3.4	343 ± 14.1	0.111 ±	0.530 ± 0.005	22 ± 12
	1.000	33 ± 4	31.0 ± 4.1	2.71 ± 0.39	32.9 ± 0.5	509 ± 147	0.074 ±	0.683 ± 0.003	29 ± 20
	3.510	28 ± 2	36.3 ± 3.2	3.42 ± 0.05	32.9 ± 0.5	799 ± 21.3	0.074 ±	0.642 ± 0.140	23 ± 6
	7.000	148 ± 20	6.8 ± 0.9	2.18 ± 0.79	31.6 ± 1.5	352 ± 266	0.074 ±	0.685 ± 0.019	50 ± 23
	8.485	88 ± 19	11.7 ± 2.3	3.82 ± 0.38	32.2 ± 2.6	1000 ± 195	0.068 ±	0.665 ± 0.033	37 ± 18
	16.96	149 ± 34	7.0 ± 1.8	1.97 ± 1.41	32.8 ± 2.2	377 ± 419	0.074 ±	0.731 ± 0.075	40 ± 18

a. Determined using the droplet diameter, droplet time of flight and the silk diffusion coefficient of 2.45×10^5 cm^2 s^{-1}.[337]

3.2.10 Microfluidic-assisted manufacture of silk nanoparticles

Silk nanoparticles were manufactured using the NanoAssemblr™ benchtop instrument version 1.5 (model number NA-1.5-16; NanoAssemblr™, Precision Nano-Systems Inc. Vancouver, Canada) equipped with a cyclic olefin copolymer microfluidic cartridge (product codes: 1207 and 1151-034 BENCHTOP CARTRIDGE), as described elsewhere.[174] Using the Y-junction of the two 25 mm inlet channels, the fluids were mixed in a 27 mm rectangular mixing channel (79 µm × 200 µm) having a series of raised grooves (31 µm × 50 µm) and four switchback turns.[338] A 1 mL volume of aqueous silk solution (0.5–3% *w/v*) and isopropanol (5 mL) were injected into separate chamber inlets, and the nanoparticles formed in the staggered herringbone mixer were collected from the outlet. The total flow rate of the isopropanol and silk mixture was varied between 0.001–1.0 mL min^{-1}, and the flow rate ratio was 5:1. The cartridge was cleaned between runs using a water wash and a prime. The water wash consisted of a flow ratio of 1:1 ultrapure H_2O/ultrapure H_2O, a total volume of 2 mL and a total flow rate of 4 mL min^{-1}; the wash was repeated in triplicate. The priming procedure consisted of a flow ratio of 5:1 isopropanol/ultrapure H_2O, a total volume of 6 mL and a total flow rate of 1 mL min^{-1}. The mother liquor suspension was incubated for no longer than 0.5 h before purification.

Calculations were based on the literature viscosity value (3.14 mPas) and density (0.837 g mL^{-1}) values for the 5:1 *v/v* isopropanol/water mixture measured at 20 °C,[339] and Newtonian flow was assumed.[301] Increasing the flow rate from 0.001 to 1 mL min^{-1} resulted in mixing time estimates of 21 to 14,500 ms respectively, according to the manufacturer's guidelines and based on an analytical model for a similar system published elsewhere, by calculating the Peclet number to achieve a coefficient of variation of < 0.1 (Table 3.5).[259] The Peclet numbers were estimated as 4.27×10^8, 2.52×10^{10}, 2.14×10^{11}, and 4.27×10^{11} using the hydraulic diameter of the channel[302] (142 µm) and the diffusion coefficient (3.5×10^{-10} m^2 s^{-1}) of the 5:1 isopropanol/water mixture.[340] The Reynolds numbers (0.04, 2.4, 20, 40) indicated laminar flow (Table 3.1). An upper limit of the residence time was estimated using

the total fluidic volume and flow rate.[303] The residence time was longer than the mixing time at all flow rates, indicating that complete mixing had occurred in the micromixer. The maximum shear rate was taken as the wall shear rate, with the assumptions that chaotic advection did not significantly affect the wall shear rate and that it created a significantly lower shear within the channel. For simplicity, the shear rate calculations used the geometry of a straight rectangular channel and did not take into account the groove depth.[341]

3.2.11 Yield of silk nanoparticles

The total mass of silk nanoparticles was recorded by transferring 450 µL of the suspension to a pre-weighed microcentrifuge tube and recording the total mass, followed by freezing at -80 °C for 5 h and freeze-drying (Christ Epsilon 1-4, Martin Christ Gefriertrocknungsanlagen GmbH, Osterode, Germany) for 24 h at -10 °C and 0.14 mbar. The dry mass was then recorded and the yield calculated using equation 2.1. This process was repeated twice, and an average yield was reported. Freeze-dried silk nanoparticles were stored in a vacuum desiccator at 25 °C until use.

3.2.12 Physicochemical characterization of the silk nanoparticles

The silk nanoparticle size (Z-average of the hydrodynamic diameter), polydispersity index and zeta potential were measured in triplicate in ultrapure H_2O at 25 °C by dynamic light scattering (DLS) (Zetasizer Nano-ZS Malvern Instrument, Worcestershire, UK). Nanoparticle suspensions were prepared for measurement by vortex application for 20 seconds and sonication twice at 30% amplitude for 30 seconds, unless otherwise stated. Refractive indices of 1.33 and 1.60 were used for H_2O and protein, respectively.

3.2.13 Secondary structure measurements of silk nanoparticles

Positive silk II controls consisted of autoclaved silk films and silk films treated with 70% *v/v* ethanol/ultrapure H_2O. Positive silk I controls were air-dried silk films and freeze-dried silk. The air-dried silk films (0.3 mL) were drop-casted from fluid handling systems following extrusion at a height of 3.5 cm using varying silk concentrations (0.5–3.0% *w/v*), flow rates (0.017–16.96 mL min^{-1}) and needle diameters (0.33–1.60 mm). The secondary structures of

silk films, freeze-dried powders and freeze-dried nanoparticles were analyzed by Fourier transform infrared spectroscopy (FTIR) on an ATR-equipped TENSOR II FTIR spectrometer (Bruker Optik GmbH, Ettlingen, Germany). Each FTIR measurement was recorded in absorption mode over the wavenumber range of 400 to 4000 cm^{-1} at 4 cm^{-1} resolution for 128 scans and then corrected for atmospheric absorption using Opus (Bruker Optik GmbH, Ettlingen, Germany). The second derivatives of the background-corrected FTIR absorption spectra were analyzed in OriginLab 19b® (Northampton, Massachusetts, USA) by adapting a literature protocol.[304] Each second derivative was smoothed twice using a seven-point Savitzky-Golay function with a polynomial order of 2. The amide I region was analyzed by interpolation of a non-zero linear baseline between 2–3 of the highest values in the 1600–1700 cm^{-1} range. Peak positions were identified by applying the second derivative, and peaks were fitted in the amide I region using non-linear least squares with a series of Gaussian curves (Figure 3.3). The position, width and height of each peak were allowed to vary, while the peak area could take any value ≤ 0. Deconvoluted spectra were then area-normalized, and the relative area of each band was used to calculate the secondary structure content according to literature band assignments.[155, 305]

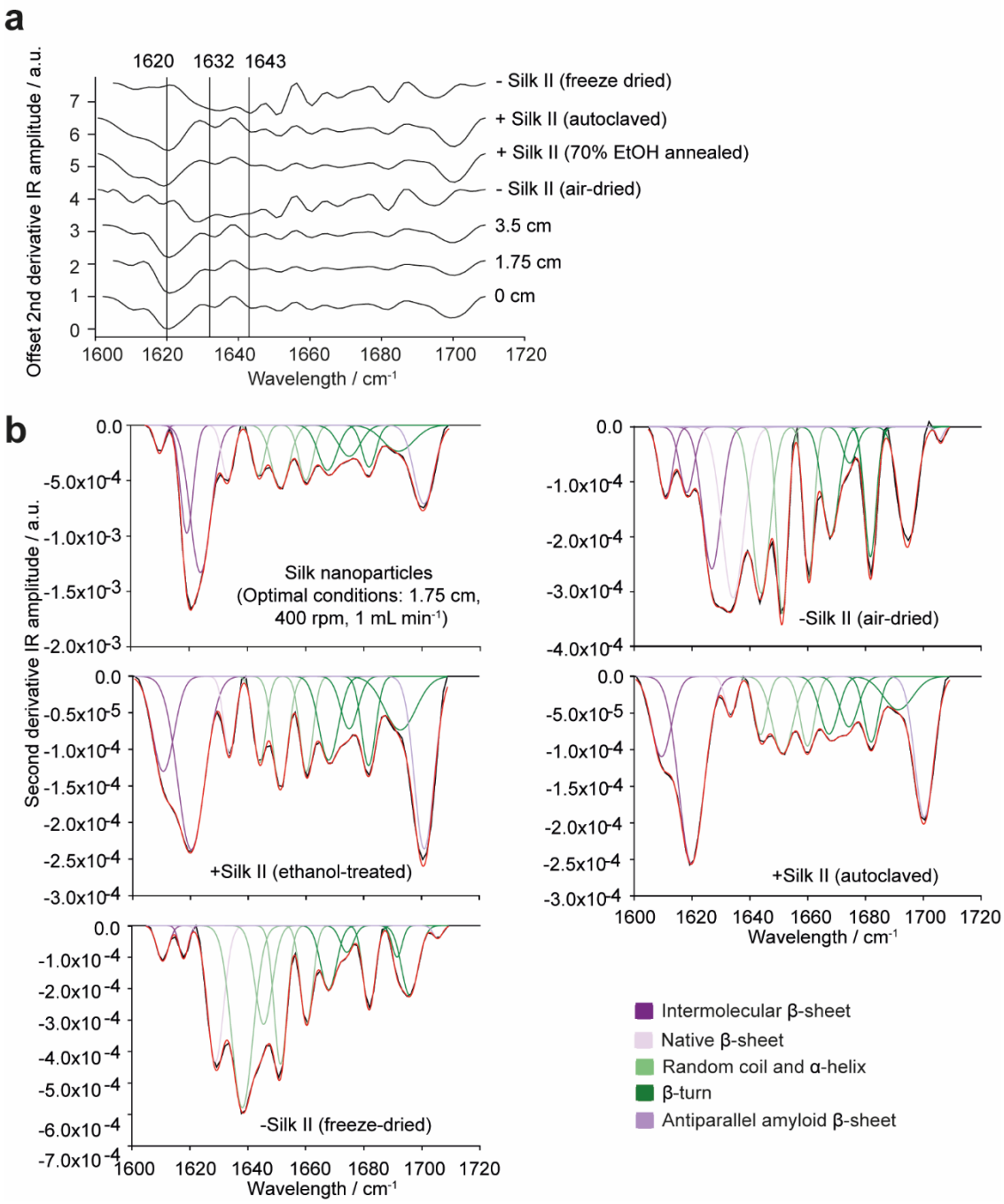

Figure 3.3. Exemplary smoothed second derivative FTIR spectra and peak assignment of silk nanoparticles manufactured by varying (a) feed addition height at a constant stirring rate of 400 rpm and a constant feed addition rate of 1 mL min^{-1} and (b) exemplary peak fitting of the amide I region for nanoparticles formulated at 1.75 cm feed height and silk II controls.

The correlation coefficients I of silk films, freeze-dried silk and nanoparticles were calculated by adaptation of a literature protocol[306] using the air-dried silk film of an aqueous

silk precursor batch as a reference. The second derivative of the FTIR absorption spectra was calculated and smoothed twice with a five-point Savitzky-Golay function and a polynomial order of 2. The processed silk sample was then compared with the reference over the spectral range 1600–1700 cm^{-1} using equation 3.1.

$$R = \frac{\sum x_i y_i}{\sqrt{\sum x_i^2 \sum y_i^2}} \qquad (\mathbf{3.1})$$

where x_i and y_i are the derivative values of the air-dried silk film and processed silk sample at the frequency i.

3.2.14 Scanning electron microscopy of silk nanoparticles

A 1 mg mL^{-1} silk nanoparticle suspension (10–20 µL) was pipetted onto a silicon wafer and lyophilized at -10 °C and 0.14 mbar for 24 h. The wafer was sputter-coated with gold (15 nm) using a low vacuum sputter coater (Agar Scientific Ltd, Essex, UK, and ACE200, Leica Microsystems, Wetzlar, Germany) and imaged with an FE-SEM SU6600 instrument (Hitachi High Technologies, Krefeld, Germany) at 5 kV and 40 k magnification or an FEI Quanta 250 FEG-ESEM instrument (Oxford Instruments, Abingdon, U.K) at 5 kV and 10, 20 and 40 k magnification. The images were processed using ImageJ v1.52n (National Institutes of Health, Bethesda, MD, U.S.A), Adobe Lightroom and Abode Illustrator (Adobe, San Jose, CA, USA).

3.2.15 Statistical analyses

Data were analyzed using Microsoft® Excel® 2019 (Microsoft Office 365 ProPlus Software, Redmond, WA, U.S.A), Minitab® (Minitab® Statistical Software, State College, PA, USA) and GraphPad Prism 8.2.1 (GraphPad Software, La Jolla, CA, U.S.A.). Normality of the data distributions was assumed throughout. The equivalence of variance for sample pairs and multiple groups was identified with the F-test and Bartlett's test. Sample pairs were analyzed using the independent *t*-test. Multiple groups across one independent variable were evaluated by one-way analysis of variance (ANOVA), followed by Tukey's pairwise multiple comparison post-hoc test, or by the Brown-Forsythe and Welch ANOVA tests, followed by the Dunnett T3 pairwise multiple comparison post-hoc test. Two-way ANOVA was used to compare multiple

groups across two independent variables, followed by Tukey's pairwise multiple comparison post-hoc test when a significant interaction was shown and by Tukey's main and simple effect multiple comparison post-hoc tests when no interaction was shown. Statistical significance, identified using post-hoc tests, was as follows: *p < 0.05, **p < 0.01, ***p < 0.001, ****p < 0.0001. All data are displayed as the mean ± standard deviation, with the number of experimental repeats (*n*) shown in each figure legend.

3.3 Results

3.3.1 Silk nanoparticle characterization

3.3.1.1 The effect of flow rate, addition height and stirring rate in closed semi-batch format

In the absence of stirring, increasing the flow rate of the silk solution from 0.017 mL min^{-1} (mixing-induced nucleation) to 7.000 mL min^{-1} (shear-induced nucleation), while also increasing the silk feed addition height, resulted in large, polydisperse nanoparticles regardless of factor levels (Figure 3.4a). Although the nanoparticles remained large and polydisperse scanning electron microscopy (SEM) indicated that moving from shear-induced to mixing-induced nucleation by increasing the needle diameter reduced the extent of self-assembly (Figure 3.4c–d).

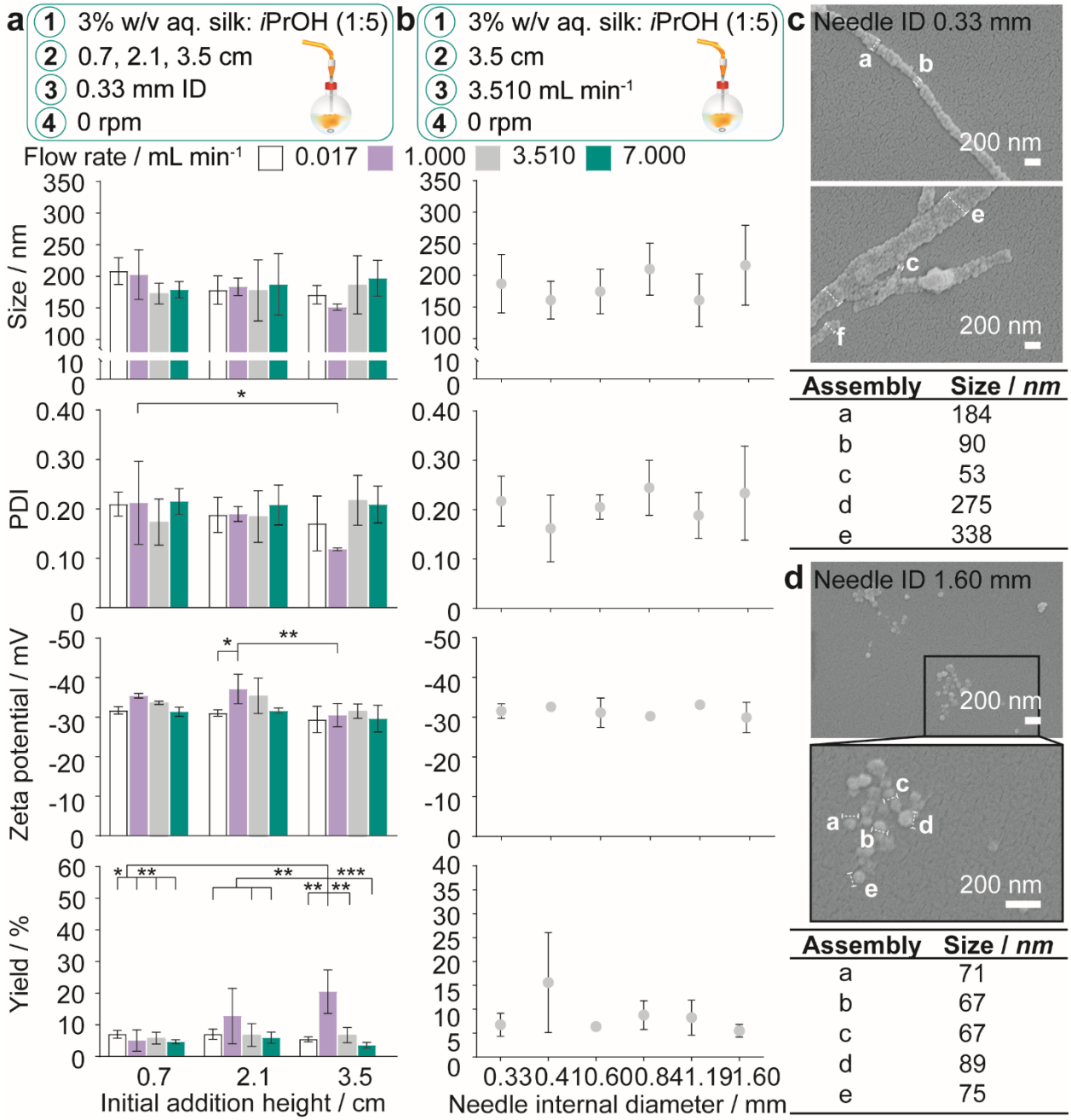

Assembly	Size / *nm*
a	184
b	90
c	53
d	275
e	338

Assembly	Size / *nm*
a	71
b	67
c	67
d	89
e	75

Figure 3.4. The impact in the drop-by-drop semi-batch closed-system by (a) initial addition height and flow rate using a constant needle diameter and by (b) needle diameter at constant flow rate and initial addition height on nanoparticle hydrodynamic diameter, polydispersity (PDI), zeta potential and yield. Scanning electron microscopy showed that curvature morphology increased with needle diameter from **(c)** 0.33mm to **(d)** 1.60 mm. Two-way ANOVA was used to compare multiple groups across feed height and flow rate, followed by Tukey's pairwise multiple comparison post-hoc test for yield and Tukey's simple effect multiple comparison post-hoc test for size, PDI and zeta potential. Multiple groups across needle diameter were evaluated by one-way ANOVA, followed by Tukey's multiple comparison post-hoc test for size, PDI and zeta potential and the Brown-Forsythe and Welch test, followed by Dunnett's T3 post-hoc test for zeta potential. Error bars are hidden in the bars and plot symbols when not visible, ± SD, *n* = 3. Asterisks denote statistical significance determined using post-hoc tests as follows: *p < 0.05, **p < 0.01, ***p <0.001, ****p < 0.0001. Scale bars 200 nm.

As manufacture in the closed, semi-batch system without stirring resulted in large nanoparticles with a wide size distribution, the effect of varying the time and shear stress of mixing was then determined at a 1.000 mL min^{-1} flow rate (shear-induced nucleation). The mixing time was reduced by increasing the stirring rate from 0 to 800 rpm and increasing the droplet velocity by raising the feed height from 0.0 cm to 3.5 cm (Table 3.5, Figure 3.2, and Table 3.6). Increasing the levels of both these factors significantly reduced the nanoparticle size and polydispersity index (Figure 3.5a). At 0 rpm, an increase in the feed height from 0.0 to 3.5 cm significantly decreased the nanoparticle size (from 232 to 151 nm) and the polydispersity index (from 0.24 to 0.12) (Figure 3.5a). Equally, an increase in the stirring rate from 0 to 800 rpm significantly decreased the nanoparticle size to 116 nm at 0.0 cm feed height and the polydispersity index from 0.25 to 0.14 at 1.75 cm feed height. The SEM views confirmed the reduction in assembly size and the increase in nanoparticle curvature as mixing time decreased (Figure 3.5b).

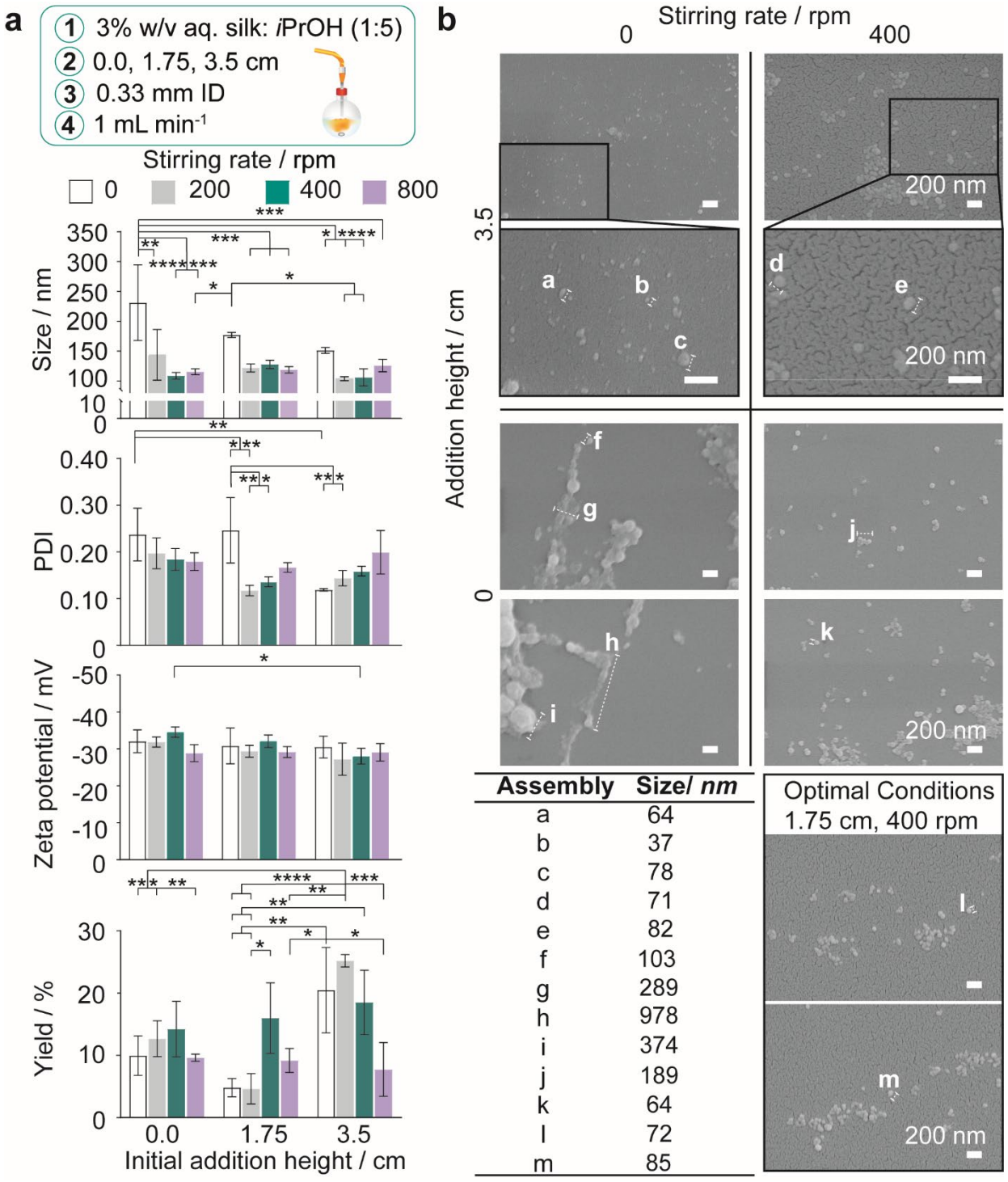

Figure 3.5. Impact of feed height and stirring rate on nanoprecipitation of 3% *w/v* aqueous silk in the semi-batch closed-system at 1 mL min^{-1} flow rate. (a) Hydrodynamic diameter, polydispersity index (PDI), zeta potential and yield of silk nanoparticles. Two-way ANOVA was used to compare multiple groups across feed height and stirring rate, followed by Tukey's pairwise multiple comparison post-hoc test for size, polydispersity index and yield and Tukey's simple effect multiple comparison post-hoc test for zeta potential. **(b)** Scanning electron microscopy showed that lower curvature morphologies were obtained as stirring rate and addition height decreased, due to an increasing degree of secondary self-assembly. Error bars are hidden in the bars and plot symbols when not visible, ± SD, *n* = 3. Asterisks denote statistical significance determined using post-hoc tests as follows: *p < 0.05, **p < 0.01, ***p <0.001, ****p < 0.0001. Scale bars 200 nm.

Generally, the nanoparticle size and size distribution were optimal at 1.75 and 3.5 cm feed heights combined with stirring rates of 200 and 400 rpm (104–128 nm; 0.12–0.16) (Figure 3.5a). As feed height increased, silk nanoparticles were also produced with a higher zeta potential at 400 rpm, and in greater yield at low stirring rates, where the yield reached a maximum of 25% at 3.5 cm and 200 rpm. Further reductions in the mixing time at 3.5 cm (Table 3.5) obtained by increasing the stirring rate to 800 rpm caused a significant drop in nanoparticle yield to 8%. Overall, the nanoparticle size, polydispersity index and zeta potential were optimized at 400 rpm stirring rate. At 1.75 cm feed height a sufficient yield was returned while maintaining low diffusion length scales and shear exposure caused by circulatory flow during droplet flight (Figure 3.2a, Figure 3.5a, and Table 3.6). These factor levels were set for further investigations of the effect of flow rate and silk concentration.

3.3.1.2 The effect of flow rate and silk concentration in closed semi-batch and microfluidic formats

Under conditions of mixing-induced nanoprecipitation in semi-batch format at a 0.017 mL min^{-1} flow rate and 400 rpm stirring rate, increasing the silk concentration from 0.5 to 2 and 3% significantly decreased the nanoparticle size (from 271 to 89 and 75 nm) and polydispersity index (from 0.47 to 0.23 and 0.13) (Figure 3.6a). Significant decreases in the nanoparticle size (from 294 to 161 and 120 nm), polydispersity index (from 0.46 to 0.45 and 0.27) and zeta potential magnitude (from -39 and -40 to -30 mV) also occurred with a concentration increase from 0.5 to 2 and 3% when operating without stirring. The SEM observations revealed an increase in particle sphericity with increasing concentration, from nanofibers and amorphous aggregates formed with 0.5% silk to spherical particles with a high polydispersity at 2% and a narrower size distribution at 3% (Figure 3.7a).

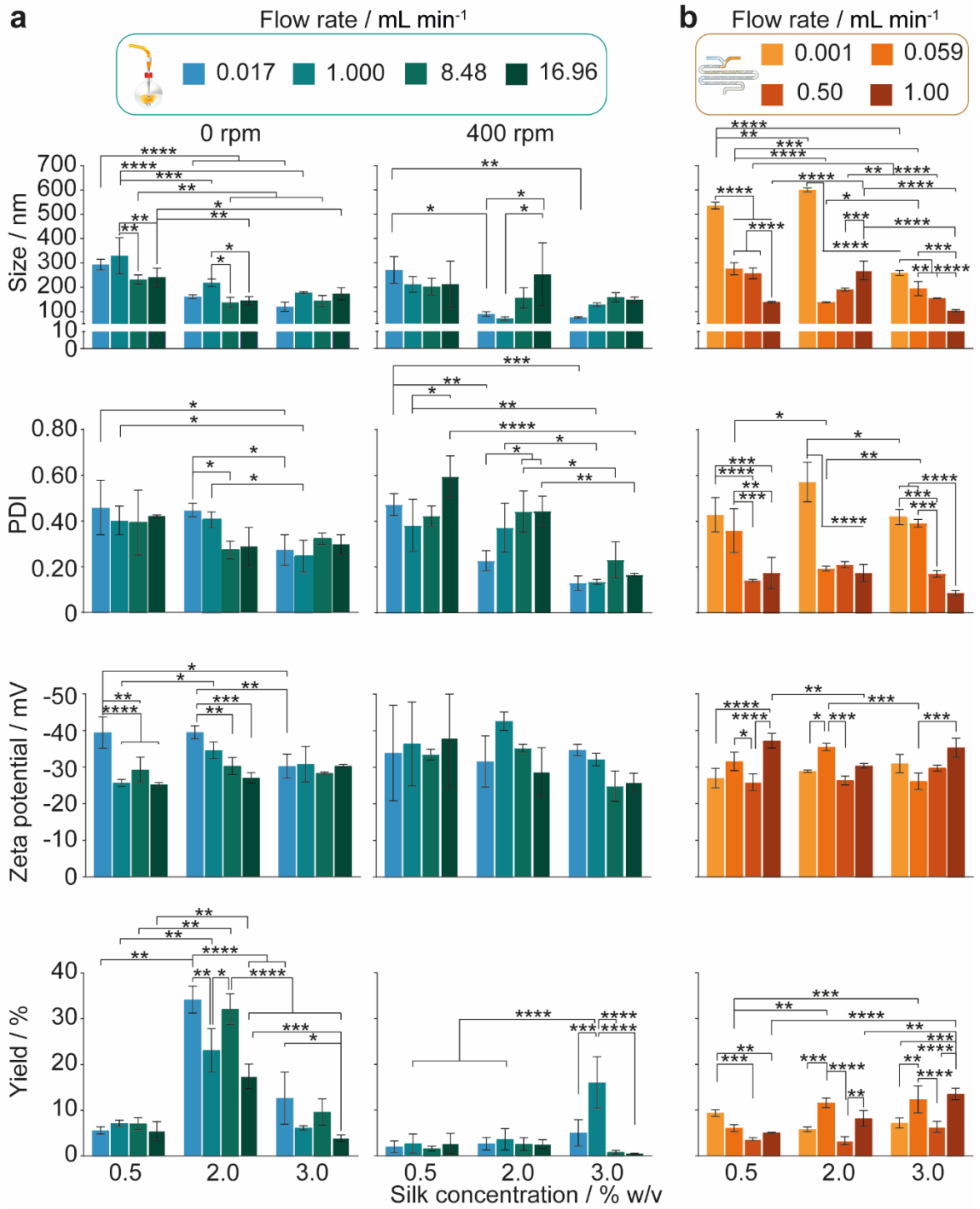

Figure 3.6. The impact of increasing the flow rate and silk feed concentration in the staggered herringbone micromixer and in semi-batch systems of high and low mixing time. The hydrodynamic diameter, polydispersity index, zeta potential and yield for **(a)** semi-batch format and **(b)** microfluidic format. For the unstirred semi-batch processes, two-way ANOVA was used to compare multiple groups across concentration and flow rate, followed by Tukey's pairwise multiple comparison post-hoc test for yield and Tukey's simple effect multiple comparison post-hoc test for size, polydispersity index and zeta potential. In stirred semi-batch format and microfluidic format, multiple groups were evaluated by two-way ANOVA, followed by Tukey's pairwise multiple comparison post-hoc test for all properties. Error bars are hidden in the bars when not visible, ± SD, *n* = 3. Asterisks denote statistical significance determined using post-hoc tests as follows: *p < 0.05, **p < 0.01, ***p <0.001, ****p < 0.0001.

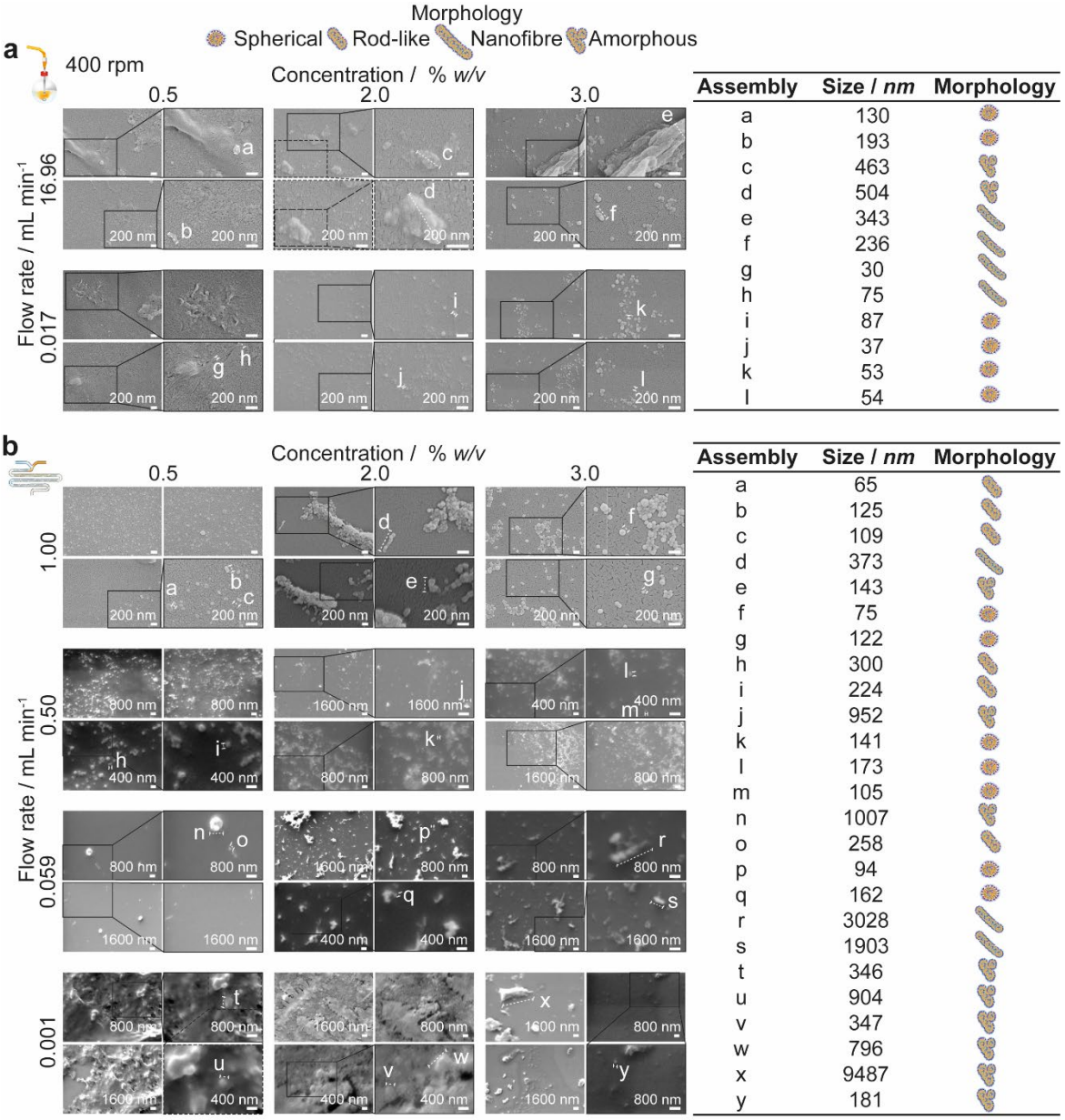

Figure 3.7. Scanning electron microscopy supported the DLS results and confirmed that for low shear processes in the (a) semi-batch format and (b) microfluidic format, the extent of self-assembly varied inversely with silk concentration while for high shear processes, the extent of assembly was maximized at the 2% silk concentration. Due to an extended growth phase associated with 0.5% silk feeds, rod-like silk nanoparticle morphologies were produced in the micromixer between 0.059–1.0 mL min^{-1}, and the particle polydispersity decreased with increasing flow rate.

Conversely, at the flow rate of 0.001 mL min^{-1} in the micromixer, increases in the silk concentration from 0.5 to 2 and 3% resulted in a significant increase, followed by a decrease, in nanoparticle size (from 536 to 600 to 259 nm), whereas the polydispersity index remained high (ranging from 0.57 to 0.42) (Figure 3.6b). Increasing the concentration from 0.5 to 3% did

not significantly affect the zeta potential or yield, which ranged from -27 to -31 mV and from 9 to 6%, respectively. The DLS results were supported by SEM observations, which showed a mixture of spherical secondary building units and amorphous aggregates for all silk feeds (Figure 3.7b).

At the 400 rpm stirring rate, moving from low to high shear by increasing the flow rate from 0.017 to 16.96 mL min^{-1} caused a significant increase in the nanoparticle size from 89 to 252 nm with 2% silk. The size distribution also significantly increased with flow rate at silk concentrations of 0.5 and 2%. SEM examinations confirmed that these results were due to a greater degree of shear-induced self-assembly for all silk feeds as the flow rate increased (Figure 3.7a). For example, at 3% silk concentration, tertiary units were present as nanofibers, while at 0.5% and 2%, amorphous, lamellar aggregates also formed. As for mixing-induced nanoprecipitation, the polydispersity index decreased significantly with increasing silk concentration from 0.5 and 2% to 3% across all high-shear flow rates. The yield increased significantly with silk concentration at a flow rate of 1.000 mL min^{-1} and reached a maximum at 3% silk (from 1 to 16%).

Similarly, for the high-shear microfluidic format at flow rates between 0.059 and 1.0 mL min^{-1}, increasing the silk concentration from 0.5% and 2% to 3% generally resulted in a significant decrease in particle size and an increase in yield (Figure 3.6b). At a flow rate of 0.059 mL min^{-1}, the size and polydispersity index significantly decreased (from 276 to 138 nm and from 0.36 to 0.19) with increased silk concentration from 0.5 to 2%. The size, polydispersity index and zeta potential magnitude subsequently increased (from 138 to 194 nm, 0.19 to 0.39 and -36 to -26 mV) as the silk concentration increased further to 3%. The SEM observations (Figure 3.7b) reinforced the DLS results and indicated that the primary assemblies formed using 2 and 3% silk stocks underwent secondary and tertiary assembly to give mixtures containing nanofiber aggregates, whereas the 0.5% silk stock formed rod-like particles in mixtures with amorphous aggregates. At 1.0 mL min^{-1}, the opposite trend was observed with an increase in the silk concentration from 0.5 to 2%, as the size and zeta

potential significantly increased (from 139 to 269 nm and -37 to -30 mV) due to the increased formation of amorphous aggregates. Subsequent increases from 2 to 3% silk resulted in a decreased nanoparticle size (to 103 nm) and an increased sphericity.

For 0.5 and 3% silk feeds, increasing the flow rate from 0.001 to 1.0 mL min^{-1} caused significant reductions in the assembly size (from 536 to 139 nm and from 259 to 103 nm, respectively) and polydispersity index (from 0.43 to 0.17 and from 0.42 to 0.09, respectively). This size reduction was supported by the observed reduction in aggregates as the flow rate increased for both silk feeds (Figure 3.7b). Increasing the flow for 3% silk feeds significantly decreased the zeta potential, from -26 mV at 0.059 mL min^{-1} to -35 mV at 1.0 mL min^{-1}. For 0.5% silk, changing the flow rate from 0.001 to 1.0 mL min^{-1} also significantly reduced the zeta potential (from -27 to -37 mV) while for 2% silk feedstocks, increasing the flow rate from 0.001 to 0.059 mL min^{-1} reduced particle size (from 600 to 138 nm), polydispersity index (from 0.57 to 0.19) and zeta potential (from -29 to -36 mV) and increased the yield (from 6 to 12%). These changes were accompanied by a morphological shift from amorphous aggregates at 0.001 mL min^{-1} to spherical nanoparticles and nanofiber agglomerates at 0.059 mL min^{-1}. Raising the flow rate to 0.5 and 1.0 mL min^{-1} increased the particle size (to 269 nm) and zeta potential (from -26 mV) while lowering the yield (to 8%). At these flow rates, amorphous and nanofiber aggregates were produced in mixtures with spherical nanoparticles. The SEM views reinforced the DLS measurements and confirmed that, at 0.5 and 1.0 mL min^{-1}, increasing the silk feed concentration resulted in a shift from rod-like particles to aggregates and then spherical particles (Figure 3.6b).

3.3.2 Secondary Structure Measurement

The correlation of the silk nanoparticle secondary structure content with formulation conditions and the shear-induced assembly of the silk precursor by extrusion through the feed needle were evaluated by attenuated total reflectance-FTIR (ATR-FTIR) analysis and deconvolution of the amide I region (Figure 3.3). The structural changes caused by the nanoprecipitation

process were also evaluated by analyzing the amide I region (1600–1700 cm^{-1}) using the spectral correlation coefficient method.[306]

3.3.2.1.1 The effect of flow rate, addition height and stirring rate in closed, semi-batch format

In the unstirred closed system, increasing the feed rate from 0.017 to 7.000 mL min^{-1} at a 3.5 cm feed height caused a decrease in the β-sheet content of silk nanoparticles from 57% to 52% (Figure 3.8a). Conversely, for the extruded silk, increasing the flow rate from 0.017 to 3.510 mL min^{-1} and 7.000 mL min^{-1} decreased the correlation coefficient from 0.78 to 0.44 and 0.34, respectively (Figure 3.8b). Further, increasing the feed height from 0.7 to 2.1 cm at a feed rate of 7.000 mL min^{-1} decreased the nanoparticle correlation coefficient from 0.47 to 0.32 (Figure 3.8a). The needle diameter had no significant effect on the nanoparticle secondary structure content (Figure 3.8c); however, reducing the needle diameter from 1.60 to 0.33 mm at 7.000 mL min^{-1} increased the β-sheet content of drop-casted films from 25% to 33% (Figure 3.8b). This increase in β-sheet crystallinity of the extruded silk with decreasing needle diameter was reinforced by the reduction in the correlation coefficient at feed rates of 3.510 and 7.000 mL min^{-1} (Figure 3.8b).

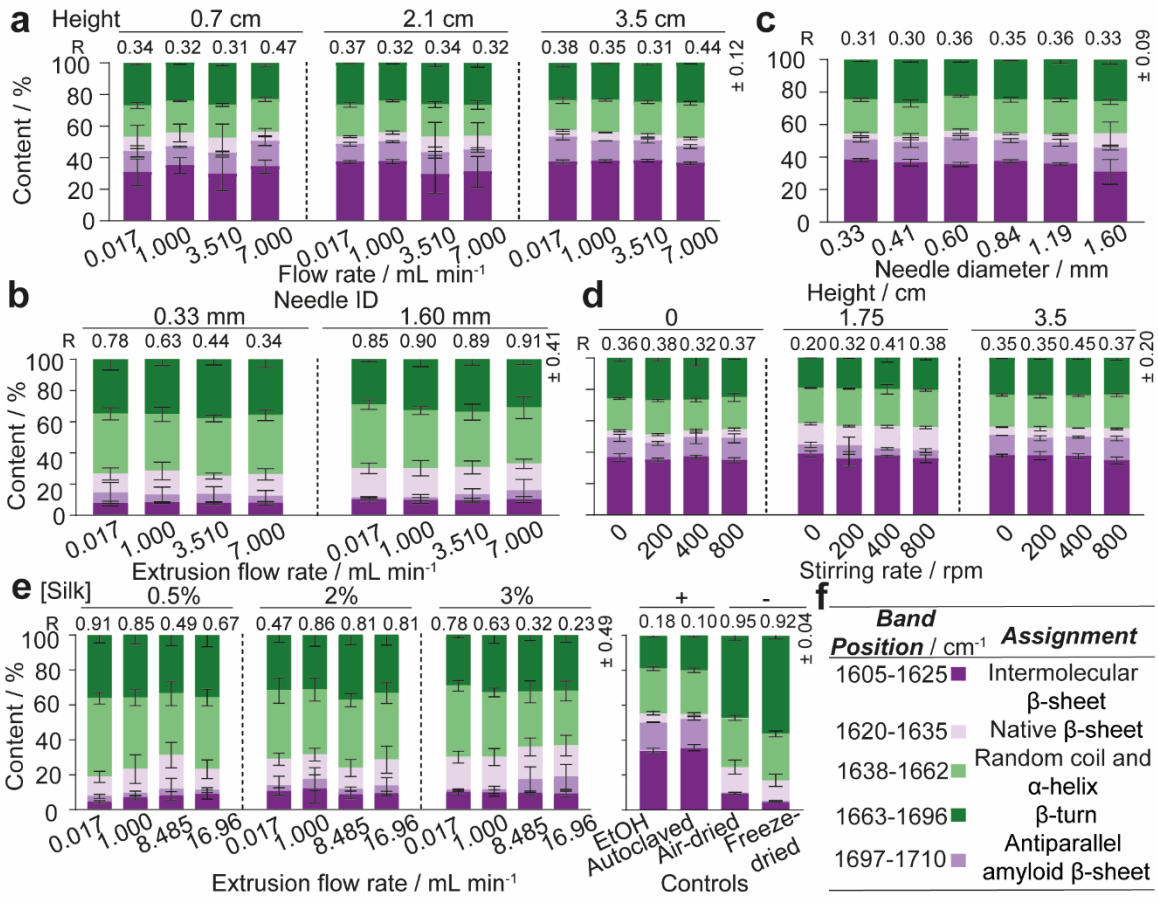

Figure 3.8. The secondary structure of silk nanoparticles manufactured at the specified formulation parameters in the semi-batch closed system at (a, c) 0 rpm, and (d) with varying initial addition height and stirring rate and (b,e) silk extruded from the closed system feed needles at the specified formulation parameters. (f) FTIR band assignments key. Silk films treated with 70 % ethanol and autoclaving to obtain high β-sheet content were used as positive controls for silk II structure, with an untreated silk film and freeze-dried silk powder serving as negative controls. Two-way ANOVA was used to compare multiple groups across feed height and flow rate (± SD, *n* = 3), followed by Tukey's pairwise multiple comparison post-hoc test for total β-sheet and anti-parallel amyloid β-sheet contents and Tukey's simple effect multiple comparison post-hoc test for β-turn, intermolecular β-sheet, native β-sheet and α-helix and random coil contents and correlation coefficients. Multiple groups across needle diameter (± SD, *n* = 3) were evaluated by one-way ANOVA, followed by Tukey's multiple comparison post-hoc test for total β-sheet, anti-parallel amyloid β-sheet, β-turn, α-helix and random coil contents and correlation coefficients while the intermolecular β-sheet and native β-sheet contents were evaluated by the Brown-Forsythe and Welch test, followed by Dunnett's T3 post-hoc test. Two-way ANOVA was used to compare multiple groups across feed height and stirring rate, followed by Tukey's simple effect multiple comparison post-hoc test for the correlation coefficients and contents. Two-way ANOVA was used to compare multiple groups across flow rate and needle diameter (± SD, *n* = 9), followed by Tukey's pairwise multiple comparison post-hoc test for correlation coefficients and Tukey's simple effect multiple comparison post-hoc test for total β-sheet contents. Two-way ANOVA was used to compare multiple groups across flow rate and concentration (± SD, *n* = 9), followed by Tukey's pairwise multiple comparison post-hoc test for total β-sheet contents and correlation coefficients. Error bars are hidden in the bars and plot symbols when not visible. Data obtained from silk II controls are as described in Chapter 2. ± SD, *n* = 3.

In the stirred system, the nanoparticle β-sheet content generally increased with feed height from 0.0 to 1.75 cm (Figure 3.8d). For example, at 200 rpm, increasing the feed height from 0.0 to 1.75 cm increased the β-sheet content from 51% to 56% (Figure 3.8d). Increasing the feed height also caused a main effect decrease in the nanoparticle β-turn content. As the stirring rate increased from 0 to 200 rpm and then to 800 rpm, the nanoparticle antiparallel β-sheet content showed a main effect decrease and then an increase, respectively (Figure 3.8d).

3.3.2.1.2 The effect of flow rate and silk concentration in closed semi-batch format

For the stirred semi-batch process, the nanoparticle β-sheet content and correlation coefficients ranged between 51–58% and 0.23–0.48, respectively, and did not vary significantly with silk concentration or flow rate (Figure 3.9a). However, at the low shear flow rate of 0.017 mL min^{-1}, increasing the silk concentration from 0.5% to 2% and 3% reduced the nanoparticle α-helix and random coil content from 25% to 19% (Figure 3.9a). Conversely, in the unstirred condition, the nanoparticle correlation coefficients decreased as the concentration increased from 0.5% to 2% and 3%, at 0.017 mL min^{-1} (from 0.27 to 0.15 and 0.15), 1.000 mL min^{-1} (from 0.33 to 0.18 and 0.20) and 8.485 mL min^{-1} (from 0.31 to 0.21 and 0.15) (Figure 3.9a). This trend was supported by the significant increase in total β-sheet content with changes from 0.5 to 2% at 0.017 mL min^{-1} (58 to 60%) and from 0.5 to 2 and 3% at 8.48 mL min^{-1} (55 to 59 and 56%). Similarly, the intermolecular β-sheet content increased with silk feed concentration from 0.5 to 3% at 0.017 (34 to 42%). Additionally, for 3% silk feedstocks, the native β-sheet content significantly increased with flow rate whereas for 0.5% silk, the intermolecular β-sheet content significantly followed flow rate. Consequently, the nanoparticle α-helix and random coil content also decreased as the silk concentration increased from 0.5 to 3% at flow rates of 0.017 (20 to 19%), 1.000 (21 to 19%), and 8.485 mL min^{-1} (20 to 19%). Similarly, the extruded silk crystallinity increased with the feedstock concentration. For instance, increasing the concentration from 2 to 3% at 8.485 mL min^{-1}

increased the extruded silk β-sheet content from 24% to 36% (Figure 3.8e). This result was paralleled by a reduction in the correlation coefficient as the concentration increased from 0.5%, at flow rates of 0.017 (0.90), 1.000 (0.85) and 16.96 mL min^{-1} (0.69), to 3.0%, at flow rates of 8.485 (0.32) and 16.96 mL min^{-1} (0.23) (Figure 3.8e).

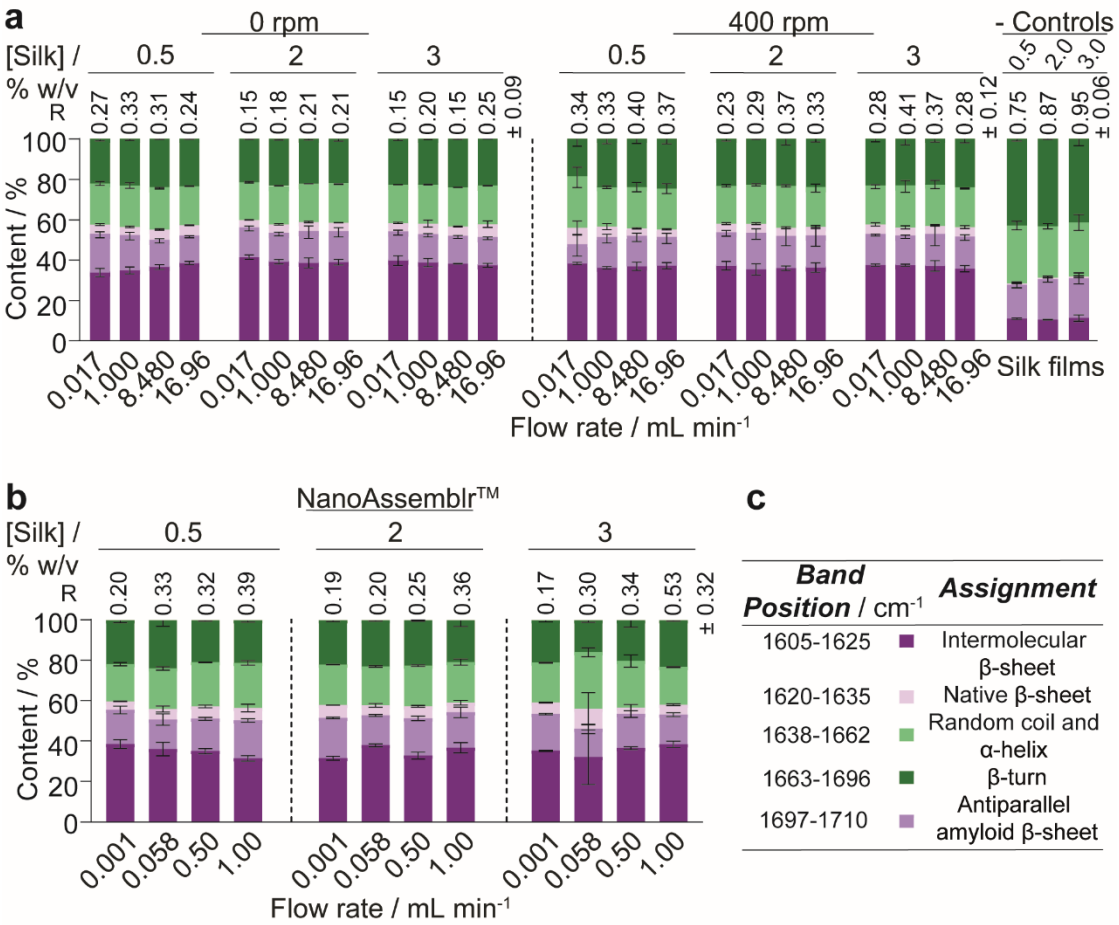

Figure 3.9. Formulation parameters had a significant impact on the secondary structure of silk nanoparticles. Secondary structure content (%) of silk nanoparticles manufactured using different silk concentrations and flow rates in the **(a)** low mixing time (400 rpm) and high mixing time (0 rpm) semi-batch processes, and **(b)** in the NanoAssemblr™. **(c)** FTIR band assignments key. Untreated silk films drop-casted using 0.5, 2 and 3% silk stocks served as negative silk II controls. Secondary structure content (%) was calculated from the relative areas of peaks in the second derivative spectrum. The correlation coefficients of silk nanoparticle second derivative amide I spectra were calculated using the silk II negative control film as reference. Two-way ANOVA was used to compare multiple groups across concentration and flow rate. In the stirred system, this was followed by Tukey's simple effect multiple comparison post-hoc test for correlation coefficients and the contents for total β-sheet, antiparallel β-sheet, intermolecular β-sheet, random coil and α-helix and β-turn. Native β-sheet content was evaluated using the Tukey pairwise multiple comparison post hoc test. In the unstirred system, total β-sheet, antiparallel β-sheet, intermolecular β-sheet, and β-turn content were evaluated using the Tukey pairwise multiple comparison post hoc test while the Tukey simple effect post hoc test was used for correlation coefficients and the contents for random coil and α-helix and native β-sheets. For the micromixer, correlation coefficients and contents were evaluated using the Tukey simple effects post hoc test except for β-turn and random coil and α-helix content, for which the Tukey pairwise comparison post hoc test was used. ± SD, n = 3.

The β-sheet content of 0.5% extruded silk increased with flow rate from 19% at 0.017 mL min^{-1} to 31% at 8.485 mL min^{-1} (Figure 3.8e). The interaction between flow rate and

concentration also significantly increased the silk β-sheet content, from 19% to 29% and 37%, as the flow rate was increased from 0.017 mL min^{-1} to 16.96 mL min^{-1} and 16.96 mL min^{-1} at silk concentrations of 0.5%, 2.0% and 3.0%, respectively (Figure 3.8e). These results were supported by the reduction in the correlation coefficient of extruded silk from 0.78 to 0.32 and 0.23 as the flow rate increased from 0.017 mL min^{-1} to 8.485 mL min^{-1} and 16.96 mL min^{-1}, respectively, at a silk concentration of 3.0% (Figure 3.8e).

In the micromixer, the nanoparticle β-sheet content did not significantly vary with silk concentration or flow rate, and the correlation coefficients displayed no general trend (Figure 3.9b). However, the nanoparticle α-helix and random coil content significantly increased with increases in silk concentration from 0.5 and 2 to 3% at 0.059 mL min^{-1} (from 20 and 19 to 28%) and decreased (from 22 to 19%) at 1.0 mL min^{-1} flow rate (Figure 3.9b). Further, the nanoparticle α-helix and random coil content generally increased with flow rate. For example, increasing the flow rate from 0.001 to 1.0 mL min^{-1} caused a significant increase from 18 to 22% for 0.5% silk feeds; by contrast, for 3% silk this content increased from 20 to 28% between 0.001 to 0.059 mL min^{-1} and decreased to 19% at 1.0 mL min^{-1}.

3.4 Discussion

In the current study, the optimized formulation variables[153, 174, 179] for preparing silk nanoparticles were used to investigate the impact of flow and mixing on silk self-assembly. Consequently, all silk feed concentrations were below the ≈10% *w/w* critical micelle concentration[301] of regenerated silk fibroin. I used the closed, semi-batch process for lab-scale nanoprecipitation, and the NanoAssemblr™ platform for the continuous process, with a commercially available staggered herringbone mixer operating under conditions of laminar flow (R_e < 2000).

3.4.1 The effect of flow rate, addition height and stirring rate in closed, semi-batch format

The flow rates between 0.017 to 16.96 mL min^{-1} resulted in Reynolds numbers < 2000 within the tubing and with all needles used; hence, laminar and Newtonian flow was used to calculate the average wall shear rate.[301] The average wall shear rates in the syringe and tubing (Table 3.1), combined with the residence times, were not expected to provide sufficient work (≈ 10^5 Pa)[313] for shear-induced nucleation of the silk molecules at flow rates between 0.017 and 16.96 mL min^{-1}. However, conditions of high shear were introduced at flow rates above 0.017 mL min^{-1} in needles with diameters less than 1.6 mm (Table 3.1).

Regenerated silk fibroin can undergo a primary assembly process into silk fibroin micellar structures (secondary building units), followed by secondary and tertiary assembly of the micellar units into nanofibers and lamellar structures (Figure 3.10).[342] The hydrophilic blocks of the silk fibroin polymer are hydrated in aqueous solution, resulting in an extended conformation.[342] The shear-induced desolvation breaks the stabilizing intermolecular bonds with water and enables hydrophobic interactions between silk molecules.[342] Scanning electron microscopy showed that shear-induced nucleation resulted in secondary and tertiary assembly of silk micelles into nanofibers and lamellar structures, prior to antisolvent addition and completion of mixing (Figure 3.4c and d, Figure 3.5b).[343] This was reinforced by the significantly lower correlation coefficients of the silk extruded from the 0.33 mm needle at all flow rates above 0.017 mL min^{-1} (Figure 3.8b).

At all feed heights, mixing of silk within free falling droplets was driven by convection due to the high fluid velocities (Table 3.6). Consequently, the impact of non-uniform silk concentration on solvent-antisolvent mixing efficiency can be neglected. However, for flow conditions of high shear, self-assembly within the droplet during flight could occur due to the microscale diffusion length of the silk molecules (Table 3.6). The incorporation of water into, and size of, shear-induced silk assemblies would increase with feed height and time of flight. The concomitant reduction in free water concentration within the droplet could have reduced

the solvent-antisolvent mixing efficiency and resulted in large, polydisperse assemblies (Figure 3.4).

Without stirring, at a 1.000 mL min^{-1} feed rate and 0.0 cm height, the shear-induced nucleation, and the antisolvent–induced dehydration resulted in nanoparticle formation at the phase boundary upon addition of the aqueous silk feed to the isopropanol bulk. This resulted in phase separation and low reproducibility due to the uncontrolled manual mixing of the two phases during purification. Increasing the stirring rate and feed height increased the rate and degree of antisolvent–induced nucleation by reducing the mixing time (Table 3.5).

Assembly growth was disfavored under conditions of low mixing time, resulting in low nanoparticle size and polydispersity with increased yield. Additionally, the shear stress of the liquid flow arising from stirring rates and feed heights of 200 rpm and 1.75 cm could exceed the shear stress of agglomerates formed during silk extrusion from the feed needle. Breaking the intermolecular bridges holding the agglomerates together, combined with desolvation, would result in kinetic locking of the secondary building units. This was supported by the increase of nanoparticle β-sheet content with feed height (Figure 3.8d) and the low curvature morphology of tertiary assemblies formed at low heights and stirring rates (Figure 3.5b).

3.4.2 The effect of flow rate and concentration in closed semi-batch and microfluidic formats

In the stirred semi-batch process, at feed rates of 0.017, 1.000, 8.485 and 16.96 mL min^{-1}, the shear rates experienced by silk in the fluid line were estimated as 0.18, 10, 88 and 176 s^{-1}, respectively, while the shear rates in the needle were estimated as 80, 4724, 40083 and 80114 s^{-1} (Table 3.1, Table 3.3). At 1.000 mL min^{-1} and above, the needle shear rates lay above the critical shear rate and work required for nucleation.[344] Shear-induced nucleation was reinforced by a decrease in the correlation coefficients of extruded silk as the flow rate increased across all concentrations and an increase in the β-sheet content of extruded silk as the flow rate increased at 0.5 and 2.0% (Figure 3.8e). Consequently, the following arguments

assume that shear-induced nucleation, followed by isopropanol-induced desolvation, occurred above a flow rate of 0.017 mL min^{-1}.

For homogenous nucleation at 0.017 mL min^{-1}, increasing the concentration from 0.5 to 3.0% reduced the assembly size and polydispersity index due to a greater degree of supersaturation in both low and high mixing time processes (Figure 3.6a). Samples prepared using 3.0% silk at flow rates of 0.017 and 1.000 mL min^{-1} and stirring at 400 rpm could be considered monodisperse. At 0.017 mL min^{-1}, the reduction in the growth phase with increasing concentration significantly increased the assembly curvature (Figure 3.7a) and packing due to decreases in the α-helix and random coil contents (Figure 3.9a). The reduced growth observed at higher silk concentrations in low-shear, semi-batch nanoprecipitation contrasts with results of previous work by D. Pham *et al.*,[312] who used lower antisolvent:silk volumetric ratios.

In the unstirred system, under high-shear conditions and at all flow rates exceeding 0.017 mL min^{-1}, increasing the silk feed concentration from 0.5 to 3.0% significantly reduced the particle size, whereas in the stirred system, the decreases in size were not significant (Figure 3.6a). A mixture of low sphericity particles and aggregates were formed under high shear at 0.5 and 2.0%, while a mixture of nanofibers, lamellar structures and spherical particles were formed at 3.0% (Figure 3.7a). This possibly reflected a balance between increased antisolvent-induced nucleation rate and increased rates of shear-induced self-assembly with concentration. The greater degree of shear-induced self-assembly with increasing concentration, from 0.5 to 3.0%, was reinforced by the increase in total and intermolecular β-sheet contents of the nanoparticles, the increased total β-sheet content of the extruded silk, the reduction in the nanoparticle correlation coefficients with concentration and the decrease in extruded silk correlation coefficients at 8.485 and 16.96 mL min^{-1} (Figure 3.8e). Consequently, as the formation of shear-induced micelles increased with feed rate, the reduced silk concentration prohibited antisolvent-induced nucleation.

The feed rate of silk also impacts mixing-induced self-assembly by altering the mixing time. For example, the droplet surface area decreased as the feed rate increased from 0.017 to 1.000 mL min^{-1} and then increased as the feed rate was raised to 16.96 mL min^{-1} (Table 3.6). The reduced sphericity of the droplets produced in the jetting regime above 7.000 mL min^{-1} (Figure 3.2a) could also cause non-uniform mixing. The effect of decreasing the mixing time as the feed rate was increased could be observed in the unstirred system at 0.5% and 2% silk feed concentrations. At these concentrations, the nanoparticle size and polydispersity index decreased with flow rate because the increase in the antisolvent-induced nucleation rates outweighed the increase in shear-induced assembly rates. Further, the feed rate controls the degree and rate of supersaturation onset of the antisolvent-induced desolvation. This means that the type and rate of antisolvent-induced nucleus growth could be impacted by the rate of silk addition. Increasing the feed rate favors mononuclear surface-controlled growth by increasing the mass transfer of silk from the solution to the assembly surface. For example, as the feed rate increased in the stirred semi-batch process for 2% silk feeds, the resulting assemblies increased in size and size distribution (Figure 3.6a).

Continuous manufacture is a well-recognized strategy that simplifies the scale-up process of nanoformulations.[255] I therefore used the NanoAssemblr™ as an example of a scale-independent process. Assuming Newtonian flow, the flow rates of 0.001 mL min^{-1} to 1 mL min^{-1} resulted in Reynolds numbers of 0.04 to 40. These numbers were below the high vorticity and low transverse flow regime (Reynolds numbers > 1000). This ensured a high mixing efficiency, with the mixing time decreasing as flow rate increased from 0.001 to 1.0 mL min^{-1}. The residence times at all flow rates were longer than the mixing times (Table 3.5), indicating that complete mixing occurred in the micromixer. The wall shear rates increased with flow rate, and when combined with the residence time, shear-induced nucleation of silk fibroin was likely to occur at all flow rates greater than 0.001 mL min^{-1}, as both the critical shear rate[344] and work[313] were exceeded. Because the shear rates in both formats were

analogous, the effects of shear and mixing in the micromixer could be compared with semi-batch processes with low and high mixing times (Figure 3.10).

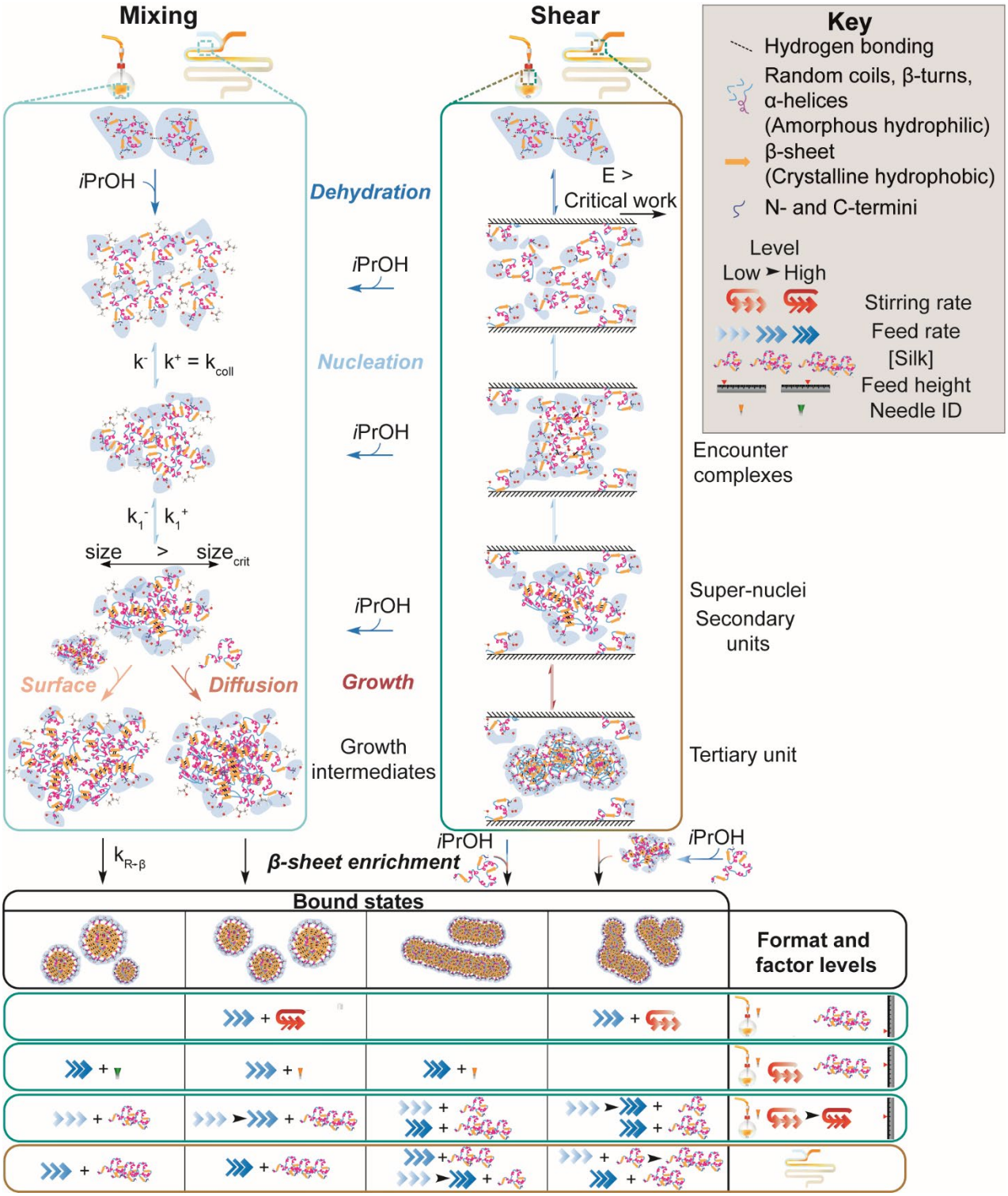

Figure 3.10. Schematic of protein-protein association and β-sheet assembly of silk fibroin *via* anti-solvent and shear-induced desolvation. The mechanism under shear flow is adapted from Dunderdale *et al.*[313] and Zhang *et al.*[342] Silk molecules, nanoparticles and stoichiometry of association are not drawn to scale.

In the micromixer and with 0.5% silk feeds, as the shear rate and mixing efficiency increased with flow rate from 0.001 to 1.0 mL min^{-1}, the assembly morphology shifted from amorphous aggregates to mixtures of rod-like and spherical particles. I speculate that the observation of rod-like morphologies only with 0.5% silk feeds was due to the low degrees of nucleation and long shear-induced and antisolvent-induced growth phases associated with insufficient surpassing of the nucleation energy barrier (Figure 3.7b). The size reduction in the nanoassemblies with increasing flow rate indicated that the enhancement of the antisolvent-induced nucleation rates dominated over the increase in shear-induced assembly rates.

The association and assembly processes were favored by an increase in the silk concentration from 0.5 to 2%,[342] which resulted in the formation of larger nanofibers and lamellar tertiary structures with a higher polydispersity index under homogenous nucleation at 0.001 mL min^{-1} (Figure 3.6b, Figure 3.7b). This effect indicated that the increase in the silk concentration still did not greatly exceed the nucleation barrier. The opposite trend was observed for semi-batch processes at low and high mixing times due to the higher saturation induced by larger initial antisolvent-to-silk ratios.

Following the increase in flow rate from 0.001 to 0.059 mL min^{-1} for 2% feeds, the reduction in the mixing time dominated over the increase in shear-induced nucleation and assembly (Figure 3.6b). The resulting particles showed spherical morphologies, although shear-induced assembly also resulted in the secondary assembly of nanoparticles into nanofibers. However, for 2% silk, further increases in the flow rate produced nanoparticles of increasing size due to secondary and tertiary growth processes that gave rise to amorphous and fiber-like assemblies. This trend was also observed for the low-mixing-time, semi-batch system, supporting the idea that the increase in the rates of shear-induced nucleation and growth in the microchannel dominated over the effect of reduced mixing time.

A silk concentration increase from 2 to 3%, under homogeneous nucleation at 0.001 mL min^{-1}, significantly reduced both the nanoparticle size and the polydispersity index due to an increase in supersaturation and the antisolvent-induced nucleation rates. Increasing the

silk concentration to 3% caused gradual increases in viscosity and rapid decreases in the surface tension.[344, 345] I speculate that these changes increased the water transport rate between the aqueous and isopropanol phases for 3% silk feeds, thereby providing less time for secondary self-assembly processes.

The extent of self-assembly for 3% silk feedstocks decreased as the flow rate increased from 0.001 to 1 mL min^{-1}, with reductions in nanoparticle size, polydispersity index and zeta potential, but particles were produced in greater yield. The lower degree of self-assembly with increasing flow rate was confirmed by the increase in particle curvature (Figure 3.7b) and the increase in α-helix and random coil content (Figure 3.9b). Increasing the silk feed concentration from 0.5 and 2% to 3% reduced the critical shear rate.[344] Consequently, at flow rates above 0.001 mL min^{-1} in the micromixer, the shear-induced nucleation rates for 3% silk were likely greater than those for 0.5 and 2% silk feeds. As the flow rate increased, the assembly growth phase period for 3% silk was shortened due to the higher shear-induced nucleation rates, combined with the increased rates of antisolvent-induced nucleation and kinetic locking of the micellar structure. The narrower growth phases compared to the lower silk concentrations were supported by the greater nanoparticle sphericities for 3% feeds. This trend was not observed with 3% silk for either the low-mixing-time or high-mixing-time semi-batch processes.

The dependence of particle morphology and properties on the flow rate through the microchannel was supported by previous demonstrations in the staggered herringbone micromixer.[174] The kinetic freezing of secondary building units observed with 3% silk at the 1 mL min^{-1} flow rate agreed with previous literature reports.[174, 179] Further, for 3% silk feeds, secondary and tertiary self-assembly were promoted by shear processing following an increase in the flow rate from 1 to 12 mL min^{-1} (shear rate 961499 s^{-1}), resulting in reduced particle curvature and increased overall size and polydispersity.[174] Consequently, a critical flow rate exists between 1 and 12 mL min^{-1} for 3% silk feeds, beyond which the increase in the antisolvent-induced nucleation rate is out-competed by the increase in the rate of shear-

induced assembly. This non-linear trend of self-assembly reflects the trend observed for 2% silk, but was shifted to higher flow rates due to the shortened growth phase occurring from greater supersaturation.

3.5 Conclusions

The flow properties of silk fibroin, which are fundamental to the natural role of the polymer as a polymorphic material, can be exploited in nanoprecipitation processes. Here, to control the morphology of silk nanoparticles, I utilized shear-induced nucleation of silk fibroin under flow in semi-batch and microfluidic formats. The morphology of the resulting silk assemblies varied with shear processing and silk precursor concentration in bulk mixing, although nanofiber and lamellar assemblies were formed as mixtures with spherical particles. Conversely, the high-shear, low-mixing-time conditions provided by the micromixer identifies this as a promising platform for tuning primary–tertiary silk self-assembly. Due to the sufficiently low mixing time, the silk concentration could be used as a controllable input factor for the formation of monodisperse, rod-like and spherical nanoassemblies suitable for use as nanomedicines. The information provided in this study delineates rational guidelines for the modulation of silk fibroin multiscale structures under shear and antisolvent-induced desolvation by varying the supersaturation, shear rate and mixing time.

Chapter 4: Volumetric Scalability of Microfluidic and Semi-Batch Silk Nanoprecipitation Methods

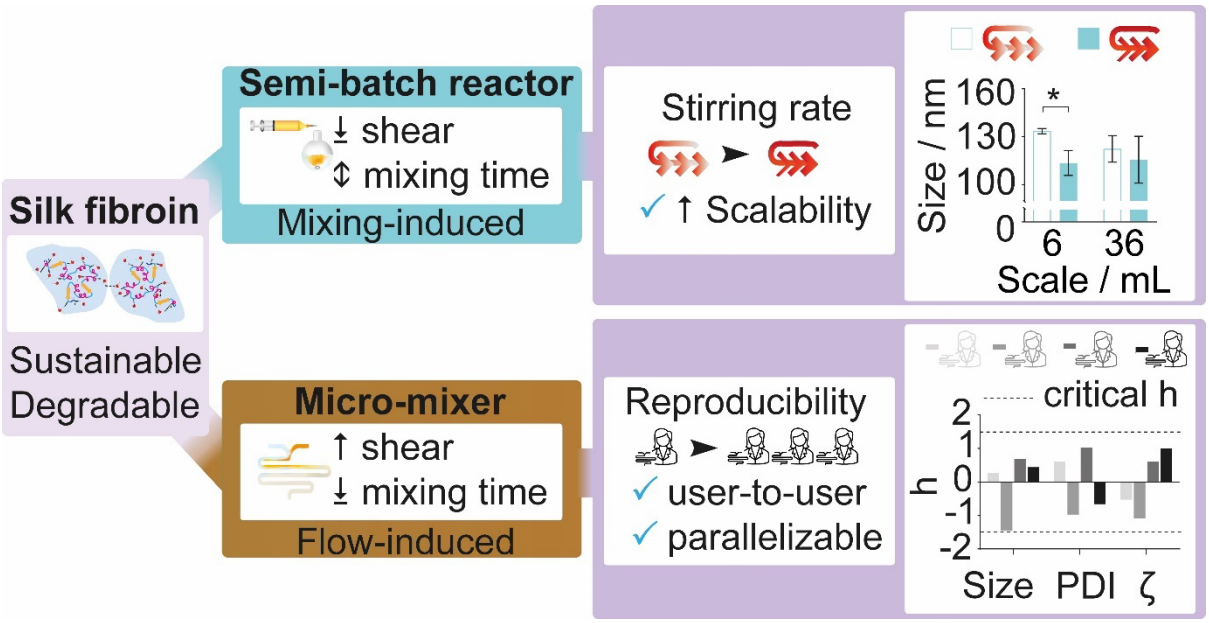

This chapter contains the results from the published article in MDPI Molecules (Matthew, S. A. L.; Rezwan, R.; Perrie, Y.; Seib, F. P. Volumetric scalability of microfluidic and semi-batch silk nanoprecipitation methods, *Molecules* **2022**, *27*, 2368. DOI: 10.3390/molecules27072368). For this work, I designed, analyzed and carried out all semi-batch experimental work and continuous work with the NanoAssemblr™ for the round robin test, as well as prepared the manuscript draft. For the round robin test, experimental work with the NanoAssemblr™ was also carried out by Refaya Rezwan, Jana Solomun and Thidarat Wongpinyochit.

4.1 Introduction

Achieving reproducibility of the critical quality attributes of nanoparticles, including the physicochemical properties, remains a significant challenge during the scale-up of nanomedicine production from the bench to the manufacturing sector.[310, 311, 346, 347] The physicochemical properties of nanoparticles affect many performance factors, including drug loading, stability on storage,[348] and *in vivo* performance.[349] Favorable attributes for drug carriers include nanoparticle sizes between 100 and 200 nm and a hydrophilic and negatively charged shell.[315]

One promising material for fabrication of nanoparticle drug carriers is reconstituted *Bombyx mori* silk fibroin, a polymer with a robust clinical track record and demonstrated biocompatibility *in vitro* and biodegradability *in vitro*.[184, 237, 291, 326] The block copolymer structure of silk fibroin, hereafter referred to as silk, allows it to assume multiple polymorphic states, ranging from the amorphous, water-soluble silk I state to the highly crystalline, insoluble silk II state.[326] In the silk I state, the primary self-assembly of the hydrated, extended silk molecules into kinetically locked nanoparticles can occur under shear-induced[342] or antisolvent-induced[153, 174, 179] desolvation. Both mechanisms involve the breakage of the intermolecular hydrogen bonds between water molecules and the hydrophilic blocks of the silk polymer.[342] The system can be stabilized by the reorganization of the biopolymer tertiary structure to establish hydrophobic interactions and β-sheet crystal structures within and between silk molecules.[342]

The micelle-like hydrophobic core and anionic hydrophilic shell structure[135, 154, 327] of *Bombyx mori* silk nanoparticles impart hemocompatibility *in vitro*[184] and enable post-synthetic, electrostatic drug loading.[153, 185, 220, 294] The polar amino acids, such as tyrosine, serine, histidine, and lysine, that are present on the nanoparticle surface are also amenable to covalent modification.[184] This has enabled the conjugation of cell-targeting agents (e.g., folate)[112] and the implementation of stealth technology, such as PEGylation,[159] to suppress

various clinically undesirable processes, such as agglomeration in physiological media,[184] blood platelet coagulation *in vitro*,[160, 184] and proinflammatory responses *in vitro*.[159, 184]

Silk nanoprecipitation in a semi-batch format is a simple, one-step procedure that involves the drop-by-drop addition of an aqueous silk solution, hereafter referred to as the silk precursor, into a water-miscible organic solvent.[153, 160, 185] The solvent must be present in at least 200% *v/v* excess and must be a poor solvent for at least one of the hydrophobic polymer blocks.[299, 331] The physicochemical properties of silk nanoparticles fabricated using semi-batch nanoprecipitation have shown a dependence on the concentration and average molecular weight of the silk[179, 312] and on the composition of the dissolved solute and antisolvent mixture.[153, 160, 185, 236, 290] Variations in the feed height and feed rate that can occur during the manual feeding of the silk precursor to the organic antisolvent has led to the adoption of semi-automated fluid handling systems to reduce the impact of these confounders.[350] For example, nanoparticles formed using the optimized formulation variables of a 5:1 *v*/*v* isopropanol:silk precursor,[153, 179] a constant flow rate of 1 mL $min^{-1,}$ and a constant feed height of 7.5 cm showed sizes (104–134 nm) and yields (9–23%) with narrow polydispersity indices (0.12–0.14) that depended on the stirring rate.[350]

The scale-up of manufacturing processes for *in vivo* clinical trials require changes in the production methodology by increasing the total volume of manufacture (volumetric scale-up) or by increasing the concentration of precursor (concentration scale-up).[347] Scale-up of fabrication techniques from the bench[298] can be further aided by computational simulations to establish appropriate flow and mixing regimes.[299, 300] However, changes in the critical process parameters, such as tank geometry and mixing time,[346] can lead to aberrant physicochemical characteristics of the nanoparticles and potentially inaccurate safety profiling.[310, 347] For example, in 2016, unreliable scale-up methods implemented with generic Doxil® formulations led to reduced drug efficacy.[310, 314] Investigating the reliability of silk nanoprecipitation outcomes across varying scales is, therefore, important to correct for changes occurring in the physicochemical properties during the transition from lab to pilot scales. However, the scalability of silk nanoprecipitation in a semi-batch format is poorly understood.

Continuous techniques have been developed and optimized[174, 179, 244] to increase the ease of volumetric scale-up.[310, 347] One effective approach includes microfluidic-assisted nanoprecipitation;[174, 179, 310] microfluidics has emerged within the last decade as an alternative bottom-up route for silk nanoparticle manufacture. Unlike batch and semi-batch processes, the addition of a silk precursor to the antisolvent is not a time-dependent process; therefore, increased control over the mixture composition is attained in the microfluidic mixing channel compared to bulk mixing. Additionally, the semi-batch processes are influenced by macro-, meso-, and micro-mixing times, whereas microfluidic-assisted nanoprecipitation is controlled only by the micro-mixing time. Common microfluidic devices used for nanoprecipitation operate under laminar flow, in which mixing occurs by diffusion across the fluid interface and mixing times are dictated by the channel dimensions.[351] To date, microfluidics has mostly been used to form silk water-in-oil emulsions. Silk emulsions of relatively high monodispersity can be achieved using flow-focusing droplet microfluidics (145–200 μm)[256] and single T-junction droplet nanofluidics (51–1500 nm).[244] However, the production throughput of silk water-in-oil microfluidics can be limited by the requirement for low total flow rates.

The staggered herringbone micromixer has been employed to address the need for high-throughput continuous manufacture of narrow polydispersity index nanoparticles (110–310 nm) by silk precursor desolvation.[174] The mixing efficiency of the aqueous silk precursor and antisolvent layers within the microchannel is high compared to conventional microfluidic designs[259, 352] and semi-batch bulk mixing[258] due to the chaotic advection caused by the presence of the 3D asymmetric bas-relief herringbone structures.[258] Use of this micromixer for nanoprecipitation showed that the physicochemical properties of the resulting nanoparticles depended on the silk molecular weight range,[179] organic antisolvent properties,[174] and the composition of the aqueous and organic mixture.[174] A flow ratio of 5:1 isopropanol to silk precursor and a total flow rate of 1 mL min^{-1} provided the optimal formulation and process parameters for nanoparticle manufacture at the lab scale in batch mode and resulted in spherical, colloidally stable nanoparticles with an average size of 110 nm, average polydispersity index of 0.14, and average zeta potential of −29.8 mV.[174] The volumetric scale-

up of production is achieved by increasing the microchannel diameters or by chip parallelization, although significant changes to the micromixer geometry and maximum flow rate limits can introduce scaling challenges. Consequently, investigating the scalability of the semi-batch manufacture of silk nanoparticles remains a topic of interest.

The aim of the present Chapter was to examine the impact of the volumetric scale-up of silk nanoprecipitation on nanoparticle critical quality attributes under semi-batch and microfluidic mixing regimes using optimized formulation and process parameters.[153, 174, 179] With the semi-batch format, I investigated the impact of the total volume of the silk precursor and antisolvent mixture (volumetric scale) on the critical quality attributes (e.g., particle size, polydispersity, zeta potential, stability, secondary structure, morphology, and yield) of the resulting silk nanoparticles. The effect of using similar mixing times and average shear rates of mixing on nanoparticle properties during scale-up were then assessed. I used the staggered herringbone micromixer in the benchtop NanoAssemblr™ platform, hereafter referred to as microfluidic format, as a scale-independent control and estimated the impact of chip parallelization on the physicochemical properties through a round robin test. To identify the bottlenecks in each format of clinical and industrial production, the throughput of both formats was estimated.

4.2 Materials and Methods

Unless otherwise stated, the studies were conducted at 18–22 °C using reagents and solvents (>98%) obtained from Acros Organics™ or Sigma Aldrich without further purification. Nanoparticle manufacture in the microfluidic format was performed in runs using the same solution of silk precursor (1 mL). Nanoparticle batches in the microfluidic format were defined as the combined product suspension from three runs using the same silk precursor solution. Independent experiments were performed in triplicate using three different silk precursor stock solutions.

4.2.1 Regeneration of *B. mori* Silk

B. mori cocoons were degummed by a 1 h treatment with sodium carbonate as detailed in Chapters 2 and 3. Silk cocoons were cut into approximately 5 × 5 mm segments, boiled for 1 h in 0.02 M aqueous Na_2CO_3 (2 L) at 98–105 °C with manual mixing, washed in ultrapure H_2O (1 L) three times for 0.33 h each and, dried at room temperature for at least 24 h.

Aqueous 25% *w/v* solutions of the silk precursor were regenerated by dissolution of the dry fibers in 9.3 M lithium bromide at 60 °C for 4 h. The silk solution was purified by dialysis (molecular weight cut off 3500 g mol^{-1}, Slide-A-Lyzer®, Thermo Scientific, Rockford, IL, USA) against ultrapure H_2O (1 L) for 48 h, and cleared by centrifugation four times, each for 0.33 h at 3000 × *g* and 5 °C (Jouan BR4i centrifuge equipped with S40 swing rotor). Gravimetry over 24 h at 60 °C was used to determine silk concentrations before adjusting to 3% *w/v* with ultrapure H_2O.

4.2.2 General Manufacture of Silk Nanoparticles in Semi-Batch Format

An aqueous solution of 3% *w/v* regenerated silk precursor was added drop by drop to isopropanol in a short-neck, round-bottom flask to achieve a total volumetric ratio of 1:5 (silk:isopropanol). The silk precursor was extruded through a BD PLASTIPACK™ syringe and blunt needle (0.33 × 6.35 mm) at a constant feed rate of 1 mL min^{-1} using a syringe pump (Harvard Apparatus 22, Holliston, MA, USA) at an inclination of 0–0.1° (Figure 4.1). Upon the complete addition of the silk precursor, the flask was stoppered and incubated at room temperature for no longer than 2 h. Then, the mixture was diluted with ultrapure H_2O in a polypropylene ultracentrifugation tube (43-mL capacity) and centrifuged at 48,400 × g at 4 °C for 2 h (Beckmann Coulter Avanti® J-E equipped with JA-20 rotor). The supernatant was aspirated and the pellet was resuspended in ultrapure H_2O (20 mL), sonicated twice for 30 s at 30% amplitude with a Sonoplus HD 2070 sonicator (ultrasonic homogenizer, Bandelin, Berlin, Germany), and ultrapure H_2O (23 mL) was added to the suspension. The centrifugation, washing, and resuspension steps were repeated three times, and the final pellet was suspended in ultrapure H_2O (2–3 mL) and stored at 4 °C until use.

The maximum shear rate of silk under flow was calculated as the wall shear rate, assuming Newtonian flow and using the literature value for dynamic viscosity (27 mPas)[301] of 3% regenerated aqueous silk precursor and the calculated density (1.02 g mL^{-1}) for the 3% *w/v* aqueous silk precursor solution (Table 4.1).[301]

Table 4.1. Estimated flow properties of the open semi-batch format and the microfluidic format.[a] Shear-induced and antisolvent-induced nucleation of silk were probable in microfluidic format and at a large volumetric scale in the semi-batch format.

Semi-Batch Format					Microfluidic Format	
Needle Internal Diameter / *mm*	**Flow Rate / *mL min^{-1}***	**Residence Time / *ms***	**Maximum Shear Rate / *s^{-1}***	**Re**	**Maximum Shear Rate / *s^{-1}***	**Re**
0.33	1.00	43	4724	2.4	80,114	40

a. The wall shear rate under laminar flow is reported assuming Newtonian flow. A simplified rectangular geometry was used for the micromixer by removing the groove depth. The linear velocity was used to calculate the residence times in the fluid line and the needle in the semi-batch system while the volumetric flow rate was used for the calculation of the micromixer residence time.

For simplicity, the needle and the 3-, 10-, and 50-mL syringes used in this study were approximated as straight cylinders using the internal diameters stated by the manufacturer (Table 4.2). The flow regime in the needle was estimated as laminar, based on the Reynolds number of 2, which was determined using the internal diameter of the needle (330 μm) (Table 4.1).[302] The upper limit of the residence time was calculated using the needle length and the linear velocity (1.94 mm s^{-1}).[303]

Table 4.2. Estimated flow characteristics of the syringes used in the open semi-batch system at a flow rate of 1.000 mL min^{-1} and volumetric flow rate of 1.67 × 10^{-8} m^3 s^{-1}.

Syringe / *mL*	Volume / *mL*	Residence time / *s*	Critical work / *10^{-3} Pa*	Maximum shear rate / *s^{-1}*	Average velocity / *10^{-5} m s^{-1}*	Cross-sectional area / *10^{-5} m^2*	R_e
3	1	18	33.2	0.261	28.3	5.89	0.093
	0.3	60	111				
10	3.65	219	18.3	0.0557	10.1	165	0.055
	6	360	30.1				
	7	420	35.2				
50	23	1380	2.96	0.00892	2.98	56.0	0.030

The stirred vessels were then characterized. The Reynolds number of the stirred vessel, estimated using cylindrical geometries of approximately 3066 to 2514 at the stirring rate of 400 rpm (Table 4.3), indicated the occurrence of turbulent flow within the vessel at 400 rpm. The power drawn by and the power per volume of the stir bar were calculated using an estimated power number for the stir bar. The power number of the stir bar was approximated by simplifying the geometry as a one-blade, flat-paddle impeller. The empirical correlation for the maximum power number in equation 4.1, as reported by Kamei and Hiraoka *et al*.,[353, 354] was then used in the fully baffled condition (as R_e > 200).

Maximum power number = 10(number of blades$^{0.7}$ × (blade height/blade diameter))$^{1.3}$ (**4.1**)

Table 4.3. Estimated flow characteristics of the reactors used in the open semi-batch system.

Volumetric Scale / *mL*	Volume / *mL*	R_e	Power per volume[d] / *W m^{-3}*	Average shear rate / *s^{-1}*	Energy dissipation / *W kg^{-1}*	Integrated shear factor / *s^{-1}*
6	5	3066 [a,c]	291	155,177	0.37	494[e]
						263[f]
	6	2514 [a,b]	242	113,442	0.29	494[e]
						263[f]
36	30	3066 [a,c]	48	25,863	0.06	329[e]
						132[f]
	36	2514 [a,b]	40	18,907	0.05	329[e]
						141[f]

a. Determined using the frequency of 42 rps, stir bar dimensions of 15 × 6 mm.
b. Determined using the dynamic viscosity (0.0032 kg ms^{-1}) and density (837 kg m^{-3}) of the 5:1 mixture of silk precursor: isopropanol.
c. Determined using the dynamic viscosity (0.0024 kg ms^{-1}) and density (785 kg m^{-3}) of isopropanol.
d. Calculated using the maximum power number of the stir bar (3.04) and power drawn (0.00145 W).
e. Determined using the reactor diameter for 6 mL scale (23 mm) and 36 mL scale (27 mm) at the top surface of the stir bar.
f. Determined using the reactor diameter for 6 mL scale (30 mm) and 36 mL scale (43–45 mm) at the isopropanol air-liquid interface.

The stir bar tip speed at 400 rpm was calculated as 1.97 ms^{-1}, using equation 4.2.[355]

Impeller tip speed = rotational speed × π × impeller diameter (**4.2**)

The integrated shear factors, using the reactor diameters at the top surface of the stir bar and at the air–liquid interface for the initial and end volumes at the 6- and 36-mL volumetric scales, were calculated using equation 4.3.[355]

Integrated shear factor = (2 × π × rotational speed × impeller diameter)/(reactor diameter – impeller diameter) (**4.3**)

The average shear rate (equation 4.4)[355] was calculated for the initial and end volumes at the 6 and 36 mL volumetric scales, using the dynamic viscosity of isopropanol and the 5:1 water:isopropanol mixture, respectively.[340]

$$\text{Average shear rate} = \sqrt{(\text{power}/(\text{dynamic viscosity} \times \text{volume}))} \quad (\mathbf{4.4})$$

The energy dissipation per unit mass (equation 4.5)[355] was calculated for the initial and end volumes at the 6 and 36 mL volumetric scales, using the density of isopropanol and the 5:1 water:isopropanol mixture, respectively.[340]

$$\text{Energy dissipation per unit mass} = \text{power}/(\text{density} \times \text{volume}) \quad (\mathbf{4.5})$$

4.2.3 Volumetric Scale-Up of Semi-Batch Silk Nanoparticle Manufacture

Silk nanoparticles were manufactured in 5 mL flasks at the 1.8 mL scale, in 10 mL flasks at the 6 mL scale, in 50 mL flasks at the 21.9, 36, and 42 mL scales, and in 150 mL flasks at the 138 mL scale. The silk precursor was added from a height of 7.5 cm, measured from the bottom of the isopropanol meniscus.

4.2.4 Dual Indicator System for Mixing Time in the Semi-Batch Format

The rotational speed of 400 rpm using an egg-shaped stir bar (15 mm × 6 mm) was investigated at the 5 mL initial antisolvent volume and an initial addition height of 7.5 cm. The rotational speed and the initial addition height at the 30-mL initial antisolvent volume were fixed at 400 rpm and 7.5 cm, respectively. Surface reflections were reduced by immersing the round-bottom flask in water within a clear acrylic box (10.3 cm × 10.3 cm × 5 cm). The flask was illuminated at a constant color temperature of 5600 K at 100% brightness by an LED panel (RALENO, Seattle, WA, USA) fixed to the back of the stirring plate.

The mixing time was measured using a dual indicator system for mixing time adapted from Melton *et al.*[332] and Weheliye *et al.*..[333, 334] Stock solutions of 0.095 mg mL^{-1} thymol blue and 0.135 mg mL^{-1} methyl red in ethanol were mixed and diluted to give a working solution of 4.3×10^{-3} mg mL^{-1} thymol blue and methyl red in 70% *v*/*v* ethanol/ultrapure H_2O. The working solution (5 or 30 mL) was acidified with 0.5 M HCl (0.5 mL L^{-1}), and the system was

equilibrated for at least 10 revolutions. An equal amount of NaOH (10.5 µL of 0.15 M NaOH for 5 mL aliquots and 10.5 µL of 0.71 M NaOH for 30 mL aliquots) was added to the mixture at a controlled feed location and height by attaching a 20-µL Eppendorf Research® plus pipette (Eppendorf, Hamburg, Germany) to a clamp stand. The mixing was recorded on an iPhone SE (Apple, Cupertino, CA, USA) reverse camera at a capture speed and resolution of 240 fps and 1080 p using FiLMiC Pro (FiLMiC Inc., Seattle, WA, USA), and images were extracted using Ffmpeg.[335] Each condition was repeated at least four times.

Custom MATLAB (Mathworks, Natick, MA, USA) scripts were used to apply rectangular masks of 18,000 pixels to the images and to calculate the standard deviation of the normalized green channel intensity according to the method of Rodriguez *et al*..[336] The standard deviation for the fully mixed solution was defined using the average of the final 10 images, and the time required to reach 95% of the fully mixed standard deviation was defined as the mixing time ($t_{95\%}$) (Figure 4.2, Table 4.4).

Table 4.4. Mixing characteristics of the semi-batch system with increasing total volume, measured using the DISMT method, and the estimated mixing properties in microfluidic format. As the volumetric scale increased in semi-batch format, the bulk mixing time increased while the micro-mixing time was unaffected by microfluidic chip parallelization.

Semi-Batch Format			Microfluidic Format	
Total Volume / mL	**Stirring Rate / rpm**	**Mixing Time / s**	**Residence Time / ms**	**Mixing Time / ms**
5	400	8.4 ± 4.4	120	21
30	400	29.4 ± 6.0		

4.2.5 Semi-Batch Droplet Analysis

4.2.5.1 Volume and Time of Flight

The average silk precursor droplet volume at the 1 mL min^{-1} flow rate was determined by capturing the number of droplets extruded over a total silk precursor volume of 1 mL using the image capture setup detailed above.

The flow rate within droplets extruded at the 1-mL min^{-1} flow rate and at feed heights of 0 and 7.5 cm was determined for at least three droplets of a 3% *w*/*v* silk precursor solution

with 0.3% *w*/*w* iron(III) oxide (a synthetic spherical particle with 99.995% < 325-mesh [~45 μm] size, >96.8% purity, 4.6 g cm^{-3} solid density, and 0.8–1.2 g cm^{-3} bulk density; Inoxia Ltd., Sweden). The droplets were imaged on an iPhone SE (Apple, Cupertino, CA, USA) reverse camera equipped with a 15× macro lens (Shenzhen Apexel Technology Co., Guangdong, Shenzhen, China) at a focal length of 1.5 cm and were illuminated at 5600 K color temperature and at 80% brightness by an LED panel (RALENO, Seattle, WA, USA) fixed behind the droplets. The droplets were recorded at a framerate of 240 fps and resolution of 1080 p using FiLMiC Pro (FiLMiC Inc., Seattle, WA, USA), and images were extracted using Ffmpeg.[335] Custom MATLAB (Mathworks, Natick, MA, USA) scripts were used for grayscale conversion, contrast-limited adaptive histogram equalization, and binary image conversion based on luminance. The particle velocities were then measured using manual tracking in ImageJ v1.52n (national Institutes of Health, Bethesda, MD, USA).

Droplet diameters were measured for at least three droplets imaged on a Photron FASTCAM SA 1.1 Model 675K M1 (Photron, San Diego, CA, US) at 3× magnification using a Photron FASTCAM Viewer (Photron, San Diego, CA, US). The Fickian diffusion length and time scales were calculated assuming a silk diffusion coefficient of 2.45 × 10^5 cm^2 s^{-1} (Table 4.5).[337]

Table 4.5. Droplet characteristics impacting flow and mixing-induced silk self-assembly at a dropping height of 7.5 cm and flow rate of 1.000 mL min^{-1}. ± SD, *n* = *3.*

Number of drops / mL^{-1}	Droplet volume / μL	Droplet diameter / *mm*	Diffusion length scale[a] / μm	Diffusion time scale[a] / *s*	Time of flight / *s*	Droplet velocity / $m\ s^{-1}$	Fluid velocity / $mm\ s^{-1}$
18 ± 1	56.6 ± 1.9	3.38 ± 0.10	40.1 ± 0.4	780 ± 48.0	0.110 ± 0.002	0.918 ± 0.020	26 ± 14

a. Determined using the droplet diameter, droplet time of flight and the silk diffusion coefficient of 2.45 × 10^5 cm^2 s^{-1}.[337]

4.2.6 Manufacture of Silk Nanoparticles in Microfluidic Format

Silk nanoprecipitation in microfluidic format was conducted using the NanoAssemblr™ benchtop instrument version 1.5 (model number NA-1.5-16; NanoAssemblr™, Precision

Nano-Systems Inc. Vancouver, BC, Canada) equipped with a cyclic olefin copolymer microfluidic cartridge (product codes: 1207 and 1151-034 Benchtop Cartridge), as described elsewhere.[174] The fluids were introduced to the 27-mm rectangular, Y-junction, staggered herringbone micromixer (79 μm × 200 μm) through two 25 mm inlet channels. The mixing channel contained a series of raised grooves (31 μm × 50 μm) and four switchback turns.[338] The isopropanol (5 mL) and 3% *w*/*v* aqueous silk precursor solution (1 mL) were introduced through the separate chamber inlets at a flow rate ratio of 5:1 and a total flow rate of 1 mL min^{-1}. The mother liquor suspension was incubated in sealed tubes for no longer than 2 h before centrifugation.

Between runs, the cartridge was cleaned with three water washes, followed by a prime. The wash procedure consisted of a 1:1-flow rate ratio of ultrapure H_2O/ultrapure H_2O (2 mL) at a total flow rate of 4 mL min^{-1}. The priming procedure used a flow rate ratio of 5:1 isopropanol/ultrapure H_2O, a total volume of 6 mL, and a total flow rate of 1 mL min^{-1}.

The optimum formulation and process parameters were used in a round robin test in the NanoAssemblr™ to estimate the repeatability and reproducibility upon parallelization. The dynamic light scattering (DLS), electrophoretic light scattering (ELS) (Zetasizer Nano-ZS Malvern Instrument, Worcestershire, UK), and yield results from four intra-laboratory participants and microfluidic chips and the β-sheet crystallinity from three participants and microfluidic chips were analyzed for consistency and precision according to ASTM E 69 (Table 4.6).[356] The mixing time was estimated at 21 ms, assuming Newtonian flow[301] and using the literature viscosity value (3.14 mPas) and density (0.837 g mL^{-1}) values for the 5:1 *v*/*v* isopropanol/water mixture measured at 20 °C.[339] The manufacturer's guidelines and an analytical model for a similar system published elsewhere[302] were used for the mixing time estimation by estimating the hydraulic diameter of the channel (142 μm) and the diffusion coefficient (3.5×10^{-10} m^2 s^{-1}) of the 5:1 isopropanol/water mixture[340] and calculating the Peclet number (4.27×10^{11}) to achieve a coefficient of variation of <0.1 (Table 4.4).[259]

Table 4.6. Participant and precision statistics of the round robin study.

Physicochemical property	$\bar{x}$	$s_{\bar{x}}$	s_r	s_R	r	R
Size / *nm*	109	4	17	6	13	17
PDI	0.11	0.02	0.02	0.03	0.06	0.09
Zeta Potential / *mV*	-32	2	3	4	5	11
Yield / %	14	2	3	4	2	4
Crystallinity / %	58	1	1	2	7	11

The flow was determined as laminar with a Reynolds number of 40. The residence time was calculated using the total fluidic volume and flow rate,[303] and complete mixing was indicated by a residence time greater than the mixing time (Table 4.4). For simplicity, the maximum shear rate was defined as the wall shear rate, with the assumption that chaotic advection created significantly lower shear in the channel and did not significantly alter the shear at the channel walls (Table 4.1). The geometry of a straight rectangular channel was used for the wall shear rate calculations, with the omission of groove depth.[341]

4.2.7 Yield of Silk Nanoparticles

The total mass and total volume of the produced silk nanoparticle suspension were recorded. A known volume of the suspension was then transferred to a pre-weighed microcentrifuge tube and the total mass was recorded. The suspension was frozen at −80 °C for 5 h, freeze-dried (Christ Epsilon 1-4, Martin Christ Gefriertrocknungsanlagen GmbH, Osterode, Germany) for 24 h at −10 °C and 0.14 mbar, and the dry mass was measured. The process was repeated in duplicate, and the average yield was calculated using equation 2.1. Freeze-dried samples were stored in a vacuum desiccator at 25 °C.

4.2.8 Physicochemical Characterization of the Silk Nanoparticles and Stability in Water

The silk nanoparticle sizes and polydispersity indexes were measured by DLS, and the zeta potentials were measured by ELS. Nanoparticle suspensions were prepared by vortexing for 20 s and sonicating twice at 30% amplitude for 30 s; measurements were made in triplicate in ultrapure H_2O at 25 °C with refractive indices of 1.33 and 1.60 used for H_2O and protein, respectively.

The silk nanoparticles from all studies were stored at 4 °C. The particle size and zeta potential of the silk nanoparticles generated in the open, semi-batch system and the NanoAssemblr™ were determined by DLS on days 0 to 42. The nanoparticles were prepared for measurement by vortexing for 20 s at $t > 0$ days.

4.2.9 Secondary Structure Measurements of Silk Nanoparticles

Fourier transform infrared spectroscopy (FTIR) on an ATR-equipped TENSOR II FTIR spectrometer (Bruker Optik GmbH, Ettlingen, Germany) was used to analyze the secondary structures of silk films, freeze-dried powders, and freeze-dried nanoparticles. Positive silk II controls consisted of autoclaved silk films and 70% *v*/*v* ethanol/ultrapure H_2O annealed silk films, whereas negative silk II controls consisted of air-dried silk films and freeze-dried silk powder. The air-dried silk films were drop-casted at a flow rate of 1 mL min^{-1} following extrusion from a height of 3.5 cm using varying silk precursor volumes (0.3–7 mL).

FTIR measurements were recorded in the absorption mode over 400 to 4000 cm^{-1} at 4-cm^{-1} resolution for 128 scans and then corrected for atmospheric absorption using Opus (Bruker Optik GmbH, Ettlingen, Germany). The second derivatives of the background-corrected FTIR absorption spectra were calculated in OriginLab 19b® (Northampton, MA, USA) and analyzed following an adapted literature protocol.[304] The second derivative was smoothed twice using a seven-point Savitzky–Golay function with a polynomial order of 2. A non-zero linear baseline was interpolated between 2–3 of the highest values in the amide I region (1600–1700 cm^{-1}). Second derivative peaks were identified in the amide I region and

fitted using non-linear least squares with a series of Gaussian curves. The peak area could take any value ≤ 0; and the position, width, and height of each peak were allowed to vary. The literature band assignments[155, 305, 357, 358] were applied to designate the relative area of each band to the relative secondary structure content.

The correlation coefficients (R) of the samples were determined according to an adapted literature protocol[306] using the air-dried silk film of an aqueous silk precursor batch as a reference. The second derivative of the absorption spectrum was calculated and smoothed twice with a five-point Savitzky–Golay function and a polynomial order of 2. The silk sample and reference were compared between 1600 and 1700 cm^{-1} according to equation 4.6.

$$R = \frac{\sum x_i y_i}{\sqrt{\sum x_i^2 \sum y_i^2}} \qquad (\mathbf{4.6})$$

where xi and yi are the derivative values of the reference and silk sample at the frequency i.

4.2.10 Thermal Analysis of Silk Nanoparticles

Freeze-dried silk nanoparticle samples (1.06–4.89 mg) were placed in aluminum pans and subjected to differential scanning calorimetry (DSC) and thermogravimetric analysis (TGA) from 20–350 °C at a scanning rate of 10 °C min^{-1} and a nitrogen flow of 50 mL min^{-1} (STA Jupiter 449, Netzsch, Gerätebau GmbH, Germany). Thermograms were analyzed using OriginLab 19b® (Northampton, MA, USA). According to previous descriptions,[307] the desorption enthalpy was normalized to the corrected mass.

4.2.11 Scanning Electron Microscopy of Silk Nanoparticles

A 1-mg mL^{-1} silk nanoparticle suspension (10–20 µL) was lyophilized at −10 °C and 0.14 mbar for 24 h on a silicon wafer and then sputter-coated with gold (15 nm) using a low vacuum sputter coater (Agar Scientific Ltd., Essex, UK, and ACE200, Leica Microsystems, Wetzlar, Germany). The wafer was imaged using an FE-SEM SU6600 instrument (Hitachi High Technologies, Krefeld, Germany) at 5 kV and 40-k magnification and the images were

processed using ImageJ v1.52n (National Institutes of Health, Bethesda, MD, USA), Adobe Lightroom, and Abode Illustrator (Adobe, San Jose, CA, USA).

4.2.12 Statistical Analyses

Data were analyzed using Microsoft® Excel® 2019 (Microsoft Office 365 ProPlus Software, Redmond, WA, USA), Minitab® (Minitab® Statistical Software, State College, PA, USA), and GraphPad Prism 8.2.1 (GraphPad Software, La Jolla, CA, USA), and normality of the data distributions was assumed. Two groups and multiple groups were analyzed for equivalence of variance with the F-test and Bartlett's test. Two groups were analyzed using the independent *t*-test, with Welch's correction applied in cases of unequal variance. Multiple groups were assessed either by one-way analysis of variance (ANOVA), followed by Tukey's pairwise multiple comparison post hoc test, or by the Brown–Forsythe and Welch ANOVA tests, followed by the Dunnett T3 pairwise multiple comparison post hoc test. Silk nanoparticle stability was evaluated by ANOVA, followed by Dunnett's or the Dunnett T3 post hoc test, to compare between $t = 0$ day control and $t > 0$ day samples. Statistical significance was identified using post hoc tests and defined as follows: * $p < 0.05$, ** $p < 0.01$, *** $p < 0.001$, and **** $p < 0.0001$. The number of experimental repeats (n) are shown in each figure legend and the data are displayed as the mean ± standard deviation.

4.3 Results

4.3.1 Silk Nanoparticle Physicochemical Characterization

4.3.2 Volumetric Scale-up in Semi-Batch Format

In the semi-batch open system (Figure 4.1 and Figure 4.2), the impact of the volumetric scale of nanoprecipitation on the physicochemical properties of silk nanoparticles was determined in the presence or absence of stirring.

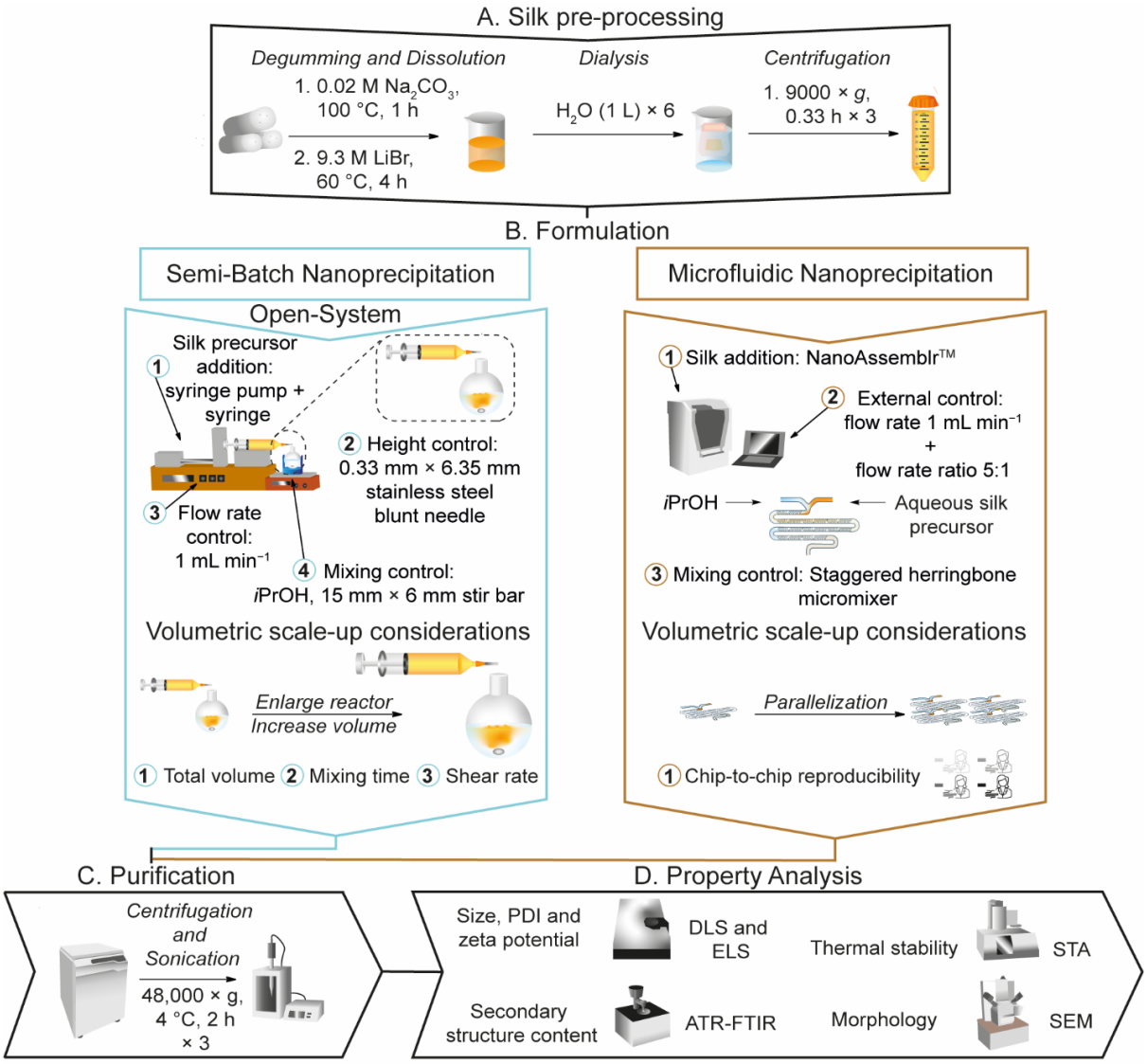

Figure 4.1. The nanoprecipitation workflow for the manufacture of silk nanoparticles in semi-batch and microfluidic formats by antisolvent-induced desolvation in isopropanol and the volumetric scale-up considerations explored in this study. The formulation process consisted of four steps in semi-batch format: (1) preparation of an aqueous silk precursor solution in a syringe equipped with a blunt needle, ensuring the silk precursor is free of bubbles; (2) fixing the needle to standardize the feed position of the silk precursor; (3) addition of the silk precursor to the antisolvent at a fixed flow rate; and (4) control of the stirring rate and mixing time during addition of the silk precursor to the antisolvent. The formulation process consisted of three steps in microfluidic format: (1) preparation of aqueous silk precursor solution and antisolvent syringes, ensuring the syringes are free of bubbles for loading into a NanoAssemblr™ microfluidic chip; (2) remote control of the flow rate ratio of isopropanol:silk precursor; and (3) remote control of the mixing time *via* the total flow rate.

To aid the translation from lab- to pilot-scale equipment, the flow properties of the semi-batch system were first characterized (Figure 4.2, Table 4.2, Table 4.3, Table 4.4 and, Table

4.5). The silk molecules within the free-falling droplets were mixed mainly by convection, due to the high fluid velocities compared to the diffusion coefficient (Figure 4.2a, Table 4.5).

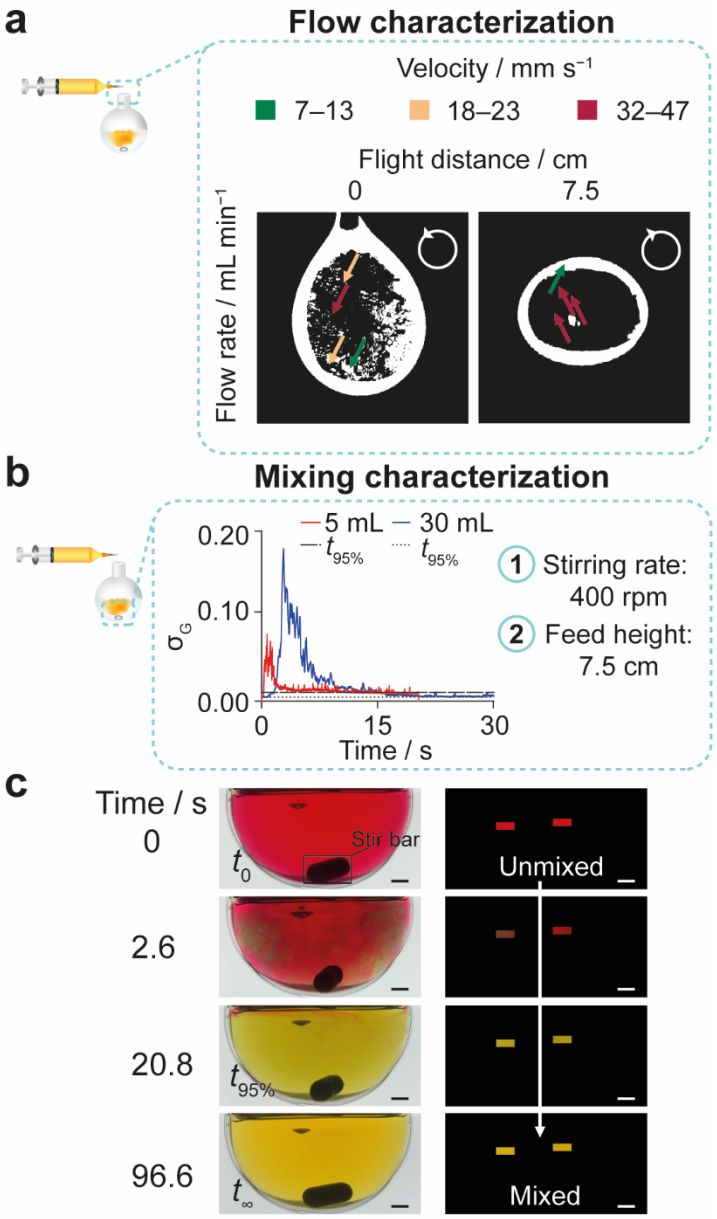

Figure 4.2. Exemplary characterization of the silk precursor droplet flow rate and the bulk mixing time in the open semi-batch system. (a) The droplets of silk precursor, spiked with iron oxide nanoparticles, showed circulatory flow when extruded from the 0.33-mm blunt needle at a flow rate of 1 mL min^{-1}. The processed binary images showed the circulatory flow field of silk precursor droplets at free-fall heights of 0 and 7.5 cm. Insets show the direction of flow in two dimensions. **(b)** The mixing time increased as the volume of antisolvent increased and was measured using the color change of a mixture of 4.3 × 10^{-3} mg L^{-1} methyl red and 4.3 × 10^{-3} mg L^{-1} thymol blue from acidic pH (red) to neutral pH (yellow). The variation in the standard deviation of the normalized green channel (σ_G) across the lower limits of the 6- and 36-mL volumetric scales in the open semi-batch system. **(c)** The raw and processed images showing the red to yellow color change observed using the DISMT method at the stirring rate of 400 rpm, feed height of 7.5 cm, and initial antisolvent volume of 30 mL. Scale bars = 5 mm.

The mixing time and shear parameters of the reactors for the semi-batch system were then characterized. The bulk mixing time of the reactors at the 6-mL and 36-mL volumetric scales were estimated using an adapted dual indicator system for the mixing time method[332-334] at the initial antisolvent volumes of 5 and 30 mL, respectively. As the mixing times for the unstirred semi-batch reactors were greater than 120 s, the reactors were also stirred at 400 rpm during the addition of the silk precursor. The similarity of the mixing times at the volumetric scales of 6 (8.4 s) and 36 mL (29.4 s) was increased by stirring at 400 rpm (Table 4.4, Figure 4.2b). The shear parameters, including the power per volume, integrated shear factor, and energy dissipation, associated with stirring at 400 rpm were estimated to describe the speed of mixing for comparison with other reactor geometries and impeller types (Table 4.3). Although the estimated impeller tip speed of 1.97 ms^{-1} at the 400 rpm stirring rate did not change, the average shear rates decreased from 113,442–155,177 s^{-1} to 18,907–25,863 s^{-1} as the volumetric scale increased from 6 to 36 mL (Table 4.3).

In the absence of stirring, an increase in volumetric scale from 1.8 to 21.9 mL significantly decreased the silk nanoparticle size from 149 nm to 116 nm (Figure 4.3a). No further reduction in size occurred with further increases in the volumetric scale from 21.9 to 138 mL. The zeta potential significantly decreased from −31 to −39 mV as the scale increased from 6 to 138 mL (Figure 4.3a). However, the polydispersity index (0.09–0.16), yield (18–49%), and spherical morphology were not significantly affected by volumetric scale changes (Figure 4.3a–c). Increasing the stirring rate from 0 to 400 rpm at the 6-mL scale significantly reduced the nanoparticle size from 134 nm to 114 nm and the yield from 23% to 9% (Figure 4.3d). In contrast to the 6-mL scale result, stirring had no similar impact when the volumetric scale was increased to 36 mL (Figure 4.3d).

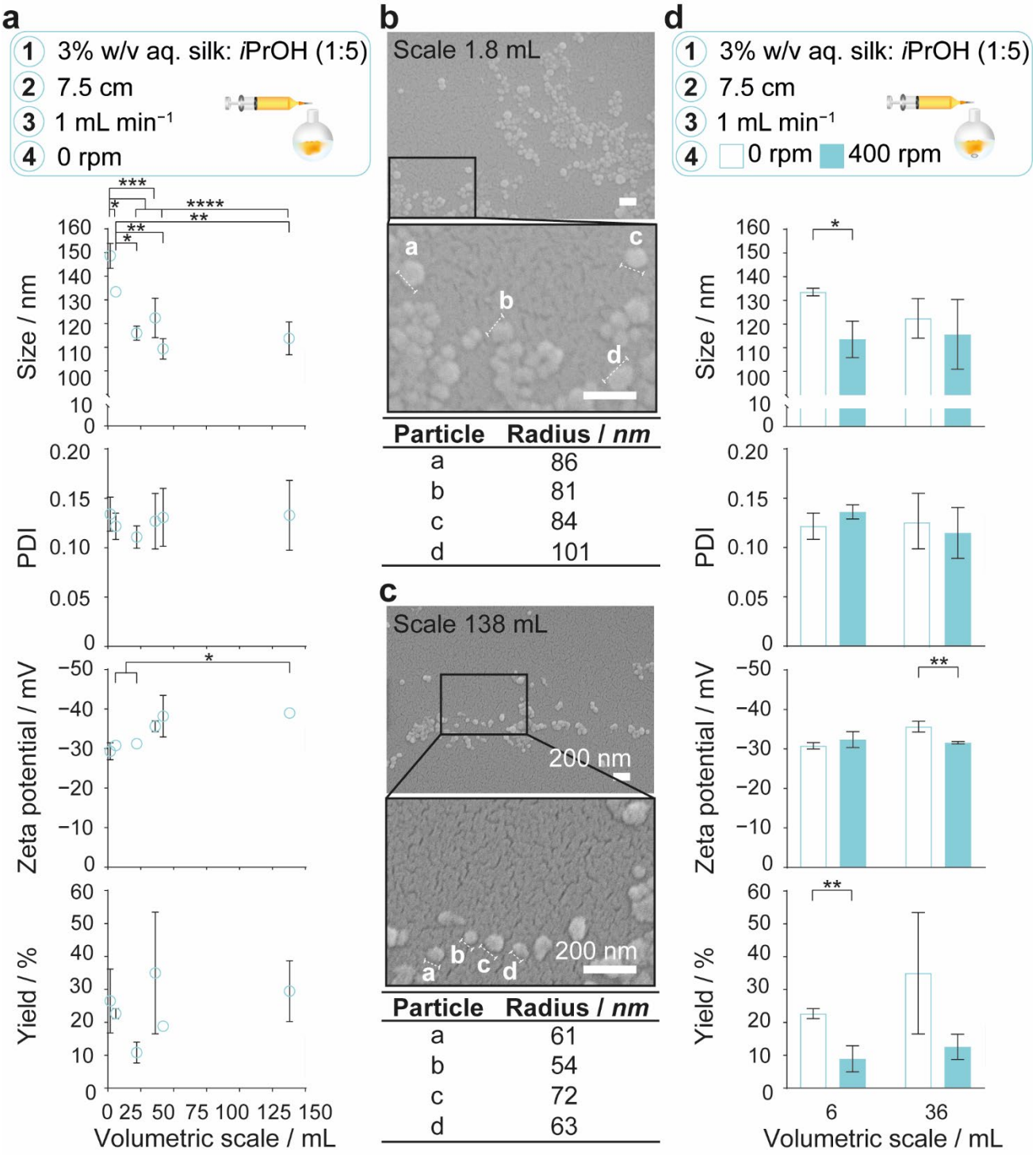

Figure 4.3. The impact of semi-batch volumetric scale on physicochemical properties and yield of silk nanoparticles. (a) Increasing the volumetric scale of silk desolvation in semi-batch format without stirring decreased the nanoparticle size and significantly increased the zeta potential. Multiple groups were evaluated by one-way ANOVA, followed by Tukey's multiple comparison post hoc test. Scanning electron microscopy of the spherical nanoparticles manufactured at **(b)** 1.8-mL and **(c)** 138-mL scales. **(d)** Impact of the stirring rate and volumetric scale on nanoparticle size and yield. Two groups were evaluated by Student's *t*-test. Data obtained from semi-batch manufacture at 6-mL scale and at 36-mL scale at the stirring rate of 400 rpm were detailed in Chapter 2 and were included to simplify the comparison. Error bars are hidden in the plot symbols when not visible, ± SD, *n* = 3. Asterisks

denote statistical significance determined using post hoc tests as follows: * $p < 0.05$, ** $p < 0.01$, *** $p < 0.001$, and **** $p < 0.0001$. Scale bars = 200 nm.

4.3.3 Volumetric Scale-Up by Parallelization in Microfluidic Format

Unlike the semi-batch format, nanoprecipitation using the microfluidic format can be run at increasing volumetric scales by parallelizing the microfluidic chips without changing their internal dimensions. Therefore, the microfluidic format provided a volumetric scale-independent process. For this reason, I used the optimum formulation and process parameters in a round robin test at the 6-mL total volume of silk precursor and antisolvent (volumetric scale) to estimate the operating boundaries upon parallelization. Four participants, each equipped with a distinct microfluidic chip, were employed in the study and each participant repeated manufacture a minimum of three times using three silk precursors. The average of each nanoparticle property obtained in the microfluidic format was estimated using the grand average of all participants and gave an average nanoparticle size of 109 nm, polydispersity index of 0.11, zeta potential of −32 mV, and yield of 14% (Figure 4.4).

The between-participant and within-participant consistencies were characterized by the h and k statistics, respectively (Figure 4.4f–g). The h statistic is defined as the ratio of the difference between one participant's average from the grand average to the standard deviation of the differences observed for all participants. The k statistic is defined as the ratio of the standard deviation for the average of one participant to the pooled standard deviation of all participants. Therefore, the h statistic indicates how comparable the averages from each participant are. Similarly, the k statistic indicates how comparable the standard deviation of the averages from each participant are. Participants that give greater variability than that of all participants are shown when the k value exceeds 1. The upper critical h and k statistics were calculated to identify outliers, by indicating whether the averages and standard deviations of each participant were sufficiently different from the others. The critical h statistic is predefined by the number of participants and replicates in the study and was calculated using equations

derived from an unpaired *t*-test at the 0.5% significance level. The critical k statistic is also predefined by the number of participants and replicates in the study and was calculated using the *F* distribution at the 0.5% significance level. No outliers were observed for the physicochemical properties, yield, or crystallinity measurements, as the data did not exceed the critical h and k values (Figure 4.4f–g).

The probable differences between nanoprecipitation results for one operator using one microfluidic chip were estimated using the 95% limit of the repeatability precision statistic. This precision statistic was calculated using the pooled standard deviation of all participants and provides a guideline for expected differences between replicates at the 95% probability level. Similarly, the 95% limit of the reproducibility precision statistic was calculated as a guideline for the differences expected to occur, with 95% probability, between nanoprecipitation results obtained using multiple microfluidic chips and operators. This precision statistic was calculated using the sum of the pooled standard deviation of all participants (within-participant component) and a between-participant standard deviation. The between-participant standard deviation was calculated using the standard deviation of the differences observed between the averages of the participants and the grand average, while accounting for the pooled standard deviation of all participants.

The 95% repeatability precision limits of nanoparticle properties indicated that, for one microfluidic chip and operator, the maximum absolute differences in nanoparticle size, polydispersity index, zeta potential, and yield of 13 nm, 0.06, 5 mV, and 7%, respectively, between multiple nanoprecipitation replicates would be expected to occur with a 95% probability (Table 4.6). Expectedly, the 95% reproducibility precision limits for multiple operators and microfluidic chips were greater than the 95% repeatability limits for one operator and microfluidic chip. The 95% reproducibility limits indicated that the maximum absolute differences of 17 nm, 0.09, 11 mV, and 11%, respectively, would be expected to occur with a 95% probability between multiple nanoprecipitation repeats using different microfluidic chips (Table 4.6).

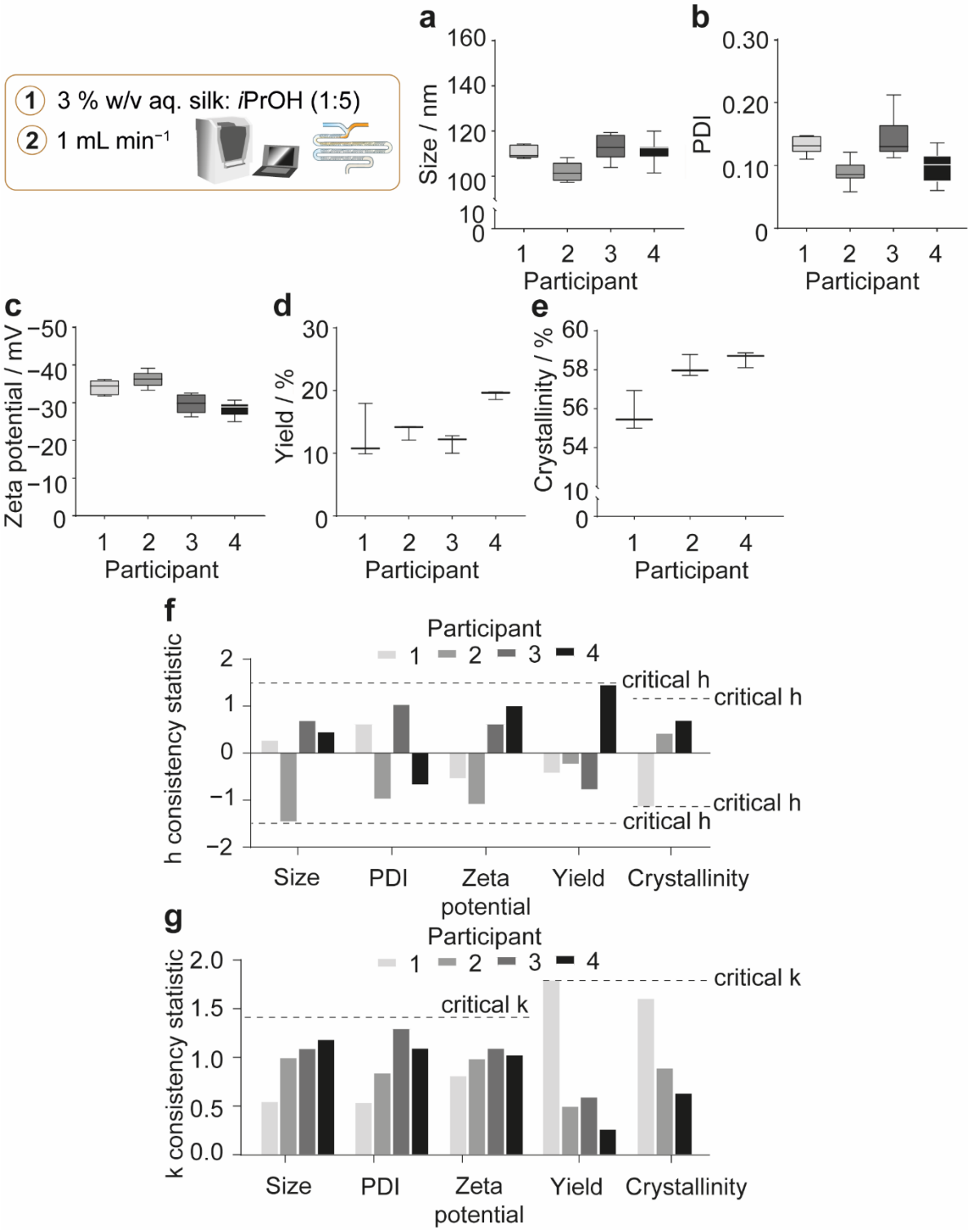

Figure 4.4. Variation observed in physicochemical properties and yield of silk nanoparticles manufactured in the NanoAssemblr™ as part of a round robin study. (a) Hydrodynamic diameter, (b) polydispersity index (PDI), **(c)** zeta potential, **(d)** yield, and **(e)** β-sheet crystallinity of silk nanoparticles. **(f)** The h and **(g)** k consistency statistics of nanoparticles manufactured using four participants for all properties except for crystallinity, which were calculated using the data from three participants. Participants 2 and 4 produced four nanoparticle batches for DLS and ELS studies, and participants 1 and 3 produced three nanoparticle batches. Yield and crystallinity were analyzed across three nanoparticle batches

for all participants. Data from participant 2 was detailed in Chapter 3. Data from participants 3[174] and 4[179] were published previously.

4.3.4 Secondary Structure Measurement

Deconvolution of the attenuated total reflectance-FTIR (ATR-FTIR) spectra in the amide I region (1600–1700 cm^{-1}) was used to assess the secondary structure content of silk nanoparticles formulated at different volumetric scales. As the critical shear rate of the 3% regenerated silk precursor[344] was exceeded in the semi-batch feed needle (Table 4.1), the impact of the volume of silk precursor extruded through the feed needle on shear-induced assembly was also assessed. In conjunction with spectral deconvolution, the spectral correlation coefficient method[306] was employed to estimate the overall change in the silk secondary structure incurred by the treatment of the silk precursor into processed silk samples, such as silk nanoparticles. The correlation coefficient calculation directly compared the spectra of processed silk samples against a reference silk II negative control (air-dried silk film), which was used in this study as a model for the silk precursor. Therefore, the correlation coefficient I indicates the similarity between the secondary structure content of processed samples and the silk precursor, where the correlation coefficient value of 1 is the maximum similarity that can be achieved. For example, the correlation coefficients of the silk II negative controls, the air-dried films (0.92–1.0), and the freeze-dried powders (0.95) demonstrated high similarity to the silk precursor (Figure 4.5). Conversely, the correlation coefficients of the silk II positive controls, the 70% *v*/*v* ethanol/ultrapure H_2O annealed silk films (0.18), and the autoclaved silk films (0.10) demonstrated low similarity to the silk precursor (Figure 4.5a). Correlation coefficient values that lay between the boundaries of the silk II negative and silk II positive controls would be expected to exhibit an intermediate secondary structure content.

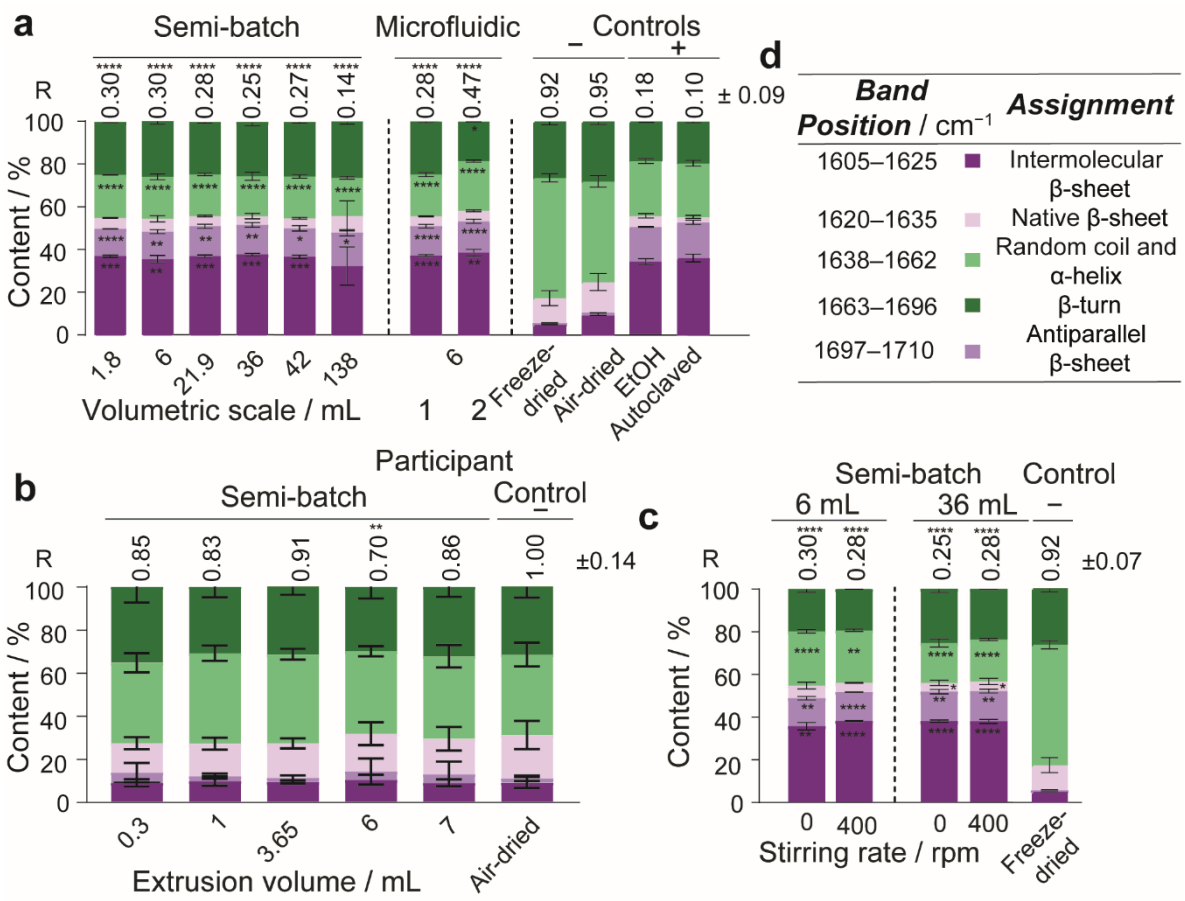

Figure 4.5. The total β-sheet content of silk nanoparticles did not vary significantly with volumetric scale when prepared by semi-batch format. FTIR secondary structure content (%) of (a) silk nanoparticles manufactured using different volumetric scales and formats of manufacture, (b) silk precursor extruded from the semi-batch open system feed needles, (c) silk nanoparticles manufactured using different volumetric scales and stirring rates, and (d) key for FTIR band assignments. The relative area of the assigned peaks in the second derivative spectrum were used to calculate the secondary structure content (%). The positive silk II controls were defined as the 70% *v*/*v* ethanol/ultrapure H_2O annealed and the autoclaved silk films. The negative silk II controls were defined as the air-dried silk film and freeze-dried silk powder. The negative silk II control (air-dried film) was defined as the reference for the spectral correlation coefficients of all sample types. For nanoparticles manufactured at different volumetric scales, the total β-sheet, β-turn, α-helix, and random coil contents and the correlation coefficients were evaluated using the one-way ANOVA tests against the negative silk II control (freeze-dried powder) followed by the Dunnett T3 multiple comparison post hoc test. For the microfluidic format, the nanoparticle correlation coefficients, total β-sheet, β-turn, α-helix, random coil, and anti-parallel β-sheet contents were evaluated by one-way ANOVA against the negative silk II control (freeze-dried powder) followed by Dunnett's multiple comparison post hoc test. For nanoparticles manufactured at a 6-mL scale with and without stirring, the correlation coefficients, total β-sheet, and β-turn values were evaluated by one-way ANOVA against the negative silk II control (freeze-dried powder) followed by Dunnett's multiple comparison post hoc test. For nanoparticles manufactured at a 36-mL scale with and without stirring, the correlation coefficients, α-helix, and random coil contents and β-turn and native β-sheet values were evaluated by one-way ANOVA against the negative silk II control (freeze-dried powder) followed by Dunnett's multiple comparison post hoc test. The remaining contents were evaluated using the Brown–Forsythe and Welch ANOVA tests. Data (±SD, n = 3) obtained from semi-batch manufacture at the 6-mL scale, the stirred 36-mL scale and the silk II controls were detailed in Chapter 2.

Data (±SD, n = 3) from participant 2 in the microfluidic format were detailed in Chapter 3. Multiple groups of a silk precursor extruded with varying volume (±SD, n = 9) were evaluated by the Brown–Forsythe and Welch ANOVA against the negative silk II control (air-dried film) followed by the Dunnett T3 multiple comparison post hoc test. Asterisks denote statistical significance determined using post hoc tests as follows: * $p < 0.05$, ** $p < 0.01$, *** $p < 0.001$, and **** $p < 0.0001$.

In the open semi-batch system, the silk nanoparticle β-sheet content ranged from 54–56% (Figure 4.5a). The crystallinity of nanoparticles manufactured at all volumetric scales in the semi-batch format compared well with those obtained using microfluidic nanoprecipitation. For example, in the microfluidic format, the grand average crystallinity of three participants was 58%, with 95% repeatability and reproducibility precision limits of 7% and 11%, respectively (Figure 4.4e,Table 4.6). The nanoparticle total β-sheet crystallinity did not depend on the volumetric scale of semi-batch nanoprecipitation (Figure 4.5a) and the silk precursor volume did not cause any general variation in the β-sheet content of liquid silk extruded from the feed needle, which ranged from 26–32% (Figure 4.5b). Additionally, the correlation coefficients, which ranged from 0.70–0.86, did not vary with the extruded silk precursor volume and reinforced the low β-sheet content measured using spectral deconvolution (Figure 4.5b). Similarly, the silk nanoparticle correlation coefficient did not significantly change for nanoparticles produced at the 1.8- to 138-mL volumetric scale and ranged between 0.14–0.30 (Figure 4.5a). The correlation coefficients at all volumetric scales compared favorably with the correlation coefficients of 0.28–0.47 obtained using the microfluidic format and provided further evidence of high β-sheet crystallinity. Nevertheless, the anti-parallel β-sheet content increased (13–16%) significantly and the intermolecular β-sheet content decreased (37–33%) significantly from the 1.8-mL to 138-mL volumetric scale. Finally, increasing the stirring rate from 0 to 400 rpm at both volumetric scales of 6 and 36 mL did not significantly affect the nanoparticle β-sheet content or the correlation coefficients (Figure 4.5c). The nanoparticle secondary structure did not significantly change with the stirring rate at the 36-mL scale. However, by increasing the stirring rate from 0 to 400 rpm at the 6-mL scale, the intermolecular

β-sheet (36% to 38%) and anti-parallel β-sheet (13% to 14%) contents increased while the α-helix and random coil content (20% to 19%) decreased.

4.3.5 Thermal Analysis

Table 4.7 and Figure 4.6 show the first-cycle simultaneous thermal analysis results for the silk nanoparticles manufactured in the open semi-batch system at volumetric scales between 1.8 and 138 mL in the microfluidic format and for the negative silk II controls (freeze-dried powder). The TGA of the residual water contents and the thermal stabilities of the silk nanoparticles showed a loss of adsorbed and strongly bound water between 20 and 140 °C and silk decomposition above 170 °C. Nanoparticles manufactured at volumetric scales between 6 and 138 mL had a significantly higher water content than the negative silk II control (freeze-dried powder) (5.8% (*w*/*w*)), ranging between 10.2% and 13.0% (*w*/*w*). The nanoparticle water content decreased significantly as the volumetric scale increased. Conversely, in the microfluidic format, the 5.2% (*w*/*w*) water content was not significantly different than that of freeze-dried silk. The onset decomposition temperature of the silk nanoparticles manufactured in semi-batch format ranged between 271.5 °C and 278.1 °C and were significantly higher than that of the negative silk II control (freeze-dried powder) (261.4 °C). Similarly, the onset decomposition temperature was significantly higher (271.2 °C) for the nanoparticles produced using the microfluidic format than for the silk II control (freeze-dried powder). This result confirmed the higher content of crystalline β-sheet structures in the silk nanoparticles compared to the negative silk II control. Finally, the nanoparticle decomposition temperatures from the semi-batch (293.1–299.6 °C) and microfluidic (293.4 °C) formats were significantly higher than for the negative silk II control.

Table 4.7. First-cycle thermal properties of silk nanoparticles produced by varying volumetric scale.

	Thermal Property	Semi-Batch						Microfluidic	Negative Silk II Control
		Volumetric Scale / *mL*							
		1.8 [1]	6	21.9	36	42	138	6	Freeze-dried Powder
DSC	T_g / °C	-	59.3 ± 0.01	57.9 [a]	58.6 ± 1.0 [b]	-	-	71.6 [a]	47.7 ± 0.5
	T_d / °C	35.7	39.1 ± 5.3	54.2 ± 15.9	43.5 ± 13.5	66.2 ± 2.8	67.5 ± 4.2	59.9 ± 0.3	60.7 ± 8.8
	ΔH_d / J g^{-1}	−267.7	−207.8 ± 98.0	−197.5 ± 4.6	−197.5 ± 30.1	−211.8 ± 15.8	−191.9 ± 8.9	−191.8 ± 0.9	−276.9 ± 4.21
	T_g' / °C	-	-	-	-	-	-	-	184.5 ± 0.7
	T_c / °C	-	-	-	-	-	-	-	241.0 ± 0.8
	ΔH_c / J g^{-1}	-	-	-	-	-	-	-	9.9 ± 2.3
	T_o / °C	274.1	274.0 ± 0.3	273.4 ± 0.6	267.4 ± 1.7	267.8 ± 0.8	265.7 ± 1.5	264.4 ± 0.1	-
	T_{dec} / °C	290.4	289.5 ± 0.5	289.5 ± 0.3	284.7 ± 0.4	284.9 ± 0.5	284.0 ± 1.0	282.1 ± 0.4	274.9 ± 1.1 [a]
TGA	Water content / % (w/w)	23.8	13.0 ± 1.7	11.7 ± 0.8	11.2 ± 0.7	10.7 ± 0.7	10.2 ± 0.6	5.2 ± 0.5	5.8 ± 0.8
	T_o / °C	278.8	277.3 ± 0.2	278.1 ± 1.0	272.3 ± 0.1	273.2 ± 0.6	271.5 ± 0.9	271.2 ± 0.5	198.5 ± 2.2
	T_o' / °C	-	-	-	-	-	-	-	261.4 ± 2.0
	T_{dec} / °C	289.7	299.6 ± 6.6	293.1 ± 4.1	299.0 ± 10.3	297.7 ± 5.5	298.1 ± 11.3	293.4 ± 5.8	222.3 ± 13.3
	T_{dec}' / °C	-	-	-	-	-	-	-	275.0 ± 2.7

a. n = 1
b. n = 2.

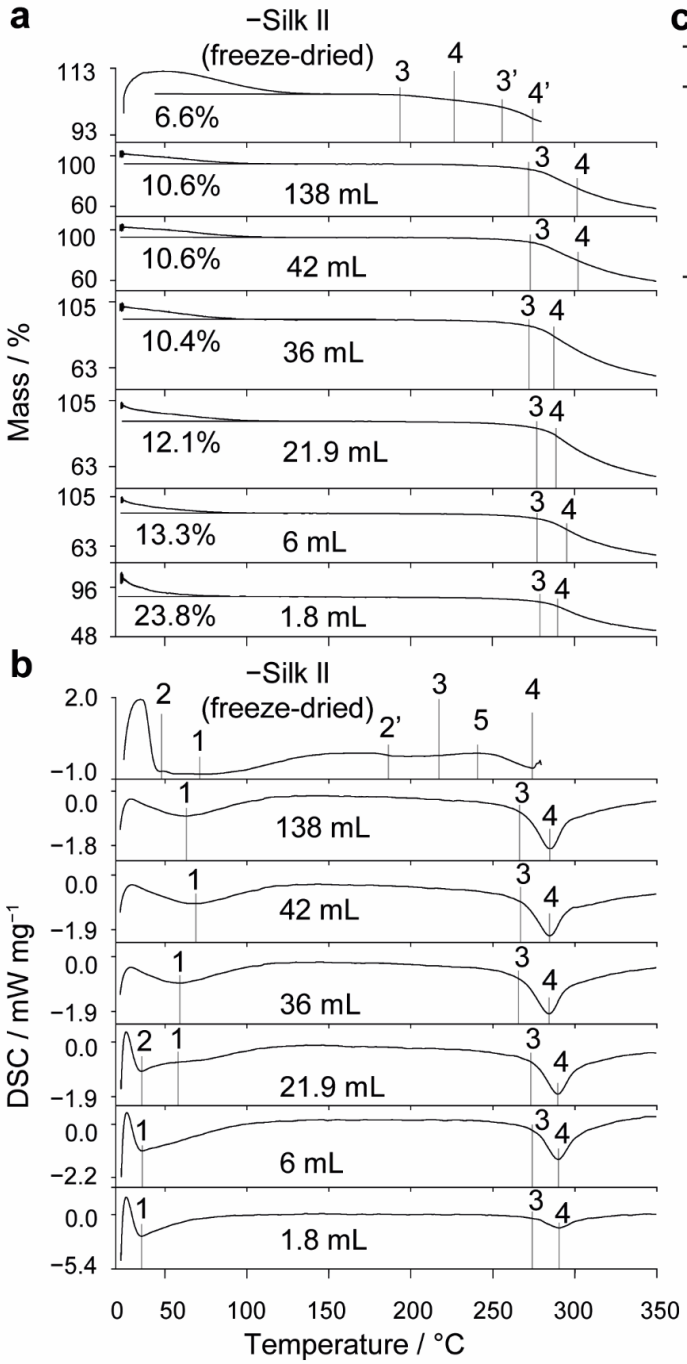

Figure 4.6. Representative first-cycle raw (a) TGA and (b) DSC thermograms of silk nanoparticles manufactured in open semi-batch format at different volumetric scales. (c) Thermal event assignment key. Water content (% (*w*/*w*)), dehydration temperature (T_d), glass transition temperatures (T_g), extrapolated onset temperature of crystallization and decomposition (T_o), crystallization temperature (T_c), and decomposition temperatures (T_{dec}) are reported. The data shown for the negative silk II control (freeze-dried powder) were detailed in Chapter 2.

The secondary structure and thermal stability of the silk nanoparticles were also evaluated by differential scanning calorimetry (Figure 4.6). The temperature of desorption (39.1–67.5 °C) of nanoparticles in the semi-batch format did not vary with volumetric scale. Additionally, the desorption enthalpy (−197.5 to −207.8 J g^{-1}) required to remove the adsorbed water did not vary significantly from the negative silk II control between 6- and 42-mL volumetric scales but was significantly reduced at the 138-mL scale (−191.9 J g^{-1}). For the microfluidic format, while the temperature of desorption (59.9 °C) did not differ from the negative silk II control (freeze-dried powder), the desorption enthalpy (−191.8 J g^{-1}) for the silk nanoparticles was significantly lower. An increase in the volumetric scale had no effect on the nanoparticle onset decomposition temperatures, which ranged from 274.0–265.7 °C and were comparable to that of the negative silk II control (freeze-dried powder). The onset decomposition temperature (264.4 °C) of silk nanoparticles from the microfluidic manufacture was also similar to the negative silk II control (freeze-dried powder). The decomposition temperatures (284.0–289.5 °C) were significantly higher than the negative silk II control (freeze-dried powder) and did not significantly change with an increasing volumetric scale. Likewise, the decomposition temperature was significantly higher for the nanoparticles produced using the microfluidic format (282.1 °C) than for the negative silk II control (freeze-dried powder). Finally, increasing the stirring rate from 0 to 400 rpm at the volumetric scale of 6 mL did not significantly impact the nanoparticle water content or thermal stability (Table 4.8).

Table 4.8. First cycle simultaneous thermal analysis data of silk nanoparticles manufactured at different stirring rates. Data was detailed in Chapter 2.

	Thermal Property	Semi-batch	
		Stirring rate / *rpm*	
		0	400
DSC	T_g / °C	59.3 ± 0.01	59.3[a]
	T_d / °C	39.1 ± 5.3	43.6 ± 13.9
	ΔH_d / J g^{-1}	-207.8 ± 98.0	-239.4 ± 18.8
	T_g' / °C	-	206.0[a]
	T_c / °C	-	-
	ΔH_c / J g^{-1}	-	-
	T_o / °C	274.0 ± 0.3	-
	T_{dec} / °C	289.5 ± 0.5	268.9 ± 9.0
TGA	Water content / % (w/w)	13.0 ± 1.7	284.2 ± 7.7
	T_o / °C	277.3 ± 0.2	12.6 ± 2.0
	T_o' / °C	-	274.3 ± 3.8
	T_{dec} / °C	299.6 ± 6.6	-
	T_{dec}' / °C	-	304.0 ± 4.6

a. $n = 1$

4.3.6 The Impact of Volumetric Scale on the Colloidal Stability of Silk Nanoparticles

The short-term aqueous stability of the nanoparticles manufactured in the open semi-batch system and in a microfluidic format at volumetric scales between 1.8 and 138 mL were determined for up to 42 days by DLS and ELS (Figure 4.7). Nanoparticles manufactured across all volumetric scales and formats showed size stability in water for the entire duration of the study (Figure 4.7a); the polydispersity index and zeta potential measurements remained consistent for nanoparticles produced in a semi-batch format at volumetric scales above 21.9 mL and in a microfluidic format (Figure 4.7b,c). Conversely, the size polydispersity of the nanoparticles manufactured at the 1.8-mL volumetric scale in a semi-batch format increased significantly at 10 days but did not significantly differ from the initial measurement thereafter. The zeta potential of the nanoparticles manufactured at the 1.8-, 6-, and 21.9-mL volumetric scales also fluctuated across the 42 days.

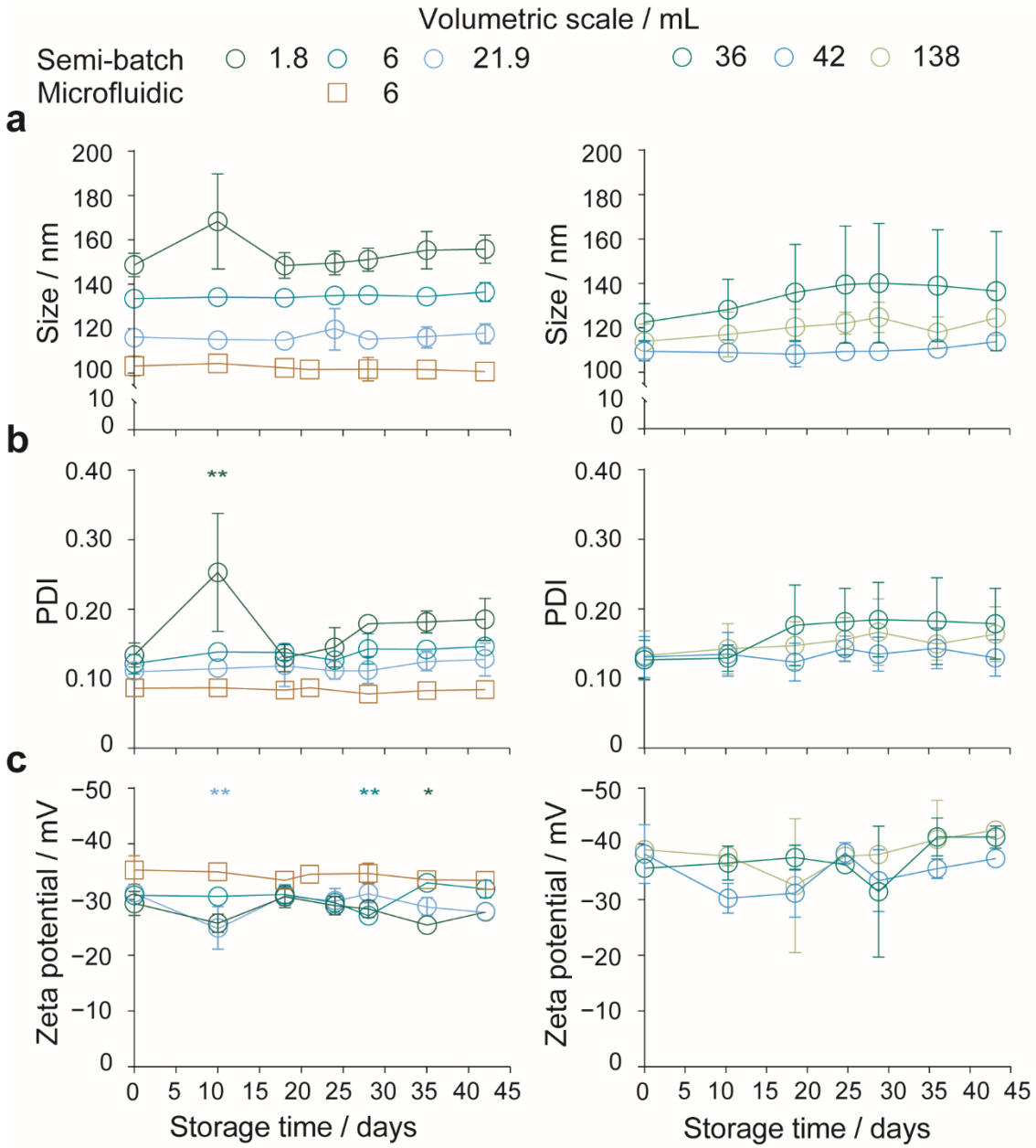

Figure 4.7. Stability of silk nanoparticles manufactured using drop-by-drop semi-batch and microfluidic formats at varying volumetric scales. (a) Hydrodynamic diameter, **(b)** polydispersity index (PDI), and **(c)** zeta potential of silk nanoparticles stored in water at 4 °C. Diluted nanoparticle suspensions were vortexed prior to DLS analysis, ±SD, n = 3. Unless otherwise stated, the silk nanoparticle stability was evaluated by one-way ANOVA followed by Dunnett's post hoc test to compare between t = 0 day control and t > 0 day samples. The zeta potential stabilities of nanoparticles manufactured at 36- and 138-mL scale were evaluated using the Brown–Forsythe and Welch ANOVA followed by Dunnett's T3 post hoc test. Asterisks denote statistical significance for each formulation between t = 0 and t > 0 days, determined using post hoc tests as follows: * p < 0.05, ** p < 0.01.

4.4 Discussion

In the current study, I compared the volumetric scalability of silk nanoprecipitation in semi-batch and microfluidic formats. I used a semi-automated, open system for the semi-batch process under conditions of antisolvent-induced desolvation. The NanoAssemblr™ Benchtop system equipped with a commercially available staggered herringbone micromixer, operated under conditions of shear- and antisolvent-induced desolvation, was used for the microfluidic format.

4.4.1 The Impact of Volumetric Scale on Reproducibility of Semi-Batch Silk Nanoprecipitation

The scaling issue of semi-batch nanoprecipitation is well documented.[320, 359] Hence, the early identification of scaling issues for a nanoprecipitation process and the critical process parameters to maintain during volumetric scale-up can expedite the movement from lab-scale manufacture to clinical and industrial scales. However, to the best of our knowledge, this is the first example of the impact of volumetric scale and stirring rate on silk nanoprecipitation in a semi-batch format. The operation of the semi-batch open system was undertaken at a range of volumetric scales that would be suitable for pre-clinical *in vitro* and *in vivo* manufacture.

To aid translation between lab-scale and pilot-scale equipment, the flow and mixing properties of the semi-batch system were characterized. The flow rate of 1 mL min^{-1} ensured laminar flow in the syringes and needle. The maximum wall shear rate in the syringes was estimated to be between 8.9 and 261 ms^{-1}, while the wall shear rate in the needle was estimated as 4724 s^{-1}. Combined with the low residence time of 33 ms, these shear rates would not be expected to provide sufficient work (i.e., ≈10^5 Pa)[313] for shear-induced nucleation of the silk molecules. In addition, the 3% *w*/*v* concentration used at all volumetric scales fell below the ≈10% *w*/*w* critical micelle concentration[301] of regenerated, aqueous silk precursors. This was confirmed by the lack of correlation between the volume of the extruded silk precursor and the β-sheet content or correlation coefficient. Consequently, the following

discussion assumes homogeneous nucleation induced by desolvation and does not consider shear-induced nucleation followed by seeded crystallization.

Keeping the flow rate and silk precursor:antisolvent ratio constant but increasing the total volume resulted in a decrease in the nanoparticle size and zeta potential, although the narrow polydispersity index and yield did not change significantly (Figure 4.3a). Studies with polymeric and protein nanoprecipitation have indicated that the particle size decreases with the increasing mass fractions of the antisolvent.[360] In the present study, maintaining a constant silk precursor droplet volume while increasing the volume of the antisolvent caused a decrease in the initial volume ratio of silk precursor to antisolvent from 25×10^{-3} at a 1.8-mL volumetric scale to 0.32×10^{-3} at a 138-mL volumetric scale. In solvent mixtures containing a higher mass fraction of the antisolvent, the solute equilibrium concentration was reduced, thereby increasing the supersaturation along with the rate and degree of nucleation. The resulting reduction in surface-controlled nuclei growth rates with reduced local solute concentration caused a shift to a diffusion-limited growth regime. Growth was disfavored because the distance required for diffusion increased with the antisolvent volume, thereby reducing the likelihood of silk association. The resultant changes to the nanoparticle packing as the antisolvent ratio increased likely caused a greater surface exposure of acidic amino acid side chains and reduced zeta potential.[325] Finally, the Reynolds number and turbulence during droplet addition increased with the antisolvent volume; this may have decreased the micro-mixing time.

The total β-sheet content and correlation coefficients were not significantly affected by the change in supersaturation throughout volumetric scale-up. However, a significant reduction in the intermolecular β-sheet content occurred for nanoparticles manufactured at a 138-mL volumetric scale. This reflected the significantly higher anti-parallel β-sheet content in those nanoparticles than in the nanoparticles produced at smaller volumetric scales. Additionally, the volumetric scale-up caused no significant difference in desorption temperature but the water content decreased and the desorption endotherm broadened and decreased with an increasing volumetric scale (Table 4.7, Figure 4.6). This may indicate that

more types of weak water-binding modes were available within the nanoparticle structure as the volumetric scale of manufacture increased. However, simultaneous thermal analysis showed no significant difference in the thermal stabilities of nanoparticles manufactured at an increasing volumetric scale (Table 4.7, Figure 4.6). This finding reinforced that the degree of β-sheet formation stayed constant[323] and indicated that the silk molecules that were incorporated into nanoparticles manufactured at a higher volumetric scale were of similar molecular weight and length distributions.[179]

I speculated that increasing the similarity of mixing times and average shear rates during volumetric scale-up can increase the reproducibility of silk nanoparticle critical quality attributes. This was important for formulation screening, which is typically conducted on a small volumetric scale. For example, the physicochemical properties were made more similar with the 6-fold volumetric scale-up from 6 to 36 mL by increasing the stirring rate to 400 rpm and thereby reducing the mixing times from >120 s to 8.4 and 29.4 s, respectively (Table 4.4). Compared to the significant reduction in nanoparticle size with stirring at the 6-mL volumetric scale, the nanoparticle size decreased only slightly with stirring at the 36-mL volumetric scale. First, at a larger volumetric scale and in the absence of stirring, an increased degree of solvent and antisolvent mixing could occur during silk precursor addition until the critical nucleation concentration was reached, thereby enabling faster nucleation rates and the formation of smaller particles. Second, the particle size had a relatively high standard deviation for both stirred and unstirred processes. This reflected the slightly different feed point positions, which had a greater effect on the fluid dynamics and mixing times at larger volumes. Insufficient centrifugation of the smaller nanoparticles could also reduce yield. However, significant differences were still observed between the α-helix and random coil and the native β-sheet secondary structure contents of nanoparticles manufactured with stirring at the 6- and 36-mL scales. Perhaps the reproducibility of the secondary structure contents could be improved by increasing the stirring rate above 400 rpm at the 36-mL scale to further reduce the mixing time and increase the average shear rate.

4.4.2 The Reproducibility of Silk Nanoprecipitation in a Parallelizable Microfluidic Format

The NanoAssemblr™ staggered herringbone micro-mixing platform provided a volumetric scale-independent platform in the microfluidic format.[255] The mixing efficiency within the microchannel depended on the flow rate and was significantly reduced at high flow rates, resulting in a high vorticity and low transverse flow (Reynolds numbers > 1000). Assuming Newtonian flow, the optimized total flow rate of 1 mL min^{-1} and the isopropanol:silk precursor flow rate ratio of 5:1 (*v*/*v*)[174, 179] resulted in a Reynolds number of 40, indicating a high mixing efficiency. The complete mixing of the aqueous and organic solvents in the microchannels was likely due to the high residence time (Table 4.4).

Considering the wall shear rate (80,114 s^{-1}) as an estimate for the maximum shear rate in the microchannel, combined with the mixing time and the residence time, the shear-induced nucleation of silk prior to the complete mixing in (and extrusion through) the microchannel exceeded both the critical shear rate[344] and critical work.[313] I speculated that the work supplied in the microchannel was sufficient for primary and secondary assembly[342] to occur in the desolvating layer prior to the complete blending of the tertiary mixture. Following the complete mixing, kinetic locking of the spherical silk nanoparticle structure was expected due to the transition from a random coil to a β-sheet secondary structure.

The microfluidic format yielded silk nanoparticles with high β-sheet crystallinity and thermal stability. The physicochemical properties of the nanoparticles were similar to those obtained using semi-batch methods with a low mixing time or high volumetric scale (e.g., ≥21.9-mL scale, stirring at 400 rpm). The low variability of the microfluidic format across batches and microfluidic chips indicated that chip parallelization with an increased total flow rate can provide a promising volumetric scale-up route. In this way, the fluid dynamics and solution composition in the micromixer are independent of volumetric scale. However, special-cause variation in micro-mixing conditions can be introduced by slight differences in the microfluidic chip dimensions. Hence, the reproducibility limit determined by the round robin

study could be used as a general guide for the differences that could be expected between nanoparticles manufactured using multiple chips (Table 4.6, Figure 4.4). Importantly, silk nucleation in the feed lines could decrease the reproducibility, thereby limiting the maximum total flow rate and reducing the scalability for microfluidic manufacture. For this reason, the feed line dimensions should be selected to reduce the wall shear rate while maintaining the laminar flow. Additionally, the low nanoparticle yield could be improved by increasing the centrifugation speed and reducing the number of centrifugation cycles to sediment small nanoparticles that could not be collected at 48,400 × *g*.

4.4.3 The Production Rates of Silk Nanoprecipitation in the Semi-Batch and Microfluidic Formats

The nanoparticle production rate of the semi-batch format was significantly greater than that of the microfluidic format. For example, in the semi-batch format, an intermediate nanoparticle production rate[202] of 0.53 g h^{-1} was estimated, assuming the 29% yield at the volumetric scale of 138 mL. This rate would enable 13 g of nanoparticles to be produced per day, which is suitable for pre-clinical *in vitro* and *in vivo* studies.[202] The low[16, 202, 361] throughput of nanoparticle production in the microfluidic format ranged from 0.040 g h^{-1} for one microfluidic chip to 0.43 g h^{-1} for 10 parallelized chips, assuming 14% yield. The resulting production of 0.96 to 10 g of nanoparticles per day would also be suitable for pre-clinical *in vitro* and *in vivo* studies but are significantly lower than the kilograms per day production rates that are required for clinical and industrial manufacture.[202] Additionally, the time and yield losses incurred by the purification process severely reduced the production rates of both formats. Consequently, increasing the centrifugation speed and reducing the centrifugation time could bring the production rates in line with industrial manufacture. In conjunction, the production throughput could be increased by raising the flow rate of the silk precursor addition to the antisolvent in the semi-batch format and by increasing the total flow rate in the microfluidic format. In both formats, increasing the flow rates can increase silk nucleation and self-assembly[174, 362] and would likely require the tuning of other key formulation and process parameters, such as the silk precursor:antisolvent ratio, mixing time, and shear rate of mixing.

4.4.4 The Impact of Volumetric Scale on the Colloidal Stability of Silk Nanoparticles

A large nanoparticle surface area is beneficial for biomedical applications, but it results in a high surface energy, which can lead to a metastable nanoparticle structure. In the absence of sufficient steric and electrostatic repulsion between nanoparticles, the surface energy will be lowered by particle agglomeration and flocculation. Nanoparticles proposed for intravenous administration need to be stable under standard storage conditions to prevent clinical problems (e.g., inaccurate dosing). The characterization of the effect of aging on nanoparticle physicochemical properties is important for maximizing shelf life and preventing undesired complications.[348] For this reason, I also examined the short-term (42 days) stability[348] of silk nanoparticles manufactured in the open, semi-batch system and in the microfluidic format at 4 °C to assess storage capabilities (Figure 4.7).

Similar to previous studies[153, 174, 179], the zeta potential of nanoparticles from all formulations on the day of manufacture was lower than −25 mV, at pH ~7.4. This indicated the presence of sufficient electrostatic repulsion between particles for moderate aqueous stability. All silk nanoparticles showed size stability over the entire study period. Fluctuations in polydispersity and zeta potential occurred for nanoparticles produced from some semi-batch formulations, and, while these changes were significant, they did not follow any trend indicative of time-dependent flocculation or coagulation.[174] Dissolution also did not occur, as the size and polydispersity remained constant throughout the study.

4.5 Conclusions

Progressing the production of silk nanomedicines from bench to market requires insight into the impact of the volumetric scale on the resulting physicochemical properties of the final nanoparticle product. Here, I assessed the scalability of silk nanoprecipitation in a semi-batch format and used silk nanoparticle manufacturing in a microfluidic format as a volumetric scale-independent control. I found that using homogeneous nucleation conditions without stirring (mixing time > 120 s) decreased the particle size, surface charge, intermolecular β-sheet

content, anti-parallel β-sheet content, and thermal properties as the volumetric scale increased (138 mL < 1.8 mL) due to an increase in initial supersaturation and a reduction in micro-mixing times. However, the narrow polydispersity index, spherical morphology, and high total β-sheet crystallinity of the silk nanoparticle batches did not vary with volumetric scale or with manufacturing format. The nanoparticles manufactured in a semi-batch format at scales equal to and greater than 21.9 mL had similar physicochemical properties to nanoparticles manufactured in the scale-independent, microfluidic format. Additionally, nanoparticles from all formulations, when stored as aqueous suspensions, showed short-term stability over 1 month at 4 °C. Nanoparticles prepared in semi-batch format showed greater reproducibility on a 6-fold volumetric scale-up from 6 to 36 mL total volume with active stirring at 400 rpm (mixing times 8.4 s and 29.4 s, respectively). Conversely, a round robin study involving four participants and microfluidic chips showed that manufacturing operating under conditions of high shear in the staggered herringbone micromixer resulted in high between-participant and within-participant reproducibility, with no outliers observed for nanoparticle size, polydispersity index, zeta potential, yield, or crystallinity. Strategies for increasing the scalability of silk nanoparticle manufacture include maintaining similar mixing times and shear rates of bulk mixing for the semi-batch format and using chip parallelization for the microfluidic format.

Chapter 5: Smart Silk Origami as Eco-sensors for Environmental Pollution

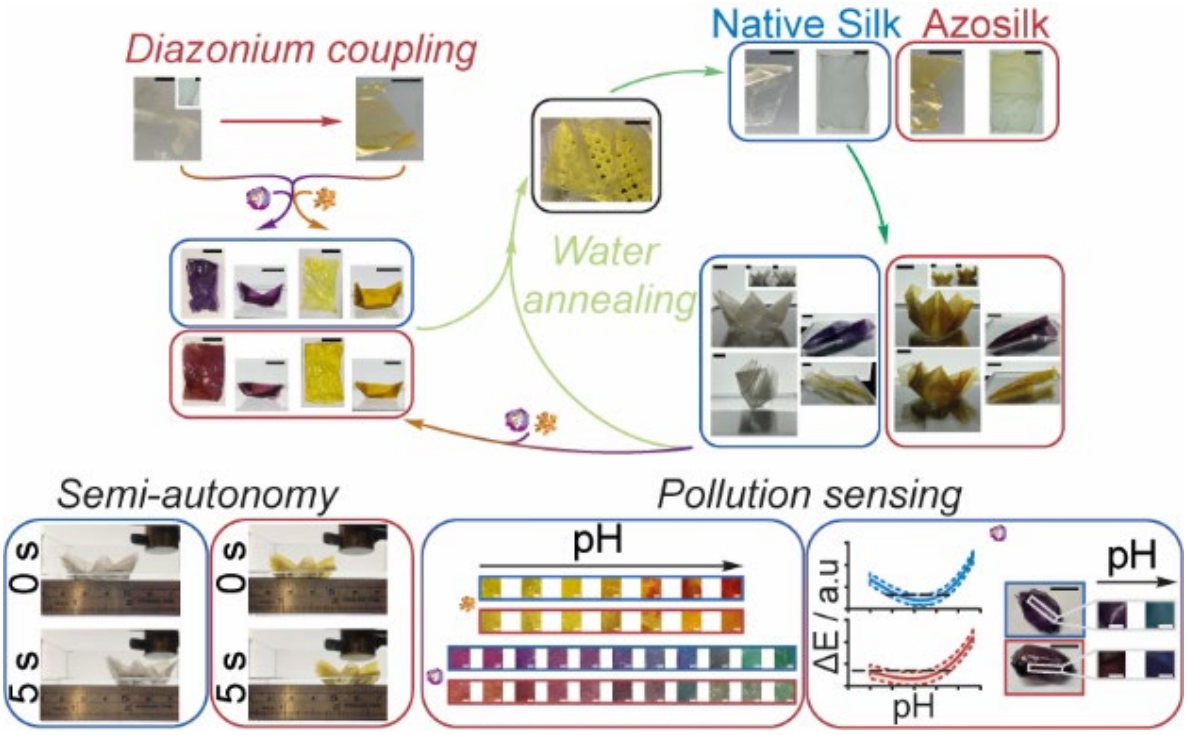

Chapter 5 contains the results from the published article in, and cover feature of, ACS Applied Bio Materials (Matthew*, S. A. L.; Egan*, G.; Witte, K.; Kaewchuchuen, J.; Phuagkhaopong, S.; Totten, J. D.; Seib, F. P. Smart Silk Origami as Eco-Sensors for Environmental Pollution, *ACS Appl. Bio Materials* **2022**, *5*, 3658–3666. DOI: 10.1021/acsabm.2c00023). For this work, I designed, analyzed, and carried out experiments in contribution with Dr Gemma Egan, Dr Kimia Witte, Dr Jirada Kaewchuchuen, Dr Suttinee Phuagkhaopong and Dr John Totten. I designed the azo-modification, the extraction and loading of anthocyanin, and optimized the origami design. In contribution with Dr Gemma Egan, I optimized the loading of curcumin and conducted the digital image colorimetry of curcumin-loaded films at pH 4.37, 7 and 9.15. I conducted and analyzed the results for STA, FTIR, film thickness, and for the azo-silk films the time of initiation of contraction and relaxation. I designed the model pollutants series and conducted and analyzed the digital image colorimetry and colorimetric stability for all anthocyanin and curcumin-loaded films as well as generated the manuscript draft.

5.1 Introduction

The craftsman art of origami has been used for over four centuries to change a flat material into a complex 3D shape.[363] Folding is an easy, cost-effective and scalable fabrication method;[363-366] therefore, origami has inspired a variety of structures over a wide size range, from DNA-origami[367] and soft robotics[366, 368] to metre-scale shelters.[369] As origami is a compliant mechanism which requires the deformation of elastic members,[365] tailoring the stiffness and softness of the flat material is important for obtaining a compliant, foldable architecture which preserves its final shape.[370] The origami folds can endow the structure with attractive mechanical properties, such as load bearing capacity[363, 371] and impact absorption;[372-374] consequently, folds are being increasingly incorporated into deployable modules.[364, 366, 370, 375]

Environmentally responsive actuators, which can convert external physical forces to mechanical force, have attracted growing interest for a diverse range of applications, including drug delivery,[376, 377] biomedical devices[376-378] and sensors.[378-380] Examples of external stimuli used as energy sources for locomotion include thermal energy,[381] humidity,[379, 382-385] chemicals,[380] and optical[381, 386] and magnetic fields.[387] Among these sources, magnetic fields typically result in rapid and directional actuation over long ranges. Materials for smart actuators range from graphene[388] and metal–organic frameworks[389] to synthetic polymers.[390] However, these materials can raise environmental sustainability issues and require harsh, multi-step reaction conditions for production; therefore, emphasis is shifting to bioresorbable metals[391] and eco-friendly polymers[380, 383, 392, 393] that are naturally sourced, renewable and biodegradable. The ecological footprint of waterborne devices is particularly important, as freshwater and marine environments are already negatively impacted by plastic and chemical pollution.[394]

A global need exists for *in situ* water quality monitoring of large or complex water distribution systems and wastewater effluents to mitigate the impact of environmental contaminants on health.[395-397] Miniaturised optical,[396] electrical,[396, 398] magnetic[396] and

chemical sensors[396, 398-400] capable of on-site detection provide a promising alternative to slow traditional analytical methods. These technologies should be inherently green themselves, so interest is growing in developing non-toxic, natural colorimetric indicators loaded within a biopolymer matrix as eco-green chemical sensors. For example, curcuminoids from turmeric and anthocyanins from red-pigmented plants are metal and pH-responsive dyes[401, 402] and have been used with biodegradable polymers including chitosan,[403, 404] corn and tapioca starch[393, 401, 405] as visual pH-sensing films. However, at present, no silk fibroin matrices or complete examples of portable eco-green sensors have been reported. The folding of biocompatible, biodegradable and sustainable[138] silk fibroin films into reusable origami devices could serve as a simple approach for the fabrication of eco-friendly early warning systems for waterborne pollutants.

5.2 Materials and Methods

5.2.1 Materials

Studies were undertaken at 18–22 °C and reagents were obtained from Sigma Aldrich at purities of ≥98%, unless otherwise stated. Dialysis of silk fibroin was conducted using Slide-A-Lyzer™ dialysis cassettes (molecular weight cut-off 3,500 g mol^{-1}, Thermo Fisher Scientific Inc., Waltham, MA, U.S.A.). Polydimethylsiloxane (PDMS) for cast molding, HPLC grade methanol, HPLC grade acetonitrile and anhydrous sodium carbonate (certified AR for analysis) were acquired from Fisher Chemical™. Aniline (99.8%), *p*-toluenesulfonic acid (99%) and anhydrous lithium bromide (99%) were obtained from Acros Organics™. Curcumin (95% total curcuminoid content from turmeric rhizome) was purchased from Alfa Aesar. Sodium nitrite (99%) was acquired from AnalaR NORMAPUR®. Boric acid (99.5% ACS reagent) and sodium tetraborate decahydrate (99.5% ACS reagent) were obtained from Sigma Aldrich. All solvents and reagents were used without additional purification.

5.2.2 Reverse engineering of *Bombyx mori* silk cocoons

B. mori cocoons (Tajima Shoji Co., Yokohama, Japan) were degummed by boiling in 0.2 M aqueous Na_2CO_3 for 0.5 h and degummed silk fibroin dissolved in 9.3 M aqueous LiBr solution at 60 °C for 3 h, as described in Chapters 2–4. The regenerated silk solution was stored at 4 °C until use.

5.2.3 Fabrication and water annealing of silk films

Liquid silk was mixed with a 10% *w/v* aqueous suspension of silk fiber (1241.9 ± 790.4 μm × 21.0 ± 2.9 μm) or 1% *w/v* iron(III) oxide (synthetic spherical particles with 99.995% < 325 mesh [~45 μm] size, > 96.8% purity, 4.6 g cm^{-3} solid density and 0.8–1.2 g cm^{-3} bulk density from Inoxia Ltd, Sweden) to give a final suspension of 3% *w/v* silk containing 0.1, 1.0 or 10.0% dopant weight per silk weight. The liquid silk and silk suspensions were mixed slowly before casting in silicone molds (Sika Everbuild Building Products Ltd, Leeds, UK) on a Perspex base (RuudraScott Plastic, Glasgow, UK) in air for 16 h.

Four molds and silk volumes were used in the study. The control mold (8 × 6 cm; 7.45 mL) was used to screen iron oxide and silk fiber loads and to cast 3% *w/v* silk with 0.1% (*w/w*) iron oxide for loading with natural indicators. The film thickness was screened by increasing the casting volume in a 10 × 14.5 cm mold from 15 mL for thin films to 22.5 mL for medium films and 30 mL for thick films. The medium thickness mold was used to cast 3% *w/v* silk with 0.1% (*w/w*) iron oxide for origami. Films were removed by scoring with a knife at a distance of at least 0.5 mm from the silicone mold boundary. All films were stored under vacuum in a dry environment before measurement to avoid structural changes.

Films for curcumin loading were directly treated with methanolic curcumin. Films for diazonium coupling and anthocyanin loading were weighed and annealed with 80% *v/v* methanol/ultrapure water (10 mL per 0.1 g film) for 0.5–1 h. The films were then dried overnight at room temperature and weighed before diazonium coupling or loading.

Dried films loaded with anthocyanin and curcumin were water annealed in a water-filled vacuum desiccator using an 85.7 kPa vacuum (70% humidity) for at least 6 h at room temperature to produce a water-insoluble, plasticised film. The films were removed from the vacuum desiccator, folded into an origami architecture within 10 min, and allowed to dry for at least 2 h. Films were refolded into alternative shapes by repeating the water annealing process.

5.2.4 Heterogeneous diazonium coupling

A cooled solution of 0.2 M aniline (1.25 mL) in acetonitrile and a 1.6 M aqueous solution of *p*-toluenesulfonic acid (0.625 mL) were combined with a cooled aqueous solution of 0.8 M $NaNO_2$ (0.625 mL). The mixture was placed in an ice bath for 15 min with continuous stirring. A silk film in 1:1 acetonitrile/0.1 M borate buffer pH 9 (total solution volume 10 mL/0.1 mg) was combined with the stock diazonium salt solution (~0.98 equivalents with respect to tyrosine, assuming 288 tyrosines and according to an H-chain molecular weight of 391 kDa), and the mixture was placed in an ice bath. After combining the silk and diazonium salt, the reaction was allowed to proceed for 1 h. The film was then treated with ultrapure water (30 mL) for 1 h. This step was repeated two further times before drying the film at room temperature in the dark.

5.2.5 Extraction of anthocyanin

Red cabbage (East Lothian, Scotland, Billy Logan, Class 1, 00096, DWW, selected on 12 July 2021) (400 g) was cut into approximately 5 × 5 mm pieces and boiled, with manual stirring, in ultrapure water (850 mL) at 98–105 °C for 0.5 h. Insoluble matter was separated from the anthocyanin solution with a sieve. The solution was concentrated at 80 °C to a final volume of 200 mL. The solution was left to cool to room temperature and then filtered through 12–15 µm qualitative filter paper (VWR, Radnor, PA, U.S.A.) and stored at 4 °C for 17 h before use.

5.2.6 Anthocyanin Loading

Native silk and azosilk films (6 × 4.5 cm and 6 × 8.5 cm) containing 0.1% iron oxide (*w/w*) were submerged in the anthocyanin solution (100 mL g^{-1}) for 17 h under constant movement on a tilt table (SSL4 see-saw rocker, Stuart®, Staffordshire, U.K.) at 10 osc min^{-1} at 25 °C. The films were then removed and washed in ultrapure water (100 mL) three times for 20 min each on an orbital shaker (Yellowline OS 5 basic, IKA, Staufen, Germany) at 240 rpm. The films were protected from light throughout the loading and washing process. Finally, the films were left to dry in the dark before being imaged on an iPhone SE (Apple, Cupertino, CA, U.S.A.) reverse camera at a focal length of 9.7 cm. Loading was repeated in triplicate for the 6 × 4.5 cm film size.

The photographs were standardised using a Datacolor SpyderCheckr® 24 (v1.3, Datacolor, NJ, U.S.A.) color chart under the same lighting conditions. The calibration photo was imported to Adobe Lightroom Classic (Adobe, San Jose, CA, U.S.A.), the angle corrected, chromatic aberration removed, perspective profile corrected using the auto or full setting, a full transformation completed, and the image cropped. The white balance was altered using cell E2, adjusting the exposure, highlights, shadows, whites, and blacks to achieve RGB values of 90% at cell E2 and 4% at cell E4. The image was then edited in SpyderCheckr® using the colorimetric mode. The resulting color profile was applied to all images under the same lighting conditions. The edited images were exported as 300 ppi JPG files, and a grid overlay was placed in ImageJ® v1.52n (National Institutes of Health, Bethesda, MD, U.S.A). The RGB values were measured for 4 boxes on the grid (595952 pixels) and the averages were calculated.

5.2.7 Curcumin loading

Native silk and azosilk fibroin films (6 × 4.5 cm and 6 × 8.5 cm) containing 0.1% iron oxide (*w/w*) were submerged in a 2.5 mg mL^{-1} solution of curcumin in methanol (100 mL g^{-1}) for 30 min under constant movement on a tilt table (SSL4 see-saw rocker, Stuart®, Staffordshire, U.K.) at 10 osc min^{-1}. The films were then removed and washed in ultrapure water (100 mL)

three times for 20 min each on an orbital shaker at 240 rpm (Yellowline OS 5 basic, IKA, Staufen, Germany). The films were protected from light throughout the loading and washing process. Finally, the films were left to dry in the dark before being imaged on an iPhone SE (Apple, Cupertino, CA, U.S.A.) or a OnePlus 8 (48MP, f/1.8 ISO320) reverse camera at a focal length of 9.7 cm. Standardisation was undertaken as for anthocyanin loading. Loading was repeated in triplicate for the 6 × 4.5 cm film size.

5.2.8 Characterization of silk films

5.2.8.1 Color change of silk films across pH and pollutant concentration

Silk films loaded with curcumin or anthocyanin were imaged after being submerged for 2 min in the following solutions: 0.2 M potassium phosphate buffer (pH 4.37, pH 6.16, pH 7.00, pH 8.16 and pH 9.15); 0.001 M potassium phosphate buffer (pH 1.98 and pH 2.92); 0.17 M sodium acetate buffer (pH 5.01); 0.1 M sodium bicarbonate buffer (pH 9.97); 0.2 M alkaline borate buffer (pH 10.50); 0.1 M glycine buffer (pH 11.36); 897 mg L^{-1} SDS; 660 mg L^{-1} CTAB; 370 mg L^{-1} Triton X-100; 242.3 mg L^{-1} $CoCl_2$; 341.5 mg L^{-1} $Co(NO_3)_2$; 3.265 mg L^{-1} $CuSO_4$; 0.15748 mg L^{-1} $AgNO_3$; 979.2 mg L^{-1} $MgCl_2$; 999.2 mg L^{-1} $MgCO_3$; 600.0 mg L^{-1} $MgOH_2$; or real, stagnant river water randomly grab sampled in Glasgow, Scotland. The images were processed as for loading. Films were washed three times in ultrapure water for 0.25 h, dabbed dry with a tissue and dried at room temperature for 0.17 h before submersion in a new solution. The relative color change (S) was calculated by subtracting the mean intensities in the red (R_o), green (G_o), and blue (B_o) channels of the loaded film from the red I, green (G) and blue (B) intensities in the films following exposure to each medium, according to equation 5.1.[406]

$$\boldsymbol{S}\,(\%) = \mathbf{100} \times \frac{(|\boldsymbol{R}-\boldsymbol{R_o}|+|\boldsymbol{G}-\boldsymbol{G_o}|+|\boldsymbol{B}-\boldsymbol{B_o}|)}{\boldsymbol{R}+\boldsymbol{G}+\boldsymbol{B}} \qquad (\mathbf{5.1})$$

The color change was also calculated based on the Lab model, according to equation 5.2.[406]

$$\boldsymbol{\Delta E} = \sqrt{(\boldsymbol{L}-\boldsymbol{L_o})^2 + (\boldsymbol{a}-\boldsymbol{a_o})^2 + (\boldsymbol{b}-\boldsymbol{b_o})^2} \qquad (\mathbf{5.2})$$

In the Lab color space published by the International Commission on Illumination (CIE), the L*, a*, and b* channels constitute image lightness, red to green intensities, and blue intensity, respectively. Each condition was repeated with three films.

5.2.8.2 Colorimetric stability of native silk and azosilk films

Native silk and azosilk films doped with 0.1% (*w/w*) iron oxide and loaded with curcumin or anthocyanin were stored for 31 days in vacuum sealed boxes at 4 °C or 20 °C in the dark. Silk films were then imaged before and after being submerged in 0.2 M potassium phosphate buffer (pH 9.15) for 2 min on an iPhone SE (Apple, Cupertino, CA, U.S.A.) reverse camera at a focal length of 9.7 cm. Photographs were standardised as described for loading, the RGB values measured for 2 boxes on the grid (42840 pixels) and the averages were calculated. Each condition was repeated with three films.

Digital image colorimetry was also achieved using the ColorAssist Lite© (FTLapps, Inc., Broadlands, VA, U.S.A.) smartphone application with a spatial sample aperture of 50 × 50 pixels, temporal sample aperture of 30 frames (1 second) and mean output intensities measured in the RGB color space. Each film was sampled in three regions and the average calculated. Each condition was repeated with three films.

5.2.8.3 Scanning electron microscopy

For surface imaging, samples were added to aluminium stubs with sticky carbon tabs, with the surface uppermost. For section imaging, a titling SEM stub was used to rotate the samples to 90° with the cross-section uppermost. Samples were sputter coated (ACE200, Leica Microsystems, Wetzlar, Germany) with a 20 nm gold layer to minimise charging in the SEM. Samples were viewed with a TM4000Plus SEM (Hitachi Ltd., Tokyo, Japan) operated at beam voltage 10000eV, probe current setting 2, standard vacuum level (M) and with data collected in backscattered electron mode at magnifications of 100×, 1000× and 10000×.

5.2.8.4 Contact angle measurement

The films were placed on a glass slide. The contact angle was measured using a DSA30 drop shape analyser (KrussGmbH, Hamburg, Germany) equipped with a manual syringe and needle (diameter 0.8 mm). Droplet size was controlled manually. Results were analysed in Advance software (KrussGmbH, Hamburg, Germany) with manual droplet shape fitting.

5.2.8.5 Fourier Transform Infrared Spectroscopy analysis

Positive silk II controls were provided by autoclaved silk films and silk films treated with 70% *v/v* ethanol/ultrapure H_2O, while air-dried silk films and freeze-dried silk were used as positive controls for silk I structure. Secondary structures of silk films, freeze-dried powders and freeze-dried particles were analysed by Fourier transform infrared spectroscopy (FTIR) on an ATR-equipped TENSOR II FTIR spectrometer (Bruker Optik GmbH, Ettlingen, Germany). Each FTIR measurement was recorded in absorption mode over the wavenumber range of 400 to 4000 cm^{-1} at 4 cm^{-1} resolution for 128 scans and then corrected for atmospheric absorption using Opus (Bruker Optik GmbH, Ettlingen, Germany). The second derivative of the background-corrected FTIR absorption spectra was analysed in OriginLab 19b® (Northampton, MA, U.S.A.) by adapting a literature protocol.[304] The second derivative was smoothed twice using a seven-point Savitzky-Golay function with a polynomial order of 2. The amide I region was analysed by interpolation of a non-zero linear baseline between 2–3 of the highest values in the 1600–1700 cm^{-1} range. Peak positions were identified by applying the second derivative, and the peaks were fitted in the amide I region using non-linear least squares with a series of Gaussian curves. The position, width and height of each peak were allowed to vary, while peak area could take any value less than or equal to 0. Deconvoluted spectra were then area-normalised, and the relative area of each band was used to calculate the secondary structure content according to literature band assignments.[155, 305]

5.2.8.6 Thermal analysis

First-cycle differential scanning calorimetry and thermogravimetric analysis were carried out on the dried samples (3–5 mg) in aluminium pans from 20–350 °C at a scanning rate of 10 °C

min^{-1} and under a nitrogen flow of 50 mL min^{-1} using an STA Jupiter 449 (Netzsch, Gerätebau GmbH, Selb, Germany). Thermograms were analysed using Proteus® (Netzsch, Gerätebau GmbH, Selb, Germany).

5.2.8.7 Swelling analysis

The swelling of silk fibroin films was monitored over 30 min. Each film was split into 3 pieces and placed in ultrapure water (20 mL), and the weight was measured at defined intervals. The films were removed, and any excess water on the film was dabbed dry with paper towels. This was repeated three times for each film.

5.2.8.8 Electromagnetic field strength

The strength of a magnetic field was measured by the ability to pull a floating rectangular silk film (0.1 g, 25 µm thickness) along the water-air interface using a N52 round cylinder magnet (25 × 20 mm Rare Earth Neodymium; $(BH)_{max}$ 52 MGOe). The magnet used in the study was moved across water-glass interface (2 mm thickness) parallel to the water-air interface (where silk was floating) at fixed distances defined by the volume of water in a 5000 mL glass beaker. Every added 50 mL was equivalent to a 1 mm increase in the distance between the silk film and the magnet. The distance from the surface of the magnet at which locomotion was first observed was converted to magnetic flux density (B) and magnetic field strength (H).

5.2.8.9 Contraction and relaxation on water

The time of contraction from the original shape of the water-annealed dried silk films (*ca*. 7 × 5 cm) was measured in seconds as the films were placed in water (floating at the water-air interface). The relaxation and return to the original shape were followed by measuring time in seconds.

5.2.8.10 Thickness and folding assessment

Film thickness was measured with digital Vernier callipers (CM145 Clarke® Precision, Clarke®, London, U.K.) by stacking 3–4 films of the same type. The folding time after annealing for 17 h was measured by removing the films (ca. 9 × 13.5 cm) from the water

annealing chamber and recording the time when the films first cracked or tore when being repeatedly folded and unfolded by hand.

5.2.9 Characterization of silk origami boat

5.2.9.1 Semi-autonomy

Origami sailboats (6 × 8.5 cm) containing 0.1% (*w/w*) iron oxide were placed on ultrapure water in a clear acrylic box (10.3 × 10.3 × 5 cm). An LED panel (RALENO, Seattle, WA, U.S.A.) was fixed at the back of the box to provide constant illumination at 5600K color temperature and at 1% brightness. An N52 round cylinder magnet (25 × 20 mm Rare Earth Neodymium) was suspended from the bow of the boat at ca. 2 mm horizontally and from the highest point of the boat sail at ca. 2 mm vertically. The distance travelled over 30 s was captured on an iPhone SE (Apple, Cupertino, CA, U.S.A.) reverse camera at a capture speed and resolution of 240 fps and 1080 p using FiLMiC Pro (FiLMiC Inc., Seattle, WA, U.S.A.). In parallel, the movement of a folded origami boat manufactured without iron oxide was used as a negative control. Each condition was repeated with three origami boats manufactured with different silk batches. Images were extracted at 240 fps using Ffmpeg.[335]

5.2.9.2 Sensing of pH and pollution

Films (4.5 × 4.5 cm) were loaded with anthocyanin and curcumin, water annealed and folded into origami canoes. Boat hulls were imaged on an iPhone SE (Apple, Cupertino, CA, U.S.A.) reverse camera at a focal length of 7.8 cm. Curcumin-silk canoes were placed on 0.2 M potassium phosphate buffer (pH 4.73 and 9.15), and anthocyanin-silk canoes were placed on 660 mg L^{-1} CTAB and 0.2 M potassium phosphate buffer (pH 9.15) for 2.5 mins before removal, drying in air and imaging. Photographs were standardised as described for loading of 2D films, the RGB values were measured for 2 boxes on the grid (42840 pixels) and the averages were calculated.

Equivalent origami sailboats (6 × 8.5 cm) were placed on 0.2 M potassium phosphate buffer (pH 9.15), 897 mg L^{-1} SDS and 3.27 mg L^{-1} copper sulphate in a clear acrylic box (10.3

× 10.3 × 5 cm). An LED panel (RALENO, Seattle, WA, U.S.A.) was fixed at the back of the box to provide constant illumination at 5600K color temperature and at 1% brightness. The color change was imaged on an iPhone SE (Apple, Cupertino, CA, U.S.A.) reverse camera at a capture speed and resolution of 60 fps and 2160 p using FiLMiC Pro (FiLMiC Inc., Seattle, WA, U.S.A.). Images were extracted at 60 fps using Ffmpeg.[335]

5.2.10 Statistical analysis and graphic design

Data were analysed using Microsoft Excel® 2019 (Microsoft Office 365 ProPlus Software, Redmond, WA, U.S.A), Minitab® (Minitab® Statistical Software, State College, PA, U.S.A.) and GraphPad Prism 8.2.1 (GraphPad Software, La Jolla, CA, U.S.A.). Normality of the data distributions and equivalence of variance for sample pairs and multiple groups were assumed throughout. Two sample groups were analysed using the independent *t*-test. A two-way ANOVA was used to compare multiple groups across two independent variables, followed by Šidák's multiple comparison, simple effects post-hoc test. Stability was analyzed using a two-way ANOVA to compare multiple groups across the storage temperature and modification as independent variables, followed by Dunnett's multiple comparison, simple effects post-hoc test against the t = 0-day control. Cubic polynomials were fitted to the color change (ΔE) data between pH values of 1.98 to 11.36 using non-linear, least squares regression in GraphPad Prism 8.2.1 (GraphPad Software, La Jolla, CA, U.S.A.) and the 95% prediction interval of each equation was calculated. Curve fitting used no special handling for outliers, medium convergence criteria, no weighting, and considered each replicate ΔE value as an individual point. Statistical significance, identified using post-hoc tests, was as follows: *$p < 0.05$, **$p < 0.01$, ***$p < 0.001$, ****$p < 0.0001$. All data are displayed as the mean ± standard deviation, with the number of experimental repeats (n) shown in each figure legend. Illustrations were made in Adobe Illustrator (1.8.2) (Adobe, San Jose, CA, U.S.A.) and ChemBioDraw® 20.0 (PerkinElmer, Waltham, MA, U.S.A.) software.

5.3 Results and Discussion

In the present Chapter, 3D silk structures were folded *via* cast molding of liquid silk and plasticisation of the 2D film through water annealing (Figure 5.1). Liquid silk was also spiked with iron oxide particles to realise semi-autonomous films which displayed a magnetic response in the presence of an electromagnetic field with a field strength (H) of 0.27×10^4 A m^{-1}, at an iron oxide doping concentration of 0.1% (*w/w*) of silk protein and 0.1 g silk film mass. The surface of water-insoluble films was also modified by diazonium coupling with benzene diazonium to increase hydrophobic repulsive forces (Figure 5.1), and this, in turn, increased the buoyancy and magnetically driven actuation of the resulting azosilk films. Both native and azosilk films could be loaded with curcumin and anthocyanin to fabricate colorimetric 3D silk boats for detection of heavy metal salts, surfactants and algae at harmful aqueous concentrations, thereby demonstrating their potential in pollution sensing applications.

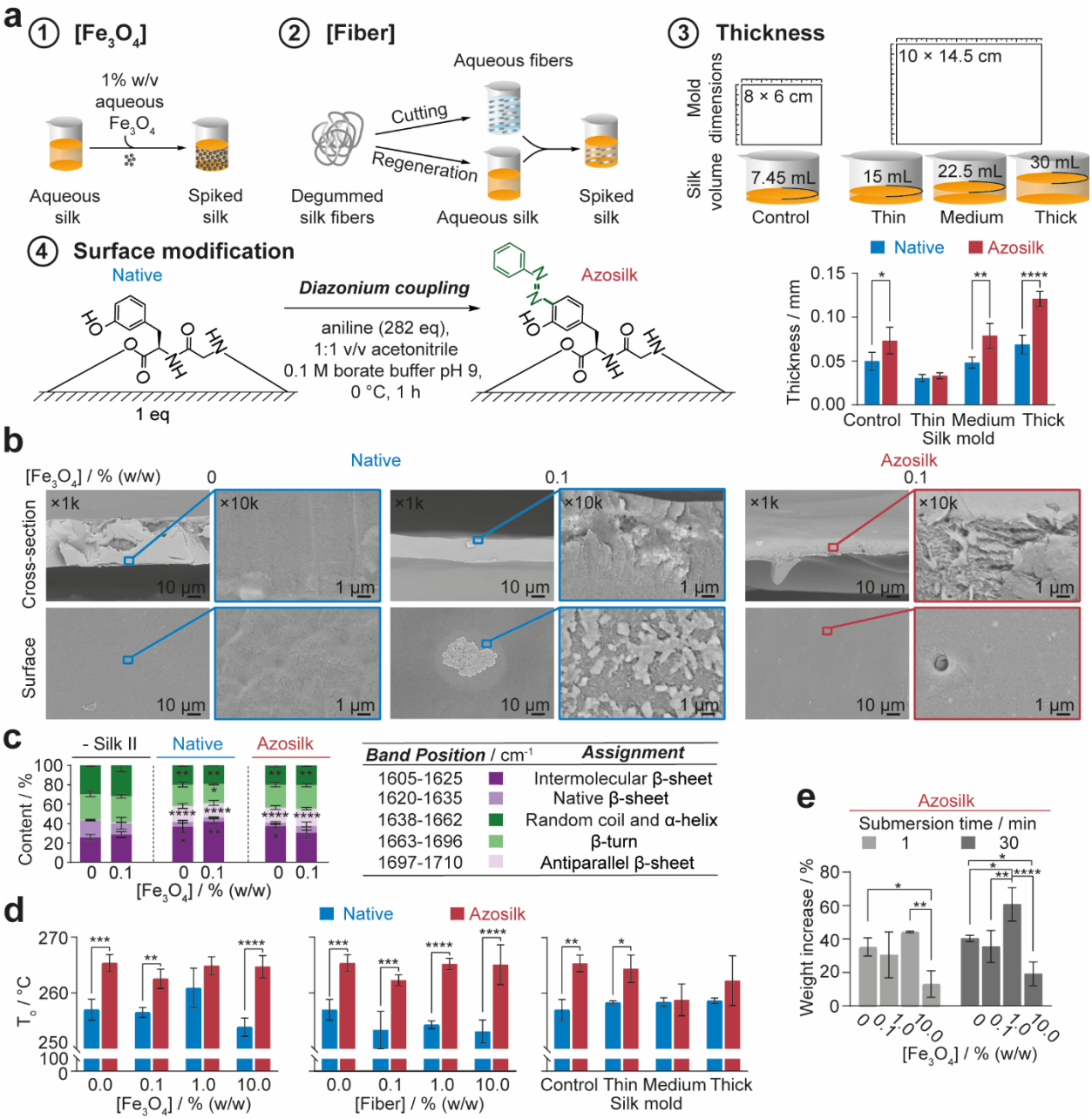

Figure 5.1. Properties of drop-casted silk films varying in diazonium coupling, fiber content, iron oxide content and thickness. (a) The factors investigated during the preparation of silk films and the thickness of silk films obtained by varying mold size and silk solution volume during casting. **(b)** SEM images of native silk and azosilk films after water annealing with 0 and 0.1% (*w/w*) iron oxide particle loads**. (c)** FTIR band assignments and schematic key. Secondary structure content of silk films drop-casted with varying iron oxide particle concentrations. Secondary structure content (%) was calculated from the relative areas of peaks in the second-derivative spectrum. Untreated silk films were used as negative controls for β-sheet content. The secondary structure contents of multiple factors were evaluated by ordinary one-way analysis of variance (ANOVA), followed by Dunnett's multiple comparison, post-hoc test against the secondary structure content of the native, negative silk II control containing 0% (*w/w*) iron oxide. **(d)** The extrapolated onset temperature of decomposition (T_o) of silk films from first-cycle DSC. **I** Swelling of silk films with varying iron oxide particle concentrations following immersion in water. **I** Error bars are hidden in the bars and plot symbols when not visible, ± SD, *n* = 3. Multiple factors were evaluated by two-way analysis of variance (ANOVA), followed by Šidák's multiple comparison, simple effects post-

hoc test. Asterisks denote statistical significance determined using post-hoc tests as follows: *p < 0.05, **p < 0.01, ***p < 0.001, ****p < 0.0001.

Casting conditions were first optimised for semi-autonomy by varying the iron oxide particle concentration, the time window for folding by tuning film thickness, and the longevity of folds upon water by tuning surface hydrophobicity and silk microfiber concentration (Figure 5.1a). The silk microfiber content was varied by doping silk feeds with a batch of silk microfibers of 1241.9 ± 790.4 μm in length and 21.0 ± 2.9 μm in width (Figure 5.2), previously manufactured by mechanically shearing degummed silk fibers. The film thickness was tuned by increasing the volume of liquid silk for mold casting. The crystallinity of silk fibroin films can increase with drying time;[138] therefore, the films were methanol annealed to induce β-sheet self-assembly for scalable origami production and to enable the loading of lipophilic dyes during this step. Water annealing was used to increase the plasticity and fracture resistance of the semicrystalline films[407, 408] during folding. The water molecules permeate the silk network and are involved in silk-water hydrogen bonding which causes structural reorganization, primarily in the amorphous regions of high α-helix and random coil secondary structure content.[407] This process significantly increases silk chain mobility, while stiffness is regained upon drying. Scanning electron microscopy (SEM) confirmed that iron oxide particles were incorporated into, and retained within, the silk film matrix following post-processing methods (Figure 5.1b). The post-casting modification of silk films by diazonium coupling[158, 409] of benzene diazonium with tyrosine and histidine residues was used to increase the hydrophobicity of the film surface. Diazonium coupling generally increased the film thickness compared to native films (Figure 5.1a) and resulted in an increase in the water contact angle, indicating a greater hydrophobicity (Figure 5.3a and b).

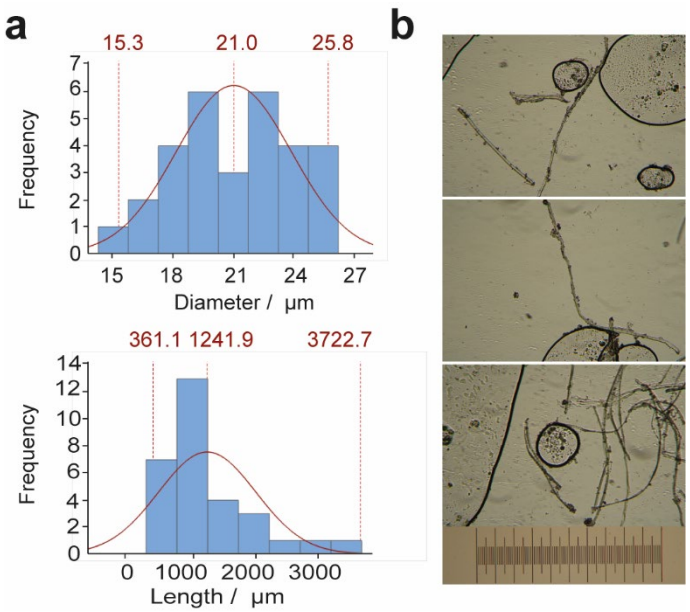

Figure 5.2. The dimensions of mechanically cut silk fibers. (a) Histograms of length and width. Reference lines show the minimum, average and maximum dimensions. *N* = 30. **(b)** Exemplar images of silk fibers at 10× magnification. Scale bar = 1 mm.

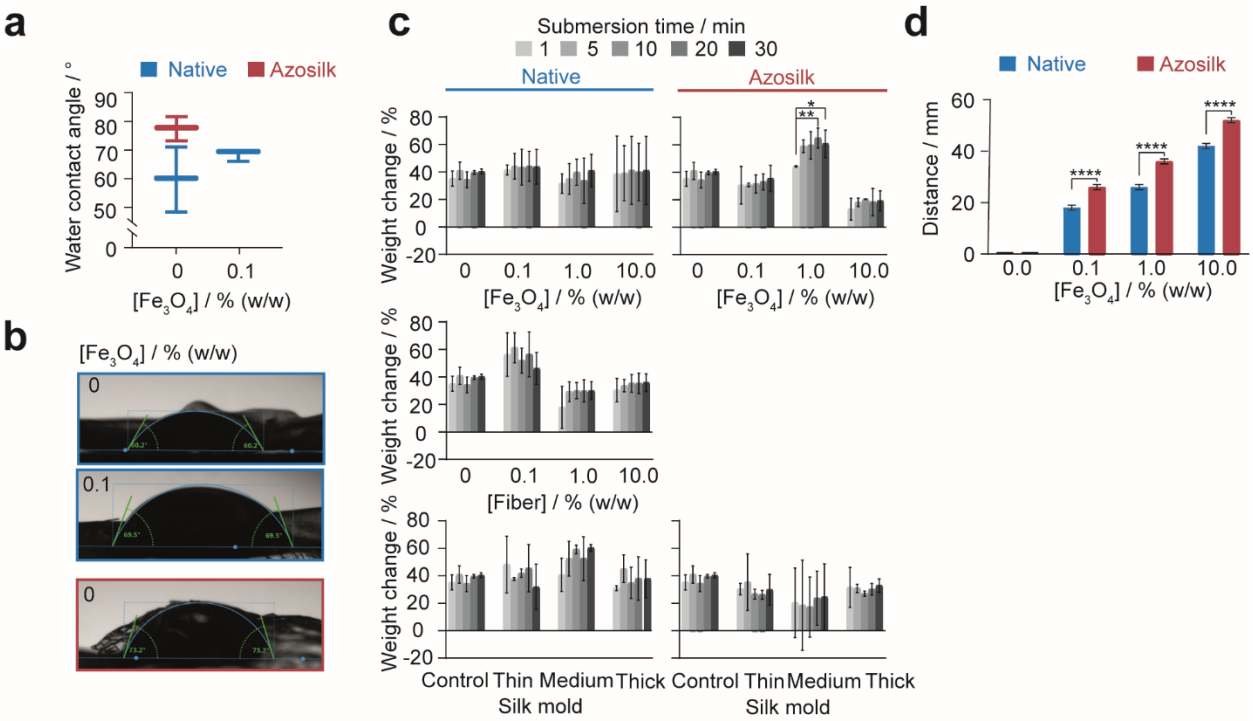

Figure 5.3. The effect of aqueous environments on silk films. (a) Water contact angle of azosilk and native silk medium thickness films without iron oxide and of native control thickness silk film containing 0.1 % (*w/w*) iron oxide. ± SD, *n* = 3. **(b)** Exemplar images of water contact angles for azosilk and native silk films. Scale bars = 0.5 cm. **(c)** Weight change of native silk and azosilk films following immersion in ultrapure water. **(d)** The distance from the surface of an N52 Rare Earth Neodymium round cylinder magnet that was able to pull a floating rectangular-shaped silk film (0.1 g, 25 µm) loaded with iron oxide particles along the water-air interface. ± SD, *n* = 3. Error bars are hidden in the bars and plot symbols when not visible. Multiple factors were evaluated by two-way analysis of variance (ANOVA), followed by Šidák's multiple comparison, simple effects post-hoc test. Asterisks denote statistical significance determined using the *t*-test and post-hoc tests as follows: *p < 0.05, **p < 0.01, ***p < 0.001, ****p < 0.0001.

All films showed stability in water due to the dominant β-sheet secondary structure, which ranged from 55 to 61% (Figure 5.1c). The thermal decomposition of silk films occurred at temperatures above 250 °C, which was consistent with a high β-sheet content,[138] and azo-modification generally increased the thermal stability (Figure 5.1d, Table 5.1, Table 5.2, Figure 5.4 and Figure 5.5). Stability at high temperature is advantageous as it increases the lifespan of the silk films across a range of atmospheric environments. A low degree of swelling in water is also desirable to preserve the stiffness and shape of the 3D architecture. All films showed a low degree of swelling in water within 30 min, ranging from 19 to 61%, although water uptake

was most significant within 5 min and levelled off thereafter (Figure 5.1e, Figure 5.3c). Weight change was not affected by the thickness or iron oxide loads of native silk films, although the water uptake over 30 min was maximal for silk films spiked with 0.1% (*w/w*) fiber at 46%. Azosilk films showed varying swelling over 30 min with iron oxide particle doping. For example, a weight change of 35% occurred at an iron oxide loading of 0.1% (*w/w*), and this Increased to 61% at 1% (*w/w*) iron oxide. Increasing the iron oxide content further to 10% (*w/w*) resulted in a lower weight increase of 19% over 30 min.

Table 5.1. First-cycle thermal analysis data of native silk films with different thickness, fiber contents and iron oxide particle contents. ± SD, *n* = *3.*

	Thermal Property	Thickness / *μm*			[silk fiber] / *% (w/w)*			[Fe_3O_4] / *% (w/w)*			-Silk II
		Thin	Medium	Thick	0.1	1	10	0.1	1	10	Silk film
DSC	T_g / *°C*	53.6 ± 0.8[a]	53.9 ± 17.5	63.3 ± 27.2	50.9 ± 18.5	47.5 ± 9.6	52.3 ± 5.7	50.4 ± 5.5	61.9 ± 25.3	50.2 ± 5.4	50.3 ± 4.9
	T_d / *°C*	61.2 ± 3.1	66.7 ± 7.9	61.3 ± 7.0	78.2 ± 22.0	70.2 ± 20.5	61.3 ± 6.4	66.0 ± 17.7	61.4 ± 6.1	65.6 ± 17.5	60.4 ± 8.6
	ΔH_d / *J g^{-1}*	-221.5 ± 19.5	-184.8 ± 41.6	-203.4 ± 40.6	-37.9 ± 17.5	-122.8 ± 54.2	-84.8 ± 52.9	-98.8 ± 20.7	-177.5 ± 15.3	-104.4 ± 27.6	-123.0 ± 103.4
	T_g' / *°C*	200.6 ± 4.5	200.2 ± 4.8	202.9 ± 3.3	194.7[b]	202.0[b]	204.8 ± 3.3[a]	203.4 ± 3.7	202.8 ± 1.7	198.6 ± 4.0	-
	T_c / *°C*	-	235.1 ± 3.0[b]	237.5 ± 2.4	228.4± 5.1[a]	-	237.0 ± 9.4[a]	236.3 ± 0.0[a]	235.8 ± 1.3[a]	229.6[b]	233.6[b]
	ΔH_c / *J g^{-1}*	-	3.18 ± 3.63[a]	5.25 ± 3.72	1.61 ± 0.30[a]	-	0.885 ± 0.447[a]	5.92 ± 0.80[a]	1.61 ± 0.82[a]	4.32[b]	3.20[b]
	T_o / *°C*	258.3 ± 0.3	258.4 ± 0.8	258.7 ± 0.5	253.4 ± 3.4	254.3 ± 0.7	253.1 ± 2.1	256.5 ± 0.9	260.9 ± 3.6	253.9 ± 1.6	257.0 ± 1.9
	T_{dec} / *°C*	277.0 ± 0.06	277.5 ± 0.0[a]	278.9 ± 0.30	277.0 ± 0.4	276.1 ± 0.36	275.9 ± 2.1	277.1 ± 0.6	278.5[b]	277.5 ± 0.7	277.8 ± 1.0
	$T_{dec'}$ / *°C*	270.5 ± 1.7	271.8 ± 1.7	272.1 ± 1.1	267.2 ± 3.1	268.3 ± 2.0	264.2 ± 5.1	270.9 ± 1.1	274.9 ± 3.4	269.8 ± 5.8	269.6 ± 2.2
TGA	**Water content / *% (w/w)***	6.5 ± 0.5	6.6 ± 1.6	6.1 ± 1.9	5.6 ± 0.4	5.9 ± 0.1	5.4 ± 1.6	4.9 ± 0.5	5.4 ± 0.4	3.9 ± 0.7	3.7 ± 0.6

T_o / °C	263.6 ± 1.1	263.9 ± 0.4	262.7 ± 0.7	264.0 ± 1.6	264.8 ± 1.3	262.4 ± 1.2	264.0 ± 0.5	263.8 ± 1.5	264.4 ± 0.8	262.8 ± 1.7
T_{dec}' / °C	278.3 ± 0.2	278.3 ± 1.0	279.0 ± 0.6	278.5 ± 0.6	278.8 ± 0.4	275.9 ± 2.7	278.8 ± 0.5	279.1 ± 0.3	278.8 ± 0.1	278.6 ± 0.6

a. *n = 2*
b. *n = 1.*

Table 5.2. First-cycle thermal analysis data of azosilk films with different thickness, fiber contents and iron oxide particle contents. ± SD, *n* = *3*.

Thermal Property		Thickness / *μm*			[silk fiber] / *% (w/w)*			[Fe_3O_4] / *% (w/w)*			- Silk II
		Thin	Medium	Thick	0.1	1	10	0.1	1	10	Silk film
DSC	T_g / °C	65.3 ± 4.0[a]	50.1 ± 0.1	75.6 ± 10.8	76.3 ± 12.3[a]	73.1 ± 6.4	71.5 ± 9.1	60.7 ± 23.5	54.7 ± 13.0	67.5 ± 18.9	38.7 ± 6.1[a]
	T_d / °C	81.9 ± 5.5	56.8 ± 0.7	71.1 ± 6.2	74.3 ± 1.8	71.6 ± 12.7	67.0 ± 2.0	62.1 ± 9.2	62.6 ± 8.6	66.0 ± 7.3	67.5 ± 4.1
	ΔH_d / *J g*$^{-1}$	-126.0 ± 90.3	-138.9 ± 41.6	-93.6 ± 53.6	-115.9 ± 53.7	-166.3 ± 31.7	-134.7 ± 29.8	-122.4 ± 12.5	-167.2 ± 80	-124.1 ± 62.1	-156.6 ± 39.5
	T_g' / °C	200.1 ± 1.1[a]	201.1[b]	201.0 ± 0.1[a]	200.0 ± 1.3[a]	197.6 ± 1.9	200.6 ± 5.2[a]	200.6 ± 0.4[a]	200.1[b]	200.2 ± 0.7	202.1 ± 0.5
	T_c / °C	237.9 ± 0.7[b]	253.7 ±2.4[b]	235.9 ± 2.2[b]	237.0[b]	228.6[b]	239.1	-	-	-	-
	ΔH_c / *J g*$^{-1}$	1.02 ± 1.17[b]	1.06 ± 0.23[b]	0.333 ± 0.472[b]	0.479[b]	0.185[b]	0.336[b]	-	-	-	-
	T_o / °C	264.4 ± 2.5	258.8 ± 2.9	262.3 ± 4.5	262.3 ± 1.0	265.2 ± 1.0	265.1 ± 3.6	262.5 ± 1.7	264.9 ± 1.6	264.7 ± 2.0 0.30	265.4 ± 1.5
	T_{dec} / °C	279.3[b]	279.0 ± 0.6[a]	-	-	-	-	-	-	-	-
	$T_{dec'}$ / °C	272.9 ± 3.2	270.4 ± 1.4	274.5 ± 3.3	272.9 ± 3.3	277.3 ± 1.9	277.0 ± 5.0	271.9 ± 4.4	276.0 ± 4.5	277.4 ± 2.8	278.8 ± 0.1
TGA	Water content / *% (w/w)*	5.7 ± 0.6	4.0 ± 0.7	6.0 ± 1.1	5.8 ± 0.3	7.2 ± 1.0	7.7 ± 0.8	5.0 ± 1.6	4.8 ± 1.4	4.4 ± 0.8	7.2 ± 1.6
	T_o / °C	262.9 ± 0.5	261.6 ± 0.3	261.4 ± 1.4	263.3 ± 0.6	262.5 ± 1.7	262.2 ± 0.5	263.5 ± 0.3	263.4 ± 1.0	263.5 ± 2.6	263.8 ± 1.8

	T_{dec}' / °C	279.1 ± 0.2	269.4 ± 11.2	276.1 ± 4.5	279.1 ± 0.2	278.5 ± 0.7	277.6 ± 1.9	279.0 ± 0.2	279.0 ± 0.2	279.0 ± 0.4	278.4 ± 0.4

a. *n = 2*
b. *n = 1.*

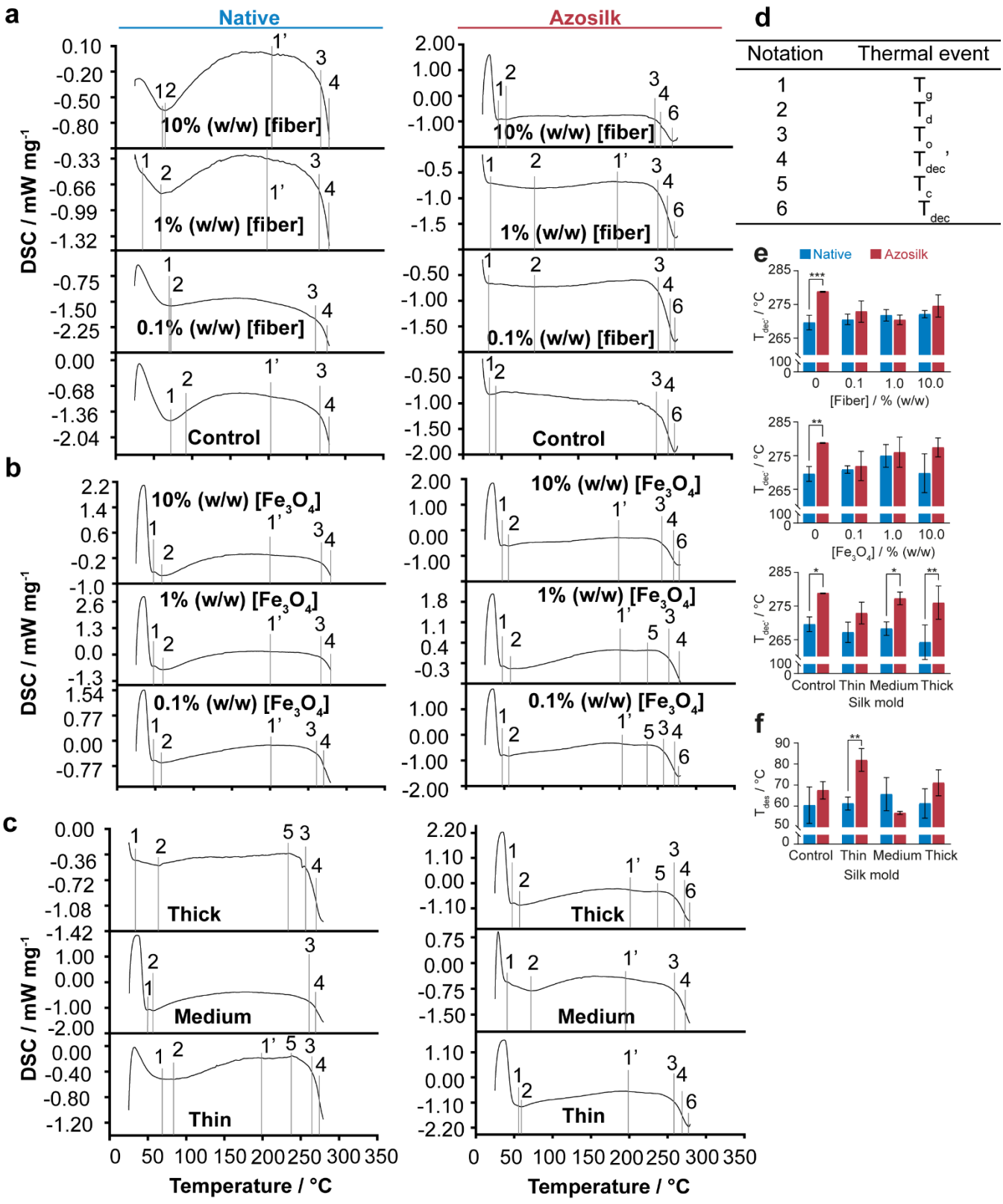

Figure 5.4. Representative first-cycle raw differential scanning calorimetry (DSC) of silk films manufactured with (a) different silk fiber concentrations, (b) iron oxide particle concentrations and (c) thicknesses. (d) Thermal event assignment key. **(e)** The temperature of maximum decomposition rate and **(f)** the water desorption temperature of silk films. ± SD, *n* = 3. Water desorption temperature ($T_{d(es)}$), glass transition temperatures (T_g), extrapolated onset temperature of decomposition (T_o), crystallization temperature (T_c),

decomposition temperature (T_{dec}) and the temperature of maximum decomposition rate (T_{dec}') are reported. Error bars are hidden in the bars and plot symbols when not visible. Multiple factors were evaluated by two-way analysis of variance (ANOVA), followed by Šidák's multiple comparison, simple effects post-hoc test. Asterisks denote statistical significance determined using the post-hoc tests as follows: *p < 0.05, **p < 0.01, ***p < 0.001, ****p < 0.0001.

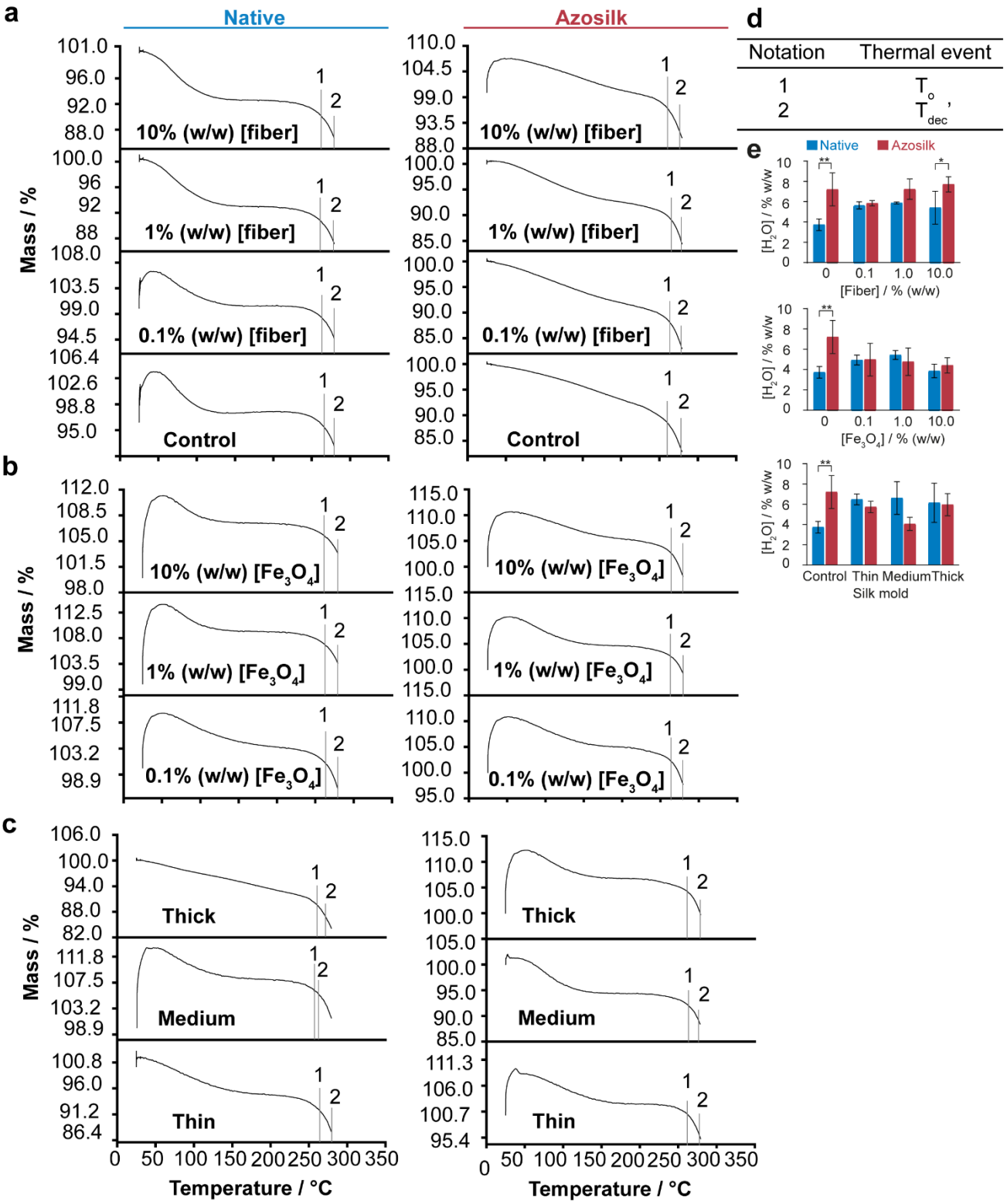

Figure 5.5. Representative first-cycle thermogravimetric analysis (TGA) thermograms of silk films manufactured with (a) different silk fiber concentrations, (b) iron oxide particle concentrations and (c) thicknesses. (d) Thermal event assignment key. **(e)** Composition of water (% (*w/w*)) in silk films determined as the percentage mass loss at 140 °C. ± SD, *n* = 3. Extrapolated onset temperature of decomposition (T_o) and the temperature of maximum decomposition rate (T_{dec}') are reported. Error bars are hidden in the bars and plot symbols when not visible. Multiple factors were evaluated by two-way analysis of variance

(ANOVA), followed by Šidák's multiple comparison, simple effects post-hoc test. Asterisks denote statistical significance determined using the post-hoc tests as follows: *$p < 0.05$, **$p < 0.01$, ***$p < 0.001$, ****$p < 0.0001$.

The silk film properties which impacted the deployment and lifetime of the origami architecture were optimised by varying the silk fiber and iron oxide content and the film thickness (Figure 5.6a–c). Following plasticisation by water annealing, the time of plastic endurance of the azosilk and native silk films in air increased with thickness due to the reduced surface area percentage for evaporation of the thicker films (Figure 5.6a). Across all thicknesses, azo-modification reduced the plasticity time window (Figure 5.6a). I hypothesised that increasing the silk fiber content could increase silk film stiffness, reduce water sorption, and prolong the architecture lifespan. The edges of the films were found to wrinkle and curl when floated on water (Figure 5.6b), a contraction process likely caused by a water sorption gradient. Relaxation of the films then occurred, and the films reassumed their original shape, possibly due to surface wetting (Figure 5.6b). The time taken for initiation of contraction and for initiation of relaxation by films when floating on the air-water interface was used as a measure of shape preservation. For the native silk films, increasing the silk fiber loading from 0 to 10% caused faster relaxation upon contact with water, while this trend was reversed by azo-modification (Figure 5.6b). Consequently, azosilk films with silk fiber contents below 10% (*w/w*) exhibited faster relaxation than native silk films. Finally, all films spiked with iron oxide showed semi-autonomy on water, as they could be pulled along the air-water interface with a cylindrical neodymium magnet (Figure 5.3d). Increasing the iron oxide load from 0.1 to 10% (*w/w*) resulted in decreased electromagnetic field strengths (H) required for magnetic response, from 2.71×10^4 to 0.45×10^4 A m^{-1} for native films and from 1.33×10^4 to 0.27×10^4 A m^{-1} for azosilk films (Figure 5.6c). I speculate that for equivalent iron oxide loadings and thereby equivalent magnetic susceptibilities, the azosilk films show semi-autonomy at longer distances compared to the native films due to reduced viscous drag for azosilk films than for native silk films. The azosilk films glide better on the water surface as the diazonium coupling

increased the presence of defects and air pockets on the film surface (Figure 5.1b) and increased hydrophobic repulsion with the water interface (Figure 5.3a). Due to the rough surface of the films, further experimentation is required to identify the reduction in viscous drag caused by the increased hydrophobicity of the azosilk films.

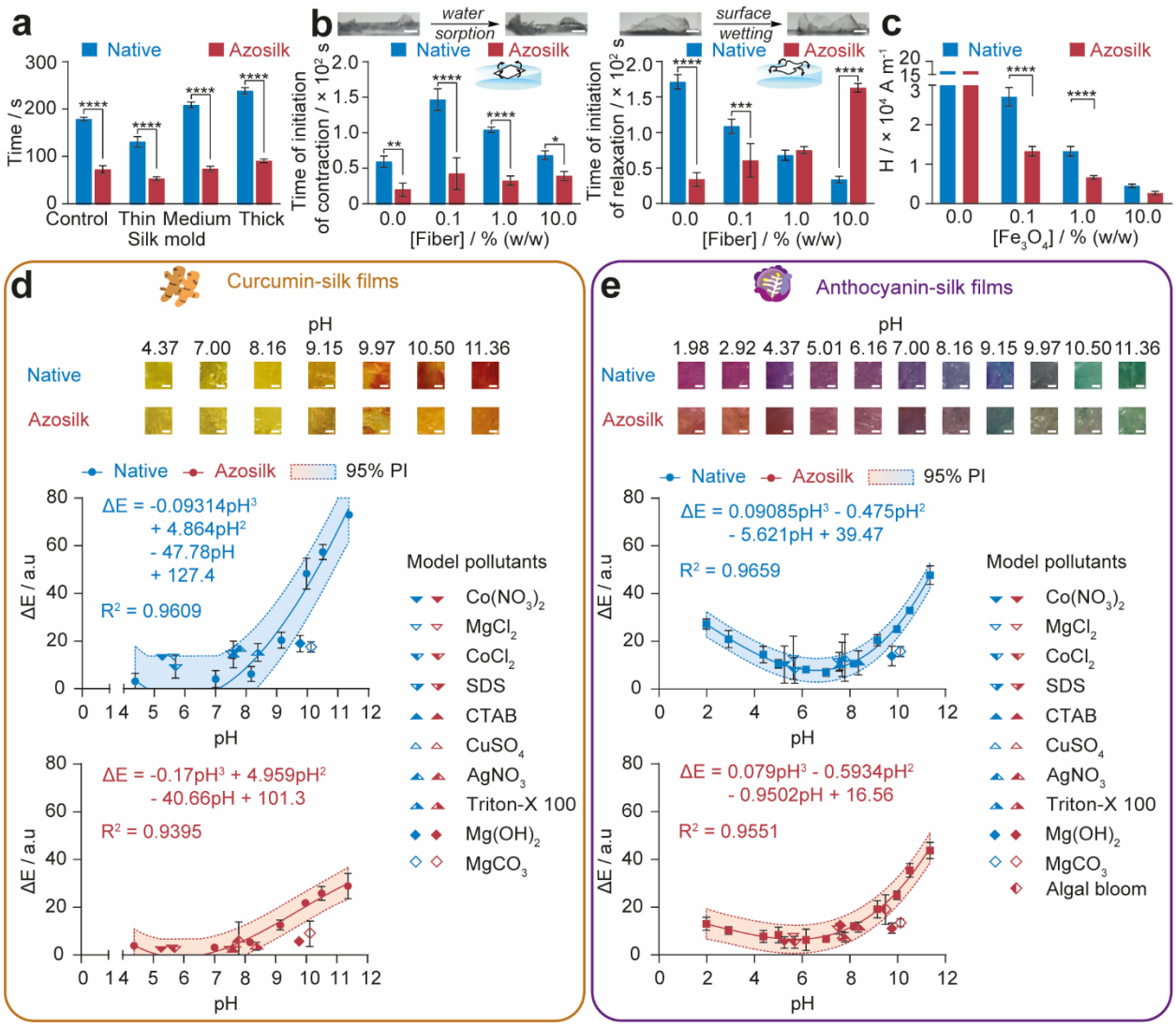

Figure 5.6. Mold-casted native silk and azosilk films demonstrate semi-autonomy and sensing capability. (a) The time window for folding silk films while plasticized following water annealing. **(b)** The time taken for initiation of contraction and initiation of relaxation by films lying on the air-water interface was used as a measure of structural stability in wet environments. **(c)** The electromagnetic field strength (H) as a function of the distance from the surface of an N52 Rare Earth Neodymium round cylinder magnet that was able to pull a floating rectangular-shaped silk film (0.1 g, 25 µm) loaded with iron oxide particles along the water-air interface. The correlation between the environmental pH and color change (ΔE) of **(d)** curcumin-loaded and **I** anthocyanin-loaded silk films, where ΔE was measured with the mean intensities in the Lab color space. The predictive accuracy of the cubic polynomial equations was evaluated using the 95% prediction interval and the measured ΔE of films treated with randomly grab sampled algal blooms and environmentally relevant concentrations of surfactants and heavy metal complexes which served as model pollutants. ± SD, *n* = 3. Error bars are hidden in the bars and plot symbols when not visible. Scale bars = 0.5 cm. Multiple factors were evaluated by two-way analysis of variance (ANOVA), followed by Šidák's multiple comparison, simple effects post-hoc test. Asterisks denote statistical significance determined using the post-hoc tests as follows: *p < 0.05, **p < 0.01, ***p < 0.001, ****p < 0.0001.

Quantification of the color change of anthocyanin and curcumin-loaded polymer films and fibers in response to pH is an active research area for the detection of ammonia produced during food spoilage.[410] Digital image colorimetry, combined with principle component analysis[401] and non-linear regression,[406] has been successfully utilized in these smart packaging systems to enable recognition of spoiled foodstuffs[401] and ammonia content[406] from the degree of the color change exhibited. However, to the best of our knowledge, I provide the first example of silk fibroin-based, eco-sensors for the detection of water-borne, environmental pollutants using curcumin and anthocyanin as natural, non-toxic pH indicators.

For sensing applications, silk films doped with 0.1% (*w/w*) iron oxide particles and casted at medium thickness were loaded with curcumin extracted from turmeric rhizome and anthocyanin extracted from fresh red cabbage (Figure 5.7). Both native and azosilk films showed a visible color change upon loading with the natural pigments (Figure 5.8) and could be used as colorimetric probes for pH changes (Figure 5.6d–e, Figure 5.9). The colors of the azosilk and native curcumin-loaded films were yellow between pH 4.37 and pH 8.16, yellow-orange between pH values of 9.15 and 10.50, and deep orange-red at pH 11.36 (Figure 5.6d, Figure 5.9). The color change confirmed the reversible tautomerisation of curcumin from the predominant yellow keto form in the acidic and neutral environments to the red enol form as basicity increased above pH 8 (Figure 5.10a).[401] The color change was analysed in the RGB color space and revealed a reduction in the green channel intensity for native and azosilk films with increasing pH above pH 8.16, in addition to a reduction in the red channel intensity of native silk films above pH 10.59 (Figure 5.9).

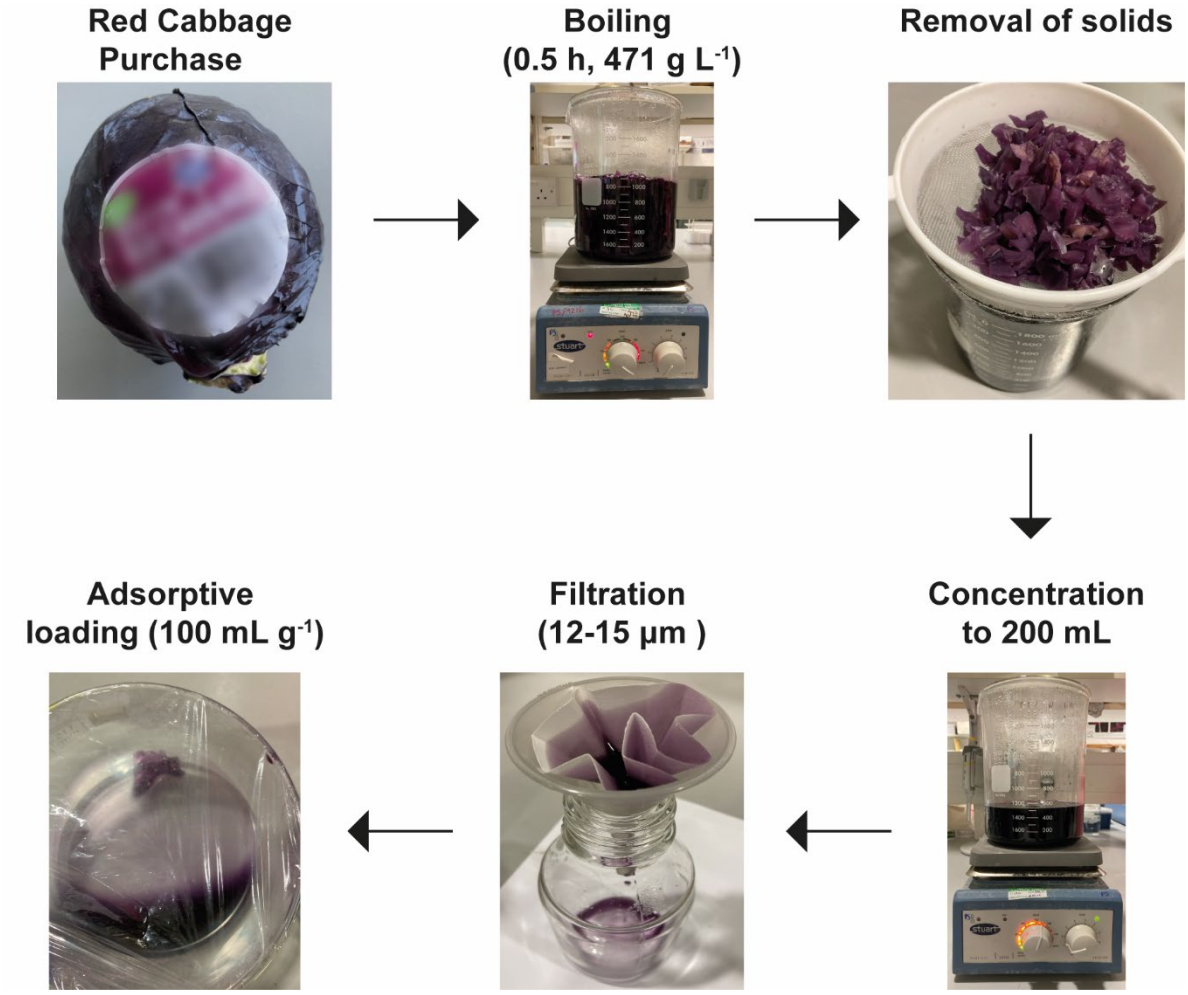

Figure 5.7. Anthocyanin extraction and silk film loading from fresh red cabbage.

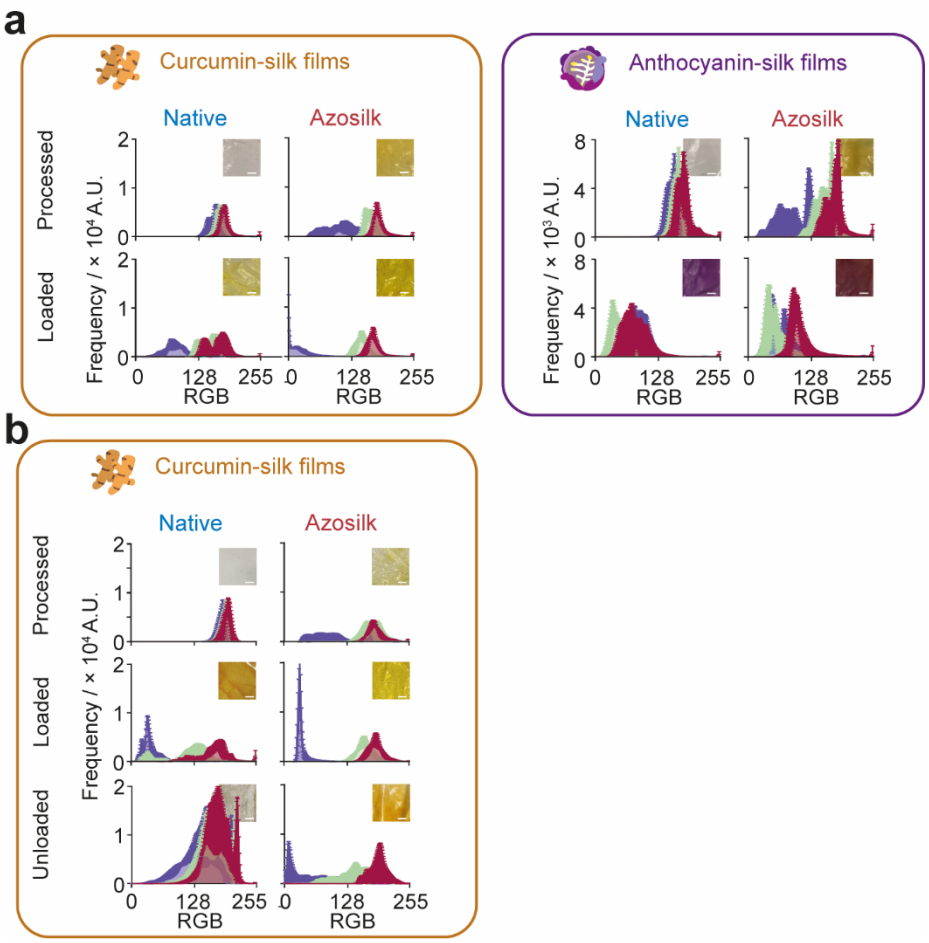

Figure 5.8. The change in pixel channel intensities upon (a) loading medium thickness films containing 0.1% (*w/w*) iron oxide particles with anthocyanin for sensing pH, heavy metal salts and surfactants and with curcumin for sensing heavy metal salts and surfactants. (b) Medium thickness films containing 0.1% (*w/w*) iron oxide particles were loaded with curcumin for sensing pH and unloaded in 0.1 M aqueous NaOH. Scale bars = 0.5 cm ± SD, *n* = 3.

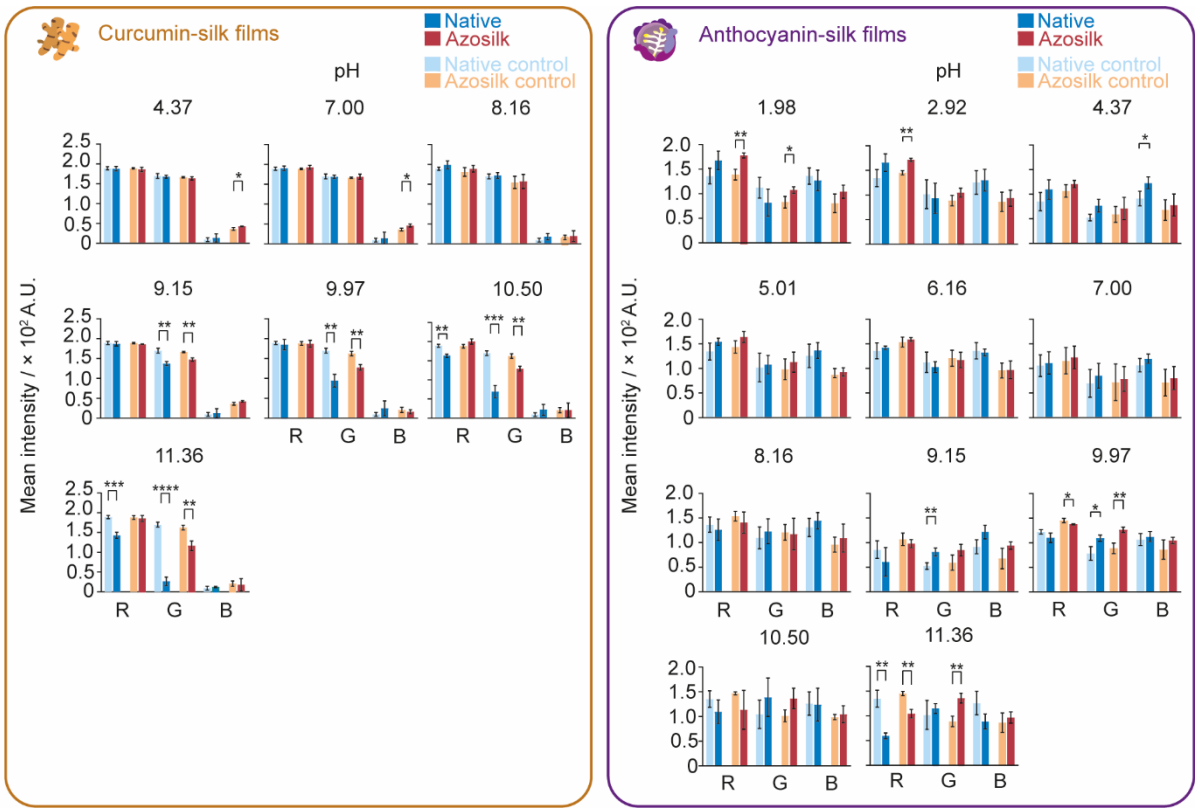

Figure 5.9. The change in mean pixel channel intensities in the RGB color space of curcumin-loaded and anthocyanin-loaded azosilk and native silk medium thickness films containing 0.1% (*w/w*) iron oxide particles in response to pH. ± SD, *n* = 3. Sample pairs were analyzed using the independent *t*-test. Asterisks denote statistical significance determined using the *t*-test as follows: *p < 0.05, **p < 0.01, ***p < 0.001, ****p < 0.0001.

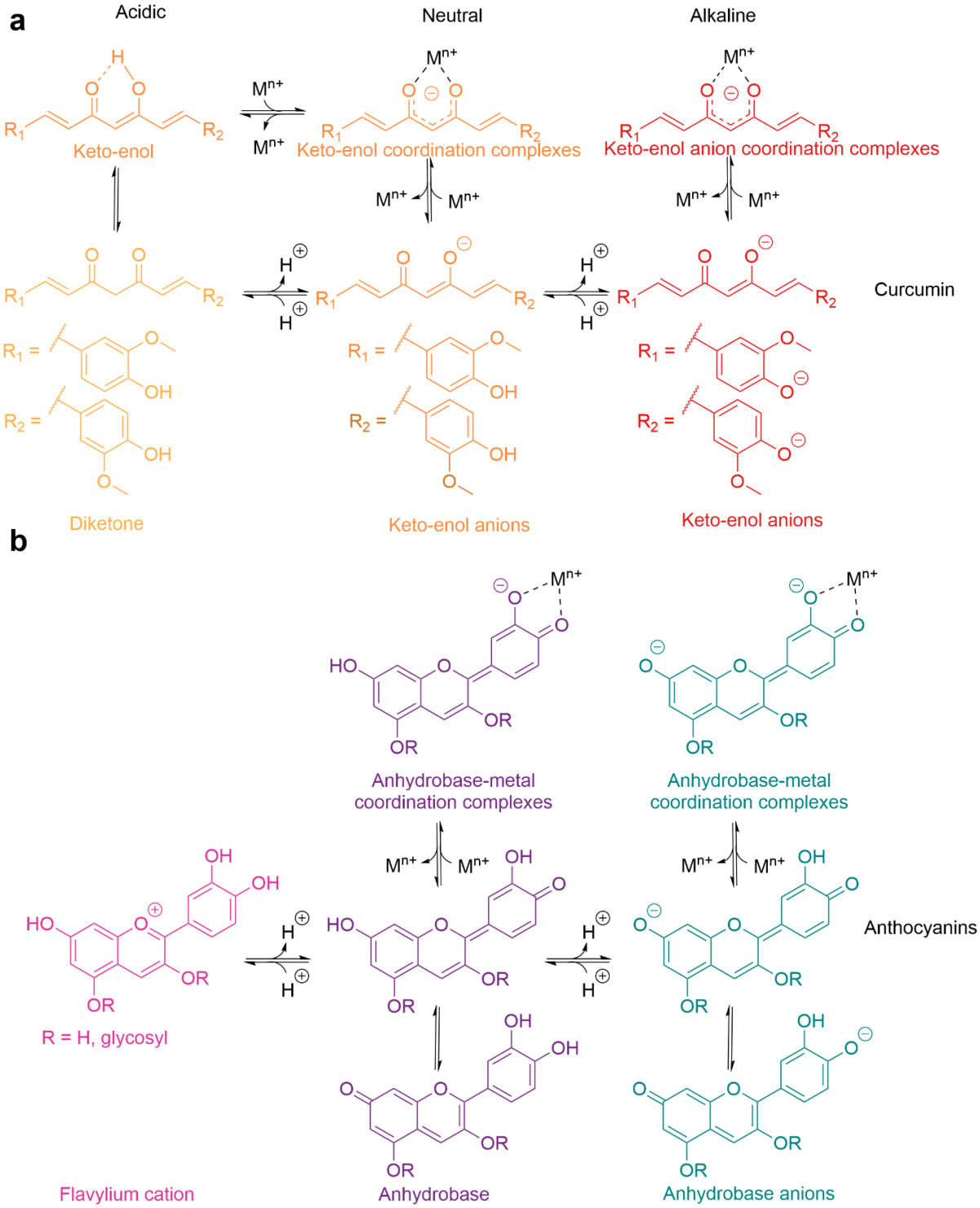

Figure 5.10. The reversible transformations and color changes of (a) curcumin[401, 411] and (b) anthocyanins[401, 412, 413] as pH of the surrounding media is raised, from acidic to neutral and to alkaline conditions.

Anthocyanin-loaded films were magenta-pink in acidic media below pH 4.37 due to the dominant cationic flavylium species,[401, 412] and purple between pH 4.37 and pH 7.00. As equilibrium favoured the quinoidal anhydrobase in alkaline media, the color of the films changed from purple-blue between pH 7.00 and pH 9.15, to blue-green between pH 9.15 and pH 11.36 (Figure 5.6e, Figure 5.9, Figure 5.10b).[401, 412] In the RGB color space, the green channel intensity of native films increased between pH 9.15 and pH 9.97, while the red channel intensity decreased for native and azosilk films as pH was raised from 1.98 to 4.37 and from 9.97 to 11.36 (Figure 5.9). Native silk films were more sensitive to pH than the azosilk films when loaded with curcumin or anthocyanin, as the relative color change was consistently greater than their azosilk counterparts across the pH range investigated (Figure 5.11a).

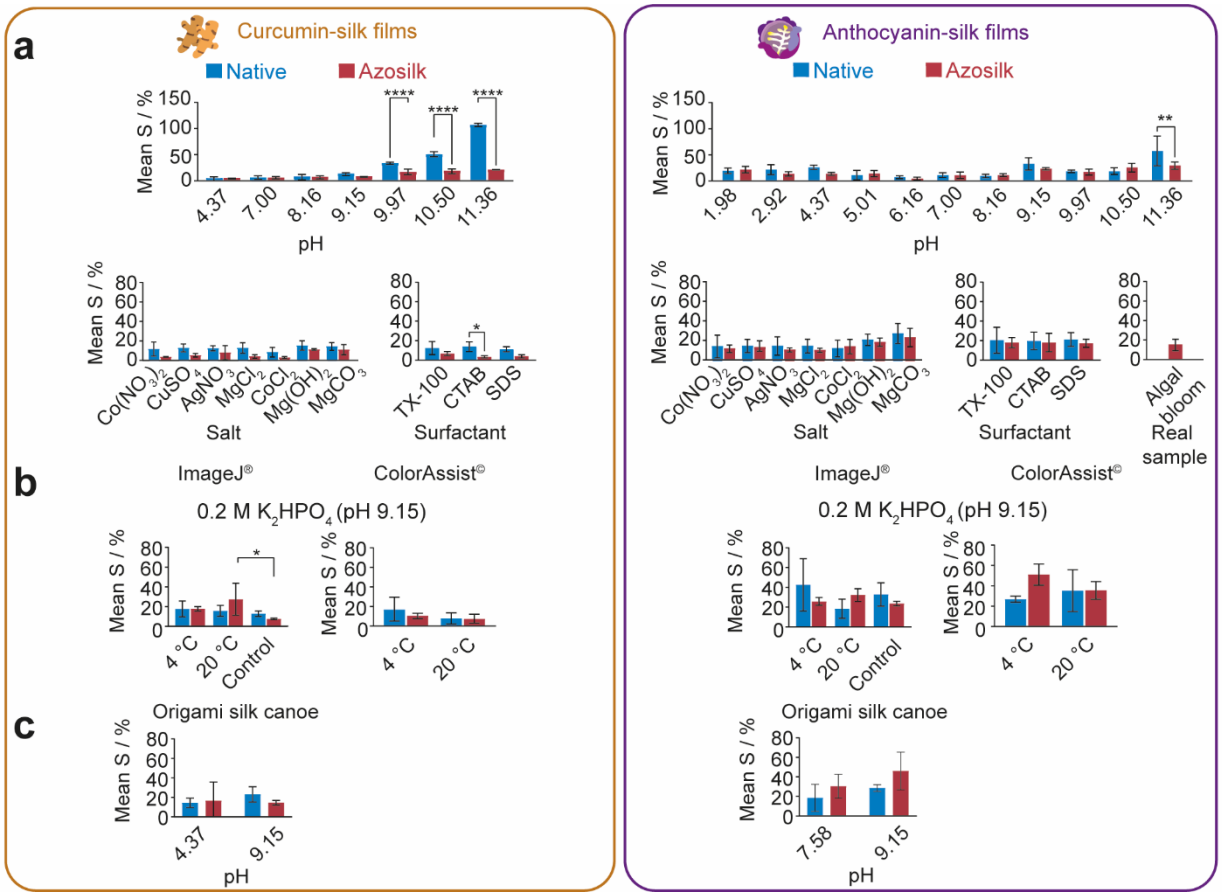

Figure 5.11. The relative color changes of (a) curcumin and anthocyanin-loaded native silk and azosilk films varying pH, surfactant, and heavy metal salt. (b) The storage stability of native silk and azosilk film relative color changes following 31 days of storage under vacuum at 4 or 20 °C using image pre-processing and ImageJ® or ColorAssist Lite© to measure mean RGB intensities. **(c)** The relative color changes of curcumin and anthocyanin-loaded native silk azosilk origami canoes varying pH. ± SD, *n* = 3. Multiple factors were evaluated by two-way analysis of variance (ANOVA), followed by Šidák's multiple comparison, simple effects post-hoc test. Stability was evaluated against the *t* = 0-day control using a two-way ANOVA followed by Dunnett's multiple comparison, simple effects post-hoc test. Asterisks denote statistical significance determined using the *t*-test and post-hoc tests as follows: *p < 0.05, **p < 0.01, ***p < 0.001, ****p < 0.0001.

Calibration curves were constructed for the color change (ΔE) of silk films at pH values between 4.37 and 11.36 for curcumin-loaded films and pH values between 1.98 and 11.36 for anthocyanin-loaded films (Figure 5.6d–e). The ΔE values of curcumin and anthocyanin-loaded films displayed a positive correlation as pH increased from 7.00 to 11.36. Also, the ΔE values for anthocyanin-loaded films showed a negative correlation as pH increased from 1.98 to 7.00. For curcumin and anthocyanin-loaded films, cubic polynomial equations were fitted to ΔE and pH at R^2 values above 0.93. The measured ΔE of all films treated with model pollutants of

domestic, industrial and municipal wastewater examples[414] in addition to randomly grab sampled algal blooms lay within the 95% prediction intervals of the calibration curves.

Although curcumin and anthocyanin can coordinate with some heavy metals, namely di- and trivalent metals (Figure 5.10),[393, 412, 415, 416] no measurable color changes were identified for the loaded native or azosilk films with 0.1% (*w/w*) iron oxide dopant at the lower limits[417-420] of toxic concentrations of heavy metals at pH values below 9.76 (Figure 5.6d–e, Figure 5.11a, Figure 5.12a). However, following exposure to $Mg(OH)_2$ (pH 9.76) and $MgCO_3$ (pH 10.12), the ΔE for curcumin and anthocyanin-loaded native and azosilk films lay out-with the 95% prediction intervals at the respective pH values (Figure 5.6d–e). This could indicate value as a novel sensing assay for the concentration of divalent heavy metals, provided pH was controlled. Curcumin-silk films could be unloaded by treatment with sodium hydroxide,[421] allowing recycling of the film and loading with alternative indicators (Figure 5.8). However, unloading the azosilk films increased the film brittleness and led to fracture. This effect was likely a by-product of polymer backbone scission and the resulting generation and growth of voids, cavities, and cracks.

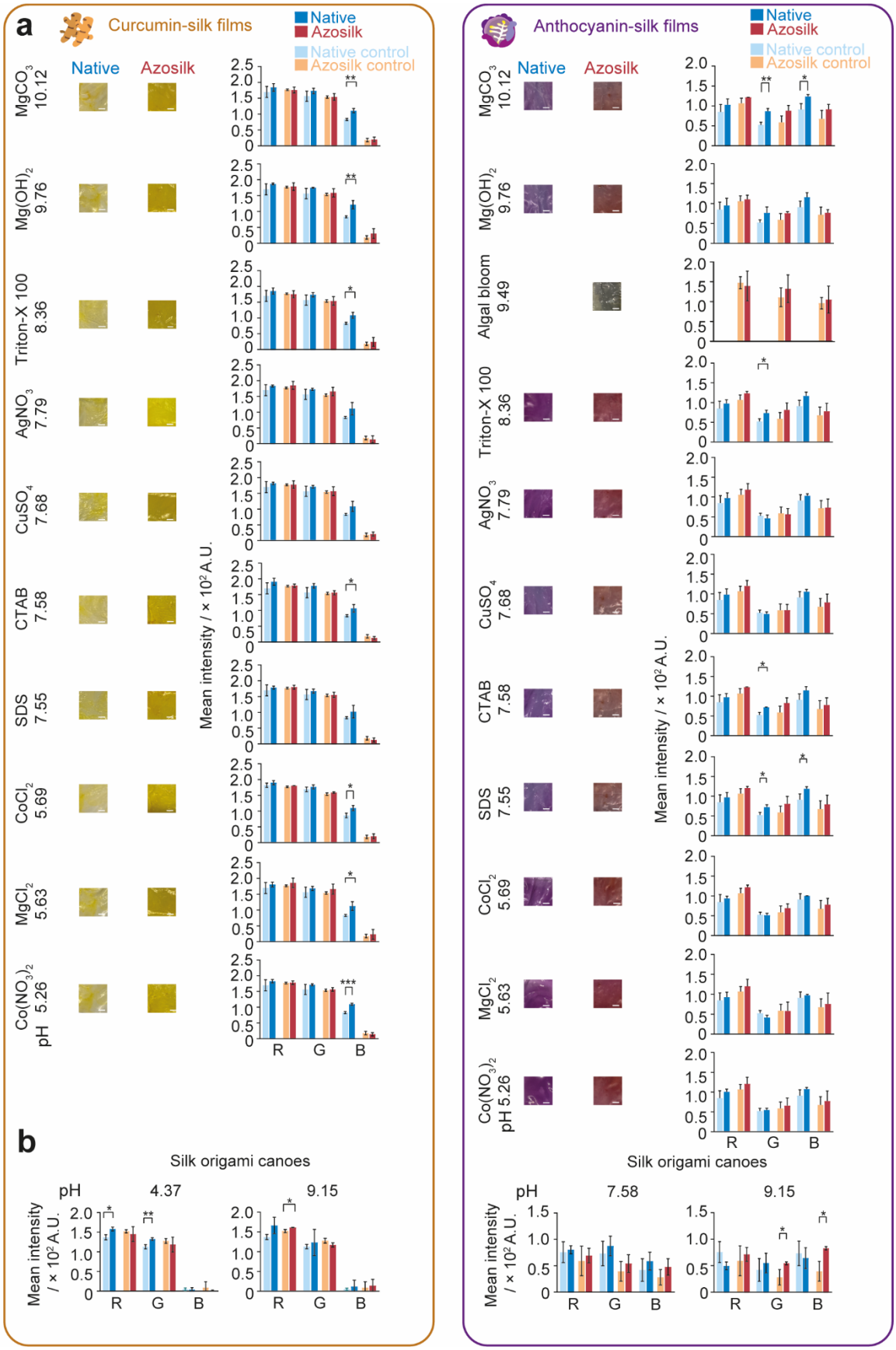

Figure 5.12. The change in color and mean pixel channel intensities of curcumin-loaded and anthocyanin-loaded azosilk and native silk medium thickness films containing 0.1% (*w/w*) iron oxide particles after exposure to (a) surfactants and heavy metal salts

serving as model pollutants, and (b) after folding into 3D origami silk canoes and exposure to media at the indicated pH. Scale bars = 0.5 cm. ±SD, *n* = 3. Sample pairs were analyzed using the independent *t*-test. Asterisks denote statistical significance determined using the *t*-test as follows: *p < 0.05, **p < 0.01, ***p < 0.001, ****p < 0.0001.

The color change of the curcumin-azosilk, anthocyanin-azosilk, and anthocyanin-silk films following exposure to 0.2 M potassium phosphate buffer (pH 9.15) was stable following storage at 4 and 20 °C *in vacuo* for 31 days (Figure 5.11b, Figure 5.13). Conversely, the curcumin-silk film only showed color stability when stored for 31 days at 4 °C (Figure 5.13). This stability was evidenced by the ΔE values for all film and indicator types following storage lying within the 95% prediction intervals of the calibration curves for the fresh films (Figure 5.13b). The mean pixel color intensity changes of all films in the RGB and Lab color spaces were determined directly using the smartphone application, ColorAssist Lite© (Figure 5.13a–b). The relative color changes of the azosilk and native silk films were not significantly different when measured directly using the smartphone application, and this reflected the results from digital postprocessing and segmentation using ImageJ® (Figure 5.11b). Agreement between the 95% prediction intervals and measured ΔE using ColorAssist Lite© were obtained for curcumin-azosilk films stored at 4 and 20 °C, curcumin-native silk films stored at 4 °C, anthocyanin-native silk stored at 20 °C and anthocyanin-azosilk films stored at 20 °C (Figure 5.13b). Consequently, the omission of the digital postprocessing step would be expected to lower the accuracy of pH prediction. It is likely that this could be improved by constructing the calibration curves with data acquired directly in ColorAssist Lite©, although the greater random error could result in larger prediction intervals and reduced sensitivity to drift in environmental pH. Nevertheless, the capability of digital image colorimetry using smartphone applications can streamline image analysis in field conditions by removing the image postprocessing and segmentation steps.[422]

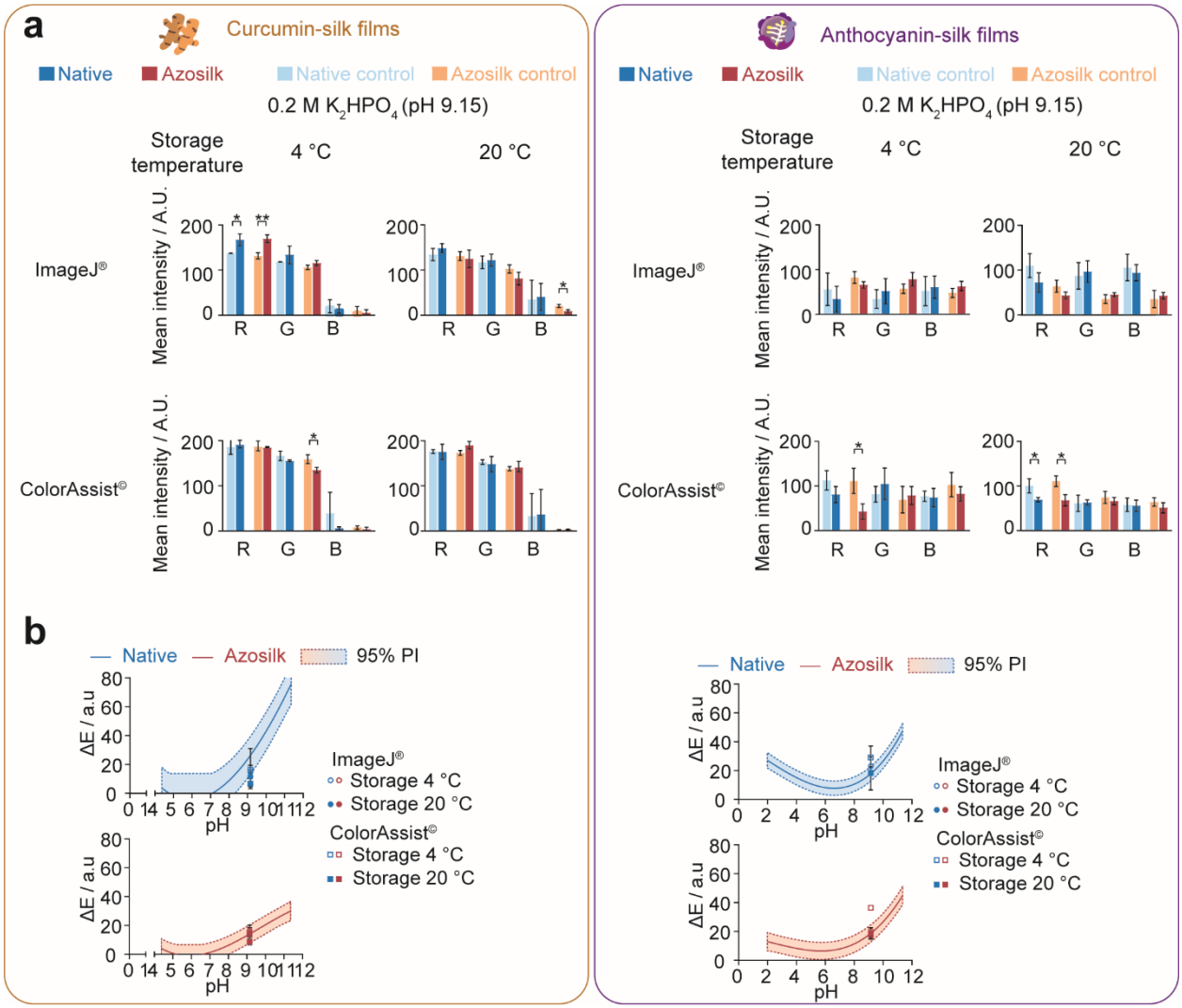

Figure 5.13. The colorimetric stability of curcumin and anthocyanin-loaded native silk and azosilk medium thickness films containing 0.1% (*w/w*) iron oxide particles. Following 31 days of storage *in vacuo* at 4 or 20 °C, the color changes after exposure to 0.2 M potassium phosphate buffer (pH 9.15) were monitored in **(a)** the RGB color space using the mean pixel channel intensities, and **(b)** in the Lab color space to calculate the color change (ΔE) of silk films. Digital image colorimetry was undertaken using image pre-processing and analysis in ImageJ® or directly in ColorAssist Lite©. ± SD, *n* = 3. Sample pairs were analyzed using the independent *t*-test. Asterisks denote statistical significance determined using the *t*-test as follows: *p < 0.05, **p < 0.01, ***p < 0.001, ****p < 0.0001. ±SD, *n* = 3.

As a proof of principle, native silk and azosilk medium thickness films containing 0.1% (*w/w*) iron oxide were then folded into a variety of 3D origami structures, including waterborne boats and airborne darts and spinners (Figure 5.14, Figure 5.15 and Figure 5.16).

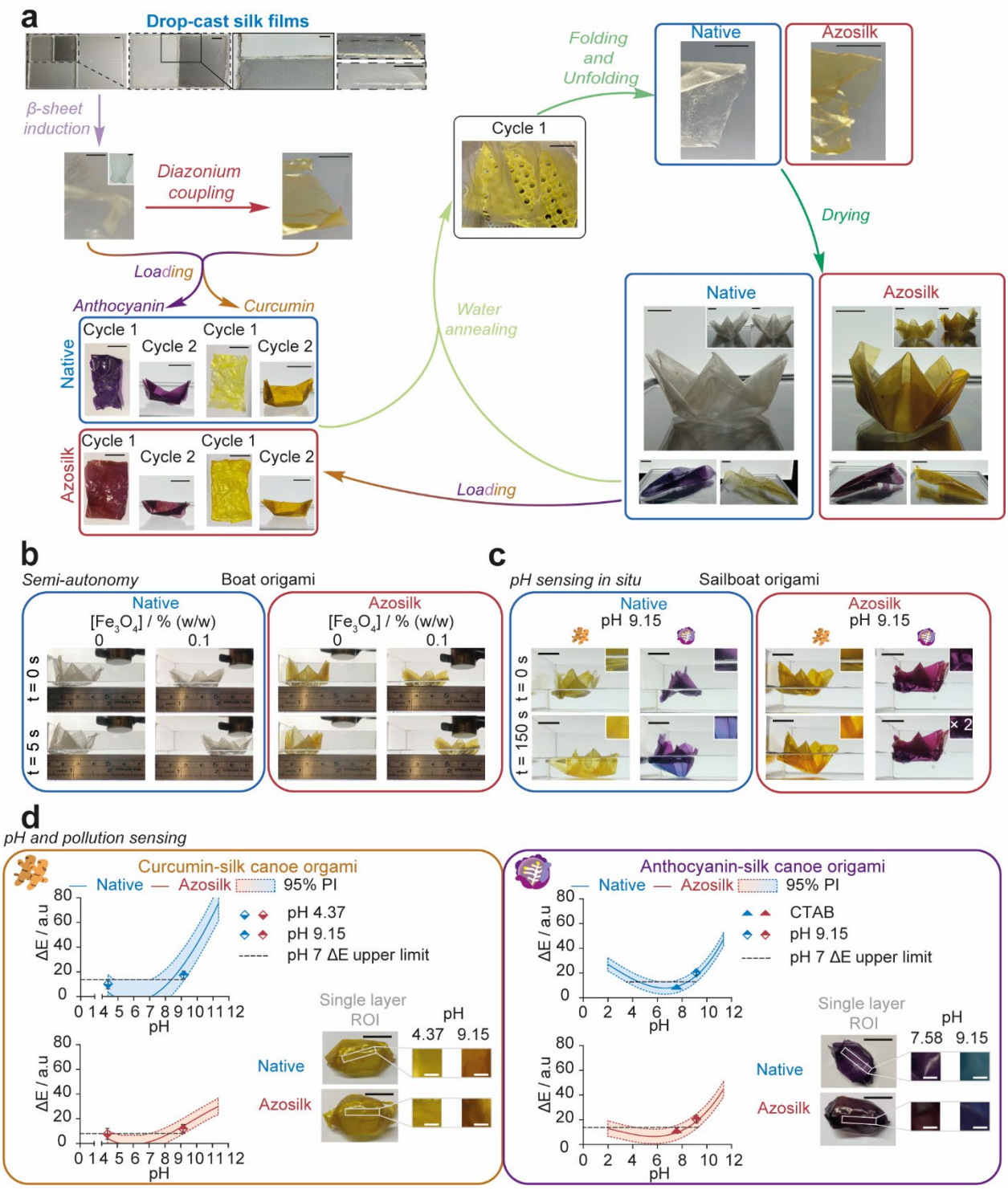

Figure 5.14. Smart silk origami as a structurally stable environmental pollution sensor. **(a)** The simplified origami workflow for the preparation of 3D, reusable devices. For the complete workflow, refer to Figure 5.16. **(b)** Semi-autonomous movement of origami silk boats across water using a magnet. **(c)** Visual detection of color changes in silk sailboat origami with pH. (d) Sensing capability of silk canoe origami to pH and contaminated environmental water models using the 95% prediction interval of the cubic polynomial calibration curves for ΔE and pH. ± SD, *n* = 3. Error bars are hidden in the bars and plot symbols when not visible. Scale bars = 2 cm. Asterisks denote statistical significance determined using the *t*-test and post-hoc tests as follows: *p < 0.05, **p < 0.01, ***p < 0.001, ****p < 0.0001.

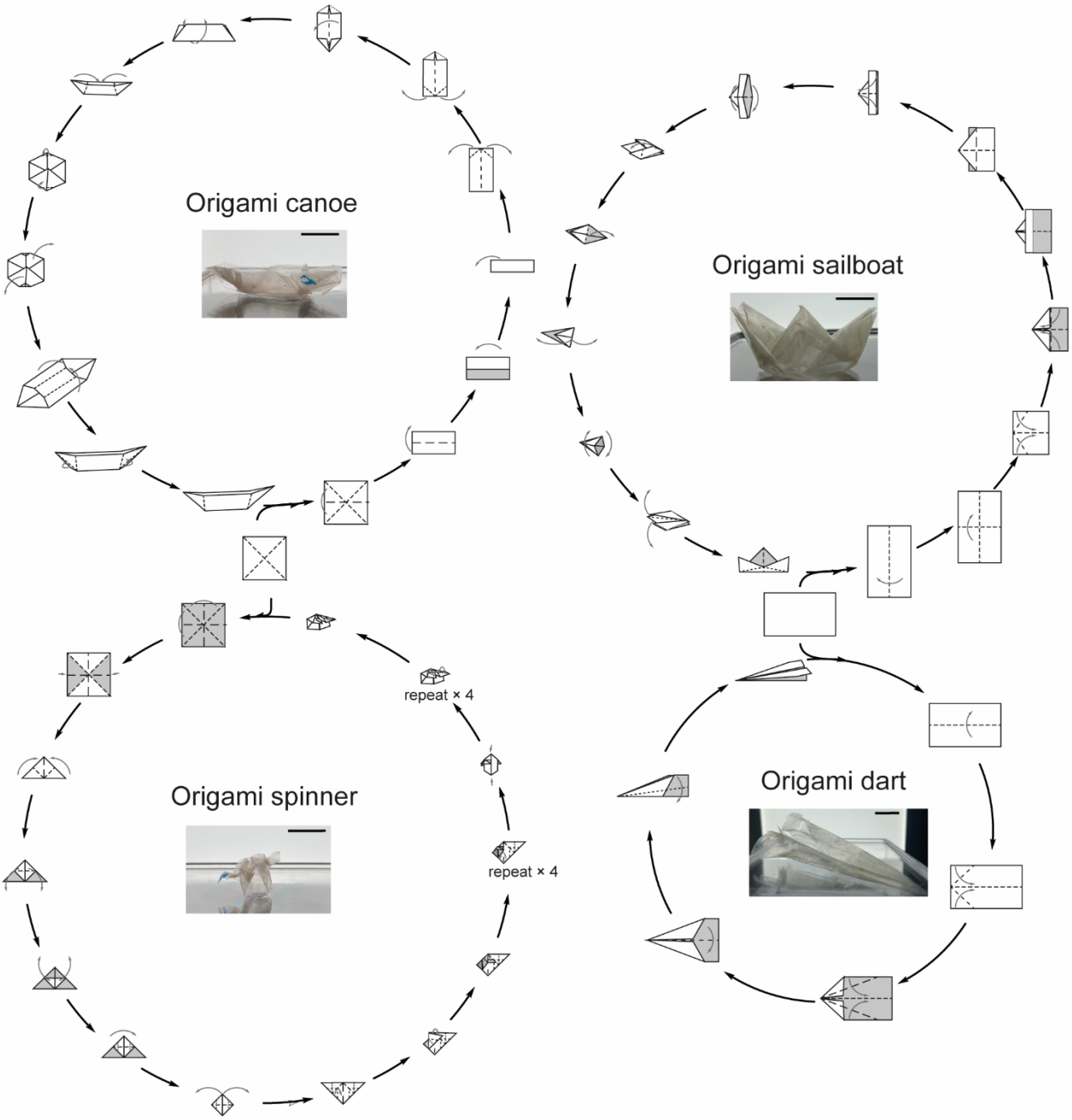

Figure 5.15. Origami folding and the resulting silk film origami structures.

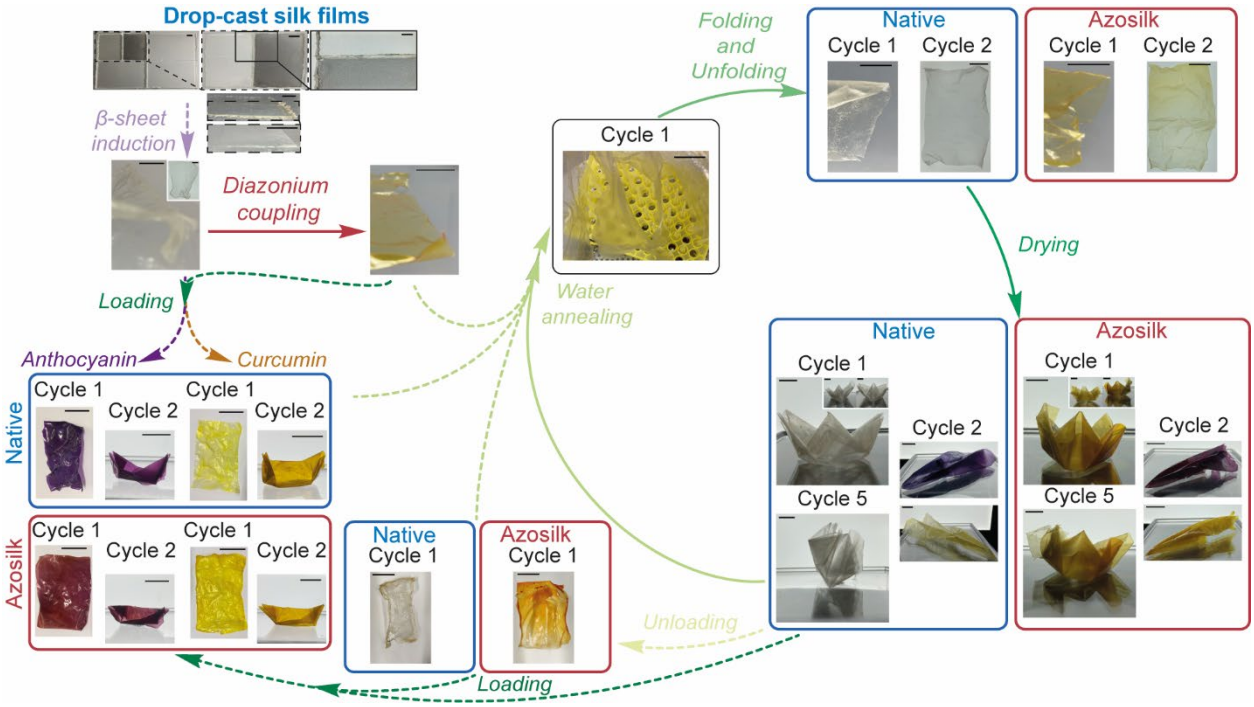

Figure 5.16. The full workflow for the lab-scale production of smart silk origami eco-sensors.

Silk origami structures could be reused for at least five cycles prior to elastic failure upon folding, and the films could also be reloaded with chemical indicators (Figure 5.14a). I speculate that the simple, manual origami manufacturing process will aid the recycling of eco-sensors in remote locations and communities. In addition, both native and azosilk examples of 3D silk origami sailboats remained structurally stable for at least 3 days on ultrapure water. An efficient method for device distribution and recovery using magnetic fields as the energy source for locomotion was achieved, as the silk origami retained semi-autonomy upon folding (Figure 5.14b). Silk origami sailboats were then used as *in situ* pH probes and showed visible color changes along their hulls within 2.5 min of exposure to a 0.2 M potassium phosphate buffer at pH 9.15 (Figure 5.14c).

The silk canoe design enabled colorimetric analysis of the keel of the boat, as this region of interest consisted of a single layer. The color changes as pH increased from 4.37 to 9.15 for curcumin-loaded canoes and from pH values of 7.58 to 9.15 for anthocyanin-loaded canoes could be modelled using the 95% prediction intervals of the cubic polynomial

correlation between ΔE and pH for the unfolded silk films (Figure 5.14, Figure 5.11c, Figure 5.12b).

Both native silk and azosilk films loaded with curcumin or anthocyanin could be used for the detection of polluted aqueous environments at alkaline pH. The pH at which the upper ΔE limit and the lower ΔE limit of the 95% prediction intervals intersected was used to identify the minimum pH change from neutrality which would be required to confirm polluted water. For example, for aqueous environments with a desired pH value of 7.00, the origami canoes could detect contamination with 95% accuracy when pH rises above pH 9. Additionally, increased aqueous acidity could also be probed with 95% accuracy using the anthocyanin-loaded, native silk origami canoes at pH values below 3. Consequently, the anthocyanin-loaded, native silk origami canoes provide the most suitable eco-sensors for the detection of contaminants ranging from excessive algae growth[423], to acid rain.[424] The simple image acquisition process means that data from deployed silk origami eco-sensors could be monitored in near real-time using field conditions or remotely by aerially acquired photography.

5.4 Conclusion

In conclusion, soft origami devices were folded from silk fibroin films and loaded with natural, non-toxic dyes for colorimetric determination of environmental pH. The boats preserved their shape for at least 3 days on water and could exhibit color changes within 1 min after exposure to solutions of basic metal salts, surfactants and algal blooms. These eco-green sensors demonstrate the practical importance of origami for engineering silk devices and enable a simple, deployable approach for direct monitoring of pH and pollution.

Chapter 6: Outcomes and Future Directions

This chapter summarizes the research outputs of the thesis, including: (i) silk nanoparticle manufacture in semi-batch format,[350] (ii) mixing and flow-induced nanoprecipitation for morphology control of silk fibroin self-assembly,[362] (iii) volumetric scalability of microfluidic and semi-batch silk nanoprecipitation methods[425] and, (iv) smart silk origami as eco-sensors for environmental pollution.[426] For future work, *in situ* drug loading of silk fibroin nanoparticles, *in vitro* and *in vivo* safety and biodistribution and, surface modification of silk fibroin materials are proposed as solutions to improve nanoparticle drug loading, estimate nanoparticle biodistribution and improve the chemospecificity of silk functionalization. Finally, the thesis is rounded up in a general conclusion.

6.1 Thesis Conclusions

The thesis was underpinned by the work of Seib, Wongpinyochit and co-workers, who showed that *B. mori* silk-based nanomedicines can be prepared by nanoprecipitation in batch[153, 185] and microfluidic processes.[174, 179] Critically, these nanoparticles could adsorb doxorubicin post-synthetically and be covalently modified using cyanuric chloride-activated mPEG[159, 160] and Alexa Fluor® 488 succinimidyl ester.[183] The PEG-bioconjugate silk nanoparticles showed reduced aggregation in cell culture medium[160] and slower biodegradation[152] compared to native silk nanoparticles. However, improved drug loading (>4% *w/w*)[185] and scalable manufacturing methods were required for the advancement of anticancer-silk nanoparticles into pre-clinical *in vivo* studies. Consequently, this thesis further explored the scalability of processing methods to obtain silk nanoparticles for anticancer nanomedicines. Due to the impact of COVID-19 (SARS-CoV-2), origami folding was used as a scalable proof-of-concept to investigate the impact of silk processing methods, such as heterogeneous chemical modification and surface adsorption of natural dyes, on properties relevant to eco-sensing applications. The principle aim of this thesis was to investigate the processing parameters which dictate the outcomes of silk nanoprecipitation for drug delivery and of silk film origami folding for eco-sensing.

The first objective was to establish a standardized process for silk nanoprecipitation in semi-batch format. Manufacture across all tested formulations achieved nanoparticles between 104 and 134 nm in size with high β-sheet content, spherical morphology and stability in aqueous media for over 1 month at 4 °C. This semi-automated drop-by-drop, semi-batch silk desolvation offered an accessible, higher throughput platform for standardization of parameters that are difficult to control using manual methodologies (Chapter 2).

The second objective was to assess and characterize the impact of key formulation and process parameters on silk nanoprecipitation using semi-batch and microfluidic formats of low and high shear. The morphology of silk assemblies could be tuned from rod-like to spherical nanoparticles by increasing supersaturation of the high-shear micro-mixing process,

thereby supporting a role for fast mixing in the production of narrow-polydispersity silk nanoparticles. This work provided new insight into the effects of shear during nanoprecipitation and provided a framework for scalable manufacture of spherical and rod-like silk nanoparticles (Chapter 3).

The third objective was to estimate the volumetric scalability of the semi-batch and microfluidic platforms using the optimized formulation parameters. In semi-batch format, increased volumetric scale resulted in significant drifts to nanoparticle performance characteristics when the mixing time and average shear rate of mixing were not standardized. However, the high repeatability and reproducibility of microfluidic manufacture strengthened chip parallelization as a production strategy for silk nanoparticles at pilot, clinical, and industrial scales (Chapter 4).

Finally, the fourth objective was to investigate the critical process parameters for the fabrication of a semi-autonomous silk eco-sensor. Semicrystalline silk films were created by doping with iron oxide particles, mold casting and annealing. Diazonium coupling aniline with doped silk films in heterogeneous format resulted in azo-silk films with reduced water contact angles compared to native films. Natural pH indicators (curcumin and anthocyanin) could be loaded onto the surface of native and azofilms and the films used to measure pH changes in environmentally relevant media. The flat silk films could be folded into 3D geometries using origami principles following plasticization. Silk origami boats performed locomotion under a magnetic field, were reusable and displayed colorimetric stability for 31 days at room temperature *in vacuo*. The critical parameters for the design of the semi-autonomous silk film, including ease of folding, shape preservation and locomotion in the presence of a magnetic field, were characterized, and pH detection was achieved by eye and by digital image colorimetry with a response time below 1 min. This work provided a platform for further optimization of origami lifetime and recovery, environmental utility, and pH-sensing ability (Chapter 5).

6.2 Future Work

The project validated the production of silk fibroin nanoparticles using semi-batch and microfluidic-assisted desolvation and demonstrated the performance of silk fibroin eco-sensors loaded with curcumin and anthocyanin as natural pH-indicators. Both semi-batch and microfluidic-assisted desolvation had disadvantages when considering scale-up. While the semi-batch format had higher throughput than microfluidic-assisted desolvation at lab-scale, the ability to parallelize microfluidic chips could increase throughput and make microfluidic-assisted desolvation more amenable to scale up. I was involved in running pilot studies to investigate the impact of different process factors on nanoparticle manufacture in semi-batch and microfluidic-assisted formats. Based on the research outputs and limitations of this study, I would expect this project to inform on future experimental design to validate: *in situ* drug loading of silk fibroin nanoparticles; the *in vitro* and *in vivo* safety and biodistribution of silk fibroin nanoparticles; and, surface functionalization of silk fibroin materials.

6.2.1 *In situ* drug loading of silk fibroin nanoparticles

In this thesis, the manufacture of native silk nanoparticles as a potential anti-cancer drug carrier was investigated (Chapters 2, 3 and, 4). Preformed native and PEGylated silk nanoparticles can be loaded with the anti-cancer chemotherapeutic doxorubicin, by surface adsorption.[160, 183] However, the drug loading achieved in these studies was below 4% *w/w*, and would need to be increased to over 10% *w/w* to be applicable for clinical development.[160, 183] Microfluidics have been used for one-step *in situ* drug encapsulation and nanoprecipitation to simplify the production process of lipid and polymeric nanoparticles.[427] To increase the drug loading capacity the concentration of drug can be increased to the solubility limit and a more hydrophobic anthracycline such as daunorubicin can be used. An alcohol screen is required to alter the nanoprecipitation process and drug adsorption properties using the 5:1 anti-solvent:aqueous total flow rate. To increase the throughput of manufacture, the flow rate should be increased from 1 mL min^{-1} and the scalability of production investigated using parallelization of the microfluidic chips. The impact of processing parameters like flow rate and

anti-solvent species on encapsulation efficiency, drug loading, particle stability, size, morphology and drug release should be monitored to progress silk fibroin nanoparticle production to pre-clinical *in vivo* studies.

6.2.2 *In vitro* and *in vivo* safety and biodistribution

Over 70% of phase II clinical trials fail due to inadequate safety and efficacy of new pharmaceuticals.[428-430] Optimization of nanocarrier morphology can improve these features of new nanomedicines by passive targeting and altered biodistribution.[431, 432] Therefore, to investigate the safety, efficacy and hemocompatibility of spherical and rod-like nanoparticles *in vitro* studies are required. Additionally, to determine if silk nanoparticles passively collect in the tumor, *in vivo* studies are required. The *in vivo* study would use the orthotopic MDA-MB-231 mouse xenograft model for triple negative breast cancer. Triple negative breast cancer is a fast-growing breast cancer with poor treatment prognosis in humans.[433] The difficulty in treatment in humans arises from the high chance of metastasis and lack of estrogen, progesterone and human epidermal growth factor receptors.[434] Consequently, triple negative breast cancer would benefit from improved drug delivery and efficacy.

The following sets of studies are proposed for future work: the impact of silk nanocarrier morphology on cellular and humoral hemostasis in human blood to reduce complement activation and inflammatory pathways; assessment of immune cell interaction to improve nanomedicine circulation time, biodistribution and drug delivery. Analysis of hemocompatibility of rod-like and spherical silk nanoparticles can be undertaken using human blood which and incubating with both nanoparticle types using Chandler Loop methodology.[435] Subsequent analysis of hemostatic and inflammatory responses (e.g., ELISA, FACS) would aid nanocarrier design to reduce complement activation and inflammatory pathways.[435] Rod-like morphology can prolong the circulation time of intravenous nanomedicines by reducing immune cell uptake.[436-439] Endocytic uptake of fluorescently labelled spherical and rod-like silk nanoparticles[159] should be imaged in isolated monocytes[435] by time-lapse live-cell fluorescence microscopy. Immune cell interactions[440] could be analyzed by flow cytometry to

improve nanomedicine circulation time, biodistribution and drug delivery. Analysis of nanoparticle circulation time can be conducted by injecting fluorescently labelled silk nanoparticles in a zebrafish (Danio rerio) model.[436, 437, 439] Physical characterization can be conducted with DLS, AFM, FTIR, STA, cryoSEM and 3D SEM.

The biodistribution of silk nanoparticles in mice models can be determined using Cyanine 5-labelled silk nanoparticles. Female xenograft mice bearing luciferase-expressing MDA-MB-231 cells with a tumor volume of 200 mm^3 should be injected in the tail vein with silk nanoparticles. The nanoparticle biodistribution can be monitored over time using the IVIS imaging system to measure live associated fluorescence and tumor reduction can be monitored over time by analyzing tumor bioluminescence intensity. The results should be corroborated by collecting tissues (e.g., heart, liver, spleen, lung, kidney and tumors) at several time points.[441]

6.2.3 Surface modification of silk fibroin materials

In this study diazonium coupling of silk fibroin films with aniline was used to alter the hydrophobicity of silk films (Chapter 5). The chemical modification of silk fibroin using diazonium coupling could be extended further to generate photo, host- and pH-responsive silk materials by installation of the azobenzene moiety. Photoactivatable azobenzene salts can result in reversible changes of thermal conductivity, fluorescence, phases and, micelle assembly with ultraviolet and visible light.[442-444] Hydrophobicity switching can occur with ultraviolet irradiation and conversion of the azo bond from *trans* to *cis* conformation. This process is reversed with the thermal back-reaction or visible light irradiation. Host-guest supramolecular assembly of azobenzene occurs in the presence of host agents, namely cyclodextrin[445-448], pillar[n]arenes[449] and, cucurbituril,[450] which can be exploited for third-generation, reversible bioconjugation. This process is reversible, with disassembly occurring upon *trans-cis* conversion following ultraviolet irradiation. The chelating agent tunes the polarity and solubility of the azobenzene substrate upon assembly,[451] leading to applications in: purification; catalysis; hydrogel assembly; and, size and shape responsiveness of

nanoparticle-assemblies. For example, azobenzene surface-decorated nanoparticles have resulted in third-generation PEGylation *via* host-guest inclusion using PEGylated-cylodextrin.[452]

Surface decoration of preformed silk nanoparticles using an azobenzene with a solubilizing linker or sulfonic acid group[453, 454] would result in aqueous solubility of the azobenzene substrate and colloidal stability of the nanoparticle product. To generate azobenzene surface-decorated nanoparticles, functionalization of liquid silk and complexation with cyclodextrin could also be conducted prior to anti-solvent desolvation.[455] The azobenzene decorated nanoparticles would be suitable for third-generation bioconjugation techniques using host agents. Additionally, cyclodextrin-silk nanoparticles can be synthesized according to literature,[456] enabling reversible hydrogel formation by complexation with azobenzene-silk nanoparticles.

Notably, azobenzene-silk materials may not be applicable for anti-cancer applications. The azo-bond can be susceptible to reduction in hypoxic conditions which results in the release of aniline, although this mechanism can be leveraged as a pro-drug methodology by designing cleavable units.[457] Further, the ultraviolet light used for the *trans* to *cis* azobenzene isomerization is poorly penetrating and can damage healthy tissue.[458] To allow for visible light activation, electron poor or electron rich azobenzene derivatives could be conjugated to silk.[458, 459]

To ensure reliable properties, aqueous solubility of azobenzene-modified silk and, colloidal stability of the resulting nanoparticles, the installation of azobenzene units on liquid silk should be chemo- and site-specific for hydrophilic regions of the silk molecule.[460] However, reliable chemo- and site-specificity is not possible due to: the silk amino acid sequence; the polydisperse silk mixture obtained from regenerating the silk cocoon; and, the kinetically-controlled formation of nanoparticles which results in heterogeneous surface chemistry. For example, conjugation of aminoazobenzenes directly with silk using carbodiimide coupling would likely result in side-reactions of activated silk esters with silk amines. This is not

desirable for phase-changes within films or hydrogels and could increase the size of resulting nanoparticles. However, amide coupling between lysine and azobenzene-activated esters provides a feasible conjugation route as it results in less potential side reactions and would occur primarily on hydrophilic regions of the silk molecule.

The development of recombinant silk means that site-specific modifications can be made. Click chemistry like the strain promoted azide-alkyne click reaction is a bio-orthogonal reaction that can be run without the need for a copper catalyst.[284, 461] Teramoto and colleagues have developed an azide-clickable silk which can be degummed using the 30 minute sodium carbonate (0.02 M) or the 30 min 0.5% *wt* $NaHCO_3$ method to preserve the azide residues. SDS-PAGE analysis and weight change from degumming from multiple groups indicate partial H- and L-chain degradation using these methods.[179, 276, 462] Importantly, the regenerated silks using these methods are suitable for biomedical applications due to complete removal of sericin. Consequently, the azidosilk could be processed into silk nanoparticles, the number of surface-accessible azides estimated and the surface azides used as click-handles for the conjugation of stealth ligands.[284, 462] By measuring the number of surface azides, the functionalization of stealth ligands could be monitored and optimized.

Azidosilk films made using the 30 minute sodium carbonate (0.02 M) degummed azidosilk have been used in heterogeneous click reactions with DBCO-PEG.[276, 285, 286, 463] To identify the number of azides on the surface of silk films, Teramoto and colleagues used the biotin-streptavidin-HRP interaction.[285] This method may not work as well for nanoparticles with sizes between 50-100 nm as the size of HRP-streptavidin is larger than 30 nm,[276, 464] and numerous centrifugation cycles are required for purification. An alternative method is to use biotin to bind avidin in the HABA-avidin fluorescent assay or the fluorescent 488-streptavidin conjugate. For example, the dithionite cleavable diazo or photocleavable DBCO-biotin HABA-avidin assay can measure the fluorescence of labelled nanoparticles.[465-472] This method assumes that sodium dithionite does not degenerate silk, all the surface azides react with DBCO-biotin, 100% of bound biotin is cleaved from surface, and that the cleaved biotin groups

are washed away from the nanoparticle surface. The avidin methods are also limited by the similar avidin size relative to the silk nanoparticles, which could result in an artificially low estimate of surface azides.

There are several feasible assays to estimate the number of surface-accessible azides. For example, click chemistry can be performed between the azidosilk nanoparticles and DBCO-fluorophore and fluorescence analysis of the unreacted DBCO-fluorophore in the supernatant used to estimate the number of surface azides. This method does not report the total number of azides just the number of DBCO-groups reacted, would require low equivalents of fluorophore for accuracy and, assumes that: the fluorophore is bound covalently; the fluorophore binds to all surface azides; the silk does not interfere with the fluorophore excitation and emission; and, the fluorophore can access the surface azides following stealth ligand binding.[160, 285]

Fluorophore binding can also be used to measure the fluorescence of the reacted nanoparticles, which tolerates low (4-10 eq) to high equivalents (~120 eq) of DBCO-fluorophore as only the fluorescence of the labelled nanoparticles will be measured. The assay can be conducted in dry TLC format using a ChemiDoc, GelDoc or fluorescence microscope without the need for purification, or in solution format using a fluorescence plate reader.[464, 473-478] This method assumes that fluorophore excitation and emission is not affected by binding to the nanoparticle surface and that all the surface azides react. Alternatively, fluorescent bleaching of fluorophore-nanoparticles can be measured using a TIRF or super-resolution fluorescence microscope, which assumes that fluorophore photobleaching is not affected by binding to the nanoparticle.[474]

In order to minimize the effect of the nanoenvironment on the fluorophore, a good emitter with pH stability should be chosen that has an excitation and emission in a different part of the spectrum to avoid overlap with silk autofluorescence[479] at excitation/emission 277 nm/345 nm.[480-482] The overall fluorophore charge should be neutral or the slightly basic to increase association with the silk nanoparticles, which is not possible with water-soluble dyes

which rely on sulfonic acid moieties. Although carboxyrhodamine 110 was used qualitatively by Teramoto and colleagues, this probe alongside TAMRA and sulforhodamine will likely reduce the accuracy of quantitative fluorescence measurements upon protein conjugation due to quenching. The use of PEGylated dyes would be favorable to reduce quenching. Cyanine dyes are all hydrophobic, and water soluble derivatives incorporate sulfonic acids which increase the negative charge at pH 7. Although the water-soluble DBCO-sulfo-Cy5.5 is useful for *in vivo* work and has been used to conjugate silk fibroin,[270] it is negatively charged at pH 7.4 and would be expected to have slow reaction kinetics at room temperature due to electrostatic repulsion. The most useful probe for further *in vivo* work due to high brightness is DBCO-PEG-Cy5.5 while the most useful probes for surface-accessible azide reactions are DBCO-PEG_4-carboxyrhodamine 110, DBCO-PEG_4-TAMRA and, DBCO-PEG_4-Sulforhodamine B. The lower solubility of these dyes in water will result in consideration of the reaction scale to ensure enough material is obtained for measurement, mixed water-organic reaction solvents such as 1:1 water:MeOH and, longer reaction times.[483]

ATR-FTIR or transmission FTIR can also be used to estimate the surface:core azide distribution. Construction of an azide-silk calibration curve by mixing a model azide (N-Boc AzidoPheAla) with control silk allows quantification of the total nanoparticle azide content at any stealth ligand:silk ratio and both pre- and post-modification. This method assumes that the azide bond is present in degummed silk at a measurable concentration, the azido absorption and extinction coefficient is not affected by the nanoparticle structure and, that the model azide spectrum does not completely overlap with the silk fibroin spectrum, allowing at least one silk nanoparticle absorption to be used in the calibration curve.[464, 484]

I propose using the fluorescence assay of bound fluorophores in TLC format, in conjunction with the construction of the FTIR calibration curve to quantify the maximum number of surface azides. The benefits of using the two methods are: quantification of the surface:core azides; flexibility of fluorescent nanoparticles in future biology studies; and, applicability of the quantification methods to all future azidosilk nanoparticle conjugation. If the

excitation/emission of the fluorophore is severely affected by the silk nanoenvironment, the fluorescence assay will not be accurate. In this situation, the fluorescence of unreacted fluorophore would be the next best alternative to quantify the surface azides.

6.3 Conclusion

In summary this thesis demonstrates that silk processing can be achieved using scalable, continuous microfluidic-assisted methods for silk fibroin nanoparticle manufacture and scalable, origami folding for silk eco-sensor fabrication. The physicochemical and morphological properties of silk nanoparticles were influenced by factors including the mixing time and silk concentration during desolvation in both semi-batch and microfluidic manufacture. However, the effect of scale-up in microfluidic format remains to be fully characterized. The performance of semi-autonomous, silk 3D boat eco-sensors was influenced by iron oxide nanoparticle content, heterogeneous modification, loaded natural dye species and origami folding technique. Overall, microfluidic methodology is particularly promising for scalable manufacture of silk fibroin-based anticancer nanomedicines, heterogeneous reactions provide an advantageous route for surface functionalization of silk materials and origami provides a scalable method to control silk film morphology.

References

(1) Iqbal, P.; Preece, J. A.; Mendes, P. M. Nanotechnology: The “Top-Down” and “Bottom-Up” Approaches. In *Supramolecular Chemistry*, John Wiley & Sons, Ltd, 2012.

(2) Duncan, R.; Gaspar, R. Nanomedicine(s) under the microscope. *Mol. Pharmaceutics* **2011**, *8*, 2101-2141. DOI: 10.1021/mp200394t.

(3) Duncan, R.; Richardson, S. C. W. Endocytosis and intracellular trafficking as gateways for nanomedicine delivery: Opportunities and challenges. *Mol. Pharmaceutics* **2012**, *9*, 2380-2402. DOI: 10.1021/mp300293n.

(4) Turanlı, E. T.; Everest, E. Nanomedicine. In *Low-Dimensional and Nanostrutured Materials and Devices. Nanoscience and Technology.*, Ünlü, H., Horing, N., Dabrowski, J. Eds.; Springer, Cham, 2016; pp 579-587.

(5) Esf, E. *Nanomedicine: An ESF-European Medical Research Councils (EMRC) Forward Look Report* Strasbourg cedex, France, 2005.

(6) Bobo, D.; Robinson, K. J.; Islam, J.; Thurecht, K. J.; Corrie, S. R. Nanoparticle-Based Medicines: A Review of FDA-Approved Materials and Clinical Trials to Date. *Pharm. Res.* **2016**, *33*, 2373-2387. DOI: 10.1007/s11095-016-1958-5.

(7) Sahay, G.; Alakhova, D. Y.; Kabanov, A. V. Endocytosis of nanomedicines. *J. Controlled Release* **2010**, *145*, 182-195. DOI: 10.1016/j.jconrel.2010.01.036.

(8) Wahlich, J.; Desai, A.; Greco, F.; Hill, K.; Jones, A. T.; Mrsny, R. J.; Pasut, G.; Perrie, Y.; Seib, F. P.; Seymour, L. W.; et al. Nanomedicines for the delivery of biologics. *Pharmaceutics* **2019**, *11*, 210-210. DOI: 10.3390/pharmaceutics11050210.

(9) Jia, Y.; Jiang, Y.; He, Y.; Zhang, W.; Zou, J.; Magar, K. T.; Boucetta, H.; Teng, C.; He, W. Approved Nanomedicine against Diseases. *Pharmaceutics* **2023**, *15*, 774. DOI: 10.3390/pharmaceutics15030774.

(10) Miao, T.; Floreani, R. A.; Liu, G.; Chen, X. *Nanotheranostics for Cancer Applications*; Springer, Cham, 2019. DOI: 10.1007/978-3-030-01775-0.

(11) Barenholz, Y. Doxil® - The first FDA-approved nano-drug: Lessons learned. *J. Controlled Release* **2012**, *160*, 117-134. DOI: 10.1016/j.jconrel.2012.03.020.

(12) Miele, E.; Spinelli, G. P.; Miele, E.; Tomao, F.; Tomao, S. Albumin-bound formulation of paclitaxel (Abraxane® ABI-007) in the treatment of breast cancer. *Int. J. Nanomed.* **2009**, *4*, 99-105. DOI: 10.2147/ijn.s3061.

(13) van der Meel, R.; Sulheim, E.; Shi, Y.; Kiessling, F.; Mulder, W. J. M.; Lammers, T. Smart cancer nanomedicine. *Nat. Nanotechnol.* **2019**, *14*, 1007-1017. DOI: 10.1038/s41565-019-0567-y.

(14) Lammers, T.; Ferrari, M. The success of nanomedicine. *Nano Today* **2020**, *31*, 100853. DOI: 10.1016/j.nantod.2020.100853.

(15) Gao, X.; Guo, L.; Li, J.; Thu, H. E.; Hussain, Z. Nanomedicines guided nanoimaging probes and nanotherapeutics for early detection of lung cancer and abolishing pulmonary metastasis: Critical appraisal of newer developments and challenges to clinical transition. *J. Controlled Release* **2018**, *292*, 29-57. DOI: 10.1016/j.jconrel.2018.10.024.

(16) Decuzzi, P.; Peer, D.; Di Mascolo, D.; Palange, A. L.; Manghnani, P. N.; Moghimi, S. M.; Farhangrazi, Z. S.; Howard, K. A.; Rosenblum, D.; Liang, T.; et al. Roadmap on nanomedicine. *Nanotechnology* **2021** *32*, 012001. DOI: 10.1088/1361-6528/abaadb.

(17) Ventola, C. L. Progress in Nanomedicine: Approved and Investigational Nanodrugs. *PT* **2017**, *42*, 742-755.

(18) Zhao, P.; Li, N.; Astruc, D. State of the art in gold nanoparticle synthesis. *Coord. Chem. Rev.* **2013**, *257*, 638-665. DOI: 10.1016/J.CCR.2012.09.002.

(19) Sharma, R.; Mody, N.; Agrawal, U.; Vyas, S. P. Theranostic Nanomedicine; A Next Generation Platform for Cancer Diagnosis and Therapy. *Mini-Rev. Med. Chem.* **2017**, *17*, 1746-1757. DOI: 10.2174/1389557516666160219122524.

(20) Shi, J.; Kantoff, P. W.; Wooster, R.; Farokhzad, O. C. Cancer nanomedicine: Progress, challenges and opportunities. *Nat. Rev. Cancer* **2017**, *17*, 20-37. DOI: 10.1038/nrc.2016.108.

(21) Lovering, F.; Bikker, J.; Humblet, C. Escape from Flatland: Increasing Saturation as an Approach to Improving Clinical Success. *J. Med. Chem.* **2009**, *52*, 6752-6756. DOI: 10.1021/jm901241e.

(22) Sindhwani, S.; Syed, A. M.; Ngai, J.; Kingston, B. R.; Maiorino, L.; Rothschild, J.; MacMillan, P.; Zhang, Y.; Rajesh, N. U.; Hoang, T.; et al. The entry of nanoparticles into solid tumours. *Nat. Mater.* **2020**, *19*, 566–575. DOI: 10.1038/s41563-019-0566-2.

(23) Ehrlich, P. Address in Pathology, ON CHEMIOTHERAPY: Delivered before the Seventeenth International Congress of Medicine. *Br. Med. J.* **1913** *2*,353–359. DOI: 10.1136/bmj.2.2746.353.

(24) Matsumura, Y.; Maeda, H. A New Concept for Macromolecular Therapeutics in Cancer Chemotherapy: Mechanism of Tumoritropic Accumulation of Proteins and the Antitumor Agent Smancs. *Cancer Res.* **1986**, *46*, 6387-6392.

(25) Natfji, A. A.; Ravishankar, D.; Osborn, H. M. I.; Greco, F. Parameters Affecting the Enhanced Permeability and Retention Effect: The Need for Patient Selection. *J. Pharm. Sci.* **2017**, *106*, 3179-3187. DOI: 10.1016/j.xphs.2017.06.019.

(26) de Lázaro, I.; Mooney, D. J. Obstacles and opportunities in a forward vision for cancer nanomedicine. *Nat. Mater.* **2021**, *20*, 1469–1479. DOI: 10.1038/s41563-021-01047-7.

(27) Farrell, D.; Ptak, K.; Panaro, N. J.; Grodzinski, P. Nanotechnology-Based Cancer Therapeutics-Promise and Challenge-Lessons Learned Through the NCI Alliance for Nanotechnology in Cancer. *Pharm. Res.* **2011**, *28*, 273–278 DOI: 10.1007/s11095-010-0214-7.

(28) Lammers, T.; Kiessling, F.; Ashford, M.; Hennink, W.; Crommelin, D.; Storm, G. Cancer nanomedicine: is targeting our target? *Nat. Rev. Mater.* **2016**, *1*, 16069. DOI: 10.1038/natrevmats.2016.69.

(29) McNeil, S. E. Evaluation of nanomedicines: stick to the basics. *Nat. Rev. Mater.* **2016**, *1*, 16073. DOI: 10.1038/natrevmats.2016.73.

(30) Sun, Q.; Zhou, Z.; Qiu, N.; Shen, Y. Rational Design of Cancer Nanomedicine: Nanoproperty Integration and Synchronization. *Adv. Mater.* **2017**, *29*, 1606628. DOI: 10.1002/adma.201606628.

(31) Wilhelm, S.; Tavares, A. J.; Dai, Q.; Ohta, S.; Audet, J.; Dvorak, H. F.; Chan, W. C. W. Analysis of nanoparticle delivery to tumours. *Nat. Rev. Mater.* **2016**, *1*, 16014. DOI: 10.1038/natrevmats.2016.14.

(32) Dai, Q.; Wilhelm, S.; Ding, D.; Syed, A. M.; Sindhwani, S.; Zhang, Y.; Chen, Y. Y.; MacMillan, P.; Chan, W. C. W. Quantifying the Ligand-Coated Nanoparticle Delivery to Cancer Cells in Solid Tumors. *ACS Nano* **2018**, *12*, 8423-8435. DOI: 10.1021/acsnano.8b03900.

(33) Harrington, K. J.; Mohammadtaghi, S.; Uster, P. S.; Glass, D.; Peters, A. M.; Vile, R. G.; Stewart, J. S. W. Effective targeting of solid tumors in patients with locally advanced cancers by radiolabeled pegylated liposomes. *Clin. Cancer Res.* **2001**, *7*, 243-254.

(34) Ouyang, B.; Poon, W.; Zhang, Y. N.; Lin, Z. P.; Kingston, B. R.; Tavares, A. J.; Zhang, Y.; Chen, J.; Valic, M. S.; Syed, A. M.; et al. The dose threshold for nanoparticle tumour delivery. *Nat. Mater.* **2020**, *19*, 1362–1371. DOI: 10.1038/s41563-020-0755-z.

(35) Lammers, T. Just dose it. *Nat. Mater.* **2020**, *19*, 1257-1258. DOI: 10.1038/s41563-020-00855-7.

(36) Altay, Y.; Cao, S.; Che, H.; Abdelmohsen, L. K. E. A.; van Hest, J. C. M. Adaptive Polymeric Assemblies for Applications in Biomimicry and Nanomedicine. *Biomacromolecules* **2019**, *20*, 4053–4064. DOI: 10.1021/acs.biomac.9b01341.

(37) Brownlee, W. J.; Seib, F. P. Impact of the hypoxic phenotype on the uptake and efflux of nanoparticles by human breast cancer cells. *Sci. Rep.* **2018**, *8*, 12318 DOI: 10.1038/s41598-018-30517-3.

(38) Patel, N. R.; Pattni, B. S.; Abouzeid, A. H.; Torchilin, V. P. Nanopreparations to overcome multidrug resistance in cancer. *Adv. Drug Delivery Rev.* **2013**, *65*, 1748-1762. DOI: 10.1016/j.addr.2013.08.004.

(39) Miller, M. A.; Zheng, Y.-R.; Gadde, S.; Pfirschke, C.; Zope, H.; Engblom, C.; Kohler, R. H.; Iwamoto, Y.; Yang, K. S.; Askevold, B.; et al. Tumour-associated macrophages act as a slow-release reservoir of nano-therapeutic Pt(IV) pro-drug. *Nat. Commun.* **2015**, *6*, 8692. DOI: 10.1038/ncomms9692.

(40) Alizadeh, D.; Zhang, L.; Hwang, J.; Schluep, T.; Badie, B. Tumor-associated macrophages are predominant carriers of cyclodextrin-based nanoparticles into gliomas. *Nanomedicine: NBM* **2010**, *6*, 382-390. DOI: 10.1016/j.nano.2009.10.001.

(41) Housman, G.; Byler, S.; Heerboth, S.; Lapinska, K.; Longacre, M.; Snyder, N.; Sarkar, S. Drug Resistance in Cancer: An Overview. *Cancers* **2014**, *6*, 1769-1792. DOI: 10.3390/cancers6031769.

(42) Mosesson, Y.; Mills, G. B.; Yarden, Y. Derailed endocytosis: An emerging feature of cancer. *Nat. Rev. Cancer* **2008**, *8*, 835-850. DOI: 10.1038/nrc2521.

(43) Sahay, G.; Kim, J. O.; Kabanov, A. V.; Bronich, T. K. The exploitation of differential endocytic pathways in normal and tumor cells in the selective targeting of nanoparticulate chemotherapeutic agents. *Biomaterials* **2010**, *31*, 923-933. DOI: 10.1016/j.biomaterials.2009.09.101.

(44) Griffiths, G.; Gruenberg, J.; Marsh, M.; Wohlmann, J.; Jones, A. T.; Parton, R. G. Nanoparticle entry into cells; the cell biology weak link. *Adv. Drug Delivery Rev.* **2022**, *188*, 114403. DOI: 10.1016/j.addr.2022.114403.

(45) Appelqvist, H.; Wäster, P.; Kågedal, K.; Öllinger, K. The lysosome: from waste bag to potential therapeutic target. *J. Mol. Cell Biol.* **2013**, *5*, 214–226. DOI: 10.1093/jmcb/mjt022.

(46) Patel, S.; Kim, J.; Herrera, M.; Mukherjee, A.; Kabanov, A. V.; Sahay, G. Brief update on endocytosis of nanomedicines. *Adv. Drug Delivery Rev.* **2019**, *144*, 90-111. DOI: 10.1016/j.addr.2019.08.004.

(47) De Duve, C.; Pressman, B. C.; Gianetto, R.; Wattiaux, R.; Appelmans, F. Tissue fractionation studies. 6. Intracellular distribution patterns of enzymes in rat-liver tissue. *Biochem J.* **1955** *60*, 604–617. DOI: 10.1042/bj0600604.

(48) De Duve, C. The Lysosome. *Sci. Am.* **1963**, *208*, 64-73. DOI: 10.2307/24936148.

(49) De Duve, C. The lysosome turns fifty. *Nat. Cell Biol.* **2005**, *7*, 847–849. DOI: 10.1038/ncb0905-847.

(50) Hu, M.; Chen, J.; Liu, S.; Xu, H. The Acid Gate in the Lysosome. *Autophagy* **2023**, *19*, 1368-1370. DOI: 10.1080/15548627.2022.2125629.

(51) Rennick, J. J.; Johnston, A. P. R.; Parton, R. G. Key principles and methods for studying the endocytosis of biological and nanoparticle therapeutics. *Nat. Nanotechnol.* **2021**, *16*, 266-276. DOI: 10.1038/s41565-021-00858-8.

(52) Cong, V. T.; Houng, J. L.; Kavallaris, M.; Chen, X.; Tilley, R. D.; Gooding, J. J. How can we use the endocytosis pathways to design nanoparticle drug-delivery vehicles to target cancer cells over healthy cells? *Chem. Soc. Rev.* **2022**, *51*, 7531-7559, 10.1039/D1CS00707F. DOI: 10.1039/D1CS00707F.

(53) Licona-Limón, I.; Garay-Canales, C. A.; Muñoz-Paleta, O.; Ortega, E. CD13 mediates phagocytosis in human monocytic cells. *J. Leukocyte Biol.* **2015**, *98*, 85-98. DOI: 10.1189/jlb.2A0914-458R.

(54) Lin, X. P.; Mintern, J. D.; Gleeson, P. A. Macropinocytosis in Different Cell Types: Similarities and Differences. *Membranes* **2020**, *10*, 177. DOI: 10.3390/membranes10080177.

(55) Cleal, K.; He, L.; D. Watson, P.; T. Jones, A. Endocytosis, Intracellular Traffic and Fate of Cell Penetrating Peptide Based Conjugates and Nanoparticles. *Curr. Pharm. Des.* **2013**, *19*, 2878-2894. DOI: 10.2174/13816128113199990297.

(56) Lim, J. P.; Gleeson, P. A. Macropinocytosis: An endocytic pathway for internalising large gulps. *Immunol. Cell Biol.* **2011**, *89*, 836-843. DOI: 10.1038/icb.2011.20.

(57) Ho, Y. T.; Kamm, R. D.; Kah, J. C. Y. Influence of protein corona and caveolae-mediated endocytosis on nanoparticle uptake and transcytosis. *Nanoscale* **2018**, *10*, 12386-12397. DOI: 10.1039/c8nr02393j.

(58) Mrsny, R. J.; Mahmood, T. WO2012036746A1 - Systems and methods of delivery of bioactive agents using bacterial toxin-derived transport sequences. 2012.

(59) Wiley, D. T.; Webster, P.; Gale, A.; Davis, M. E. Transcytosis and brain uptake of transferrin-containing nanoparticles by tuning avidity to transferrin receptor. *PNAS* **2013**, *110* 8662-8667. DOI: 10.1073/pnas.1307152110.

(60) Cui, J.; Alt, K.; Ju, Y.; Gunawan, S. T.; Braunger, J. A.; Wang, T.-Y.; Dai, Y.; Dai, Q.; Richardson, J. J.; Guo, J.; et al. Ligand-Functionalized Poly(ethylene glycol) Particles for

Tumor Targeting and Intracellular Uptake. *Biomacromolecules* **2019**, *20*, 3592–3600. DOI: 10.1021/acs.biomac.9b00925.

(61) Das, S.; Pati, D.; Tiwari, N.; Nisal, A.; Sen Gupta, S. Synthesis of silk fibroin-glycopolypeptide conjugates and their recognition with lectin. *Biomacromolecules* **2012**, *13*, 3695-3702. DOI: 10.1021/bm301170u.

(62) Cohen-Karni, T.; Jeong, K. J.; Tsui, J. H.; Reznor, G.; Mustata, M.; Wanunu, M.; Graham, A.; Marks, C.; Bell, D. C.; Langer, R.; et al. Nanocomposite gold-silk nanofibers. *Nano Lett.* **2012**, *12*, 5403-5406. DOI: 10.1021/nl302810c.

(63) Schierling, M. B.; Doblhofer, E.; Scheibel, T. Cellular uptake of drug loaded spider silk particles. *Biomater. Sci.* **2016**, *4*, 1515-1515. DOI: 10.1039/c6bm00435k.

(64) Hemalatha, A.; Mayor, S. Recent advances in clathrin-independent endocytosis *F1000Res.* **2019**, *8*. DOI: 10.12688/f1000research.16549.1.

(65) Conner, S. D.; Schmid, S. L. Regulated portals of entry into the cell. *Nature* **2003**, *422*, 37–44. DOI: 10.1038/nature01451.

(66) Watanabe, S.; Boucrot, E. Fast and ultrafast endocytosis. *Curr. Opin. Cell Biol.* **2017**, *47*, 64-71. DOI: 10.1016/j.ceb.2017.02.013.

(67) Trouet, A.; Deprez-De Campeneere, D.; De Duve, C. Chemotherapy through Lysosomes with a DNA-Daunorubicin Complex. *Nature New Biol.* **1972**, *239*, 110-112. DOI: 10.1038/newbio239110a0.

(68) Trouet, A.; Deprez-De Campeneere, D.; De Smedt-Malengreaux, M.; Atassi, G. Experimental leukemia chemotherapy with a “lysosomotropic” adriamycin-DNA complex. *Eur. J. Cancer (1965)* **1974**, *10*, 405-411. DOI: 10.1016/0014-2964(74)90022-X.

(69) De Duve, C.; De Barsy, T.; Poole, B.; Trouet, A.; Tulkens, P.; Van Hoof, F. Lysosomotropic agents. *Biochem. Pharmacol.* **1974**, *23*, 2495-2531. DOI: 10.1016/0006-2952(74)90174-9.

(70) De Duve, C.; Trouet, A. Lysosomes and Lysosomotropic Drugs in Host-Parasite Relationship. In *Non-Specific Factors Influencing Host Resistance: A Reexamination*, Braun, W., Ungar, J. Eds.; S.Karger AG, 1973; pp 153-170.

(71) Sorkin, A.; Von Zastrow, M. Endocytosis and signalling: Intertwining molecular networks. *Nat. Rev. Mol. Cell* **2009**, *10*, 609-622. DOI: 10.1038/nrm2748.

(72) Srinivasarao, M.; Galliford, C. V.; Low, P. S. Principles in the design of ligand-targeted cancer therapeutics and imaging agents. *Nat. Rev. Drug Discov.* **2015**, *14*, 203-219. DOI: 10.1038/nrd4519.

(73) Dawidczyk, C. M.; Kim, C.; Park, J. H.; Russell, L. M.; Lee, K. H.; Pomper, M. G.; Searson, P. C. State-of-the-art in design rules for drug delivery platforms: Lessons learned from FDA-approved nanomedicines. *J. Controlled Release* **2014**, *187*, 133-144. DOI: 10.1016/j.jconrel.2014.05.036.

(74) Markman, J. L.; Rekechenetskiy, A.; Holler, E.; Ljubimova, J. Y. Nanomedicine therapeutic approaches to overcome cancer drug resistance. *Adv. Drug Delivery Rev.* **2013**, *65*, 1866-1879. DOI: 10.1016/j.addr.2013.09.019.

(75) Seynhaeve, A. L. B.; Dicheva, B. M.; Hoving, S.; Koning, G. A.; ten Hagen, T. L. M. Intact Doxil is taken up intracellularly and released doxorubicin sequesters in the lysosome: Evaluated by in vitro/in vivo live cell imaging. *J. Controlled Release* **2013**, *172*, 330-340. DOI: 10.1016/j.jconrel.2013.08.034.

(76) Waterhouse, D. N.; Tardi, P. G.; Mayer, L. D.; Bally, M. B. A Comparison of Liposomal Formulations of Doxorubicin with Drug Administered in Free Form. *Drug Saf.* **2001**, *24*, 903-920. DOI: 10.2165/00002018-200124120-00004.

(77) Wu, D.; Si, M.; Xue, H.; Wong, H. Nanomedicine applications in the treatment of breast cancer: current state of the art. *Int. J. Nanomedicine* **2017**, *12*, 5879-5892. DOI: 10.2147/IJN.S123437.

(78) López-Laguna, H.; Cubarsi, R.; Unzueta, U.; Mangues, R.; Vázquez, E.; Villaverde, A. Endosomal escape of protein nanoparticles engineered through humanized histidine-rich peptides. *Sci. China Mater.* **2020**, *63*, 644-653. DOI: 10.1007/s40843-019-1231-y.

(79) Selby, L. I.; Cortez-Jugo, C. M.; Such, G. K.; Johnston, A. P. R. Nanoescapology: progress toward understanding the endosomal escape of polymeric nanoparticles. *WIREs Nanomedicine and Nanobiotechnology* **2017**, *9*, e1452. DOI: 10.1002/wnan.1452.

(80) Ahmad, A.; Khan, J. M.; Haque, S. Strategies in the design of endosomolytic agents for facilitating endosomal escape in nanoparticles. *Biochimie* **2019**, *160*, 61-75. DOI: 10.1016/j.biochi.2019.02.012.

(81) Overchuk, M.; Zheng, G. Overcoming obstacles in the tumor microenvironment: Recent advancements in nanoparticle delivery for cancer theranostics. *Biomaterials* **2018**, *156*, 217-237. DOI: 10.1016/j.biomaterials.2017.10.024.

(82) Shi, Y.; van der Meel, R.; Chen, X.; Lammers, T. The EPR effect and beyond: Strategies to improve tumor targeting and cancer nanomedicine treatment efficacy. *Theranostics* **2020**, *10*, 7921–7924. DOI: 10.7150/thno.49577.

(83) Lee, H.; Shields, A. F.; Siegel, B. A.; Miller, K. D.; Krop, I.; Ma, C. X.; LoRusso, P. M.; Munster, P. N.; Campbell, K.; Gaddy, D. F.; et al. ^{64}Cu-MM-302 Positron Emission Tomography Quantifies Variability of Enhanced Permeability and Retention of Nanoparticles in Relation to Treatment Response in Patients with Metastatic Breast Cancer. *Clin. Cancer Res.* **2017**, *23*, 4190-4202. DOI: 10.1158/1078-0432.Ccr-16-3193.

(84) Choi, M.-R.; Stanton-Maxey, K. J.; Stanley, J. K.; Levin, C. S.; Bardhan, R.; Akin, D.; Badve, S.; Sturgis, J.; Robinson, J. P.; Bashir, R.; et al. A Cellular Trojan Horse for Delivery of Therapeutic Nanoparticles into Tumors. *Nano Lett.* **2007**, *7*, 3759-3765. DOI: 10.1021/nl072209h.

(85) Choi, M.-R.; Bardhan, R.; Stanton-Maxey, K. J.; Badve, S.; Nakshatri, H.; Stantz, K. M.; Cao, N.; Halas, N. J.; Clare, S. E. Delivery of nanoparticles to brain metastases of breast cancer using a cellular Trojan horse. *Cancer Nanotechnol.* **2012**, *3*, 47-54. DOI: 10.1007/s12645-012-0029-9.

(86) Shah, S.; Rangaraj, N.; Singh, S. B.; Srivastava, S. Exploring the unexplored avenues of surface charge in nano-medicine. *Colloid Interface Sci. Commun.* **2021**, *42*, 100406. DOI: 10.1016/j.colcom.2021.100406.

(87) Xu, M.; Qi, Y.; Liu, G.; Song, Y.; Jiang, X.; Du, B. Size-Dependent In Vivo Transport of Nanoparticles: Implications for Delivery, Targeting, and Clearance. *ACS Nano* **2023**, *17*, 20825-20849. DOI: 10.1021/acsnano.3c05853.

(88) Shen, Z.; Ye, H.; Yi, X.; Li, Y. Membrane Wrapping Efficiency of Elastic Nanoparticles during Endocytosis: Size and Shape Matter. *ACS Nano* **2019**, *13*, 215-228. DOI: 10.1021/acsnano.8b05340.

(89) Rejman, J.; Oberle, V.; Zuhorn, I. S.; Hoekstra, D. Size-dependent internalization of particles via the pathways of clathrin-and caveolae-mediated endocytosis. *Biochem. J.* **2004**, *377*, 159-169. DOI: 10.1042/BJ20031253.

(90) Pan, R.; Liu, G.; Li, Y.; Wei, Y.; Li, S.; Tao, L. Size-dependent endocytosis and a dynamic-release model of nanoparticles. *Nanoscale* **2018**, *10*, 8269-8274. DOI: 10.1039/c8nr00830b.

(91) Arvizo, R. R.; Miranda, O. R.; Thompson, M. A.; Pabelick, C. M.; Bhattacharya, R.; David Robertson, J.; Rotello, V. M.; Prakash, Y. S.; Mukherjee, P. Effect of nanoparticle surface charge at the plasma membrane and beyond. *Nano Lett.* **2010**, *10*, 2543-2548. DOI: 10.1021/nl101140t.

(92) Gratton, S. E. A.; Ropp, P. A.; Pohlhaus, P. D.; Luft, J. C.; Madden, V. J.; Napier, M. E.; DeSimone, J. M. The effect of particle design on cellular internalization pathways. *PNAS* **2008**, *105*, 11613-11618. DOI: 10.1073/pnas.0801763105.

(93) Lagarrigue, P.; Moncalvo, F.; Cellesi, F. Non-spherical Polymeric Nanocarriers for Therapeutics: The Effect of Shape on Biological Systems and Drug Delivery Properties. *Pharmaceutics* **2023**, *15*, 32. DOI: 10.3390/pharmaceutics15010032.

(94) Geng, Y.; Dalhaimer, P.; Cai, S.; Tsai, R.; Tewari, M.; Minko, T.; Discher, D. E. Shape effects of filaments versus spherical particles in flow and drug delivery. *Nature Nanotech.* **2007**, *2*, 249-255. DOI: 10.1038/nnano.2007.70.

(95) Souri, M.; Soltani, M.; Moradi Kashkooli, F.; Kiani Shahvandi, M.; Chiani, M.; Shariati, F. S.; Mehrabi, M. R.; Munn, L. L. Towards principled design of cancer nanomedicine to accelerate clinical translation. *Mater. Today Bio* **2022**, *13*, 100208. DOI: 10.1016/j.mtbio.2022.100208.

(96) Nguyen, V. H.; Lee, B. J. Protein corona: A new approach for nanomedicine design. *Int. J. Nanomed.* **2017**, *12*, 3137-3151. DOI: 10.2147/IJN.S129300.

(97) Caracciolo, G. Clinically approved liposomal nanomedicines: Lessons learned from the biomolecular corona. *Nanoscale* **2018**, *10*, 4167-4172. DOI: 10.1039/c7nr07450f.

(98) Hui, Y.; Yi, X.; Wibowo, D.; Yang, G.; Middelberg, A. P. J.; Gao, H.; Zhao, C.-X. Nanoparticle elasticity regulates phagocytosis and cancer cell uptake. *Sci. Adv.* **2020**, *6*, eaaz4316. DOI: 10.1126/sciadv.aaz4316.

(99) Fraguas-Sánchez, A. I.; Lozza, I.; Torres-Suárez, A. I. Actively Targeted Nanomedicines in Breast Cancer: From Pre-Clinal Investigation to Clinic. *Cancers* **2022**, *14*, 1198. DOI: 10.3390/cancers14051198.

(100) Bortot, B.; Mangogna, A.; Di Lorenzo, G.; Stabile, G.; Ricci, G.; Biffi, S. Image-guided cancer surgery: a narrative review on imaging modalities and emerging nanotechnology strategies. *J. Nanobiotechnol.* **2023**, *21*, 155. DOI: 10.1186/s12951-023-01926-y.

(101) Hare, J. I.; Lammers, T.; Ashford, M. B.; Puri, S.; Storm, G.; Barry, S. T. Challenges and strategies in anti-cancer nanomedicine development: An industry perspective. *Adv. Drug Delivery Rev.* **2017**, *108*, 25-38. DOI: 10.1016/j.addr.2016.04.025.

(102) Sondak, V. K.; King, D. W.; Zager, J. S.; Schneebaum, S.; Kim, J.; Leong, S. P. L.; Faries, M. B.; Averbook, B. J.; Martinez, S. R.; Puleo, C. A.; et al. Combined Analysis of Phase III Trials Evaluating [99mTc]Tilmanocept and Vital Blue Dye for Identification of Sentinel Lymph Nodes in Clinically Node-Negative Cutaneous Melanoma. *Ann. Surg. Oncol.* **2013**, *20*, 680-688. DOI: 10.1245/s10434-012-2612-z.

(103) Wallace, A. M.; Han, L. K.; Povoski, S. P.; Deck, K.; Schneebaum, S.; Hall, N. C.; Hoh, C. K.; Limmer, K. K.; Krontiras, H.; Frazier, T. G.; et al. Comparative Evaluation of [99mTc]Tilmanocept for Sentinel Lymph Node Mapping in Breast Cancer Patients: Results of Two Phase 3 Trials. *Ann. Surg. Oncol.* **2013**, *20*, 2590-2599. DOI: 10.1245/s10434-013-2887-8.

(104) Leong, S. P. Detection of melanoma, breast cancer and head and neck squamous cell cancer sentinel lymph nodes by Tc-99m Tilmanocept (Lymphoseek®). *Clin. Exp. Metastasis* **2022**, *39*, 39-50. DOI: 10.1007/s10585-021-10137-4.

(105) Fan, D.; Cao, Y.; Cao, M.; Wang, Y.; Cao, Y.; Gong, T. Nanomedicine in cancer therapy. *Sig. Transduct. Target. Ther.* **2023**, *8*, 293. DOI: 10.1038/s41392-023-01536-y.

(106) Lee, N. K.; Lee, E. J.; Kim, S.; Nam, G. h.; Kih, M.; Hong, Y.; Jeong, C.; Yang, Y.; Byun, Y.; Kim, I. S. Ferritin nanocage with intrinsically disordered proteins and affibody: A platform for tumor targeting with extended pharmacokinetics. *J. Controlled Release* **2017**, *267*, 172-180. DOI: 10.1016/j.jconrel.2017.08.014.

(107) Bian, X.; Wu, P.; Sha, H.; Qian, H.; Wang, Q.; Cheng, L.; Yang, Y.; Yang, M.; Liu, B. Anti-EGFR-iRGD recombinant protein conjugated silk fibroin nanoparticles for enhanced tumor targeting and antitumor efficiency. *OncoTargets Ther.* **2016**, *9*, 3153-3162. DOI: 10.2147/OTT.S100678.

(108) Ye, Z.; Zhang, Y.; Liu, Y.; Liu, Y.; Tu, J.; Shen, Y. Egfr targeted cetuximab-valine-citrulline (Vc)-doxorubicin immunoconjugates-loaded bovine serum albumin (bsa) nanoparticles for colorectal tumor therapy. *Int. J. Nanomed.* **2021**, *16*, 2443-2459. DOI: 10.2147/IJN.S289228.

(109) Lammers, T.; Hennink, W. E.; Storm, G. Tumour-targeted nanomedicines: principles and practice. *Br. J. Cancer* **2008**, *99*, 392-397. DOI: 10.1038/sj.bjc.6604483.

(110) Daniels, T. R.; Delgado, T.; Helguera, G.; Penichet, M. L. The transferrin receptor part II: Targeted delivery of therapeutic agents into cancer cells. *Clin. Immunol.* **2006**, *121*, 159-176. DOI: 10.1016/j.clim.2006.06.006.

(111) Sabharanjak, S.; Mayor, S. Folate receptor endocytosis and trafficking. *Adv. Drug Delivery Rev.* **2004**, *56*, 1099-1109. DOI: 10.1016/j.addr.2004.01.010.

(112) Subia, B.; Chandra, S.; Talukdar, S.; Kundu, S. C. Folate conjugated silk fibroin nanocarriers for targeted drug delivery. *Integr. Biol.* **2014**, *6*, 203-214. DOI: 10.1039/c3ib40184g.

(113) Julyan, P. J.; Seymour, L. W.; Ferry, D. R.; Daryani, S.; Boivin, C. M.; Doran, J.; David, M.; Anderson, D.; Christodoulou, C.; Young, A. M.; et al. Preliminary clinical study of the distribution of HPMA copolymers bearing doxorubicin and galactosamine. *J. Controlled Release* **1999**, *57*, 281-290. DOI: 10.1016/S0168-3659(98)00124-2.

(114) Mao, B.; Liu, C.; Zheng, W.; Li, X.; Ge, R.; Shen, H.; Guo, X.; Lian, Q.; Shen, X.; Li, C. Cyclic cRGDfk peptide and Chlorin e6 functionalized silk fibroin nanoparticles for targeted drug delivery and photodynamic therapy. *Biomaterials* **2018**, *161*, 306-320. DOI: 10.1016/j.biomaterials.2018.01.045.

(115) Schellenberger, V.; Wang, C. W.; Geething, N. C.; Spink, B. J.; Campbell, A.; To, W.; Scholle, M. D.; Yin, Y.; Yao, Y.; Bogin, O.; et al. A recombinant polypeptide extends the in vivo half-life of peptides and proteins in a tunable manner. *Nat. Biotechnol.* **2009**, *27*, 1186-1190. DOI: 10.1038/nbt.1588.

(116) Anand, R.; Vallooran, J. *Polypeptides: PASylation and XTEN*; Woodhead Publishing, 2018. DOI: 10.1016/B978-0-08-101750-0.00011-8.

(117) Haeckel, A.; Appler, F.; De Schellenberger, A. A.; Schellenberger, E. XTEN as biological alternative to PEGylation allows complete expression of a protease-activatable killin-based cytostatic. *PLoS ONE* **2016**, *11*, 1-13. DOI: 10.1371/journal.pone.0157193.

(118) Brandl, F.; Busslinger, S.; Zangemeister-Wittke, U.; Plückthun, A. Optimizing the anti-tumor efficacy of protein-drug conjugates by engineering the molecular size and half-life. *J. Controlled Release* **2020**, *327*, 186-197. DOI: 10.1016/j.jconrel.2020.08.004.

(119) Haeckel, A.; Appler, F.; Figge, L.; Kratz, H.; Lukas, M.; Michel, R.; Schnorr, J.; Zille, M.; Hamm, B.; Schellenberger, E. XTEN-annexin a5: XTEN allows complete expression of long-circulating protein-based imaging probes as recombinant alternative to pegylation. *J. Nucl. Med.* **2014**, *55*, 508-514. DOI: 10.2967/jnumed.113.128108.

(120) Ding, S.; Song, M.; Sim, B. C.; Gu, C.; Podust, V. N.; Wang, C. W.; McLaughlin, B.; Shah, T. P.; Lax, R.; Gast, R.; et al. Multivalent antiviral XTEN-peptide conjugates with long in vivo half-life and enhanced solubility. *Bioconjugate Chem.* **2014**, *25*, 1351-1359. DOI: 10.1021/bc500215m.

(121) Podust, V. N.; Sim, B. C.; Kothari, D.; Henthorn, L.; Gu, C.; Wang, C. W.; McLaughlin, B.; Schellenberger, V. Extension of in vivo half-life of biologically active peptides via chemical conjugation to XTEN protein polymer. *Protein Eng., Des. Sel.* **2013**, *26*, 743-753. DOI: 10.1093/protein/gzt048.

(122) Podust, V. N.; Balan, S.; Sim, B. C.; Coyle, M. P.; Ernst, U.; Peters, R. T.; Schellenberger, V. Extension of in vivo half-life of biologically active molecules by XTEN protein polymers. *J. Controlled Release* **2016**, *240*, 52-66. DOI: 10.1016/j.jconrel.2015.10.038.

(123) Thomas, O. S.; Weber, W. Overcoming Physiological Barriers to Nanoparticle Delivery—Are We There Yet? *Front. Bioeng. Biotechnol.* **2019**, *7*, 415. DOI: 10.3389/fbioe.2019.00415.

(124) Binder, U.; Skerra, A. PASylation®: A versatile technology to extend drug delivery. *Curr. Opin. Colloid Interface Sci.* **2017**, *31*, 10-17. DOI: 10.1016/j.cocis.2017.06.004.

(125) Tesarova, B.; Dostalova, S.; Smidova, V.; Goliasova, Z.; Skubalova, Z.; Michalkova, H.; Hynek, D.; Michalek, P.; Polanska, H.; Vaculovicova, M.; et al. Surface-PASylation of ferritin to form stealth nanovehicles enhances in vivo therapeutic performance of encapsulated ellipticine. *Applied Materials Today* **2020**, *18*, 100501. DOI: 10.1016/j.apmt.2019.100501.

(126) Schlapschy, M.; Binder, U.; Börger, C.; Theobald, I.; Wachinger, K.; Kisling, S.; Haller, D.; Skerra, A. PASylation: A biological alternative to PEGylation for extending the plasma half-life of pharmaceutically active proteins. *Protein Eng., Des. Sel.* **2013**, *26*, 489-501. DOI: 10.1093/protein/gzt023.

(127) Kundu, S. C.; Kundu, B.; Talukdar, S.; Bano, S.; Nayak, S.; Kundu, J.; Mandal, B. B.; Bhardwaj, N.; Botlagunta, M.; Dash, B. C.; et al. Invited review: Nonmulberry silk biopolymers. *Biopolymers* **2012**, *97*, 455-467. DOI: 10.1002/bip.22024.

(128) Arakawa, K.; Kono, N.; Malay, A. D.; Tateishi, A.; Ifuku, N.; Masunaga, H.; Sato, R.; Tsuchiya, K.; Ohtoshi, R.; Pedrazzoli, D.; et al. 1000 spider silkomes: Linking sequences to silk physical properties. *Sci. Adv.* **2022**, *8*, eabo6043. DOI: 10.1126/sciadv.abo6043.

(129) Rajendra, P. K. M.; Nidamanuri, B. S. S.; Balan, A. P.; Venkatachalam, S.; Jawahar, N. A review on structure, preparation and applications of silk fibroin-based nano-drug delivery systems. *J. Nanopart. Res.* **2022**, *24*, 141. DOI: 10.1007/s11051-022-05526-z.

(130) Holland, C.; Numata, K.; Rnjak-Kovacina, J.; Seib, F. P. The Biomedical Use of Silk: Past, Present, Future. *Adv. Healthcare Mater.* **2019**, *8*, 1800465-1800465. DOI: 10.1002/adhm.201800465.

(131) Sofregen. *Sofregen Receives 510(k) Clearance for Silk Voice®*. 2019. https://www.sofregen.com/press-release-3/press-release-3 (accessed 2023 21/06/2023).

(132) Murphy, A. R.; Kaplan, D. L. Biomedical applications of chemically-modified silk fibroin. *J. Mater. Chem.* **2009**, *19*, 6443-6450. DOI: 10.1039/b905802h.

(133) Rockwood, D. N.; Preda, R. C.; Yücel, T.; Wang, X.; Lovett, M. L.; Kaplan, D. L. Materials Fabrication from Bombyx mori Silk Fibroin. *Nat. Protoc.* **2011**, *6*, 1612-1631. DOI: 10.1038/nprot.2011.379.

(134) Vepari, C.; Kaplan, D. L. Silk as a biomaterial. *Prog. Polym. Sci.* **2007**, *32*, 991-1007. DOI: 10.1016/j.progpolymsci.2007.05.013.

(135) Seib, F. P. Silk nanoparticles-an emerging anticancer nanomedicine. *AIMS Bioeng.* **2017**, *4*, 239-258. DOI: 10.3934/bioeng.2017.2.239.

(136) Yao, X.; Zou, S.; Fan, S.; Niu, Q.; Zhang, Y. Bioinspired silk fibroin materials: From silk building blocks extraction and reconstruction to advanced biomedical applications. *Mater. Today Bio* **2022**, *16*, 100381. DOI: 10.1016/j.mtbio.2022.100381.

(137) Ebrahimi, D.; Tokareva, O.; Rim, N. G.; Wong, J. Y.; Kaplan, D. L.; Buehler, M. J. Silk-Its Mysteries, How It Is Made, and How It Is Used. *ACS Biomater. Sci. Eng.* **2015**, *1*, 864-876. DOI: 10.1021/acsbiomaterials.5b00152.

(138) Debari, M. K.; King, C. I.; Altgold, T. A.; Abbott, R. D. Silk Fibroin as a Green Material. *ACS Biomater. Sci. Eng.* **2021**, *7*, 3530-3544. DOI: 10.1021/acsbiomaterials.1c00493.

(139) Kim, H. J.; Kim, M. K.; Lee, K. H.; Nho, S. K.; Han, M. S.; Um, I. C. Effect of degumming methods on structural characteristics and properties of regenerated silk. *Int. J. Biol. Macromol.* **2017**, *104*, 294-302. DOI: 10.1016/j.ijbiomac.2017.06.019.

(140) Zhou, G.; Shao, Z.; Knight, D. P.; Yan, J.; Chen, X. Silk Fibers Extruded Artificially from Aqueous Solutions of Regenerated Bombyx mori Silk Fibroin are Tougher than their Natural Counterparts. *Adv. Mater.* **2009**, *21*, 366-370. DOI: 10.1002/adma.200800582.

(141) Xu, Z.; Wu, M.; Gao, W.; Bai, H. A sustainable single-component “Silk nacre”. *Sci. Adv.* **2022**, *8*, eabo0946. DOI: 10.1126/sciadv.abo0946.

(142) Wang, H.-Y.; Zhang, Y.-Q.; Wei, Z.-G. Dissolution and processing of silk fibroin for materials science. *Crit. Rev. Biotechnol.* **2021**, *41*, 406-424. DOI: 10.1080/07388551.2020.1853030.

(143) Wang, Q.; Chen, Q.; Yang, Y.; Shao, Z. Effect of various dissolution systems on the molecular weight of regenerated silk fibroin. *Biomacromolecules* **2013**, *14*, 285-289. DOI: 10.1021/bm301741q.

(144) Padaki, N. V.; Das, B.; Basu, A. 1 - Advances in understanding the properties of silk. In *Advances in Silk Science and Technology*, Basu, A. Ed.; Woodhead Publishing, 2015; pp 3-16.

(145) Matthew, S. A. L.; Seib, F. P. Silk Bioconjugates: From Chemistry and Concept to Application. *ACS Biomater. Sci. Eng.* **2024**, *10*, 12–28. DOI: 10.1021/acsbiomaterials.2c01116.

(146) Billroth, T.; Dent, C. T. *Clinical Surgery: Extracts from the Reports of Surgical Practice Between the Years 1860-1876*; New Sydenham Society, 1881.

(147) Sabbatani, S.; Catena, F.; Neri, F.; Vallicelli, C.; Ansaloni, L.; Sartelli, M.; Coccolini, F.; Di Saverio, S.; Catena, R.; Lazzareschi, D.; et al. The Bolognese surgeon Giuseppe Ruggi: how and why the aseptic surgery was introduced in Bologna in the middle half of the XIX century. *J. Surg. Res.* **2014**, *192*, 555-563. DOI: 10.1016/j.jss.2014.04.018.

(148) Thomson, W. Report on surgery. *Dublin J. Med. Sci. (1872-1920)* **1883**, *75*, 240-255.

(149) Seeley, R. C. Maxillofacial injuries: Reconstructive surgery of the dehiscent parotid duct and dehiscent peripheral facial nerve. *Am. J. Surg.* **1947**, *73*, 551-563. DOI: 10.1016/0002-9610(47)90376-0.

(150) Tillmanns, R. H. *The Principles of surgery and surgical pathology*; D. Appleton, 1894.

(151) Mayer, L. The evolution of modern tendon surgery. *Ann. R. Coll. Surg. Engl.* **1952**, *11*, 69-86.

(152) Wongpinyochit, T.; Johnston, B. F.; Seib, F. P. Degradation Behavior of Silk Nanoparticles-Enzyme Responsiveness. *ACS Biomater. Sci. Eng.* **2018**, *4*, 942-951. DOI: 10.1021/acsbiomaterials.7b01021.

(153) Wongpinyochit, T.; Johnston, B. F.; Seib, F. P. Manufacture and drug delivery applications of silk nanoparticles. *J. Visualized Exp.* **2016**, e54669-e54669. DOI: 10.3791/54669.

(154) Lu, Q.; Zhu, H.; Zhang, C.; Zhang, F.; Zhang, B.; Kaplan, D. L. Silk Self-Assembly Mechanisms and Control From Thermodynamics to Kinetics. *Biomacromolecules* **2012**, *13*, 826-832. DOI: 10.1021/bm201731e.

(155) Shimanovich, U.; Ruggeri, F. S.; De Genst, E.; Adamcik, J.; Barros, T. P.; Porter, D.; Müller, T.; Mezzenga, R.; Dobson, C. M.; Vollrath, F.; et al. Silk micrococoons for protein stabilisation and molecular encapsulation. *Nat. Commun.* **2017**, *8*, 15902-15902. DOI: 10.1038/ncomms15902.

(156) Li, A. B.; Kluge, J. A.; Guziewicz, N. A.; Omenetto, F. G.; Kaplan, D. L. Silk-based stabilization of biomacromolecules. *J. Controlled Release* **2015**, *219*, 416-430. DOI: 10.1016/j.jconrel.2015.09.037.

(157) Chen, J.; Venkatesan, H.; Hu, J. Chemically Modified Silk Proteins. *Adv. Eng. Mater.* **2018**, *20*, 1-14. DOI: 10.1002/adem.201700961.

(158) Murphy, A. R.; John, P. S.; Kaplan, D. L. Modification of silk fibroin using diazonium coupling chemistry and the effects on hMSC proliferation and differentiation. *Biomaterials* **2008**, *29*, 2829-2838. DOI: 10.1016/j.biomaterials.2008.03.039.

(159) Totten, J. D.; Wongpinyochit, T.; Carrola, J.; Duarte, I. F.; Seib, F. P. PEGylation-Dependent Metabolic Rewiring of Macrophages with Silk Fibroin Nanoparticles. *ACS Appl. Mater. Interfaces* **2019**, *11*, 14515-14525. DOI: 10.1021/acsami.8b18716.

(160) Wongpinyochit, T.; Uhlmann, P.; Urquhart, A. J.; Seib, F. P. PEGylated Silk Nanoparticles for Anticancer Drug Delivery. *Biomacromolecules* **2015**, *16*, 3712-3722. DOI: 10.1021/acs.biomac.5b01003.

(161) Ramirez, S. M. V.; De Moraes, M. A.; Beppu, M. M. Assessing the influence of silkworm cocoon's age on the physicochemical properties of silk fibroin-based materials. *J. Mater. Res.* **2019**, *34*, 1944-1949. DOI: 10.1557/jmr.2019.108.

(162) Pritchard, E. M.; Hu, X.; Finley, V.; Kuo, C. K.; Kaplan, D. L. Effect of Silk Protein Processing on Drug Delivery from Silk Films. *Macromol. Biosci.* **2013**, *13*, 311-320. DOI: 10.1002/mabi.201200323.

(163) Jiang, P.; Liu, H.; Wang, C.; Wu, L.; Huang, J.; Guo, C. Tensile behavior and morphology of differently degummed silkworm (Bombyx mori) cocoon silk fibres. *Mater. Lett.* **2006**, *60*, 919-925. DOI: 10.1016/j.matlet.2005.10.056.

(164) Wang, Z.; Yang, H.; Li, W.; Li, C. Effect of silk degumming on the structure and properties of silk fibroin. *J. Text. Inst.* **2019**, *110*, 134-140. DOI: 10.1080/00405000.2018.1473074.

(165) Wray, L. S.; Hu, X.; Gallego, J.; Georgakoudi, I.; Omenetto, F. G.; Schmidt, D.; Kaplan, D. L. Effect of processing on silk-based biomaterials: Reproducibility and biocompatibility. *J. Biomed. Mater. Res. Part B: Appl. Biomater.* **2011**, *99*, 89-101. DOI: 10.1002/jbm.b.31875.

(166) Rohela, G. K.; Shukla, P.; Muttanna; Kumar, R.; Chowdhury, S. R. Mulberry (Morus spp.): An ideal plant for sustainable development. *Trees, Forests and People* **2020**, *2*, 100011. DOI: 10.1016/j.tfp.2020.100011.

(167) Zhu, L.; Lin, J.; Pei, L.; Luo, Y.; Li, D.; Huang, Z. Recent Advances in Environmentally Friendly and Green Degumming Processes of Silk for Textile and Non-Textile Applications. *Polymers* **2022**, *14*, 659. DOI: 10.3390/polym14040659.

(168) Ruiz-Alcaraz, A. J.; Núñez-Sánchez, M. Á.; Asensio Ruiz, M. A.; Martínez-Sánchez, M. A.; Oliva-Bolarín, A.; Martínez Martínez, T.; Pérez Cuadrado, J. J.; Ramos-Molina, B.; Lozano-Pérez, A. A. Optimizing the Preparation of Silk Fibroin Nanoparticles and Their Loading with Polyphenols: Towards a More Efficient Anti-Inflammatory Effect on Macrophages. *Pharmaceutics* **2023**, *15*, 263. DOI: 10.3390/pharmaceutics15010263.

(169) Lammel, A. S.; Hu, X.; Park, S. H.; Kaplan, D. L.; Scheibel, T. R. Controlling silk fibroin particle features for drug delivery. *Biomaterials* **2010**, *31*, 4583-4591. DOI: 10.1016/j.biomaterials.2010.02.024.

(170) Yang, P.; Dong, Y.; Huang, D.; Zhu, C.; Liu, H.; Pan, X.; Wu, C. Silk fibroin nanoparticles for enhanced bio-macromolecule delivery to the retina. *Pharm. Dev. Technol.* **2019**, *24*, 575-583. DOI: 10.1080/10837450.2018.1545236.

(171) Xu, H.-L.; ZhuGe, D.-L.; Chen, P.-P.; Tong, M.-Q.; Lin, M.-T.; Jiang, X.; Zheng, Y.-W.; Chen, B.; Li, X.-K.; Zhao, Y.-Z. Silk fibroin nanoparticles dyeing indocyanine green for imaging-guided photo-thermal therapy of glioblastoma. *Drug Delivery* **2018**, *25*, 364-375. DOI: 10.1080/10717544.2018.1428244.

(172) Takeuchi, I.; Shimamura, Y.; Kakami, Y.; Kameda, T.; Hattori, K.; Miura, S.; Shirai, H.; Okumura, M.; Inagi, T.; Terada, H.; et al. Transdermal delivery of 40-nm silk fibroin nanoparticles. *Colloids Surf., B* **2019**, *175*, 564-568. DOI: 10.1016/j.colsurfb.2018.12.012.

(173) Haque, S.; Whittaker, M. R.; McIntosh, M. P.; Pouton, C. W.; Kaminskas, L. M. Disposition and safety of inhaled biodegradable nanomedicines: Opportunities and challenges. *Nanomedicine: NBM* **2016**, *12*, 1703-1724. DOI: 10.1016/j.nano.2016.03.002.

(174) Wongpinyochit, T.; Totten, J. D.; Johnston, B. F.; Seib, F. P. Microfluidic-assisted silk nanoparticle tuning. *Nanoscale Adv.* **2019**, *1*, 873-883. DOI: 10.1039/c8na00208h.

(175) Zou, X.; Jiang, Z.; Li, L.; Huang, Z. Selenium nanoparticles coated with pH responsive silk fibroin complex for fingolimod release and enhanced targeting in thyroid cancer. *Artif. Cells, Nanomed., Biotechnol.* **2021**, *49*, 83-95. DOI: 10.1080/21691401.2021.1871620.

(176) Wang, X.; Yucel, T.; Lu, Q.; Hu, X.; Kaplan, D. L. Silk nanospheres and microspheres from silk/pva blend films for drug delivery. *Biomaterials* **2010**, *31*, 1025-1035. DOI: 10.1016/j.biomaterials.2009.11.002.

(177) Hu, Y.; Yu, J.; Liu, L.; Fan, Y. Preparation of natural amphoteric silk nanofibers by acid hydrolysis. *J. Mater. Chem. B* **2019**, *7*, 1450-1459. DOI: 10.1039/c8tb03005g.

(178) Kinahan, M. E.; Filippidi, E.; Hu, X.; Evans, H. M.; Pfohl, T.; Kaplan, D. L.; Wong, J. Tunable Silk: Using Microfluidics to Fabricate Silk Fibers with Controllable Properties. *Biomacromolecules* **2011**, *12*, 1504–1511. DOI: 10.1021/bm1014624.

(179) Solomun, J. I.; Totten, J. D.; Wongpinyochit, T.; Florence, A. J.; Seib, F. P. Manual versus Microfluidic-assisted Nanoparticle Manufacture : Impact of Silk Fibroin Stock on

Nanoparticle Characteristics. *ACS Biomater. Sci. Eng.* **2020**, *6*, 2796–2804. DOI: 10.1021/acsbiomaterials.0c00202.

(180) Meng, L.; Li, M.; Zhang, Y.; Tu, F.; Zhang, B.; Dong, F.; Wang, J. Modification and release of calcitonin gene-related peptide on silk fibroin film. *Text. Res. J.* **2023**, *93*, 317-325. DOI: 10.1177/00405175221117855.

(181) Wongpinyochit, T.; Vassileiou, A. D.; Gupta, S.; Mushrif, S. H.; Johnston, B. F.; Seib, F. P. Unraveling the Impact of High-Order Silk Structures on Molecular Drug Binding and Release Behaviors. *J. Phys. Chem. Lett.* **2019**, *10*, 4278-4284. DOI: 10.1021/acs.jpclett.9b01591.

(182) Harush-Frenkel, O.; Rozentur, E.; Benita, S.; Altschuler, Y. Surface Charge of Nanoparticles Determines Their Endocytic and Transcytotic Pathway in Polarized MDCK Cells. *Biomacromolecules* **2008**, *9*, 435-443. DOI: 10.1021/bm700535p.

(183) Totten, J. D.; Wongpinyochit, T.; Seib, F. P. Silk nanoparticles: proof of lysosomotropic anticancer drug delivery at single-cell resolution. *J. Drug Targeting* **2017**, *25*, 865-872. DOI: 10.1080/1061186X.2017.1363212.

(184) Maitz, M. F.; Sperling, C.; Wongpinyochit, T.; Herklotz, M.; Werner, C.; Seib, F. P. Biocompatibility assessment of silk nanoparticles: hemocompatibility and internalization by human blood cells. *Nanomedicine: NBM* **2017**, *13*, 2633-2642. DOI: 10.1016/j.nano.2017.07.012.

(185) Seib, F. P.; Jones, G. T.; Rnjak-Kovacina, J.; Lin, Y.; Kaplan, D. L. pH-Dependent Anticancer Drug Release from Silk Nanoparticles. *Adv. Healthcare Mater.* **2013**, *2*, 1606-1611. DOI: 10.1002/adhm.201300034.

(186) Albertazzi, L.; Serresi, M.; Albanese, A.; Beltram, F. Dendrimer Internalization and Intracellular Trafficking in Living Cells. *Mol. Pharmaceutics* **2010**, *7*, 680-688. DOI: 10.1021/mp9002464.

(187) Perumal, O. P.; Inapagolla, R.; Kannan, S.; Kannan, R. M. The effect of surface functionality on cellular trafficking of dendrimers. *Biomaterials* **2008**, *29*, 3469-3476. DOI: 10.1016/j.biomaterials.2008.04.038.

(188) Horo, H.; Bhattacharyya, S.; Mandal, B.; Kundu, L. M. Synthesis of functionalized silk-coated chitosan-gold nanoparticles and microparticles for target-directed delivery of antitumor agents. *Carbohydr. Polym.* **2021**, *258*, 117659. DOI: 10.1016/j.carbpol.2021.117659.

(189) Mottaghitalab, F.; Kiani, M.; Farokhi, M.; Kundu, S. C.; Reis, R. L.; Gholami, M.; Bardania, H.; Dinarvand, R.; Geramifar, P.; Beiki, D.; et al. Targeted Delivery System Based on Gemcitabine-Loaded Silk Fibroin Nanoparticles for Lung Cancer Therapy. *ACS Appl. Mater. Interfaces* **2017**, *9*, 31600-31611. DOI: 10.1021/acsami.7b10408.

(190) Pandey, V.; Haider, T.; Chandak, A. R.; Chakraborty, A.; Banerjee, S.; Soni, V. Technetium labeled doxorubicin loaded silk fibroin nanoparticles: Optimization, characterization and in vitro evaluation. *J. Drug Delivery Sci. Technol.* **2020**, *56*, 101539. DOI: 10.1016/j.jddst.2020.101539.

(191) Arumugam, M.; Murugesan, B.; Pandiyan, N.; Chinnalagu, D. K.; Rangasamy, G.; Mahalingam, S. Electrospinning cellulose acetate/silk fibroin/Au-Ag hybrid composite nanofiber for enhanced biocidal activity against MCF-7 breast cancer cell. *Mat. Sci. Eng. C* **2021**, *123*, 112019. DOI: 10.1016/j.msec.2021.112019.

(192) Zhang, X.; Huang, Y.; Song, H.; Canup, B. S. B.; Gou, S.; She, Z.; Dai, F.; Ke, B.; Xiao, B. Inhibition of growth and lung metastasis of breast cancer by tumor-homing triple-bioresponsive nanotherapeutics. *J. Controlled Release* **2020**, *328*, 454-469. DOI: 10.1016/j.jconrel.2020.08.066.

(193) Gou, S.; Huang, Y.; Wan, Y.; Ma, Y.; Zhou, X.; Tong, X.; Huang, J.; Kang, Y.; Pan, G.; Dai, F.; et al. Multi-bioresponsive silk fibroin-based nanoparticles with on-demand cytoplasmic drug release capacity for CD44-targeted alleviation of ulcerative colitis. *Biomaterials* **2019**, *212*, 39-54. DOI: 10.1016/j.biomaterials.2019.05.012.

(194) Tan, M.; Chen, Y.; Guo, Y.; Yang, C.; Liu, M.; Guo, D.; Wang, Z.; Cao, Y.; Ran, H. A low-intensity focused ultrasound-assisted nanocomposite for advanced triple cancer therapy: local chemotherapy, therapeutic extracellular vesicles and combined immunotherapy. *Biomater. Sci.* **2020**, *8*, 6703-6717. DOI: 10.1039/D0BM00804D.

(195) Bari, E.; Serra, M.; Paolillo, M.; Bernardi, E.; Tengattini, S.; Piccinini, F.; Lanni, C.; Sorlini, M.; Bisbano, G.; Calleri, E. Silk fibroin nanoparticle functionalization with Arg-Gly-Asp cyclopentapeptide promotes active targeting for tumor site-specific delivery. *Cancers* **2021**, *13*, 1185. DOI: 10.3390/cancers13051185.

(196) Bossi, A. M.; Bucciarelli, A.; Maniglio, D. Molecularly Imprinted Silk Fibroin Nanoparticles. *ACS Appl. Mater. Interfaces* **2021**, *13*, 31431-31439. DOI: 10.1021/acsami.1c05405.

(197) Sun, N.; Lei, R.; Xu, J.; Kundu, S. C.; Cai, Y.; Yao, J.; Ni, Q. Fabricated porous silk fibroin particles for pH-responsive drug delivery and targeting of tumor cells. *J. Mater. Sci.* **2019**, *54*, 3319-3330. DOI: 10.1007/s10853-018-3022-9.

(198) Florczak, A.; Deptuch, T.; Kucharczyk, K.; Dams-Kozlowska, H. Systemic and local silk-based drug delivery systems for cancer therapy. *Cancers* **2021**, *13*, 5389. DOI: 10.3390/cancers13215389.

(199) Kim, S. Y.; Naskar, D.; Kundu, S. C.; Bishop, D. P.; Doble, P. A.; Boddy, A. V.; Chan, H.-K.; Wall, I. B.; Chrzanowski, W. Formulation of biologically-inspired silk-based drug carriers for pulmonary delivery targeted for lung cancer. *Sci. Rep.* **2015**, *5*, 1-13. DOI: 10.1038/srep11878.

(200) Martínez-López, A. L.; Pangua, C.; Reboredo, C.; Campión, R.; Morales-Gracia, J.; Irache, J. M. Protein-based nanoparticles for drug delivery purposes. *Int. J. Pharm.* **2020**, *581*, 119289. DOI: 10.1016/j.ijpharm.2020.119289.

(201) Xu, J.; Wong, D. H. C.; Byrne, J. D.; Chen, K.; Bowerman, C.; DeSimone, J. M. Future of the Particle Replication in Nonwetting Templates (PRINT) Technology. *Angew. Chem., Int. Ed.* **2013**, *52*, 6580-6589. DOI: 10.1002/anie.201209145.

(202) Lim, J.-M.; Swami, A.; Gilson, L. M.; Chopra, S.; Choi, S.; Wu, J.; Langer, R.; Karnik, R.; Farokhzad, O. C. Ultra-High Throughput Synthesis of Nanoparticles with Homogeneous Size Distribution Using a Coaxial Turbulent Jet Mixer. *ACS Nano* **2014**, *8*, 6056-6065. DOI: 10.1021/nn501371n.

(203) Pal, R. K.; Kurland, N. E.; Jiang, C.; Kundu, S. C.; Zhang, N.; Yadavalli, V. K. Fabrication of precise shape-defined particles of silk proteins using photolithography. *Eur. Polym. J.* **2016**, *85*, 421-430. DOI: 10.1016/j.eurpolymj.2016.10.038.

(204) Webb, C.; Ip, S.; Bathula, N. V.; Popova, P.; Soriano, S. K. V.; Ly, H. H.; Eryilmaz, B.; Nguyen Huu, V. A.; Broadhead, R.; Rabel, M.; et al. Current Status and Future Perspectives on MRNA Drug Manufacturing. *Mol. Pharmaceutics* **2022**, *19*, 1047-1058. DOI: 10.1021/acs.molpharmaceut.2c00010.

(205) Leong, H. S.; Butler, K. S.; Brinker, C. J.; Azzawi, M.; Conlan, S.; Dufés, C.; Owen, A.; Rannard, S.; Scott, C.; Chen, C.; et al. On the issue of transparency and reproducibility in nanomedicine. *Nat. Nanotechnol.* **2019**, *14*, 629-635. DOI: 10.1038/s41565-019-0496-9.

(206) Lammers, T.; Storm, G. Setting standards to promote progress in bio–nano science. *Nat. Nanotechnol.* **2019**, *14*, 626. DOI: 10.1038/s41565-019-0497-8.

(207) Florindo, H. F.; Madi, A.; Satchi-Fainaro, R. Challenges in the implementation of MIRIBEL criteria on nanobiomed manuscripts. *Nat. Nanotechnol.* **2019**, *14*, 627-628. DOI: 10.1038/s41565-019-0498-7.

(208) Kazemimostaghim, M.; Rajkhowa, R.; Wang, X. Drug loading and release studies for milled silk particles of different sizes. *Powder Technol.* **2015**, *283*, 321-327. DOI: 10.1016/j.powtec.2015.05.042.

(209) Kazemimostaghim, M.; Rajkhowa, R.; Tsuzuki, T.; Wang, X. Production of submicron silk particles by milling. *Powder Technol.* **2013**, *241*, 230-235. DOI: 10.1016/j.powtec.2013.03.004.

(210) Kazemimostaghim, M.; Rajkhowa, R.; Wang, X. Comparison of milling and solution approach for production of silk particles. *Powder Technol.* **2014**, *262*, 156-161. DOI: 10.1016/j.powtec.2014.04.011.

(211) Rajkhowa, R.; Wang, L.; Wang, X. Ultra-fine silk powder preparation through rotary and ball milling. *Powder technol.* **2008**, *185*, 87-95. DOI: 10.1016/j.powtec.2008.01.005.

(212) Pham, D. T.; Tiyaboonchai, W. Fibroin nanoparticles : a promising drug delivery system. *Drug Delivery* **2020**, *27*, 431-448. DOI: 10.1080/10717544.2020.1736208.

(213) Kankala, R. K.; Chen, B.-Q.; Liu, C.-G.; Tang, H.-X.; Wang, S.-B.; Chen, A.-Z. Solution-enhanced dispersion by supercritical fluids: an ecofriendly nanonization approach for processing biomaterials and pharmaceutical compounds. *Int. J. Nanomed.* **2018**, *13*, 4227-4245. DOI: 10.2147/IJN.S166124.

(214) Zhao, Z.; Li, Y.; Chen, A.-Z.; Zheng, Z.-J.; Hu, J.-Y.; Li, J.-S.; Li, G. Generation of Silk Fibroin Nanoparticles via Solution-Enhanced Dispersion by Supercritical CO2. *Ind. Eng. Chem. Res.* **2013**, *52*, 3752-3761. DOI: 10.1021/ie301907f.

(215) Chen, B. Q.; Kankala, R. K.; He, G. Y.; Yang, D. Y.; Li, G. P.; Wang, P.; Wang, S. B.; Zhang, Y. S.; Chen, A. Z. Supercritical Fluid-Assisted Fabrication of Indocyanine Green-Encapsulated Silk Fibroin Nanoparticles for Dual-Triggered Cancer Therapy. *ACS Biomater. Sci. Eng.* **2018**, *4*, 3487-3497. DOI: 10.1021/acsbiomaterials.8b00705.

(216) Gholami, A.; Tavanai, H.; Moradi, A. R. Production of fibroin nanopowder through electrospraying. *J. Nanopart. Res.* **2011**, *13*, 2089-2098. DOI: 10.1007/s11051-010-9965-7.

(217) Qu, J.; Liu, Y.; Yu, Y.; Li, J.; Luo, J.; Li, M. Silk fibroin nanoparticles prepared by electrospray as controlled release carriers of cisplatin. *Mater. Sci. Eng., C* **2014**, *44*, 166-174. DOI: 10.1016/j.msec.2014.08.034.

(218) Huang, Y.; Lu, Q.; Li, M.; Zhang, B.; Zhu, H. Silk fibroin microsphere drug carriers prepared under electric fields. *Sci. China. Press* **2011**, *56*, 1013-1018.

(219) Lu, Q.; Huang, Y.; Li, M.; Zuo, B.; Lu, S.; Wang, J.; Zhu, H.; Kaplan, D. L. Silk fibroin electrogelation mechanisms. *Acta Biomater.* **2011**, *7*, 2394-2400. DOI: 10.1016/j.actbio.2011.02.032.

(220) Wenk, E.; Wandrey, A. J.; Merkle, H. P.; Meinel, L. Silk fibroin spheres as a platform for controlled drug delivery. *J. Controlled Release* **2008**, *132*, 26-34. DOI: 10.1016/j.jconrel.2008.08.005.

(221) Gupta, V.; Aseh, A.; Ríos, C. N.; Aggarwal, B. B.; Mathur, A. B. Fabrication and characterization of silk fibroin-derived curcumin nanoparticles for cancer therapy. *Int. J. Nanomed.* **2009**, *4*, 115-122. DOI: 10.2147/ijn.s5581.

(222) Pham, D. T.; Saelim, N.; Tiyaboonchai, W. Alpha mangostin loaded crosslinked silk fibroin-based nanoparticles for cancer chemotherapy. *Colloids Surf., B* **2019**, *181*, 705-713. DOI: 10.1016/j.colsurfb.2019.06.011.

(223) Wang, Y.; Cheng, Q.; Liu, J.; Tariq, Z.; Zheng, Z.; Li, G.; Kaplan, D. L.; Wang, X. Tuning Microcapsule Shell Thickness and Structure with Silk Fibroin and Nanoparticles for Sustained Release. *ACS Biomater. Sci. Eng.* **2020**, *6*, 4583–4594. DOI: 10.1021/acsbiomaterials.0c00835.

(224) Li, L.; Puhl, S.; Meinel, L.; Germershaus, O. Silk fibroin layer-by-layer microcapsules for localized gene delivery. *Biomaterials* **2014**, *35*, 7929-7939. DOI: 10.1016/j.biomaterials.2014.05.062.

(225) Bai, S.; Liu, S.; Zhang, C.; Xu, W.; Lu, Q.; Han, H.; Kaplan, D. L.; Zhu, H. Controllable transition of silk fibroin nanostructures: An insight into in vitro silk self-assembly process. *Acta Biomater.* **2013**, *9*, 7806-7813. DOI: 10.1016/j.actbio.2013.04.033.

(226) Wu, J.; Zheng, Z.; Li, G.; Kaplan, D. L.; Wang, X. Control of silk microsphere formation using polyethylene glycol (PEG). *Acta Biomater.* **2016**, *39*, 156-168. DOI: 10.1016/j.actbio.2016.05.019.

(227) Wang, X.; Wenk, E.; Hu, X.; Castro, G. R.; Meinel, L.; Wang, X.; Li, C.; Merkle, H.; Kaplan, D. L. Silk coatings on PLGA and alginate microspheres for protein delivery. *Biomaterials* **2007**, *28*, 4161-4169. DOI: 10.1016/j.biomaterials.2007.05.036.

(228) Tomeh, M. A.; Mansor, M. H.; Hadianamrei, R.; Sun, W.; Zhao, X. Optimization of large-scale manufacturing of biopolymeric and lipid nanoparticles using microfluidic swirl mixers. *Int. J. Pharm.* **2022**, *620*, 121762. DOI: 10.1016/j.ijpharm.2022.121762.

(229) Myung, S. J.; Kim, H.-S. S.; Kim, Y.; Chen, P.; Jin, H.-J. J. Fluorescent silk fibroin nanoparticles prepared using a reverse microemulsion. *Macromol. Res.* **2008**, *16*, 604-608. DOI: 10.1007/BF03218567.

(230) Wang, X.; Wenk, E.; Matsumoto, A.; Meinel, L.; Li, C.; Kaplan, D. L. Silk microspheres for encapsulation and controlled release. *J. Controlled Release* **2007**, *117*, 360-370. DOI: 10.1016/j.jconrel.2006.11.021.

(231) Baimark, Y.; Srihanam, P.; Srisuwan, Y.; Phinyocheep, P. Preparation of porous silk fibroin microparticles by a water-in-oil emulsification-diffusion method. *J. Appl. Polym. Sci.* **2010**, *118*, 1127-1133. DOI: 10.1002/app.32506 (acccessed 2023/11/24).

(232) Han, Q.; Zheng, T.; Zhang, L.; Wu, N.; Liang, J.; Wu, H.; Li, G. Metformin loaded injectable silk fibroin microsphere for the treatment of spinal cord injury. *J. Biomater. Sci., Polym. Ed.* **2022**, *33*, 747-768. DOI: 10.1080/09205063.2021.2014113.

(233) DeFrates, K.; Markiewicz, T.; Gallo, P.; Rack, A.; Weyhmiller, A.; Jarmusik, B.; Hu, X. Protein Polymer-Based Nanoparticles: Fabrication and Medical Applications. *Int. J. Mol. Sci.* **2018**, *19*, 1717. DOI: 10.3390/ijms19061717.

(234) Mathur, A. B.; Gupta, v. Silk fibroin-derived nanoparticles for biomedical applications. *Nanomedicine* **2010**, *5*, 807-820. DOI: 10.2217/nnm.10.51.

(235) Gobin, A. S.; Rhea, R.; Newman, R. A.; Mathur, A. B. Silk-fibroin-coated liposomes for long-term and targeted drug delivery. *Int. J. Nanomed.* **2006**, *1*, 81-87. DOI: 10.2147/nano.2006.1.1.81.

(236) Zhang, Y.-Q.; Shen, W.-D.; Xiang, R.-L.; Zhuge, L.-J.; Gao, W.-J.; Wang, W.-B. Formation of silk fibroin nanoparticles in water-miscible organic solvent and their characterization. *J. Nanopart. Res.* **2007**, *9*, 885–900. DOI: 10.1007/s11051-006-9162-x.

(237) Lozano-Pérez, A. A.; Montalbán, M. G.; Aznar-Cervantes, S. D.; Cragnolini, F.; Cenis, J. L.; Víllora, G. Production of silk fibroin nanoparticles using ionic liquids and high-power ultrasounds. *J. Appl. Polym. Sci.* **2015**, *132*, 41702. DOI: 10.1002/app.41702.

(238) Srisuwan, Y.; Srihanam, P.; Baimark, Y. Preparation of Silk Fibroin Microspheres and Its Application to Protein Adsorption. *J. Macromol. Sci., Part A* **2009**, *46*, 521-525. DOI: 10.1080/10601320902797780.

(239) Xie, M.; Fan, D.; Li, Y.; He, X.; Chen, X.; Chen, Y.; Zhu, J.; Xu, G.; Wu, X.; Lan, P. Supercritical carbon dioxide-developed silk fibroin nanoplatform for smart colon cancer therapy. *Int. J. Nanomed.* **2017**, *12*, 7751-7761. DOI: 10.2147/IJN.S145012.

(240) Beck-Broichsitter, M.; Rytting, E.; Lebhardt, T.; Wang, X.; Kissel, T. Preparation of nanoparticles by solvent displacement for drug delivery: A shift in the " ouzo region" upon drug loading. *Eur. J. Pharm. Sci.* **2010**, *41*, 244-253. DOI: 10.1016/j.ejps.2010.06.007.

(241) Kaewpirom, S.; Boonsang, S. Influence of alcohol treatments on properties of silk-fibroin-based films for highly optically transparent coating applications. *RSC Adv.* **2020**, *10*, 15913-15923. DOI: 10.1039/D0RA02634D.

(242) Kundu, J.; Chung, Y.-I.; Kim, Y. H.; Tae, G.; Kundu, S. C. Silk fibroin nanoparticles for cellular uptake and control release. *Int. J. Pharm.* **2010**, *388*, 242-250. DOI: 10.1016/j.ijpharm.2009.12.052.

(243) Shaidani, S.; Jacobus, C.; Sahoo, J. K.; Harrington, K.; Johnson, H.; Foster, O.; Cui, S.; Hasturk, O.; Falcucci, T.; Chen, Y.; et al. Silk Nanoparticle Synthesis: Tuning Size, Dispersity, and Surface Chemistry for Drug Delivery. *ACS Appl. Nano Mater.* **2023**, *6*, 18967-18977. DOI: 10.1021/acsanm.3c03451.

(244) Toprakcioglu, Z.; Challa, P. K.; Morse, D. B.; Knowles, T. Attoliter protein nanogels from droplet nanofluidics for intracellular delivery. *Sci. Adv.* **2020**, *6*, eaay7952. DOI: 10.1126/sciadv.aay7952.

(245) Vargas Montoya, N.; Peterson, R.; Ornell, K. J.; Albrecht, D. R.; Coburn, J. M. Silk Particle Production Based on Silk/PVA Phase Separation Using a Microfabricated Co-flow Device. *Molecules* **2020**, *25*, 890. DOI: 10.3390/molecules25040890.

(246) Kastner, E.; Kaur, R.; Lowry, D.; Moghaddam, B.; Wilkinson, A.; Perrie, Y. High-throughput manufacturing of size-tuned liposomes by a new microfluidics method using enhanced statistical tools for characterization. *Int. J. Pharm.* **2014**, *477*, 361-368. DOI: 10.1016/j.ijpharm.2014.10.030.

(247) Guimarães Sá Correia, M.; Briuglia, M. L.; Niosi, F.; Lamprou, D. A. Microfluidic manufacturing of phospholipid nanoparticles: Stability, encapsulation efficacy, and drug release. *Int. J. Pharm.* **2017**, *516*, 91-99. DOI: 10.1016/j.ijpharm.2016.11.025.

(248) Gdowski, A.; Johnson, K.; Shah, S.; Gryczynski, I.; Vishwanatha, J.; Ranjan, A. Optimization and scale up of microfluidic nanolipomer production method for preclinical and potential clinical trials. *J. Nanobiotechnol.* **2018**, *16*, 12. DOI: 10.1186/s12951-018-0339-0.

(249) Martins, J. P.; Torrieri, G.; Santos, H. A. The importance of microfluidics for the preparation of nanoparticles as advanced drug delivery systems. *Expert Opin. Drug Delivery* **2018**, *15*, 469-479. DOI: 10.1080/17425247.2018.1446936.

(250) Mukhopadhyay, R. When PDMS isn't the best. *Anal. Chem.* **2007**, *79*, 3248-3253. DOI: 10.1021/ac071903e.

(251) Bettinger, C. J.; Cyr, K. M.; Matsumoto, A.; Langer, R.; Borenstein, J. T.; Kaplan, D. L. Silk Fibroin Microfluidic Devices. *Adv. Mater.* **2007**, *19*, 2847-2850. DOI: 10.1002/adma.200602487.

(252) Zhou, M.; Shi, X.; Li, X.; Xiao, G.; Liang, L.; Ju, J.; Wang, F.; Xia, Q.; Sun, W.; Qiao, Y.; et al. Constructing Silk Fibroin-Based Three-Dimensional Microfluidic Devices via a Tape Mask-Assisted Multiple-Step Etching Technique. *ACS Appl. Bio Mater.* **2021**, *4*, 8039-8048. DOI: 10.1021/acsabm.1c00948.

(253) Mukhopadhyay, R. When Microfluidic Devices Go Bad. *Anal. Chem.* **2005**, *77*, 429 A-432 A. DOI: 10.1021/ac053496h.

(254) Shepherd, S. J.; Issadore, D.; Mitchell, M. J. Microfluidic formulation of nanoparticles for biomedical applications. *Biomaterials* **2021**, *274*, 120826. DOI: 10.1016/j.biomaterials.2021.120826.

(255) Webb, C.; Forbes, N.; Roces, C. B.; Anderluzzi, G.; Lou, G.; Abraham, S.; Ingalls, L.; Marshall, K.; Leaver, T. J.; Watts, J. A.; et al. Using microfluidics for scalable manufacturing of nanomedicines from bench to GMP: A case study using protein-loaded liposomes. *Int. J. Pharm.* **2020**, *582*, 119266. DOI: 10.1016/j.ijpharm.2020.119266.

(256) Breslauer, D. N.; Muller, S. J.; Lee, L. P. Generation of monodisperse silk microspheres prepared with microfluidics. *Biomacromolecules* **2010**, *11*, 643-647. DOI: 10.1021/bm901209u.

(257) Toprakcioglu, Z.; Levin, A.; Knowles, T. P. J. Hierarchical Biomolecular Emulsions Using 3-D Microfluidics with Uniform Surface Chemistry. *Biomacromolecules* **2017**, *18*, 3642-3651. DOI: 10.1021/acs.biomac.7b01159.

(258) Kee, S. P.; Gavriilidis, A. Design and characterisation of the staggered herringbone mixer. *Chem. Eng. J.* **2008**, *142*, 109-121. DOI: 10.1016/j.cej.2008.02.001.

(259) Williams, M. S.; Longmuir, K. J.; Yager, P. A practical guide to the staggered herringbone mixer. *Lab Chip* **2008**, *8*, 1121-1129. DOI: 10.1039/b802562b.

(260) Hou, J.; Ci, H.; Wang, P.; Wang, C.; Lv, B.; Miao, L.; You, G. Nanoparticle tracking analysis versus dynamic light scattering: Case study on the effect of Ca2+ and alginate on the aggregation of cerium oxide nanoparticles. *J. Hazard. Mater.* **2018**, *360*, 319-328. DOI: 10.1016/j.jhazmat.2018.08.010.

(261) Elahi, M. F.; Guan, G.; Wang, L. Hemocompatibility of surface modified silk fibroin materials: a review. *Rev. Adv. Mater. Sci.* **2014**, *38*, 148-159.

(262) Liu, H.; Sun, Z.; Guo, C. Chemical Modification of Silk Proteins: Current Status and Future Prospects. *Adv. Fiber Mater.* **2022**, *4*, 705-719. DOI: 10.1007/s42765-022-00144-9.

(263) Leier, S.; Richter, S.; Bergmann, R.; Wuest, M.; Wuest, F. Radiometal-containing aryl diazonium salts for chemoselective bioconjugation of tyrosine residues. *ACS Omega* **2019**, *4*, 22101-22107. DOI: 10.1021/acsomega.9b03248.

(264) Yan, H.-B.; Zhang, Y.-Q.; Ma, Y.-L.; Zhou, L.-X. Biosynthesis of insulin-silk fibroin nanoparticles conjugates and in vitro evaluation of a drug delivery system. *J. Nanopart. Res.* **2009**, *11*, 1937-1946. DOI: 10.1007/s11051-008-9549-y.

(265) Migneault, I.; Dartiguenave, C.; Bertrand, M. J.; Waldron, K., C. . Glutaraldehyde: behavior in aqueous solution, reaction with proteins, and application to enzyme crosslinking. *BioTechniques* **2004**, *37*, 790-802. DOI: 10.2144/04375RV01.

(266) Imanzadeh, G. H.; Zamanloo, M. R.; Mansoori, Y.; Khodayari, A. Aqueous Media Oxidation of Alcohols with Ammonium Persulfate. *Chin. J. Chem.* **2007**, *25*, 836-838. DOI: 10.1002/cjoc.200790153.

(267) Behrman, E. J. The Persulfate Oxidation of Phenols and Arylamines (The Elbs and the Boyland–Sims Oxidations). *Org. React.* **2004**, *35*, 421-511. DOI: 10.1002/0471264180.or035.02.

(268) Leung, A. C. W.; Hrapovic, S.; Lam, E.; Liu, Y.; Male, K. B.; Mahmoud, K. A.; Luong, J. H. T. Characteristics and properties of carboxylated cellulose nanocrystals prepared from a novel one-step procedure. *Small* **2011**, *7*, 302-305. DOI: 10.1002/smll.201001715.

(269) McGill, M.; Grant, J. M.; Kaplan, D. L. Enzyme-Mediated Conjugation of Peptides to Silk Fibroin for Facile Hydrogel Functionalization. *Ann. Biomed. Eng.* **2020**, *48*, 1905-1915. DOI: 10.1007/s10439-020-02503-2.

(270) Moh, E. S. X.; Packer, N. H. Enzymatic Azido-GalNAc-Functionalized Silk Fibroin for Click Chemistry Conjugation. *Biomacromolecules* **2021**, *22*, 1752–1755. DOI: 10.1021/acs.biomac.0c01791.

(271) Thirumurugan, P.; Matosiuk, D.; Jozwiak, K. Click chemistry for drug development and diverse chemical-biology applications. *Chem. Rev.* **2013**, *113*, 4905-4979. DOI: 10.1021/cr200409f.

(272) Zhang, X.; Liang, J.; Chen, Z.; Donley, C.; Liu, Y.; Cheng, G. Chemical modification of Bombyx mori silk fibers with vinyl groups for thiol-ene click chemistry. *BMC Chem.* **2019**, *13*, 114 DOI: 10.1186/s13065-019-0630-7.

(273) Hardy, J. G.; Pfaff, A.; Leal-Egaña, A.; Müller, A. H. E.; Scheibel, T. R. Glycopolymer Functionalization of Engineered Spider Silk Protein-based Materials for Improved Cell Adhesion. *Macromol. Biosci.* **2014**, *14*, 936-942. DOI: 10.1002/mabi.201400020.

(274) Boyatzis, A. E.; Bringans, S. D.; Piggott, M. J.; Duong, M. N.; Lipscombe, R. J.; Arthur, P. G. Limiting the Hydrolysis and Oxidation of Maleimide–Peptide Adducts Improves Detection of Protein Thiol Oxidation. *J. Proteome Res.* **2017**, *16*, 2004-2015. DOI: 10.1021/acs.jproteome.6b01060.

(275) Harvey, D.; Bardelang, P.; Goodacre, S. L.; Cockayne, A.; Thomas, N. R. Antibiotic Spider Silk: Site-Specific Functionalization of Recombinant Spider Silk Using “Click” Chemistry. *Adv. Mater.* **2017**, *29*, 1604245. DOI: 10.1002/adma.201604245.

(276) Teramoto, H.; Kojima, K. Production of Bombyx mori silk fibroin incorporated with unnatural amino acids. *Biomacromolecules* **2014**, *15*, 2682-2690. DOI: 10.1021/bm5005349.

(277) Teramoto, H. In vivo Incorporation of an Alkyne-Bearing Amino Acid into Bombyx mori Silk Fibroin. *J. Insect Biotechnol. Sericol.* **2017**, *86*, 3_113-113_121. DOI: 10.11416/jibs.86.3_113.

(278) Teramoto, H.; Kojima, K. Incorporation of methionine analogues into Bombyx mori silk fibroin for click modifications. *Macromol. Biosci.* **2015**, *15*, 719-727. DOI: 10.1002/mabi.201400482.

(279) Spieß, K.; Wohlrab, S.; Scheibel, T. Structural characterization and functionalization of engineered spider silk films. *Soft Matter* **2010**, *6*, 4168-4174. DOI: 10.1039/B927267D.

(280) Herold, H. M.; Aigner, T. B.; Grill, C. E.; Krüger, S.; Taubert, A.; Scheibel, T. SpiderMAEn: recombinant spider silk-based hybrid materials for advanced energy technology. *Bioinspired, Biomimetic Nanobiomater.* **2019**, *8*, 99-108. DOI: 10.1680/jbibn.18.00007.

(281) Lang, G.; Grill, C.; Scheibel, T. Site-Specific Functionalization of Recombinant Spider Silk Janus Fibers. *Angew. Chem., Int. Ed.* **2022**, *61*, e202115232. DOI: 10.1002/anie.202115232.

(282) Teramoto, H.; Kojima, K. Residue-specific incorporation of phenylalanine analogues into protein biosynthesis in silkworm cultured cells. *J. Insect Biotechnol. Sericol.* **2013**, *82*, 3_061-063_069. DOI: 10.11416/jibs.82.3_061.

(283) Tian, Y.; Iga, M.; Tsuboi, H.; Teramoto, H. A Novel Transgenic Silkworm Line for Mass Production of Azido-Incorporated Silk Fiber. *The Journal of Silk Science and Technology of Japan* **2022**, *30*, 75-85. DOI: 10.11417/silk.30.75.

(284) Teramoto, H.; Nakajima, K.-I.; Kojima, K. Azide-Incorporated Clickable Silk Fibroin Materials with the Ability to Photopattern. *ACS Biomater. Sci. Eng.* **2016**, *2*, 251-258. DOI: 10.1021/acsbiomaterials.5b00469.

(285) Teramoto, H.; Shirakawa, M.; Tamada, Y. Click Decoration of Bombyx mori Silk Fibroin for Cell Adhesion Control. *Molecules* **2020**, *25*, 4106. DOI: 10.3390/molecules25184106.

(286) Teramoto, H.; Amano, Y.; Iraha, F.; Kojima, K.; Ito, T.; Sakamoto, K. Genetic Code Expansion of the Silkworm Bombyx mori to Functionalize Silk Fiber. *ACS Synth. Biol.* **2018**, *7*, 801-806. DOI: 10.1021/acssynbio.7b00437.

(287) Teramoto, H.; Kojima, K.; Iga, M.; Yoshioka, T. Unique Material Properties of Bombyx mori Silk Fiber Incorporated with 3-Azidotyrosine. *Biomacromolecules* **2023**, *24*, 4208-4217. DOI: 10.1021/acs.biomac.3c00533.

(288) Janani, G.; Kumar, M.; Chouhan, D.; Moses, J. C.; Gangrade, A.; Bhattacharjee, S.; Mandal, B. B. Insight into Silk-Based Biomaterials: From Physicochemical Attributes to Recent Biomedical Applications. *ACS Appl. Bio Mater.* **2019**, *2*, 5460–5491. DOI: 10.1021/acsabm.9b00576.

(289) Wenk, E.; Merkle, H. P.; Meinel, L. Silk fibroin as a vehicle for drug delivery applications. *J. Controlled Release* **2011**, *150*, 128-141. DOI: 10.1016/j.jconrel.2010.11.007.

(290) Mehrotra, S.; Chouhan, D.; Konwarh, R.; Kumar, M.; Jadi, P. K.; Mandal, B. B. Comprehensive Review on Silk at Nanoscale for Regenerative Medicine and Allied Applications. *ACS Biomater. Sci. Eng.* **2019**, *5*, 2054-2078. DOI: 10.1021/acsbiomaterials.8b01560.

(291) Chouhan, D.; Mandal, B. B. Silk biomaterials in wound healing and skin regeneration therapeutics: From bench to bedside. *Acta Biomater.* **2020**, *103*, 24-51. DOI: 10.1016/j.actbio.2019.11.050.

(292) Xiao, L.; Lu, G.; Lu, Q.; Kaplan, D. L. Direct Formation of Silk Nanoparticles for Drug Delivery. *ACS Biomater. Sci. Eng.* **2016**, *2*, 2050-2057. DOI: 10.1021/acsbiomaterials.6b00457.

(293) Xu, Z.; Shi, L.; Yang, M.; Zhu, L. Preparation and biomedical applications of silk fibroin-nanoparticles composites with enhanced properties - A review. *Mater. Sci. Eng., C* **2019**, *95*, 302-311. DOI: 10.1016/j.msec.2018.11.010.

(294) Konwarh, R. Can the venerated silk be the next-generation nanobiomaterial for biomedical-device designing, regenerative medicine and drug delivery? Prospects and hitches. *Bio-Des. Manuf.* **2019**, *2*, 278-286. DOI: 10.1007/s42242-019-00052-9.

(295) Crivelli, B.; Perteghella, S.; Bari, E.; Sorrenti, M.; Tripodo, G.; Chlapanidas, T.; Torre, M. L. Silk nanoparticles: from inert supports to bioactive natural carriers for drug delivery. *Soft Matter* **2018**, *14*, 546-557. DOI: 10.1039/c7sm01631.

(296) Zhao, Z.; Li, Y.; Xie, M.-B. Silk fibroin-based nanoparticles for drug delivery. *Int. J. Mol. Sci.* **2015**, *16*, 4880-4903. DOI: 10.3390/ijms16034880.

(297) Tarhini, M.; Greige-Gerges, H.; Elaissari, A. Protein-based nanoparticles: From preparation to encapsulation of active molecules. *Int. J. Pharm.* **2017**, *522*, 172-197. DOI: 10.1016/j.ijpharm.2017.01.067.

(298) Vauthier, C.; Bouchemal, K. Methods for the Preparation and Manufacture of Polymeric Nanoparticles. *Pharm. Res.* **2009**, *26*, 1025-1058. DOI: 10.1007/s11095-008-9800-3.

(299) Botet, R.; Roger, K. How do interactions control droplet size during nanoprecipitation? *Curr. Opin. Colloid Interface Sci.* **2016**, *22*, 108-112. DOI: 10.1016/j.cocis.2016.03.003.

(300) Baldyga, J.; Pohorecki, R. Turbulent micromixing in chemical reactors - a review. *Chem. Eng. J.* **1995**, *58*, 183-195. DOI: 10.1016/0923-0467(95)02982-6.

(301) Nisal, A.; Kalelkar, C.; Bellare, J.; Lele, A. Rheology and microstructural studies of regenerated silk fibroin solutions. *Rheol. Acta* **2013**, *52*, 833-840. DOI: 10.1007/s00397-013-0723-5.

(302) Ianovska, M. A.; Mulder, P. P. M. F. A.; Verpoorte, E. Development of small-volume, microfluidic chaotic mixers for future application in two-dimensional liquid chromatography. *RSC Adv.* **2017**, *7*, 9090-9099. DOI: 10.1039/c6ra28626g.

(303) Rode García, T.; García Ac, A.; Lalloz, A.; Lacasse, F.-X.; Hildgen, P.; Rabanel, J.-M.; Banquy, X. Unified Scaling of the Structure and Loading of Nanoparticles Formed by Diffusion-Limited Coalescence. *Langmuir* **2018**, *34*, 5772-5780. DOI: 10.1021/acs.langmuir.8b00652.

(304) Yang, H.; Yang, S.; Kong, J.; Dong, A.; Yu, S. Obtaining information about protein secondary structures in aqueous solution using Fourier transform IR spectroscopy. *Nat. Protoc.* **2015**, *10*, 382-396. DOI: 10.1038/nprot.2015.024.

(305) Hu, X.; Kaplan, D.; Cebe, P. Determining beta-sheet crystallinity in fibrous proteins by thermal analysis and infrared spectroscopy. *Macromolecules* **2006**, *39*, 6161-6170. DOI: 10.1021/ma0610109.

(306) Griebenow, K.; Santos, A. M.; Carrasquillo, K. G. Secondary structure of proteins in the amorphous dehydrated state probed by FTIR spectroscopy. Dehydration-induced structural changes and their prevention. *Internet J.Vib.Spectrosc.* **1999**, *3*, 1-2.

(307) Riesen, R.; Vogel, K.; Schubnell, M. DSC by the TGA/SDTA851e considering mass changes. *J. Therm. Anal. Calorim.* **2001**, *64*, 243-252. DOI: 10.1023/A:1011505617274.

(308) Thermal Analysis of Polymers. Fundamentals and applications. Menczel, J. D., Prime, R. B. Eds.; Wiley, 2009.

(309) Mottaghitalab, F.; Farokhi, M.; Shokrgozar, M. A.; Atyabi, F.; Hosseinkhani, H. Silk fibroin nanoparticle as a novel drug delivery system. *J. Controlled Release* **2015**, *206*, 161-176. DOI: 10.1016/j.jconrel.2015.03.020.

(310) Agrahari, V.; Agrahari, V. Facilitating the translation of nanomedicines to a clinical product: challenges and opportunities. *Drug Discov. Today* **2018**, *23*, 974-991. DOI: 10.1016/j.drudis.2018.01.047.

(311) Muthu, M. S.; Wilson, B. Challenges posed by the scale-up of nanomedicines. *Nanomedicine* **2012**, *7*, 307-309. DOI: 10.2217/NNM.12.3.

(312) Pham, D. T.; Saelim, N.; Tiyaboonchai, W. Design of experiments model for the optimization of silk fibroin based nanoparticles. *Int. J. Appl. Pharm.* **2018**, *10*, 195-201. DOI: 10.22159/ijap.2018v10i5.28139.

(313) Dunderdale, G. J.; Davidson, S. J.; Ryan, A. J.; Mykhaylyk, O. O. Flow-induced crystallisation of polymers from aqueous solution. *Nat. Commun.* **2020**, *11*, 3372-3372. DOI: 10.1038/s41467-020-17167-8.

(314) Anselmo, A. C.; Mitragotri, S. Nanoparticles in the clinic. *Bioeng. Transl. Med.* **2016**, *1*, 10-29. DOI: 10.1002/btm2.10003.

(315) Wacker, M. Nanocarriers for intravenous injection - The long hard road to the market. *Int. J. Pharm.* **2013**, *457*, 50-62. DOI: 10.1016/j.ijpharm.2013.08.079.

(316) Rahimnejad, M.; Najafpour, G.; Bakeri, G. Investigation and modeling effective parameters influencing the size of BSA protein nanoparticles as colloidal carrier. *Colloids Surf., A* **2012**, *412*, 96-100. DOI: 10.1016/j.colsurfa.2012.07.022.

(317) Crucho, C. I. C.; Barros, M. T. Polymeric nanoparticles: A study on the preparation variables and characterization methods. *Mater. Sci. Eng., C* **2017**, *80*, 771-784. DOI: 10.1016/j.msec.2017.06.004.

(318) Camacho, C. J.; Kimura, S. R.; DeLisi, C.; Vajda, S. Kinetics of desolvation-mediated protein-protein binding. *Biophys. J.* **2000**, *78*, 1094-1105. DOI: 10.1016/S0006-3495(00)76668-9.

(319) You, H.; Fang, J. Particle-mediated nucleation and growth of solution-synthesized metal nanocrystals: A new story beyond the LaMer curve. *Nano Today* **2016**, *11*, 145-167. DOI: 10.1016/j.nantod.2016.04.003.

(320) Galisteo-González, F.; Molina-Bolívar, J. A. Systematic study on the preparation of BSA nanoparticles. *Colloids Surf., B* **2014**, *123*, 286-292. DOI: 10.1016/j.colsurfb.2014.09.028.

(321) Gao, G.; Wang, Y.; Cao, G. W. Y. *Nanostructures and Nanomaterials Synthesis, Properties, and Applications*; World scientific, 2011.

(322) Motta, A.; Fambri, L.; Migliaresi, C. Regenerated silk fibroin films: Thermal and dynamic mechanical analysis. *Macromol. Chem. Phys.* **2002**, *203*, 1658-1665. DOI: 10.1002/1521-3935(200207)203:10/11<1658::AID-MACP1658>3.0.CO;2-3.

(323) Um, I. C.; Kweon, H. Y.; Park, Y. H.; Hudson, S. Structural characteristics and properties of the regenerated silk fibroin prepared from formic acid. *Int. J. Biol. Macromol.* **2001**, *29*, 91-97. DOI: 10.1016/S0141-8130(01)00159-3.

(324) Thanh, N. T. K.; Maclean, N.; Mahiddine, S. Mechanisms of nucleation and growth of nanoparticles in solution. *Chem. Rev.* **2014**, *114*, 7610-7630. DOI: 10.1021/cr400544s.

(325) Seib, F. P.; Maitz, M. F.; Hu, X.; Werner, C.; Kaplan, D. L. Impact of processing parameters on the haemocompatibility of Bombyx mori silk films. *Biomaterials* **2012**, *33*, 1017-1023. DOI: 10.1016/j.biomaterials.2011.10.063.

(326) Tomeh, M. A.; Hadianamrei, R.; Zhao, X. Silk Fibroin as a Functional Biomaterial for Drug and Gene Delivery. *Pharmaceutics* **2019**, *11*, 494-494. DOI: 10.3390/pharmaceutics11100494.

(327) Jin, H.-J.; Kaplan, D. L. Mechanism of silk processing in insects and spiders. *Nature* **2003**, *424*, 1057-1061. DOI: 10.1038/nature01809.

(328) Richtering, W.; Alberg, I.; Zentel, R. Nanoparticles in the Biological Context: Surface Morphology and Protein Corona Formation. *Small* **2020**, *16*, 1-8. DOI: 10.1002/smll.202002162.

(329) Arno, M. C.; Inam, M.; Weems, A. C.; Li, Z.; Binch, A. L. A.; Platt, C. I.; Richardson, S. M.; Hoyland, J. A.; Dove, A. P.; O'Reilly, R. K. Exploiting the role of nanoparticle shape in enhancing hydrogel adhesive and mechanical properties. *Nat. Commun.* **2020**, *11*, 1420-1420. DOI: 10.1038/s41467-020-15206-y.

(330) Zhao, J.; Stenzel, M. H. Entry of nanoparticles into cells: The importance of nanoparticle properties. *Polym. Chem.* **2018**, *9*, 259-272. DOI: 10.1039/c7py01603d.

(331) Lepeltier, E.; Bourgaux, C.; Couvreur, P. Nanoprecipitation and the "Ouzo effect": Application to drug delivery devices. *Adv. Drug Delivery Rev.* **2014**, *71*, 86-97. DOI: 10.1016/j.addr.2013.12.009.

(332) Melton, L. A.; Lipp, C. W.; Spradling, R. W.; Paulson, K. A. DISMT - Determination of mixing time through color changes. *Chem. Eng. Commun.* **2002**, *189*, 322-338. DOI: 10.1080/00986440212077.

(333) Weheliye, W.; Rodriguez, G.; Anderlei, T.; Micheletti, M.; Yianneskis, M.; Ducci, A. Appraisal of shaken bioreactor mixing efficiency for different operating conditions. In *Proceedings of the 14th European Conference on Mixing*, Warszawa, Warsaw, Poland, 2012; pp 503-508.

(334) Rodriguez, G.; Weheliye, W.; Anderlei, T.; Micheletti, M.; Yianneskis, M.; Ducci, A. Mixing time and kinetic energy measurements in a shaken cylindrical bioreactor. *Chem. Eng. Res. Des.* **2013**, *91*, 2084-2097. DOI: 10.1016/j.cherd.2013.03.005.

(335) Tomar, S. Converting video formats with FFmpeg. *Linux Journal* **2006**, *146*, 10.

(336) Rodriguez, G.; Anderlei, T.; Micheletti, M.; Yianneskis, M.; Ducci, A. On the measurement and scaling of mixing time in orbitally shaken bioreactors. *Biochem. Eng. J.* **2014**, *82*, 10-21. DOI: 10.1016/j.bej.2013.10.021.

(337) Jiang, X.; Zheng, L.; Wu, H.; Zhang, J. Investigations into the role of non-bond interaction on gelation mechanism of silk fibroin hydrogel. *MBE* **2021**, *18*, 4071-4083. DOI: 10.3934/mbe.2021204.

(338) Xu, Z.; Lu, C.; Riordon, J.; Sinton, D.; Moffitt, M. G. Microfluidic Manufacturing of Polymeric Nanoparticles: Comparing Flow Control of Multiscale Structure in Single-Phase Staggered Herringbone and Two-Phase Reactors. *Langmuir* **2016**, *32*, 12781-12789. DOI: 10.1021/acs.langmuir.6b03243.

(339) Pang, F.-M.; Seng, C.-E.; Teng, T.-T.; Ibrahim, M. H. Densities and viscosities of aqueous solutions of 1-propanol and 2-propanol at temperatures from 293.15 K to 333.15 K. *J. Mol. Liq.* **2007**, *136*, 71-78. DOI: 10.1016/j.molliq.2007.01.003.

(340) Mialdun, A.; Yasnou, V.; Shevtsova, V.; Königer, A.; Köhler, W.; Alonso De Mezquia, D.; Bou-Ali, M. M. A comprehensive study of diffusion, thermodiffusion, and Soret coefficients of water-isopropanol mixtures. *J. Chem. Phys.* **2012**, *136*, 244512. DOI: 10.1063/1.4730306.

(341) Son, Y. Determination of shear viscosity and shear rate from pressure drop and flow rate relationship in a rectangular channel. *Polymer* **2007**, *48*, 632-637. DOI: 10.1016/j.polymer.2006.11.048.

(342) Zhang, Y.; Zuo, Y.; Wen, S.; Hu, Y.; Min, Y. Distinctive Stress-Stiffening Responses of Regenerated Silk Fibroin Protein Polymers under Nanoscale Gap Geometries: Effect of Shear on Silk Fibroin-Based Materials. *Biomacromolecules* **2018**, *19*, 1223-1233. DOI: 10.1021/acs.biomac.8b00070.

(343) Zainuddin; Le, T. T.; Park, Y.; Chirila, T. V.; Halley, P. J.; Whittaker, A. K. The behavior of aged regenerated Bombyx mori silk fibroin solutions studied by ^{1}H NMR and rheology. *Biomaterials* **2008**, *29*, 4268-4274. DOI: 10.1016/j.biomaterials.2008.07.041.

(344) Matsumoto, A.; Lindsay, A.; Abedian, B.; Kaplan, D. L. Silk fibroin solution properties related to assembly and structure. *Macromol. Biosci.* **2008**, *8*, 1006-1018. DOI: 10.1002/mabi.200800020.

(345) Chung, D. E.; Um, I. C. Effect of molecular weight and concentration on crystallinity and post drawing of wet spun silk fibroin fiber. *Fibers Polym.* **2014**, *15*, 153-160. DOI: 10.1007/s12221-014-0153-8.

(346) Đorđević, S.; Gonzalez, M. M.; Conejos-Sánchez, I.; Carreira, B.; Pozzi, S.; Acúrcio, R. C.; Satchi-Fainaro, R.; Florindo, H. F.; Vicent, M. J. Current hurdles to the translation of nanomedicines from bench to the clinic. *Drug Deliv. Transl. Res.* **2022**, *12*, 500-525. DOI: 10.1007/s13346-021-01024-2.

(347) Liu, X.; Meng, H. Consideration for the scale-up manufacture of nanotherapeutics—A critical step for technology transfer. *VIEW* **2021**, *2*, 20200190. DOI: 10.1002/VIW.20200190.

(348) Muthu, M. S.; Feng, S.-S. Pharmaceutical stability aspects of nanomedicines. *Nanomedicine* **2009**, *4*, 857-860. DOI: 10.2217/nnm.09.75.

(349) McNeil, S. E. Nanoparticle therapeutics: A personal perspective. *Wiley Interdiscip. Rev.: Nanomed. Nanobiotechnol.* **2009**, *1*, 264-271. DOI: 10.1002/wnan.6.

(350) Matthew, S. A. L.; Totten, J. D.; Phuagkhaopong, S.; Egan, G.; Witte, K.; Perrie, Y.; Seib, F. P. Silk Nanoparticle Manufacture in Semi-Batch Format. *ACS Biomater. Sci. Eng.* **2020**, *6*, 6748-6759. DOI: 10.1021/acsbiomaterials.0c01028.

(351) Hamdallah, S. I.; Zoqlam, R.; Erfle, P.; Blyth, M.; Alkilany, A. M.; Dietzel, A.; Qi, S. Microfluidics for pharmaceutical nanoparticle fabrication: The truth and the myth. *Int. J. Pharm.* **2020**, *584*, 119408. DOI: 10.1016/j.ijpharm.2020.119408.

(352) Stroock, A. D.; Dertinger, S. K. W.; Ajdari, A.; Mezic´, I. M.; Stone, H. A.; Whitesides, G. M. Chaotic Mixer for Microchannels. *Science* **2002**, *295*, 647-651. DOI: 10.1126/science.1066238.

(353) Xie, M.-h.; Zhou, G.-z.; Xia, J.-y.; Zou, C.; Yu, P.-q.; Zhang, S.-l. Comparison of power number for paddle-type impellers by three methods. *J. Chem. Eng. Jpn.* **2011**, *44*, 840-844. DOI: 10.1252/jcej.11we115.

(354) Kamei, N.; Hiraoka, S.; Kato, Y.; Tada, Y.; Iwata, K.; Murai, K.; Lee, Y.; Yamaguchi, T.; Koh, S. Effects of impeller and baffle dimensions on power consumption under turbulent flow in an agitated vessel with paddle impeller. *Kagaku Kogaku Ronbunshu* **1996**, *22*, 49–256.

(355) Berry, A. L. Effects of shear and mixing on a continuously-fed stirred tank reactor for aerobic, biological wastewater treatment. PhD Thesis, Cranfield University, Milton Keynes, UK, 2002.

(356) ASTM-E691-19e1. *Standard Practice for Conducting an Interlaboratory Study to Determine the Precision of a Test Method*; West Conshohocken, PA, USA, 2019.

(357) Aggarwal, N.; Eliaz, D.; Cohen, H.; Rosenhek-Goldian, I.; Cohen, S. R.; Kozell, A.; Mason, T. O.; Shimanovich, U. Protein nanofibril design via manipulation of hydrogen bonds. *Commun. Chem.* **2021**, *4*, 62. DOI: 10.1038/s42004-021-00494-2.

(358) Paquet-Mercier, F.; Lefèvre, T.; Auger, M.; Pézolet, M. Evidence by infrared spectroscopy of the presence of two types of β-sheets in major ampullate spider silk and silkworm silk. *Soft Matter* **2013**, *9*, 208-215. DOI: 10.1039/C2SM26657A.

(359) Galindo-Rodríguez, S. A.; Puel, F.; Briançon, S.; Allémann, E.; Doelker, E.; Fessi, H. Comparative scale-up of three methods for producing ibuprofen-loaded nanoparticles. *Eur. J. Pharm. Sci.* **2005**, *25*, 357-367. DOI: 10.1016/j.ejps.2005.03.013.

(360) Joye, I. J.; McClements, D. J. Production of nanoparticles by anti-solvent precipitation for use in food systems. *Trends Food Sci. Technol.* **2013**, *34*, 109-123. DOI: 10.1016/j.tifs.2013.10.002.

(361) Operti, M. C.; Bernhardt, A.; Grimm, S.; Engel, A.; Figdor, C. G.; Tagit, O. PLGA-based nanomedicines manufacturing: Technologies overview and challenges in industrial scale-up. *Int. J. Pharm.* **2021**, *605*, 120807. DOI: 10.1016/j.ijpharm.2021.120807.

(362) Matthew, S. A.; Rezwan, R.; Kaewchuchuen, J.; Perrie, Y.; Seib, F. P. Mixing and flow-induced nanoprecipitation for morphology control of silk fibroin self-assembly. *RSC Adv.* **2022**, *12*, 7357-7373. DOI: 10.1039/D1RA07764C.

(363) Li, S.; Fang, H.; Sadeghi, S.; Bhovad, P.; Wang, K. W. Architected Origami Materials: How Folding Creates Sophisticated Mechanical Properties. *Adv. Mater.* **2019**, *31*, 1805282. DOI: 10.1002/adma.201805282.

(364) Baek, S.-M.; Yim, S.; Chae, S.-H.; Lee, D.-Y.; Cho, K.-J. Ladybird beetle–inspired compliant origami. *Science Robotics* **2020**, *5*, eaaz6262. DOI: 10.1126/scirobotics.aaz6262.

(365) Francis, K. C.; Blanch, J. E.; Magleby, S. P.; Howell, L. L. Origami-like creases in sheet materials for compliant mechanism design. *Mech. Sci.* **2013**, *4*, 371-380. DOI: 10.5194/ms-4-371-2013.

(366) Ryu, J.; Mohammadifar, M.; Tahernia, M.; Chun, H. i.; Gao, Y.; Choi, S. Paper Robotics: Self-Folding, Gripping, and Locomotion. *Adv. Mater. Technol.* **2020**, *5*, 1901054. DOI: 10.1002/admt.201901054.

(367) Dey, S.; Fan, C.; Gothelf, K. V.; Li, J.; Lin, C.; Liu, L.; Liu, N.; Nijenhuis, M. A. D.; Saccà, B.; Simmel, F. C.; et al. DNA origami. *Nat. Rev. Methods Primers* **2021**, *1*, 13. DOI: 10.1038/s43586-020-00009-8.

(368) Fang, H.; Zhang, Y.; Wang, K. W. Origami-based earthworm-like locomotion robots. *Bioinspir. Biomim.* **2017**, *12*, 065003. DOI: 10.1088/1748-3190/aa8448.

(369) Melancon, D.; Gorissen, B.; García-Mora, C. J.; Hoberman, C.; Bertoldi, K. Multistable inflatable origami structures at the metre scale. *Nature* **2021**, *592*, 545-550. DOI: 10.1038/s41586-021-03407-4.

(370) Mintchev, S.; Shintake, J.; Floreano, D. Bioinspired dual-stiffness origami. *Sci. Robotics* **2018**, *3*, eaau0275. DOI: 10.1126/scirobotics.aau0275.

(371) Zhai, Z.; Wang, Y.; Jiang, H. Origami-inspired, on-demand deployable and collapsible mechanical metamaterials with tunable stiffness. *PNAS* **2018**, *115*, 2032-2037. DOI: 10.1073/pnas.1720171115.

(372) Qi, J.; Li, C.; Tie, Y.; Zheng, Y.; Duan, Y. Energy absorption characteristics of origami-inspired honeycomb sandwich structures under low-velocity impact loading. *Mater. Des.* **2021**, *207*, 109837. DOI: 10.1016/j.matdes.2021.109837.

(373) Yuan, L.; Shi, H.; Ma, J.; You, Z. Quasi-static impact of origami crash boxes with various profiles. *Thin-Walled Structures* **2019**, *141*, 435-446. DOI: 10.1016/j.tws.2019.04.028.

(374) Xiang, X. M.; Lu, G.; You, Z. Energy absorption of origami inspired structures and materials. *Thin-Walled Structures* **2020**, *157*, 107130. DOI: 10.1016/j.tws.2020.107130.

(375) Faber, J. A.; Arrieta, A. F.; Studart, A. R. Bioinspired spring origami. *Science* **2018**, *359*, 1386-1391. DOI: 10.1126/science.aap7753.

(376) Sitti, M.; Wiersma, D. S. Pros and Cons: Magnetic versus Optical Microrobots. *Adv. Mater.* **2020**, *32*, 1906766. DOI: 10.1002/adma.201906766.

(377) Medina-Sánchez, M.; Magdanz, V.; Guix, M.; Fomin, V. M.; Schmidt, O. G. Swimming Microrobots: Soft, Reconfigurable, and Smart. *Adv. Funct. Mater.* **2018**, *28*, 1707228. DOI: 10.1002/adfm.201707228.

(378) Wei, M.; Gao, Y.; Li, X.; Serpe, M. J. Stimuli-responsive polymers and their applications. *Polym. Chem.* **2017**, *8*, 127-143. DOI: 10.1039/c6py01585a.

(379) Zhou, J.; Wu, C.; Wu, D.; Wang, Q.; Chen, Y. Humidity-sensitive polymer xerogel actuators prepared by biaxial pre-stretching and drying. *Chem. Commun.* **2018**, *54*, 11610-11613. DOI: 10.1039/c8cc06750c.

(380) Wang, Y.; Huang, W.; Huang, W.; Wang, Y.; Mu, X.; Ling, S.; Yu, H.; Chen, W.; Guo, C.; Watson, M. C.; et al. Stimuli-responsive composite biopolymer actuators with selective spatial deformation behavior. *PNAS* **2020**, *117*, 14602-14608. DOI: 10.1073/pnas.2002996117.

(381) Kim, J. H.; Pyo, J. B.; Kim, T. S. Highly Mobile Levitating Soft Actuator Driven by Multistimuli-Responses. *Adv. Mater. Interfaces* **2020**, *7*, 2001051. DOI: 10.1002/admi.202001051.

(382) Xu, W.; Zheng, H.; Liu, Y.; Zhou, X.; Zhang, C.; Song, Y.; Deng, X.; Leung, M.; Yang, Z.; Xu, R. X.; et al. A droplet-based electricity generator with high instantaneous power density. *Nature* **2020**, *578*, 392-396. DOI: 10.1038/s41586-020-1985-6.

(383) Zhao, Z.; Hwang, Y.; Yang, Y.; Fan, T.; Song, J.; Suresh, S.; Cho, N.-j. Actuation and locomotion driven by moisture in paper made with natural pollen. *PNAS* **2020**, *117*, 8711-8718. DOI: 10.1073/pnas.1922560117.

(384) Wani, O. M.; Verpaalen, R.; Zeng, H.; Priimagi, A.; Schenning, A. P. H. J. An Artificial Nocturnal Flower via Humidity-Gated Photoactuation in Liquid Crystal Networks. *Adv. Mater.* **2019**, *31*, 1805985. DOI: 10.1002/adma.201805985.

(385) Ge, Y.; Cao, R.; Ye, S.; Chen, Z.; Zhu, Z.; Tu, Y.; Ge, D.; Yang, X. A bio-inspired homogeneous graphene oxide actuator driven by moisture gradients. *Chem. Commun.* **2018**, *54*, 3126-3129. DOI: 10.1039/c8cc00394g.

(386) Li, Y.; Zheng, W.; Huang, F. All-silicon photovoltaic detectors with deep ultraviolet selectivity. *PhotoniX* **2020**, *1*, 15. DOI: 10.1186/s43074-020-00014-w.

(387) Ji, Z.; Yan, C.; Yu, B.; Wang, X.; Zhou, F. Multimaterials 3D Printing for Free Assembly Manufacturing of Magnetic Driving Soft Actuator. *Adv. Mater. Interfaces* **2017**, *4*, 1700629. DOI: 10.1002/admi.201700629.

(388) Jia, G.; Zheng, A.; Wang, X.; Zhang, L.; Li, L.; Li, C.; Zhang, Y.; Cao, L. Flexible, biocompatible and highly conductive MXene-graphene oxide film for smart actuator and humidity sensor. *Sens. Actuators, B* **2021**, *346*, 130507. DOI: 10.1016/j.snb.2021.130507.

(389) Park, J. H.; Lach, S.; Polev, K.; Granick, S.; Grzybowski, B. A. Metal-Organic Framework "swimmers" with Energy-Efficient Autonomous Motility. *ACS Nano* **2017**, *11*, 10914-10923. DOI: 10.1021/acsnano.7b04644.

(390) Du, L.; Xu, Z. Y.; Huang, C. L.; Zhao, F. Y.; Fan, C. J.; Dai, J.; Yang, K. K.; Wang, Y. Z. From a body temperature-triggered reversible shape-memory material to high-sensitive bionic soft actuators. *Applied Materials Today* **2020**, *18*, 100463. DOI: 10.1016/j.apmt.2019.100463.

(391) Hartmann, F.; Baumgartner, M.; Kaltenbrunner, M. Becoming Sustainable, The New Frontier in Soft Robotics. *Adv. Mater.* **2021**, *33*, 2004413. DOI: 10.1002/adma.202004413.

(392) Wei, J.; Jia, S.; Wei, J.; Ma, C.; Shao, Z. Tough and Multifunctional Composite Film Actuators Based on Cellulose Nanofibers toward Smart Wearables. *ACS Appl. Mater. Interfaces* **2021**, *13*, 38700-38711. DOI: 10.1021/acsami.1c09653.

(393) Boonkanon, C.; Phatthanawiwat, K.; Wongniramaikul, W.; Choodum, A. Curcumin nanoparticle doped starch thin film as a green colorimetric sensor for detection of boron. *Spectrochim. Acta, Part A* **2020**, *224*, 117351. DOI: 10.1016/j.saa.2019.117351.

(394) Aracri, S.; Giorgio-Serchi, F.; Suaria, G.; Sayed, M. E.; Nemitz, M. P.; Mahon, S.; Stokes, A. A. Soft Robots for Ocean Exploration and Offshore Operations: A Perspective. *Soft Robotics* **2021**, *8*, 625-639. DOI: 10.1089/soro.2020.0011.

(395) Dhanwani, R.; Prajapati, A.; Dimri, A.; Varmora, A.; Shah, M. Smart Earth Technologies: a pressing need for abating pollution for a better tomorrow. *Environ. Sci. Pollut. Res.* **2021**, *28*, 35406-35428. DOI: 10.1007/s11356-021-14481-6.

(396) Vikesland, P. J. Nanosensors for water quality monitoring. *Nat. Nanotechnol.* **2018**, *13*, 651-660. DOI: 10.1038/s41565-018-0209-9.

(397) Muñoz, J.; Pumera, M. Accounts in 3D-Printed Electrochemical Sensors: Towards Monitoring of Environmental Pollutants. *ChemElectroChem* **2020**, *7*, 3404-3413. DOI: 10.1002/celc.202000601.

(398) Horne, J.; McLoughlin, L.; Bury, E.; Koh, A. S.; Wujcik, E. K. Interfacial Phenomena of Advanced Composite Materials toward Wearable Platforms for Biological and Environmental Monitoring Sensors, Armor, and Soft Robotics. *Adv. Mater. Interfaces* **2020**, *7*, 1901851. DOI: 10.1002/admi.201901851.

(399) Nawaz, H.; Zhang, X.; Chen, S.; You, T.; Xu, F. Recent studies on cellulose-based fluorescent smart materials and their applications: A comprehensive review. *Carbohydr. Polym.* **2021**, *267*, 118135. DOI: 10.1016/j.carbpol.2021.118135.

(400) Kim, B. H.; Li, K.; Kim, J.-T.; Park, Y.; Jang, H.; Wang, X.; Xie, Z.; Won, S. M.; Yoon, H.-J.; Lee, G.; et al. Three-dimensional electronic microfliers inspired by wind-dispersed seeds. *Nature* **2021**, *597*, 503-510. DOI: 10.1038/s41586-021-03847-y.

(401) Chen, H. z.; Zhang, M.; Bhandari, B.; Yang, C. h. Novel pH-sensitive films containing curcumin and anthocyanins to monitor fish freshness. *Food Hydrocolloids* **2020**, *100*, 105438. DOI: 10.1016/j.foodhyd.2019.105438.

(402) Wiczkowski, W.; Szawara-Nowak, D.; Topolska, J. Red cabbage anthocyanins: Profile, isolation, identification, and antioxidant activity. *Food Res. Int.* **2013**, *51*, 303-309. DOI: 10.1016/j.foodres.2012.12.015.

(403) Halász, K.; Csóka, L. Black chokeberry (Aronia melanocarpa) pomace extract immobilized in chitosan for colorimetric pH indicator film application. *Food Packag. Shelf Life* **2018**, *16*, 185-193. DOI: 10.1016/j.fpsl.2018.03.002.

(404) Fernández-Marín, R.; Fernandes, S. C. M.; Sánchez, M. Á. A.; Labidi, J. Halochromic and antioxidant capacity of smart films of chitosan/chitin nanocrystals with curcuma oil and anthocyanins. *Food Hydrocolloids* **2022**, *123*, 107119. DOI: 10.1016/j.foodhyd.2021.107119.

(405) Luchese, C. L.; Sperotto, N.; Spada, J. C.; Tessaro, I. C. Effect of blueberry agro-industrial waste addition to corn starch-based films for the production of a pH-indicator film. *Int. J. Biol. Macromol.* **2017**, *104*, 11-18. DOI: 10.1016/j.ijbiomac.2017.05.149.

(406) Zhang, J.; Huang, X.; Zou, X.; Shi, J.; Zhai, X.; Liu, L.; Li, Z.; Holmes, M.; Gong, Y.; Povey, M.; et al. A visual indicator based on curcumin with high stability for monitoring the freshness of freshwater shrimp, Macrobrachium rosenbergii. *J. Food Eng.* **2021**, *292*, 110290. DOI: 10.1016/j.jfoodeng.2020.110290.

(407) Hu, X.; Shmelev, K.; Sun, L.; Gil, E. S.; Park, S. H.; Cebe, P.; Kaplan, D. L. Regulation of silk material structure by temperature-controlled water vapor annealing. *Biomacromolecules* **2011**, *12*, 1686-1696. DOI: 10.1021/bm200062a.

(408) Jin, H. J.; Park, J.; Karageorgiou, V.; Kim, U. J.; Valluzzi, R.; Cebe, P.; Kaplan, D. L. Water-stable silk films with reduced β-sheet content. *Adv. Funct. Mater.* **2005**, *15*, 1241-1247. DOI: 10.1002/adfm.200400405.

(409) Zhao, H.; Heusler, E.; Jones, G.; Li, L.; Werner, V.; Germershaus, O.; Ritzer, J.; Luehmann, T.; Meinel, L. Decoration of silk fibroin by click chemistry for biomedical application. *J. Struct. Biol.* **2014**, *186*, 420-430. DOI: 10.1016/j.jsb.2014.02.009.

(410) Etxabide, A.; Maté, J. I.; Kilmartin, P. A. Effect of curcumin, betanin and anthocyanin containing colourants addition on gelatin films properties for intelligent films development. *Food Hydrocolloids* **2021**, *115*, 106593. DOI: 10.1016/j.foodhyd.2021.106593.

(411) Mary, C. P. V.; Vijayakumar, S.; Shankar, R. Metal chelating ability and antioxidant properties of Curcumin-metal complexes – A DFT approach. *J. Mol. Graphics Modell.* **2018**, *79*, 1-14. DOI: 10.1016/j.jmgm.2017.10.022.

(412) Fenger, J. A.; Moloney, M.; Robbins, R. J.; Collins, T. M.; Dangles, O. The influence of acylation, metal binding and natural antioxidants on the thermal stability of red cabbage anthocyanins in neutral solution. *Food Funct.* **2019**, *10*, 6740-6751. DOI: 10.1039/c9fo01884k.

(413) Fedenko, V. S.; Shemet, S. A.; Landi, M. UV–vis spectroscopy and colorimetric models for detecting anthocyanin-metal complexes in plants: An overview of in vitro and in vivo techniques. *J. Plant Physiol.* **2017**, *212*, 13-28. DOI: 10.1016/j.jplph.2017.02.001.

(414) Emmanuel, E.; Hanna, K.; Bazin, C.; Keck, G.; Clément, B.; Perrodin, Y. Fate of glutaraldehyde in hospital wastewater and combined effects of glutaraldehyde and surfactants on aquatic organisms. *Environment International* **2005**, *31*, 399-406. DOI: 10.1016/j.envint.2004.08.011.

(415) Shiono, M.; Matsugaki, N.; Takeda, K. Structure of the blue cornflower pigment. *Nature* **2005**, *436*, 791. DOI: 10.1038/436791a.

(416) Prasad, S.; Dubourdieu, D.; Srivastava, A.; Kumar, P.; Lall, R. Metal–curcumin complexes in therapeutics: An approach to enhance pharmacological effects of curcumin. *Int. J. Mol. Sci.* **2021**, *22*, 7094. DOI: 10.3390/ijms22137094.

(417) WHO. *Hardness in Drinking-water Background document for development of WHO Guidelines for Drinking-water Quality*; Geneva, CH., 2011.

(418) WHO. *Copper in Drinking-water Background document for development of WHO Guidelines for Drinking-water Quality*; Geneva, CH., 2004.

(419) WQA. *Technical Application Bulletin Silver Recognized Treatment Techniques For Meeting Drinking Water Regulations For The Reduction Of Silver From Drinking Water Supplies Using Point-of-Use/Point-of-Entry Devices And Systems*; Illinois, U.S.A., 2004.

(420) US-EPA. *Cobalt Compounds Hazard Summary*; Washington, D.C., U.S.A., 2000.

(421) Aboudiab, B.; Tehrani-Bagha, A. R.; Patra, D. Curcumin degradation kinetics in micellar solutions: Enhanced stability in the presence of cationic surfactants. *Colloids Surf., A* **2020**, *592*, 124602. DOI: 10.1016/j.colsurfa.2020.124602.

(422) Fan, Y.; Li, J.; Guo, Y.; Xie, L.; Zhang, G. Digital image colorimetry on smartphone for chemical analysis: A review. *Measurement* **2021**, *171*, 108829. DOI: 10.1016/j.measurement.2020.108829.

(423) Wallace, J.; Champagne, P.; Hall, G. Multivariate statistical analysis of water chemistry conditions in three wastewater stabilization ponds with algae blooms and pH fluctuations. *Water Research* **2016**, *96*, 155-165. DOI: 10.1016/j.watres.2016.03.046.

(424) Liu, X.; Meng, M.; Zhang, Y.; Li, C.; Ma, S.; Li, Q.; Ren, Q.; Zhang, Y.; Zhang, J. Effects of sulfuric, nitric, and mixed acid rain on the decomposition of fine root litter in Southern China. *Ecol. Process.* **2021**, *10*, 65. DOI: 10.1186/s13717-021-00334-0.

(425) Matthew, S. A.; Rezwan, R.; Perrie, Y.; Seib, F. P. Volumetric scalability of microfluidic and semi-batch silk nanoprecipitation methods. *Molecules* **2022**, *27*, 2368. DOI: 10.3390/molecules27072368.

(426) Matthew, S. A.; Egan, G.; Witte, K.; Kaewchuchuen, J.; Phuagkhaopong, S.; Totten, J. D.; Seib, F. P. Smart silk origami as eco-sensors for environmental pollution. *ACS Appl. Bio Mater.* **2022**, *5*, 3658-3666. DOI: 10.1021/acsabm.2c00023.

(427) Liu, Y.; Yang, G.; Hui, Y.; Ranaweera, S.; Zhao, C.-X. Microfluidic Nanoparticles for Drug Delivery. *Small* **2022**, *18*, 2106580. DOI: 10.1002/smll.202106580.

(428) Wouters, O. J.; McKee, M.; Luyten, J. Estimated Research and Development Investment Needed to Bring a New Medicine to Market, 2009-2018. *JAMA* **2020**, *323*, 844-853. DOI: 10.1001/jama.2020.1166.

(429) Prasad, V.; Mailankody, S. Research and Development Spending to Bring a Single Cancer Drug to Market and Revenues After Approval. *JAMA Intern. Med.* **2017**, *177*, 1569-1575. DOI: 10.1001/jamainternmed.2017.3601.

(430) Pretorius, S.; Grignolo, A. Phase III trial failures: Costly, but preventable. *Applied Clinical Trials* **2016**, *25*.

(431) De, R.; Mahata, M. K.; Kim, K. T. Structure-Based Varieties of Polymeric Nanocarriers and Influences of Their Physicochemical Properties on Drug Delivery Profiles. *Adv. Sci.* **2022**, *9*, 2105373. DOI: 10.1002/advs.202105373.

(432) Hadji, H.; Bouchemal, K. Effect of micro-and nanoparticle shape on biological processes. *J. Controlled Release* **2022**, *342*, 93-110. DOI: 10.1016/j.jconrel.2021.12.032.

(433) Stewart, R. L.; Updike, K. L.; Factor, R. E.; Henry, N. L.; Boucher, K. M.; Bernard, P. S.; Varley, K. E. A Multigene Assay Determines Risk of Recurrence in Patients with Triple-Negative Breast Cancer. *Cancer Res.* **2019**, *79*, 3466-3478. DOI: 10.1158/0008-5472.CAN-18-3014.

(434) Gonçalves, H., Jr.; Guerra, M. R.; Duarte Cintra, J. R.; Fayer, V. A.; Brum, I. V.; Bustamante Teixeira, M. T. Survival Study of Triple-Negative and Non-Triple-Negative Breast Cancer in a Brazilian Cohort. *Clin. Med. Insights Oncol.* **2018**, *12*, 1179554918790563. DOI: 10.1177/1179554918790563.

(435) Gorbet, M.; Sperling, C.; Maitz, M. F.; Siedlecki, C. A.; Werner, C.; Sefton, M. V. The blood compatibility challenge. Part 3: Material associated activation of blood cascades and cells. *Acta Biomater.* **2019**, *94*, 25-32. DOI: 10.1016/j.actbio.2019.06.020.

(436) Pensado-López, A.; Fernández-Rey, J.; Reimunde, P.; Crecente-Campo, J.; Sánchez, L.; Torres Andón, F. Zebrafish models for the safety and therapeutic testing of nanoparticles with a focus on macrophages. *Nanomaterials* **2021**, *11*, 1784. DOI: 10.3390/nano11071784.

(437) Saez Talens, V.; Arias-Alpizar, G.; Makurat, D.; Davis, J.; Bussmann, J.; Kros, A.; Kieltyka, R. E. Stab2-mediated clearance of supramolecular polymer nanoparticles in zebrafish embryos. *Biomacromolecules* **2020**, *21*, 1060-1068. DOI: 10.1021/acs.biomac.9b01318.

(438) Peng, G.; He, Y.; Wang, X.; Cheng, Y.; Zhang, H.; Savolainen, K.; Mädler, L.; Pokhrel, S.; Lin, S. Redox activity and Nano–bio interactions determine the skin injury potential of Co3O4-based metal oxide nanoparticles toward Zebrafish. *ACS Nano* **2020**, *14*, 4166-4177. DOI: 10.1021/acsnano.9b08938.

(439) Dal, N. J. K.; Kocere, A.; Wohlmann, J.; Van Herck, S.; Bauer, T. A.; Resseguier, J.; Bagherifam, S.; Hyldmo, H.; Barz, M.; De Geest, B. G.; et al. Zebrafish embryos allow prediction of nanoparticle circulation times in mice and facilitate quantification of nanoparticle–cell interactions. *Small* **2020**, *16*, 1906719. DOI: 10.1002/smll.201906719.

(440) Besford, Q. A.; Weiss, A. C.; Schubert, J.; Ryan, T. M.; Maitz, M. F.; Tomanin, P. P.; Savioli, M.; Werner, C.; Fery, A.; Caruso, F. Protein component of oyster glycogen nanoparticles: An anchor point for functionalization. *ACS Appl. Mater. Interfaces* **2020**, *12*, 38976-38988. DOI: 10.1021/acsami.0c10699.

(441) Liu, Y.; Tseng, Y.-c.; Huang, L. Biodistribution studies of nanoparticles using fluorescence imaging: a qualitative or quantitative method? *Pharm. Res.* **2012**, *29*, 3273-3277. DOI: 10.1007/s11095-012-0818-1.

(442) Chen, M.; Yao, B.; Kappl, M.; Liu, S.; Yuan, J.; Berger, R.; Zhang, F.; Butt, H. J.; Liu, Y.; Wu, S. Entangled Azobenzene-Containing Polymers with Photoinduced Reversible Solid-to-Liquid Transitions for Healable and Reprocessable Photoactuators. *Adv. Funct. Mater.* **2020**, *30*, 1906752. DOI: 10.1002/adfm.201906752.

(443) Shin, J.; Sung, J.; Kang, M.; Xie, X.; Lee, B.; Lee, K. M.; White, T. J.; Leal, C.; Sottos, N. R.; Braun, P. V.; et al. Light-triggered thermal conductivity switching in azobenzene polymers. *PNAS* **2019**, *116*, 5973-5978. DOI: 10.1073/pnas.1817082116.

(444) Ercole, F.; Davis, T. P.; Evans, R. A. Photo-responsive systems and biomaterials: Photochromic polymers, light-triggered self-assembly, surface modification, fluorescence modulation and beyond. *Polym. Chem.* **2010**, *1*, 37-54. DOI: 10.1039/b9py00300b.

(445) Velmurugan, K.; Mohan, M.; Li, B.; Wang, K.; Zuo, M.; Hu, X.-Y. Macrocycles-assisted Polymeric Self-Assemblies Fabricated by Host−Guest Complexation and Their Applications. *Mater. Adv.* **2020**, *1*, 2646-2662. DOI: 10.1039/D0MA00625D.

(446) Mei, X.; Yang, S.; Chen, D.; Li, N.; Li, H.; Xu, Q.; Ge, J.; Lu, J. Light-triggered reversible assemblies of azobenzene-containing amphiphilic copolymer with β-cyclodextrin-modified hollow mesoporous silica nanoparticles for controlled drug release. *Chem. Comm.* **2012**, *48*, 10010-10012. DOI: 10.1039/c2cc33995a.

(447) Zheng, X.; Bian, Q.; Ye, C.; Wang, G. Visible light-, pH-, and cyclodextrin-responsive azobenzene functionalized polymeric nanoparticles. *Dyes Pigm.* **2019**, *162*, 599-605. DOI: 10.1016/j.dyepig.2018.10.063.

(448) Abid, J. P.; Frigoli, M.; Pansu, R.; Szeftel, J.; Zyss, J.; Larpent, C.; Brasselet, S. Light-driven directed motion of azobenzene-coated polymer nanoparticles in an aqueous medium. *Langmuir* **2011**, *27*, 7967-7971. DOI: 10.1021/la200682p.

(449) Zhang, C. C.; Li, S. H.; Zhang, C. F.; Liu, Y. Size Switchable Supramolecular Nanoparticle Based on Azobenzene Derivative within Anionic Pillar[5]arene. *Sci. Rep.* **2016**, *6*, 37014 DOI: 10.1038/srep37014.

(450) Stoffelen, C.; Voskuhl, J.; Jonkheijm, P.; Huskens, J. Dual stimuli-responsive self-assembled supramolecular nanoparticles. *Angew. Chem., Int. Ed.* **2014**, *53*, 3400-3404. DOI: 10.1002/anie.201310829.

(451) Chu, Z.; Han, Y.; Bian, T.; De, S.; Král, P.; Klajn, R. Supramolecular Control of Azobenzene Switching on Nanoparticles. *J. Am. Chem. Soc.* **2019**, *141*, 1949-1960. DOI: 10.1021/jacs.8b09638.

(452) Arima, H.; Arizono, M.; Higashi, T.; Yoshimatsu, A.; Ikeda, H.; Motoyama, K.; Hattori, K.; Takeuchi, T.; Hirayama, F.; Uekama, K. Potential use of folate-polyethylene glycol (PEG)-appended dendrimer (G3) conjugate with α-cyclodextrin as DNA carriers to tumor cells. *Cancer Gene Ther.* **2012**, *19*, 358-366. DOI: 10.1038/cgt.2012.9.

(453) Samanta, S.; Beharry, A. A.; Sadovski, O.; McCormick, T. M.; Babalhavaeji, A.; Tropepe, V.; Woolley, G. A. Photoswitching Azo compounds in vivo with red light. *J. Am. Chem. Soc.* **2013**, *135*, 9777-9784. DOI: 10.1021/ja402220t.

(454) Bléger, D.; Schwarz, J.; Brouwer, A. M.; Hecht, S. o-fluoroazobenzenes as readily synthesized photoswitches offering nearly quantitative two-way isomerization with visible light. *J. Am. Chem. Soc* **2012**, *134*, 20597-20600. DOI: 10.1021/ja310323y.

(455) Dubey, P.; Chowdhury, P. K.; Ghosh, S. Modulation of aggregation of silk fibroin by synergistic effect of the complex of curcumin and β-cyclodextrin. *Biochim. Biophys. Acta, Proteins Proteomics* **2019**, *1867*, 416-425. DOI: 10.1016/j.bbapap.2019.01.009.

(456) Liu, L.; Han, Y.; Lv, S. Design of Self-Healing and Electrically Conductive Silk Fibroin-Based Hydrogels. *ACS Appl. Mater. Interfaces* **2019**, *11*, 20394-20403. DOI: 10.1021/acsami.9b04871.

(457) Huang, J.; Wu, Y.; Zeng, F.; Wu, S. An activatable near-infrared chromophore for multispectral optoacoustic imaging of tumor hypoxia and for tumor inhibition. *Theranostics* **2019**, *9*, 7313-7324. DOI: 10.7150/thno.36755.

(458) Jia, S.; Fong, W. K.; Graham, B.; Boyd, B. J. Photoswitchable Molecules in Long-Wavelength Light-Responsive Drug Delivery: From Molecular Design to Applications. *Chem. Mater.* **2018**, *30*, 2873-2887. DOI: 10.1021/acs.chemmater.8b00357.

(459) Weis, P.; Wu, S. Light-Switchable Azobenzene-Containing Macromolecules: From UV to Near Infrared. *Macromol. Rapid Commun.* **2018**, *39*, 1700220. DOI: 10.1002/marc.201700220.

(460) Wang, D.; Wang, X. Amphiphilic azo polymers: Molecular engineering, self-assembly and photoresponsive properties. *Prog. Polym. Sci.* **2013**, *38*, 271-301. DOI: 10.1016/j.progpolymsci.2012.07.003.

(461) Boutureira, O.; Bernardes, G. J. L. Advances in chemical protein modification. *Chem. Rev.* **2015**, *115*, 2174-2195. DOI: 10.1021/cr500399p.

(462) Allardyce, B. J.; Rajkhowa, R.; Dilley, R. J.; Atlas, M. D.; Kaur, J.; Wang, X. The impact of degumming conditions on the properties of silk films for biomedical applications. *Text. Res. J.* **2016**, *86*, 275-287. DOI: 10.1177/0040517515586166.

(463) Teramoto, H.; Iga, M.; Tsuboi, H.; Nakajima, K. Characterization and Scaled-Up Production of Azido-Functionalized Silk Fiber Produced by Transgenic Silkworms with an Expanded Genetic Code. *Int. J. Mol. Sci.* **2019**, *20*, 616. DOI: 10.3390/ijms20030616.

(464) Rojas-Sánchez, L.; Sokolova, V.; Riebe, S.; Voskuhl, J.; Epple, M. Covalent Surface Functionalization of Calcium Phosphate Nanoparticles with Fluorescent Dyes by Copper-Catalysed and by Strain-Promoted Azide-Alkyne Click Chemistry. *ChemNanoMat* **2018**, *5*, 436-446. DOI: 10.1002/cnma.201800509.

(465) Koopmans, T.; Dekker, F. J.; Martin, N. I. A photocleavable affinity tag for the enrichment of alkyne-modified biomolecules. *RSC Adv.* **2012**, *2*, 2244-2246. DOI: 10.1039/c2ra20082a.

(466) Yang, Y.-Y.; Grammel, M.; Raghavan, A. S.; Charron, G.; Hang, H. C. Comparative analysis of cleavable diazobenzene-based affinity tags for bioorthogonal chemical proteomics. *Chem. Biol.* **2010**, *17*, 1212-1222. DOI: 10.1016/j.chembiol.2010.09.012.

(467) Landi, F.; Johansson, C. M.; Campopiano, D. J.; Hulme, A. N. Synthesis and application of a new cleavable linker for "click"-based affinity chromatography. *Org. Biomol. Chem.* **2010**, *8*, 56-59. DOI: 10.1039/b916693a.

(468) Wang, J.; Zhang, C.-J.; Zhang, J.; He, Y.; Lee, Y. M.; Chen, S.; Lim, T. K.; Ng, S.; Shen, H.-M.; Lin, Q. Mapping sites of aspirin-induced acetylations in live cells by quantitative acid-cleavable activity-based protein profiling (QA-ABPP). *Sci. Rep.* **2015**, *5*, 7896 DOI: 10.1038/srep07896.

(469) Szychowski, J.; Mahdavi, A.; Hodas, J. J. L.; Bagert, J. D.; Ngo, J. T.; Landgraf, P.; Dieterich, D. C.; Schuman, E. M.; Tirrell, D. A. Cleavable Biotin Probes for Labeling of Biomolecules via Azide-Alkyne Cycloaddition. *J. Am. Chem. Soc.* **2010**, *132*, 18351–18360. DOI: 10.1021/ja1083909.

(470) Kla, P.; Bochet, C. G.; Blanc, A.; Givens, R.; Rubina, M.; Popik, V.; Kostikov, A.; Wirz, J. Photoremovable Protecting Groups in Chemistry and Biology: Reaction Mechanisms and Efficacy. *Chem. Rev.* **2013**, *113*, 119–191. DOI: 10.1021/cr300177k.

(471) Rayamajhi, S.; Aryal, S. Surface functionalization strategies of extracellular vesicles. *J. Mater. Chem. B* **2020**, *8*, 4552-4569. DOI: 10.1039/d0tb00744g.

(472) Sakai, R.; Iguchi, H.; Maruyama, T. Quantification of azide groups on a material surface and a biomolecule using a clickable and cleavable fluorescent compound. *RSC Adv.* **2019**, *9*, 4621-4625. DOI: 10.1039/C8RA09421G.

(473) Abarca, C.; Ali, M. M.; Bowie, D.; Pelton, R. H. A simple assay for azide surface groups on clickable polymeric nanoparticles. *Colloids Surf., A* **2016**, *508*, 192-196. DOI: 10.1016/j.colsurfa.2016.08.015.

(474) Fornasier, M.; Porcheddu, A.; Casu, A.; Raghavan, S. R.; Jönsson, P.; Schillén, K.; Murgia, S. Surface-modified nanoerythrosomes for potential optical imaging diagnostics. *J. Colloid Interface Sci.* **2021**, *582*, 246-253. DOI: 10.1016/j.jcis.2020.08.032.

(475) Staff, R. H.; Willersinn, J.; Musyanovych, A.; Landfester, K.; Crespy, D. Janus nanoparticles with both faces selectively functionalized for click chemistry. *Polym. Chem.* **2014**, *5*, 4097-4104. DOI: 10.1039/c4py00085d.

(476) Xiao, Y.; Liu, Q.; Clulow, A. J.; Li, T.; Manohar, M.; Gilbert, E. P.; de Campo, L.; Hawley, A.; Boyd, B. J. PEGylation and surface functionalization of liposomes containing drug nanocrystals for cell-targeted delivery. *Colloids Surf., B* **2019**, *182*, 110362. DOI: 10.1016/j.colsurfb.2019.110362.

(477) Kasuya, M.; Taniguchi, T.; Motokawa, R.; Kohri, M.; Kishikawa, K.; Nakahira, T. Quantification of ATRP initiator density on polymer latex particles by fluorescence labeling technique using copper-catalyzed azide-alkyne cycloaddition. *J. Polym. Sci., Part A: Polym. Chem.* **2013**, *51*, 4042-4051. DOI: 10.1002/pola.26800.

(478) Baier, G.; Siebert, M.; Landfester, K.; Musyanovych, A. Surface Click Reactions on Polymeric Nanocapsules for Versatile Functionalization. *Macromolecules* **2012**, *45*, 3419–3427. DOI: 10.1021/ma300312n.

(479) Amirikia, M.; Mohammad, S.; Shariatzadeh, A.; Gholam, S.; Jorsaraei, A.; Malek; Mehranjani, S. Auto-fluorescence of a silk fibroin-based scaffold and its interference with fluorophores in labeled cells. *Eur. Biophys. J.* **2018**, *47*, 573-581. DOI: 10.1007/s00249-018-1279-1.

(480) Debets, M. F.; Van Berkel, S. S.; Schoffelen, S.; Rutjes, F. P. J. T.; Van Hest, J. C. M.; Van Delft, F. L. Aza-dibenzocyclooctynes for fast and efficient enzyme PEGylation via copper-free (3+2) cycloaddition. *Chem. Comm.* **2010**, *46*, 97-99. DOI: 10.1039/b917797c.

(481) Pickens, C. J.; Johnson, S. N.; Pressnall, M. M.; Leon, M. A.; Berkland, C. J. Practical Considerations, Challenges, and Limitations of Bioconjugation via Azide−Alkyne Cycloaddition. *Bioconjugate Chem.* **2018**, *29*, 686–701. DOI: 10.1021/acs.bioconjchem.7b00633.

(482) Sletten, E. M.; Bertozzi, C. R. Bioorthogonal chemistry: Fishing for selectivity in a sea of functionality. *Angew. Chem. Int. Ed* **2009**, *48*, 6974-6998. DOI: 10.1002/anie.200900942.

(483) Dommerholt, J.; Rutjes, F. P. J. T.; van Delft, F. L. Strain-Promoted 1,3-Dipolar Cycloaddition of Cycloalkynes and Organic Azides. *Top. Curr. Chem. (Cham).* **2016**, *374*, 16. DOI: 10.1007/s41061-016-0016-4.

(484) Morillo, C. *Quantitative Analysis of Powdered Solids with FTIR-ATR*. JASCO, https://jascoinc.com/applications/quantitative-analysis-of-powdered-solids-with-ftir-atr/ (accessed 2021 04/03/2021).

Appendix A

Abstract accepted for poster presentation at the 2023 3rd International Workshop on Insect Bio-inspired Technologies 17 November 2022 09:00 – 18 November 2022 12:30, Edinburgh, United Kingdom.

Silk fibroin-anthracycline nano-sized delivery systems for breast cancer treatment

S. A. L. Matthew, S. Phuagkhaopong, Y. Perrie, F. P. Seib

Anthracyclines have been prescribed as a first or second-line neoadjuvant chemotherapy for over 30 years.[1,2] Today, they are the most widely used chemotherapy agents due to their effectiveness against several cancer types, including triple-negative breast cancer.[2,4] However, as systemic administration of the free drug is dose limited by cardiotoxicity, alternative platforms to limit adverse side effects have been provided by drug delivery systems comprising a nanoparticle carrier and encapsulated drug payload.[1] Drug delivery systems can reduce systemic drug exposure and accumulate preferentially in the inflammatory tumour environment due to the enhanced permeability and retention effect.[5] Notably, PEGylated liposomal anthracycline formulations (e.g., Caelyx®) have shown reduced cardiotoxicity compared with the free drug,[2,6] but can be associated with side effects such as infusion reactions[6] and have not raised the anticancer efficacy.[2] Therefore, there remains a need for developing alternative chemotherapeutics with higher potency and reduced side effects. *B. mori* derived silk fibroin nanoparticles provide a promising drug carrier material.[7,8,9,10] However, the scalability of manufacture[11] and the drug loading capability[7,8,9] require optimisation for clinical significance.

The objective of this study was to optimise the drug loading of silk fibroin-anthracycline nanoparticles by using a post-synthetic incubation with daunorubicin or doxorubicin. We first generated silk fibroin nanoparticles using microfluidic-assisted desolvation in isopropanol.[11] Then, we post-synthetically loaded the nanoparticles in 5: 1 *v/v* alcohol: ultrapure water mixtures with anthracycline, and varied the alcohol polarity by using isopropanol, 1:1 ethanol: isopropanol, and ethanol. The optimal silk fibroin-daunorubicin nanoparticles (size 124 ± 9, PDI 0.28 ± 0.05, zeta potential -20 ± 9 mV, 23 ± 9% *w/w* daunorubicin/silk) and silk fibroin-doxorubicin nanoparticles (size 215 ± 21, PDI 0.26 ± 0.06, zeta potential -17 ± 6 mV, 38 ± 2% *w/w* doxorubicin/silk) were identified. We demonstrated their short-term aqueous stability, spherical morphology, and pH-dependent *in vitro* release behaviour. Post-synthetically loaded silk fibroin-anthracycline nanoparticles could be manufactured as sterile nanoformulations with clinically relevant drug loads (>10% *w/w*) and showed significant cytotoxicity to the human breast cancer cell line MDA-MB-231. The limitations of this study include: the indirect method for drug loading estimation; the *in vitro* cancer model; and, native silk fibroin drug carriers lacking stealth or targeting agents, such as polyethylene glycol and folate.

Nevertheless, this work improves the clinical relevance of anthracycline-silk nanoparticles reported previously[7,8,9] by increasing drug loading beyond 10% *w/w* and using a sterile, scalable, higher throughput manufacturing method.[11] The scalable manufacture of silk fibroin nanoparticles with improved drug loading capability supports the production of cheaper, more efficacious silk nanomedicines.

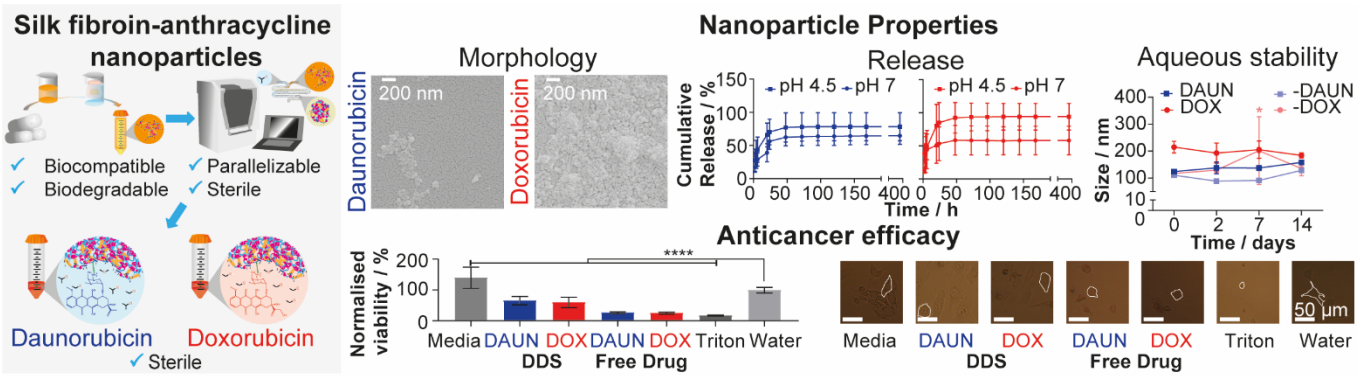

References

1. O. Tacar, P. Sriamornsak, C. R. Dass, *J. Pharm. Pharmacol.*, **2012**, *65*, 157–170. DOI: 10.1111/j.2042-7158.2012.01567.x.

2. Y. L. Franco, T. R. Vaidya, S. Ait-Oudhia, *Breast cancer*, **2018**, *10*, 131–141. DOI: 10.2147/BCTT.S170239.

3. R. E. Nicoletto, C. M. Ofner, *Cancer Chemother. Pharmacol.*, **2022**, *89*, 285–311. DOI: 10.1007/s00280-022-04400-y.

4. A. Mandapati, K.E. Lukong, *J. Cancer Res. Clin. Oncol.*, **2022**. DOI: 10.1007/s00432-022-04189-6.

5. Y. Zi, K. Yang, J. He, Z. Wu, J. Liu, W. Zhang, *Adv. Drug Delivery Rev.*, **2022**, *188*, 114449. DOI: 10.1016/j.addr.2022.114449.

6. A. T. Perez, G. H. Domenech, C. Frankel, C. L. Vogel, *Cancer Invest.*, **2002**, *20*, 22–29. DOI: 10.1081/CNV-120014883.

7. F. P. Seib, G. T. Jones, J. Rnjak-Kovacina, Y. Lin, D. L. Kaplan, *Adv. Healthcare Mater.*, **2013**, *2*, 1606–1611. DOI: 10.1002/adhm.201300034.

8. T. Wongpinyochit, B. F. Johnston, F. P. Seib, *J. Vis. Exp.*, **2016**, *116*, e54669, DOI:10.3791/54669.

9. J. D. Totten, T. Wongpinyochit, F. P. Seib, *J. Drug Targeting*, **2017**, *25*, 865–872. DOI: 10.1080/1061186X.2017.1363212.

10. A. S. Lammel, X. Hu, S-H. Park, D. L. Kaplan, T. R. Scheibel, *Biomaterials*, **2010**, *31*, 4583–4591. DOI: 10.1016/j.biomaterials.2010.02.024.

11. S. A. L. Matthew, R. Rezwan, Y. Perrie, F. P. Seib, *Molecules,* **2022**, *27*, 2368. DOI: 10.3390/molecules27072368.

Appendix B

Abstract accepted for poster presentation at the 2022 RSC Chemical Nanoscience and Nanotechnology Network Annual Symposium 17 January 2022 12:00 – 18 January 2022 14:00, London, United Kingdom.

Morphology control of silk fibroin nanoprecipitation under bulk and microfluidic mixing regimes

SAPHIA A L MATTHEW [A], REFAYA REZWAN [B], YVONNE PERRIE [A], F. PHILIPP SEIB[A,C]

[A] Strathclyde Institute of Pharmacy and Biomedical Sciences, University of Strathclyde, 161 Cathedral Street, Glasgow, G4 0RE, U.K; [B] Department of Pharmacy, ASA University Bangladesh, 23/3 Bir Uttam A.N.M Nuruzzaman Sarak, Dhaka 1207, Bangladesh; [C] EPSRC Future Manufacturing Research Hub for Continuous Manufacturing and Advanced Crystallisation (CMAC), University of Strathclyde, Technology and Innovation Centre, 99 George Street, Glasgow G1 1RD, U.K.

Abstract

The control of silk fibroin multiscale structure by shear processing is fundamental to the biopolymer function in the natural world and can be harnessed in nanoprecipitation. Here, we report the modulation of silk fibroin primary–tertiary self-assembly by varying factors which control shear and mixing during nanoprecipitation in semi-batch and micro-mixers. Under high shear regimes and bulk mixing conditions, the size and polydispersity index of assemblies decreased with mixing time, as stirring rate (800, 400 < 0 rpm) and feed addition height (3.5 < 0 cm) increased. Using the optimised conditions for low bulk mixing times, moving from low to high shear processing increased the extent of self-assembly (0.017 < 16.96 mL min^{-1}) for 0.5, 2 and 3% *w/v* silk. Finally, in conditions of high shear and low mixing time, the feed concentration controlled the assembly shape, size, and polydispersity index in microfluidic (0.5, 3.0 < 2% *w/v*) and semi-batch format (3.0 < 0.5% *w/v*). Although the multiscale structure was varied with silk precursor concentration in high shear, fast bulk mixing, mixtures of spherical nanoparticles with nanofiber, lamellar and gel-like assemblies were formed. Due to the sufficiently low micro-mixing times in high shear, microfluidic format, the particle morphology was tuned from monodisperse, worm-like to spherical nanoparticles by increasing concentration from 0.5 to 3% *w/v* silk precursor. This comparative work provides new insight into morphology control of silk nanoparticles using silk concentration as a controllable input factor.

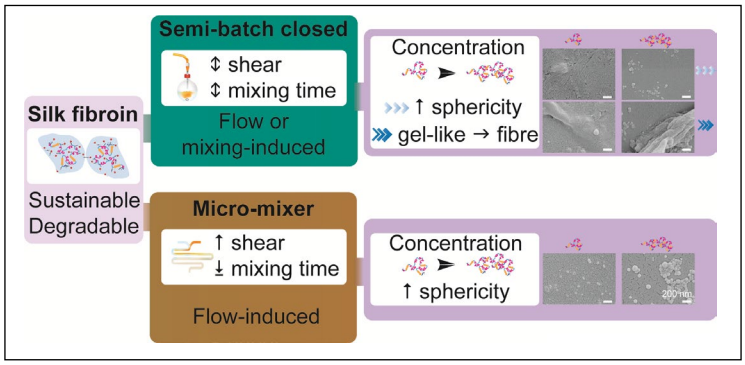

Figure 1 - The silk feed shear and solvent-antisolvent mixing time influences nanoprecipitation of the silk biopolymer. Assemblies were characterized from low and high shear semi-batch nanofabrication platforms and a high shear micro-mixer.

Acknowledgements (optional): The authors thank Professor Andrea Ducci (University College London), Professor Nigel Mottram (University of Glasgow), Dr Alice Turner, Dr Deborah Bowering and Dr Maider Olasolo (University of Strathclyde) for providing training and technical advice. The authors acknowledge that this work was carried out in part at the EPSRC Future Manufacturing Research Hub for Continuous Manufacturing and Advanced Crystallisation (CMAC) (EP/P006965/1). S.A.L.M. is supported by a Medical Research Scotland Ph.D. Studentship (PhD-1292-2018).

Appendix C

Abstract accepted for oral presentation at the 2022 RSC Particle Characterization Interest Group The FORGE: Hybrid Conference on Particle Characterization 23 March 2022 09:00 – 24 March 2022 13:00, Belfast, United Kingdom.

Flow control of silk fibroin nanoparticle morphology in microfluidic and semi-batch mixing regimes

Saphia A L Matthew,[A] Refaya Rezwan,[B] Jirada Kaewchuchuen,[A] Yvonne Perrie[A] and F. Philipp Seib[A,C]

[A] Strathclyde Institute of Pharmacy and Biomedical Sciences, University of Strathclyde, 161 Cathedral Street, Glasgow, G4 0RE, U.K; [B] Department of Pharmacy, ASA University Bangladesh, 23/3 Bir Uttam A.N.M Nuruzzaman Sarak, Dhaka 1207, Bangladesh; [C] EPSRC Future Manufacturing Research Hub for Continuous Manufacturing and Advanced Crystallisation (CMAC), University of Strathclyde, Technology and Innovation Centre, 99 George Street, Glasgow G1 1RD, U.K

Abstract

Nanoprecipitation of reverse-engineered silk fibroin provides a reproducible bottom-up manufacturing route for colloidal nanoparticles. These particles are suited to drug delivery, by virtue of the narrow polydispersity and spherical morphology obtained in continuous[1,2] and semi-batch formats.[1–3] Tuning silk nanoparticle morphology could increase therapeutic benefit, by altering the biological interface and rheological properties.[4–6] Here, we report the modulation of silk fibroin self-assembly by varying factors which control shear and supersaturation during nanoprecipitation in semi-batch bulk mixing and micro-mixing. In bulk mixing conditions, at high stirring rate (low mixing time) shear-induced self-assembly increased as flow rate increased (0.017 < 16.96 mL min^{-1}) in the feed needle and the critical shear rate was surpassed, resulting in polydisperse mixtures of lamellar, nanofibre and nanoparticle assemblies for 0.5, 2 and 3% *w/v* silk. Conversely, at low stirring rate (high mixing time), the reduction to mixing time with increased flow rate dominated over shear effects causing reductions to assembly size and polydispersity index (0.017 > 16.96 mL min^{-1}) for 0.5 and 2% *w/v* silk, by increasing the rate of kinetic locking. Similarly, the mixing time was the dominant factor controlling self-assembly in the micromixer, with the greater shear-induced and antisolvent-induced nucleation rates at high flow rate resulting in narrow polydispersity nanoparticles (1 µL min^{-1} > 1 mL min^{-1}) for 0.5, 2 and 3% *w/v* silk. In bulk and micromixing processes, at flow rates where the shear rate lay below the critical shear rate for silk (low shear processes), increasing the concentration of silk resulted in particle populations of increased sphericity (0.5% *w/v* < 3% *w/v*), lower size, and lower polydispersity index (0.5% *w/v* > 3% *w/v*). At high flow rates where the critical shear rate was exceeded (high shear processes), the increase in supersaturation as concentration increased was counteracted by

increased rates of shear-induced assembly. Morphology could be tuned from narrow polydispersity rod-like to spherical assemblies by increasing supersaturation in the high shear micro-mixing processes (0.5% *w/v* to 3% *w/v*), supporting the role of fast mixing in the production of monodisperse silk particles. This work provides new insight into the effects of shear during nanoprecipitation and provides a framework for scalable manufacture of low polydispersity, spherical and rod-like silk nanoparticles.

References

1 T. Wongpinyochit, B. F. Johnston and F. P. Seib, *J. Visualized Exp.*, 2016, e54669.

2 J. I. Solomun, J. D. Totten, T. Wongpinyochit, A. J. Florence and F. P. Seib, *ACS Biomater. Sci. Eng.*, 2020, **6**, 2796–2804.

3 S. A. L. Matthew, J. D. Totten, S. Phuagkhaopong, G. Egan, K. Witte, Y. Perrie and F. P. Seib, *ACS Biomaterials Science and Engineering*, 2020, **6**, 6748–6759.

4 J. Zhao and M. H. Stenzel, *Polymer Chemistry*, 2018, **9**, 259–272.

5 W. Richtering, I. Alberg and R. Zentel, *Small*, 2020, **16**, 1–8.

6 M. C. Arno, M. Inam, A. C. Weems, Z. Li, A. L. A. Binch, C. I. Platt, S. M. Richardson, J. A. Hoyland, A. P. Dove and R. K. O'Reilly, *Nature Communications*, 2020, **11**, 1420.